PHD

Glasses under extreme conditions

Pizzey, Keiron

Award date:
2015

Awarding institution:
University of Bath

Glasses Under Extreme Conditions

submitted by

Keiron J. Pizzey

for the degree of Doctor of Philosophy

of the

University of Bath

Department of Physics

June 3, 2015

Abstract

The method of *in situ* high-pressure neutron diffraction was used to measure the structural transformations that take place upon cold-compression of several network-forming amorphous materials. The chalcogenide glasses $GeSe_2$, $GeSe_4$, and As_2Se_3, and the silicate glass $CaSiO_3$, were investigated using a Paris-Edinburgh press to provide compression. Where possible, the neutron diffraction results were compared to experimental results and molecular dynamics (MD) simulations provided by other research groups.

Amorphous $GeSe_2$ was studied at pressures up to 16.1 GPa using a combination of neutron diffraction, neutron diffraction with isotope substitution (NDIS), and first-principles molecular dynamics (FPMD) simulations. It was found that the network transformations occurred in two stages. In the first stage up to ~ 8 GPa, the structure re-arranged on an intermediate length scale by re-organising corner and edge-sharing $GeSe_4$ tetrahedra. Above 8 GPa, both 5- and 6-fold coordinated Ge atoms began to form as the mean nearest-neighbour coordination number $\overline{n}$ and mean nearest-neighbour bond distance $\overline{r}$ both increased. A disagreement between the neutron diffraction and FPMD results above 8.5 GPa is attributed to the presence of an energy barrier. This barrier inhibits structural rearrangement in a cold-compression diffraction experiment, but allows them to occur via a high-temperature annealing stage in the simulations.

Amorphous $GeSe_4$ was studied at pressures up to 14.4 GPa using a combination of neutron diffraction and FPMD. The nearest-neighbour coordination environment was found to vary little across the measured pressure range, but structural transformations took place on an intermediate length scale as seen by the pressure-dependence of the second nearest-neighbour distance in the neutron diffraction results. The new experimental results are in accord with FPMD results and with those obtained from a study using x-ray diffraction (XRD). There are, however, major inconsistencies with the results obtained from a different study in which XRD was combined with empirical potential structure refinement (EPSR). It is hypothesised that this disagreement is due to the difficulty of modelling XRD results with EPSR for glasses in the Ge-Se system, where the x-ray atomic form factors of Ge and Se are similar. The reduced-density ρ/ρ_0 dependence of the results was compared to that obtained for amorphous $GeSe_2$, where ρ is the atomic number density at pressure and ρ_0 is the atomic number density at ambient pressure. It was found that for both materials the local coordination environment does not change for $\rho/\rho_0 < 1.6$.

Amorphous As_2Se_3 was studied at pressures up to 14.4 GPa using a mixture of neutron diffraction, NDIS, and FPMD. At the total structure factor level, no change was observed to the nearest-neighbour coordination environment. The NDIS results do, however, suggest a change to the nearest-neighbour coordination environment begin-

ning at 6 GPa. The results were compared to those found for two crystalline polymorphs of As_2Se_3, one prepared at ambient pressure and the other recovered to ambient conditions from high-pressure and -temperature. The differences between the coordination environments of these crystalline polymorphs pointed to some possible densification mechanisms in the glass. Ambient-pressure NDIS was also used to measure the full set of partial pair-distribution functions.

Amorphous $CaSiO_3$ was studied at pressures up to 17.5 GPa using neutron diffraction. The Si-O coordination number started to increase beyond a threshold pressure of 13 GPa, as compared to 15 GPa for amorphous SiO_2. The results were used to test the validity of two sets of MD simulations that used different interatomic potentials and thermal processes for producing the glass. The results were found to agree with the MD simulations that used a cold-compression protocol.

Acknowledgements

I thank my supervisor Phil Salmon for his advice and support during my PhD, and particularly thank him for his help in writing up my thesis. I thank my colleagues in the Liquids and Amorphous Materials (LAM) group: Anita Zeidler, Dean Whittaker, Kamil Wezka, Ruth Rowlands, and Annalisa Polidori, for their help and friendship during my time in Bath. I also thank Harry Bone, Phil Jones, Paul Reddish, Wendy Lambson, and Simon Dodd from the University of Bath for their help and support.

From the ILL I thank Henry Fischer, Alain Bertoni, and Jean-Luc Laborier for their help with D4c experiments. From ISIS, I thank Craig Bull, Matt Tucker, Phil Hawkins for their help with my PEARL experiments. I would also like to thank Alex Hannon, Ross Stewart, Jon Taylor, and Evgeniy Goremychkin for their help with GEM and MARI/MERLIN experiments which were not presented in this thesis.

I thank Stefan Klotz for sharing his expertise on high pressure physics and Lawrie Skinner and Richard Weber for their advice in the preparation of amorphous $CaSiO_3$. I thank Assil Bouzid and Carlo Massobrio for providing first-principles molecular dynamics (FPMD) simulations of $GeSe_2$ and $GeSe_4$, Lawrie Skinner again for providing $GeSe_4$ x-ray diffraction data, Bora Kalkan for providing his $GeSe_4$ x-ray diffraction and empirical potential structure refinement (EPSR) results, Matthieu Micoulaut for providing As_2Se_3 FPMD simulations, Emmanuel Soignard for providing As_2Se_3 density measurements, and Gavin Mountjoy for providing $CaSiO_3$ simulations.

I thank the Engineering and Physical Sciences Research Council (EPSRC) for financial support. I also thank the organisers of the Oxford Neutron Training School for the theoretical training they provided.

I thank my friends, family, and loved ones. They have been a source of constant support that have helped me to complete this PhD. Finally, I'd like to thank the $\sim 10^{23}$ neutrons that helped in getting my results.

List of publications

- K. Wezka, A. Bouzid, K. J. Pizzey, P. S. Salmon, A. Zeidler, S. Klotz, H. E. Fischer, C. L. Bull, M. G. Tucker, M. Boero, S. Le Roux, C. Tugène and C. Massobrio. The density-driven defect-mediated network collapse of $GeSe_2$ glass. *Phys. Rev. B*, 90:054206, 2014

Contents

1. Introduction

Liquids and glasses have extensive importance in several areas of modern science and technology, including photonics and opto-electronics [1–14], geophysics [15, 16], and biological systems [17, 18]. Glasses are a subset of amorphous materials, and are one of the most common materials in our every day lives.

Structurally, glasses do not exhibit the long-range order (LRO) that is found in crystalline materials. They do, however, show short-range order (SRO) up to 4 Å, and intermediate-range order (IRO) which can extend up to ~ 10 Å. Some glasses can even show extended-range order (ERO) on a nanometre length-scale. The origin of SRO is due to structural motifs, such as the SiO_4 tetrahedron in SiO_2, whilst the IRO and ERO primarily occur from the joining of these structural motifs to one another.

The application of extreme conditions such as high-pressures and/or -temperatures to glassy materials can be used to gradually change their physico-chemical properties, or to cause sudden changes as in so-called polyamorphic phase transitions [19–21]. Material properties such as the electrical conductivity, elastic moduli, and glass forming ability can all change when extreme conditions are applied [11, 21–28]. The possibility of glass-to-crystal transitions, as used in phase-change memory applications with the application of a laser to produce intense heat over a small area [29, 30], and semiconductor-to-metal transitions [31–34] are also of interest. It is of further interest to recover glasses to ambient conditions with suitably modified physico-chemical properties, as this would allow glasses to be "tuned" through the application of heat and pressure [35–39].

Investigating the structure of liquids under extreme conditions, such as magmatic liquids, is experimentally difficult [40]. However, glasses are able to explore localities on an energy landscape that are inaccessible to a crystal. It is hoped that by studying the structure of glasses under extreme conditions, new insights can be found into the structure of compressed liquids under extreme conditions that are not easily accessible by experiment.

Neutron and x-ray diffraction can be used to measure the structure of amorphous materials. If neutron diffraction with isotopic substitution is used, then site-specific in-

formation can be extracted on local coordination environments. The theory of diffraction for neutrons and x-rays is broadly the same, however the physical processes by which they scatter from a sample are different. Neutrons scatter directly from the atomic nuclei and as such they provide a direct probe of the atomic positions. X-rays, on the other hand, scatter from the electron clouds that surrounds the nuclei.

For both neutrons and x-rays, the diffraction pattern for a system of n different chemical species is comprised of $n(n+1)/2$ so-called Faber-Ziman (FZ) partial structure factors $S^{\mathrm{FZ}}_{\alpha\beta}(Q)$, where $\hbar Q$ is the momentum transfer associated with the scattering event. These functions describe the pair-correlations between atoms of species α and β. The corresponding real space information is gained by Fourier transformation, allowing the pair-distributions of atoms about a central atom to be investigated directly. This real space information can be used to calculate parameters such as coordination numbers, bond distances, and bond angle distributions.

In this thesis, neutron diffraction is used to probe the atomic structure of glasses *in situ* under high-pressure conditions. The investigated systems include the chalcogenide glasses $GeSe_2$, $GeSe_4$, and As_2Se_3, and the silicate glass $CaSiO_3$. The thesis is organised as follows:-

- Chapter 2 - The theory required for neutron diffraction experiments is presented, beginning with the neutron itself, progressing to include the theory of both reciprocal and real space, and finishing with neutron diffraction with isotope substitution (NDIS). High-pressure equations of state are also considered.

- Chapter 3 - The operation of the D4c and PEARL diffractometers, based at the Institut Laue-Langevin and the ISIS pulsed neutron source, respectively, is discussed. The experimental details necessary to conduct *in situ* high-pressure neutron diffraction measurements using a Paris-Edinburgh press are also presented. Finally, the data analysis procedures are discussed.

- Chapter 4 - The chalcogenide glass $GeSe_2$ is investigated at pressures up to 16.1(5) GPa using both the D4c and PEARL diffractometers. The D4c results make use of NDIS to provide information at the first-order difference function level [41]. The results are complemented by first-principles molecular dynamics (FPMD) simulations [42]. The neutron diffraction and FPMD results are used to form a new theory for the density-driven densification mechanisms of $GeSe_2$.

- Chapter 5 - The chalcogenide glass $GeSe_4$ is investigated at pressures up to 14.4(5) GPa using both the D4c and PEARL diffractometers. The neutron diffraction results are compared with FPMD results [42], with x-ray diffraction results [43] and with x-ray diffraction and empirical potential structure refinement

(EPSR) results [44]. The results for $GeSe_4$ are also compared to the results presented in chapter 4 on $GeSe_2$ glass.

- Chapter 6 - Amorphous As_2Se_3 is investigated at pressures up to 14.4(5) GPa using both the D4c and PEARL diffractometers. The D4c results make use of NDIS to provide information at the first-order difference function level. The results are compared at ambient pressure to reverse Monte Carlo calculations derived from anomalous x-ray scattering measurements [45] and FPMD results [45–47].

- Chapter 7 - Amorphous $CaSiO_3$ is investigated at pressures up to 17.5(5) GPa using the PEARL diffractometer. The results are used to test the validity of two competing sets of molecular dynamics (MD) simulations [48, 49]. The results are also compared to the results for amorphous SiO_2 [50].

- Chapter 8 - Conclusions are presented together with some examples of potential future work.

2. Theory

This chapter outlines the basic theory for neutron diffraction experiments, including the basic properties of neutrons, how structural information can be accessed from diffraction patterns, and how isotope substitution can be used to glean further information. A brief outline of the theory of equations of state is also discussed. A review of using neutron diffraction to study networks under pressure can be found in Ref. [51].

2.1 The neutron

Neutron scattering is an experimental technique that can be utilised to study both the structure and dynamics of materials. Neutrons have zero charge, allowing them to interact with nuclei directly through the strong force. This direct interaction allows for the accurate measurement of both the structure and dynamics (*e.g.* vibrational properties) of a system.

The kinetic energy E of a neutron is given by

$$E = \frac{m_\mathrm{n}|\mathbf{v}|^2}{2} = \frac{|\mathbf{p}|^2}{2m_\mathrm{n}}, \tag{2.1}$$

where m_n is the mass of a neutron, $\mathbf{v}$ is its velocity, and $\mathbf{p}$ its momentum. The de Broglie wavelength of a neutron is given by

$$\lambda = \frac{h}{|\mathbf{p}|} = \frac{h}{m_\mathrm{n}|\mathbf{v}|}, \tag{2.2}$$

where $h = 6.626 \times 10^{-34}\,\mathrm{J\,s}$ is Planck's constant and $|\mathbf{x}|$ indicates the absolute value of $\mathbf{x}$. Finally the magnitude of a neutron's wavevector $\mathbf{k}$ is given by

$$|\mathbf{k}| = \frac{2\pi}{\lambda}. \tag{2.3}$$

2.2 Neutron scattering

Consider a neutron with incident wavevector $\mathbf{k_i}$ and kinetic energy E_i which undergoes scattering such that the final wavevector is $\mathbf{k_f}$ and the final kinetic energy is E_f. Then the scattering vector is given by

$$\mathbf{Q} = \mathbf{k_i} - \mathbf{k_f}. \tag{2.4}$$

For such a scattering event the momentum transfer is defined as

$$\Delta\mathbf{p} = \hbar\mathbf{k_i} - \hbar\mathbf{k_f} = \hbar\mathbf{Q}, \tag{2.5}$$

where $\hbar = h/2\pi$ is the reduced Planck's constant. The corresponding energy transfer is given by

$$\Delta E = E_i - E_f = \frac{\hbar^2|\mathbf{k_i}|^2}{2m_\mathrm{n}} - \frac{\hbar^2|\mathbf{k_f}|^2}{2m_\mathrm{n}}. \tag{2.6}$$

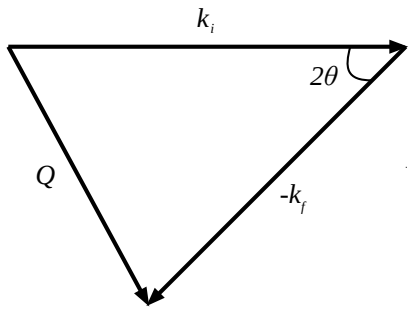

Figure 2-1: The scattering triangle.

The scattering triangle is shown in figure 2-1. Applying the cosine rule to the scattering triangle gives, for a scattering angle of 2θ,

$$Q^2 = k_i^2 + k_f^2 - 2k_ik_f\cos(2\theta), \tag{2.7}$$

where $Q = |\mathbf{Q}|$, $k_i = |\mathbf{k_i}|$, and $k_f = |\mathbf{k_f}|$. In the static approximation, which is often used in total scattering studies, $\frac{\Delta E}{E_i} << 0$ and the incident and final wavevectors are approximately equal *i.e.*

$$|\mathbf{k_i}| = \frac{2\pi}{\lambda_i} \approx |\mathbf{k_f}| = \frac{2\pi}{\lambda_f}. \tag{2.8}$$

In the static approximation equation (2.7) can be simplified to

$$Q = \frac{4\pi}{\lambda}\sin(\theta). \tag{2.9}$$

2.3 Neutron diffraction

Consider a neutron diffraction experiment as shown in figure 2-2. A collimated beam of incident neutrons with flux Φ is scattered by the nuclei within a system. Neutrons are scattered into a detector of area $\mathrm{d}S$ at a distance $|\mathbf{R}|$ from the sample position, where the detector subtends a small solid angle $\mathrm{d}\Omega = \mathrm{d}S/|\mathbf{R}|^2$. In such a neutron scattering experiment the differential scattering cross-section is given by [52]

$$\frac{\mathrm{d}\sigma}{\mathrm{d}\Omega} = \frac{\text{Number of particles scattered into } \mathrm{d}\Omega \text{ per second}}{\Phi\,\mathrm{d}\Omega}. \tag{2.10}$$

It is also possible to define the differential scattering cross-section in terms of Q, where the relation between Q and 2θ is given by equation (2.9).

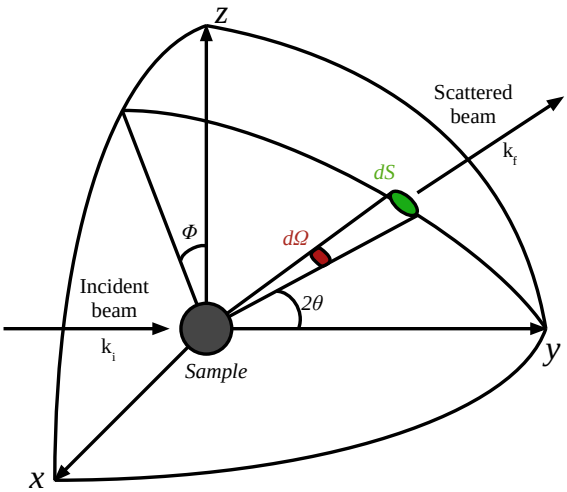

Figure 2-2: Diagram showing the scattering of neutrons by a system into a detector of surface area $\mathrm{d}S$.

The scattering cross-section for a single spin-less bound nucleus of chemical species α is given by

$$\sigma_\alpha = 4\pi b_\alpha^2 \tag{2.11}$$

where b_α is the so-called scattering length and describes how strongly a neutron scatters from a nucleus of chemical species α. It is possible for isotopes of the same chemical species to have very different scattering lengths [53].

For a sample of N scattering centres containing n different chemical species the differential scattering cross-section is given by

$$\frac{1}{N}\frac{\mathrm{d}\sigma}{\mathrm{d}\Omega}(Q) = F(Q) + \sum_{\alpha=1}^{n} c_\alpha \left(b_{\mathrm{coh},\alpha}^2 + b_{\mathrm{inc},\alpha}^2\right)\left[1 + P_\alpha\left(Q\right)\right], \tag{2.12}$$

where $F(Q)$ is the total structure factor; c_α is the concentration of chemical species α; b_α and $b_{\alpha,\mathrm{inc}}$ are the bound coherent and incoherent scattering lengths of chemical species α, respectively; and $P_\alpha(Q)$ is an inelasticity correction. The total structure factor contains information on the structure of the system. The second term, known as the self-scattering term, arises from scattering by individual nuclei. The inelasticity correction is necessary to account for finite recoil in the neutron-nucleus interactions and therefore arises from a breakdown of the static approximation. The inelasticity correction is more severe for light nuclei due to the similar masses of the nucleus and a neutron. The correction is smaller for heavy nuclei and $P_\alpha(Q)$ is typically calculated in a procedure first outlined in Ref. [54].

The total structure factor can be broken down as

$$F(Q) = \sum_{\alpha=1}^{n}\sum_{\beta=1}^{n} c_\alpha c_\beta b_\alpha b_\beta \left[S_{\alpha\beta}^{\mathrm{FZ}}(Q) - 1\right], \tag{2.13}$$

where $S_{\alpha\beta}^{\mathrm{FZ}}(Q)$ is the Faber-Ziman [55] partial structure factor for chemical species α and β. Thus, for a binary system $\mathrm{A_xB_{1-x}}$ ($0 \leq x \leq 1$) there are four partial structure factors: $S_{\mathrm{AA}}^{\mathrm{FZ}}(Q)$, $S_{\mathrm{BB}}^{\mathrm{FZ}}(Q)$, $S_{\mathrm{AB}}^{\mathrm{FZ}}(Q)$, and $S_{\mathrm{BA}}^{\mathrm{FZ}}(Q)$. It is found for glasses, however, that $S_{\mathrm{AB}}^{\mathrm{FZ}}(Q) = S_{\mathrm{BA}}^{\mathrm{FZ}}(Q)$ *i.e.* only three partial structure factors need to be considered.

The formalism for diffraction experiments is in reciprocal space but through Fourier transformation it is possible to find the information about atomic positions in real space. For an isotropic system, such as a glass, the Faber-Ziman partial structure factors can be Fourier transformed to give the so-called partial pair-distribution functions $g_{\alpha\beta}^{\mathrm{FZ}}(r)$. The Fourier transform relationships are given by

$$S_{\alpha\beta}^{\mathrm{FZ}}(Q) - 1 = \frac{4\pi\rho}{Q}\int_0^\infty r\left[g_{\alpha\beta}^{\mathrm{FZ}}(r) - 1\right]\sin(Qr)\,\mathrm{d}r, \tag{2.14}$$

and

$$g_{\alpha\beta}^{\mathrm{FZ}}(r) - 1 = \frac{1}{2\pi^2 r\rho}\int_0^\infty Q\left[S_{\alpha\beta}^{\mathrm{FZ}}(Q) - 1\right]\sin(Qr)\,\mathrm{d}Q, \tag{2.15}$$

where ρ is the atomic number density, and r is a distance in real space. The partial pair-distribution function $g_{\alpha\beta}^{\mathrm{FZ}}(r)$ describes the probability of finding an atom of chem-

ical species β at a radial distance r away from a central atom of chemical species α. The coordination number, $\overline{n}_{\alpha}^{\beta}$, gives the mean number of atoms of chemical species β contained in a volume defined by two spheres of radii r_1 and r_2 centred on a central atom of chemical species α

$$\overline{n}_{\alpha}^{\beta} = 4\pi\rho c_{\beta} \int_{r_1}^{r_2} r^2 g_{\alpha\beta}^{\mathrm{FZ}}(r)\,\mathrm{d}r. \tag{2.16}$$

The total structure factor $F(Q)$ can be Fourier transformed to give the total pair-distribution function

$$\begin{aligned} G(r) &= \frac{1}{2\pi^2 r\rho} \int_0^{\infty} QF(Q)\sin(Qr)\,\mathrm{d}Q \\ &= \sum_{\alpha=1}^{n}\sum_{\beta=1}^{n} c_{\alpha}c_{\beta}b_{\alpha}b_{\beta}\left[g_{\alpha\beta}^{\mathrm{FZ}}(r) - 1\right]. \end{aligned} \tag{2.17}$$

At distances below the minimum separation between atoms, $g_{\alpha\beta}^{\mathrm{FZ}}(r) = g_{\alpha\beta}^{\mathrm{FZ}}(r \to 0) = 0$ such that

$$G(r) = G(r \to 0) = -\sum_{\alpha=1}^{n}\sum_{\beta=1}^{N} c_{\alpha}c_{\beta}b_{\alpha}b_{\beta} = -\langle b\rangle^2, \tag{2.18}$$

where $\langle b\rangle = \sum c_{\alpha}b_{\alpha}$ is the average coherent scattering length.

In a neutron diffraction experiment, the Q-range is limited to a finite value Q_{max}. As such, $F(Q)$ is truncated by a modification function $M(Q)$ such that

$$M(Q) = \begin{cases} 1 & \text{if } Q \leq Q_{\mathrm{max}} \\ 0 & \text{if } Q > Q_{\mathrm{max}}. \end{cases} \tag{2.19}$$

The total pair-distribution function $G(r)$ can then be re-defined as

$$G(r) = \frac{1}{2\pi^2 r\rho} \int_0^{\infty} QM(Q)F(Q)\sin(Qr)\,\mathrm{d}Q. \tag{2.20}$$

Consider the scenario where $F(Q)$ shows finite oscillations at Q_{max}. In such a case, Fourier transform artefacts will affect the total pair-distribution function. The severity of these Fourier transform artefacts can be reduced by using a Lorch modification function in place of a step function for $M(Q)$ [56]. The Lorch modification function is defined as

$$M(Q) = \begin{cases} \frac{\sin(aQ)}{aQ} & \text{if } Q \leq Q_{\max} \\ 0 & \text{if } Q > Q_{\max}, \end{cases} \tag{2.21}$$

where $a = \pi/Q_{\max}$ [57]. The reduction of sharp Fourier transformation artefacts caused by the use of a Lorch modification function occurs at the expense of broadened r-space features.

As well as using the Faber-Ziman formalism it is also possible to describe the total structure factor of a binary system in terms of the Bhatia-Thornton partial structure factors [58]. These partial structure factors describe the number-number (N-N), concentration-concentration (C-C), and number-concentration (N-C) correlations, and are denoted by $S^{\mathrm{BT}}_{\mathrm{NN}}(Q)$, $S^{\mathrm{BT}}_{\mathrm{CC}}(Q)$, and $S^{\mathrm{BT}}_{\mathrm{NC}}(Q)$, respectively. In this case the total structure factor can be re-written as

$$\begin{aligned} F(Q) = \langle b \rangle^2 \left[S^{\mathrm{BT}}_{\mathrm{NN}}(Q) - 1 \right] + \\ c_\alpha c_\beta \left(b_\alpha - b_\beta \right)^2 \left\{ \left[\frac{S^{\mathrm{BT}}_{\mathrm{CC}}(Q)}{c_\alpha c_\beta} \right] - 1 \right\} + \\ 2 \langle b \rangle \left(b_\alpha - b_\beta \right) S^{\mathrm{BT}}_{\mathrm{NC}}(Q). \end{aligned} \tag{2.22}$$

$S^{\mathrm{BT}}_{\mathrm{NN}}(Q)$ contains information on the global structure of a sample and treats all atomic sites equally without concern for the chemical species. Consider the case when $b_\alpha = b_\beta$. Then $S^{\mathrm{BT}}_{\mathrm{CC}}(Q)$ and $S^{\mathrm{BT}}_{\mathrm{NC}}(Q)$ are both eliminated meaning that a diffraction experiment can be made which measures $S^{\mathrm{BT}}_{\mathrm{NN}}(Q)$ directly, *i.e.*

$$F(Q) = \langle b \rangle^2 \left[S^{\mathrm{BT}}_{\mathrm{NN}}(Q) - 1 \right]. \tag{2.23}$$

Such a scenario can occur fortuitously, as in the case of the $\mathrm{Ge}_x\mathrm{Se}_{1-x}$ system where the scattering lengths for atoms having the natural isotopic abundance are $b_{\mathrm{Ge}} = 8.185\,\mathrm{fm}$ and $b_{\mathrm{Se}} = 7.97\,\mathrm{fm}$, or through the careful application of isotope substitution. The Fourier transform of $S^{\mathrm{BT}}_{\mathrm{NN}}(Q)$ is denoted by $g^{\mathrm{BT}}_{\mathrm{NN}}(r)$ and is related to the probability of finding any atom at a distance r away from a central atom. Using $g^{\mathrm{BT}}_{\mathrm{NN}}(r)$ the coordination number averaged over all types of chemical species can be calculated using [59]

$$\overline{n} = 4\pi\rho \int_{r_1}^{r_2} r^2 g^{\mathrm{BT}}_{\mathrm{NN}}(r)\,\mathrm{d}r. \tag{2.24}$$

$S^{\mathrm{BT}}_{\mathrm{CC}}(Q)$ contains information on the chemical ordering of the species α and β with respect to the sites specified by $S^{\mathrm{BT}}_{\mathrm{NN}}(Q)$. The Fourier transform of $S^{\mathrm{BT}}_{\mathrm{CC}}(Q)$, denoted by $g^{\mathrm{BT}}_{\mathrm{CC}}(r)$, contains information on the relative nature of so-called homopolar and heteropolar correlations, where a positive peak at a given distance is indicative of a preference for heteropolar correlations at that distance and, vice versa, a negative peak at a given distance indicates a preference for homopolar correlations. $S^{\mathrm{BT}}_{\mathrm{NC}}(Q)$ relates to the correlation between atomic sites and their chemical occupancy [60].

It is possible to fit the partial pair-distribution functions contained within a total pair-distribution function. This fitting can be used to calculate accurate mean coordination numbers when there are overlapping correlations, but can also be used to take into account the finite Q-range that diffractometers make measurements over. The differential correlation function can be defined as

$$D_{\mathrm{exp}}(r) = \frac{2}{\pi}\int_0^\infty Q\frac{F(Q)}{\left|G(0)\right|}\sin(Qr)M(Q)\,\mathrm{d}Q. \tag{2.25}$$

The normalisation by $\left|G(0)\right|$ ensures that the weighting factors for the $g^{\mathrm{FZ}}_{\alpha\beta}(r)$ functions sum to unity. The modification function

$$M(Q) = \begin{cases} 1 & \text{if } Q \leq Q_{\mathrm{max}} \\ 0 & \text{if } Q > Q_{\mathrm{max}}. \end{cases} \tag{2.26}$$

is used to account for the finite cutoff Q_{max}. Equation (2.25) can be written as [61]

$$\begin{aligned} D_{\mathrm{exp}}(r) &= 4\pi\rho r\frac{G(r)}{\left|G(0)\right|} \otimes P(r) \\ &= 4\pi\rho\sum_{\alpha=1}^{n}\sum_{\beta=1}^{n}\frac{c_\alpha c_\beta b_\alpha b_\beta}{\left|G(0)\right|} r g^{\mathrm{FZ}}_{\alpha\beta}(r) \otimes P(r) - 4\pi\rho r, \end{aligned} \tag{2.27}$$

where

$$\begin{aligned} P(r) &= \frac{1}{\pi}\int_0^{Q_{\mathrm{max}}}\cos(Qr)\,\mathrm{d}Q \\ &= \frac{Q_{\mathrm{max}}}{\pi}\mathrm{sinc}(Q_{\mathrm{max}}r) \end{aligned} \tag{2.28}$$

is the real-space manifestation of the modification function $M(Q)$.

Each peak in real-space can then be represented by a sum of weighted Gaussian

functions, given by

$$D_{\text{fit}}\left(r; r_{\alpha\beta}, \overline{n}_{\alpha}^{\beta}, \sigma_{\alpha\beta}\right) = \sum_{i} \left(w_{\alpha\beta}(i) \, \frac{\overline{n}_{\alpha}^{\beta}(i)}{c_{\beta}(i) r_{\alpha\beta}(i)} \frac{1}{\sqrt{2\pi}\sigma_{\alpha\beta}(i)} \times \right.$$
$$\left. \exp\left\{ \frac{-\left[r - r_{\alpha\beta}(i)\right]^2}{2\left[\sigma_{\alpha\beta}(i)\right]^2} \right\} \otimes P(r) \right) - 4\pi\rho r, \tag{2.29}$$

where $r_{\alpha\beta}$ is a vector of peak positions, $\overline{n}_{\alpha}^{\beta}$ is a vector of coordination numbers, $\sigma_{\alpha\beta}$ is a vector of Gaussian widths, $w_{\alpha\beta} = 2c_{\alpha}c_{\beta}b_{\alpha}b_{\beta}/\left|G(0)\right|$ for $\alpha \neq \beta$ and $w_{\alpha\beta} = c_{\alpha}^2 b_{\alpha}^2/\left|G(0)\right|$ for $\alpha = \beta$, and (i) denotes the parameter for the i'th Gaussian function. This $D_{\text{fit}}(r)$ function can be optimised with respect to the fitting parameters by minimising the R_{χ} function, defined as [62]

$$R_{\chi}\left(r_{\alpha\beta}, \overline{n}_{\alpha}^{\beta}, \sigma_{\alpha\beta}\right) = \sqrt{\frac{\sum_i \left[D_{\text{exp}}(r_i) - D_{\text{fit}}(r_i)\right]^2}{\sum_i D_{\text{exp}}^2(r_i)}}. \tag{2.30}$$

Once the fitting is complete, the mean coordination numbers and peak positions for each set of correlations is then known from the parameters.

2.4 Isotopic substitution

In a diffraction experiment the total structure factor as defined by equation (2.13) is measured, meaning that inferences must be made to relate specific features with specific correlation functions. It is therefore desirable to measure the full set of partial structure factors.

Consider a sample of n chemical species with $m = (n+1)n/2$ partial structure factors. If m measurements are made on samples that are identical in every aspect, except that the scattering length of one or more chemical species has been modified, then it is possible to find the full set of partial structure factors through matrix inversion. Consider a binary system ($n = 2$) for which $m = 3$ measurements are made to measure the total structure factors $F_1(Q)$, $F_2(Q)$, and $F_3(Q)$. Then a scattering matrix can be defined as

$$\begin{pmatrix} F_1(Q) \\ F_2(Q) \\ F_3(Q) \end{pmatrix} = \begin{pmatrix} c_\alpha^2 b_{\alpha,1}^2 & c_\beta^2 b_{\beta,1}^2 & 2c_\alpha c_\beta b_{\alpha,1} b_{\beta,1} \\ c_\alpha^2 b_{\alpha,2}^2 & c_\beta^2 b_{\beta,2}^2 & 2c_\alpha c_\beta b_{\alpha,2} b_{\beta,2} \\ c_\alpha^2 b_{\alpha,3}^2 & c_\beta^2 b_{\beta,3}^2 & 2c_\alpha c_\beta b_{\alpha,3} b_{\beta,3} \end{pmatrix} \cdot \begin{pmatrix} S_{\alpha\alpha}(Q) - 1 \\ S_{\beta\beta}(Q) - 1 \\ S_{\alpha\beta}(Q) - 1 \end{pmatrix} \tag{2.31}$$

or

$$\mathbf{F}(\mathbf{Q}) = \mathbf{A} \cdot \mathbf{S}(\mathbf{Q}), \tag{2.32}$$

where $\mathbf{F}(\mathbf{Q})$ and $\mathbf{S}(\mathbf{Q})$ are column vectors and $\mathbf{A}$ is a matrix. By inverting the matrix it is possible to solve for the partial structure factors

$$\mathbf{S}(\mathbf{Q}) = \mathbf{A}^{-\mathbf{1}} \cdot \mathbf{F}(\mathbf{Q}). \tag{2.33}$$

To conduct an experiment to measure the full set of partial structure factors is difficult and expensive. A large contrast is required between the scattering lengths for a given element, high counting statistics are necessary, and systematic errors must be minimised due to the (typically) large numerical values for the elements of the inverse matrix $\mathbf{A}^{-\mathbf{1}}$. In general it is not possible to measure the full set of partial structure factors in a high-pressure neutron diffraction experiment because the sample sizes are necessarily small and the background scattering (from the high-pressure equipment) is usually large.

Site-specific structural information can, however, be obtained by measuring the so-called first-order difference functions. In a first-order difference function, a single partial structure is eliminated by subtracting either unweighted or weighted total structure factors. This allows for a reduction of the complexity of correlations associated with a single total structure factor, and can help to understand overlapping features by removing one of the correlation functions at a time.

Consider an experiment made to study the structure of a binary sample $\mathrm{A}_{c_\alpha}\mathrm{B}_{c_\beta}$ where two samples are measured that are identical in every respect, except that the scattering length of chemical species B is modified through isotope substitution. In this case two total structure factors $F_1(Q)$ and $F_2(Q)$ are measured such that

$$\begin{aligned} F_1(Q) = c_\alpha^2 b_\alpha^2 \left[S_{\alpha\alpha}^{\mathrm{FZ}}(Q) - 1 \right] + c_\beta^2 b_{\beta,1}^2 \left[S_{\beta\beta}^{\mathrm{FZ}}(Q) - 1 \right] + \\ 2c_\alpha b_\alpha c_\beta b_{\beta,1} \left[S_{\alpha\beta}^{\mathrm{FZ}}(Q) - 1 \right] \end{aligned} \tag{2.34}$$

and

$$F_2(Q) = c_\alpha^2 b_\alpha^2 \left[S_{\alpha\alpha}^{\mathrm{FZ}}(Q) - 1\right] + c_\beta^2 b_{\beta,2}^2 \left[S_{\beta\beta}^{\mathrm{FZ}}(Q) - 1\right] + 2c_\alpha b_\alpha c_\beta b_{\beta,2} \left[S_{\alpha\beta}^{\mathrm{FZ}}(Q) - 1\right]. \tag{2.35}$$

The partial structure factor $S_{\alpha\alpha}^{\mathrm{FZ}}(Q)$ can be removed by subtracting the total structure factors without any weighting

$$\begin{aligned}\Delta F(Q)_{\text{no } \alpha\text{-}\alpha} &= F_2(Q) - F_1(Q) \\ &= c_\beta^2 \left(b_{\beta,2}^2 - b_{\beta,1}^2\right) \left[S_{\beta\beta}^{\mathrm{FZ}}(Q) - 1\right] + 2c_\alpha c_\beta b_\alpha \left(b_{\beta,2} - b_{\beta,1}\right) \left[S_{\alpha\mathrm{A}}^{\mathrm{FZ}}(Q) - 1\right].\end{aligned} \tag{2.36}$$

By weighting one of the total structure factors it is also possible to remove one of the other partial structure factors. For example, the partial structure factor $S_{\beta\beta}^{\mathrm{FZ}}(Q)$ can be removed by using

$$\begin{aligned}\Delta F(Q)_{\text{no } \beta\text{-}\beta} &= F_1(Q) - \frac{b_{\beta,1}^2}{b_{\beta,2}^2} F_2(Q) \\ &= c_\alpha^2 b_\alpha^2 \left(1 - \frac{b_{\beta,1}^2}{b_{\beta,2}^2}\right) \left[S_{\alpha\alpha}^{\mathrm{FZ}}(Q) - 1\right] + 2c_\alpha c_\beta b_\alpha \left(b_{\beta,1} - \frac{b_{\beta,1}^2}{b_{\beta,2}}\right) \left[S_{\beta\beta}^{\mathrm{FZ}}(Q) - 1\right].\end{aligned} \tag{2.37}$$

Similarly, the partial structure factor $S_{\alpha\beta}^{\mathrm{FZ}}(Q)$ can be removed by using

$$\begin{aligned}\Delta F(Q)_{\text{no } \alpha\text{-}\beta} &= \frac{b_{\beta,1}}{b_{\beta,2}} F_2(Q) - F_1(Q) \\ &= c_\alpha^2 b_\alpha^2 \left(\frac{b_{\beta,1}}{b_{\beta,2}} - 1\right) \left[S_{\alpha\alpha}^{\mathrm{FZ}}(Q) - 1\right] + c_\beta^2 \left(b_{\beta,2} b_{\beta,1} - b_{\beta 1}^2\right) \left[S_{\beta\beta}^{\mathrm{FZ}}(Q) - 1\right].\end{aligned} \tag{2.38}$$

The real space information corresponding to $\Delta F(Q)_X$ (X = no α-α, no β-β, or no-α-β) is obtained by Fourier transformation to provide a first-order pair-distribution function, *e.g.*

$$\begin{aligned}\Delta G(r)_{\text{no } \alpha\text{-}\beta} &= \frac{1}{2\pi^2 r\rho}\int_0^\infty Q\Delta F(Q)_{\text{no } \alpha\text{-}\beta}\sin(Qr)\,\mathrm{d}Q \\ &= \frac{b_{\beta,1}}{b_{\beta,2}}G_2(Q) - G_1(Q) \\ &= c_\alpha^2 b_\alpha^2\left(\frac{b_{\beta,1}}{b_{\beta,2}} - 1\right)g_{\alpha\alpha}^{\text{FZ}}(r) + c_\beta^2\left(b_{\beta,2}b_{\beta,1} - b_{\beta,1}^2\right)g_{\beta\beta}^{\text{FZ}}(r) + \Delta G(0)_{\text{no } \alpha\text{-}\beta},\end{aligned} \tag{2.39}$$

where $\Delta G(0)_{\text{no } \alpha\text{-}\beta} = \frac{b_{\beta,1}}{b_{\beta,2}}G_2(0) - G_1(0)$ is the low-r limit.

2.5 Equations of state

The thermodynamic state of a system can be described by an equation of state (EOS), usually defined in terms of the state variables pressure (P), temperature (T), and specific volume (V) [15]. A state variable denoted with a subscript '0' (*e.g.* V_0) is defined as the state variable at $P = 0$ GPa [63, 64].

When using neutron diffraction to study materials under extreme conditions (such as high pressures or extreme temperatures) it is necessary to know the number density ρ for the data correction process and also to allow for Fourier transformation between reciprocal and real space. The primary variable needed is the compression, $\eta = V/V_0$. This compression can be used to calculate the number density at high pressure using

$$\rho(P) = \frac{\rho_0}{\eta(P)} = \frac{\rho_0 V_0}{V(P)}. \tag{2.40}$$

The majority of equations of state will therefore be defined in terms of this variable.

Within this thesis the main *'extreme conditions'* studied are those at high pressures. As such, this section will primarily discuss isothermal equations of state that relate the pressure of a system to its specific volume, *i.e.* the effects of temperature are ignored.

The bulk modulus B is used to describe the resistance to volume change under uniform pressure

$$B = -V\frac{\partial P}{\partial V} = -\frac{\partial P}{\partial \ln V}, \tag{2.41}$$

and is the reciprocal of compressibility. The low-pressure bulk modulus is defined as B_0 and is used extensively as a parameter within equations of state for solids. The derivative of this bulk modulus with respect to pressure (B_0') is also used as a parameter within equations of state. Further derivatives (B_0'', B_0''', ...) can be used although their

use is unnecessary in all but the most complicated and accurate measurements which are beyond the scope of this work.

The Murnaghan equation of state [65] makes the assumption that the bulk modulus increases linearly with pressure, that is $B(P) = B_0 + PB_0'$. The Murnaghan equation of state is defined as

$$P(V; V_0, B_0, B_0') = \frac{B_0}{B_0'}\left[\left(\frac{V}{V_0}\right)^{-B_0'} - 1\right]. \tag{2.42}$$

Within the literature it is sometimes assumed that $B_0' = 4$ such that the EOS is parameterised using only B_0 and V_0 [63]. The Murnaghan equation of state is usually sufficient for small compressions ($\eta \geq 0.9$) but due to the assumption of a linearly increasing bulk modulus it fails for higher compressions [66].

The most commonly used equation of state is the so-called Birch-Murnaghan equation of state (BM-EOS) [67]. The BM-EOS is based on finite strain theory with a full derivation being available in Ref. [64]. The Eulerian strain is defined as

$$f_E(V; V_0) = \frac{1}{2}\left[\left(\frac{V}{V_0}\right)^{-\frac{2}{3}} - 1\right]. \tag{2.43}$$

The BM-EOS is a Taylor expansion in terms of the Eulerian strain and, when expanded up to the fourth order, is given by

$$P(f_E; B_0, B_0') = 3B_0 f_E \left(1 + 2f_E\right)^{\frac{5}{2}} \times \left\{1 + \frac{3}{2}\left(B_0' - 4\right) f_E + \frac{3}{2}\left[B_0 B_0'' + \left(B_0' - 4\right)\left(B_0' - 3\right) + \frac{35}{9}\right] f_E^2\right\}. \tag{2.44}$$

Typically, however, the BM-EOS is used only to third order. Higher orders require the second (and possibly beyond) derivatives of B_0 with respect to P to be treated as fitting parameters which is fraught with complications and difficulty [63].

If the equation for the Eulerian strain given by equation (2.43) is combined with equation (2.44) then the 3rd order Birch-Murnaghan EOS can be written in terms of P and V/V_0 as

$$P(V;V_0,B_0,B_0') = \frac{3B_0}{2}\left[\left(\frac{V}{V_0}\right)^{-\frac{7}{3}} - \left(\frac{V}{V_0}\right)^{-\frac{5}{3}}\right] \times \left\{1 + \frac{3}{4}\left(B_0' - 4\right)\left[\left(\frac{V}{V_0}\right)^{-\frac{2}{3}} - 1\right]\right\}. \quad (2.45)$$

To obtain the 2nd order BM-EOS, it is assumed that $B_0' = 4$ (this is, incidentally, why B_0' is often assumed to be 4 in the Murnaghan equation of state as discussed above) and so the EOS simplifies to

$$P(V;V_0,B_0) = \frac{3B_0}{2}\left[\left(\frac{V}{V_0}\right)^{-\frac{7}{3}} - \left(\frac{V}{V_0}\right)^{-\frac{5}{3}}\right]. \quad (2.46)$$

Within the literature, equations (2.45) and (2.46) are the most commonly used when discussing the BM-EOS due to their simplicity in combining the specific volume and pressure in one equation.

Using equation (2.44) it is possible to define a 'normalised pressure'

$$F_E = \frac{P}{3f_E\left(1+2f_E\right)^{\frac{5}{2}}} = B_0\left\{1 + \frac{3}{2}\left(B_0' - 4\right)f_E + \frac{3}{2}\left[B_0B_0'' + \left(B_0' - 4\right)\left(B_0' - 3\right) + \frac{35}{9}\right]f_E^2\right\}, \quad (2.47)$$

such that the relationship between F_E and f_E can be constant, linear, or quadratic, depending on how many terms are used in the equation *i.e.* the order of BM-EOS that is chosen. This relation provides an easy way for analysing experimental data, especially regarding the choice of order for the BM-EOS. Figure 2-3 shows a case where an example data set is fitted with three different orders of BM-EOS. A second order BM-EOS is not sufficient to capture the behaviour of the data accurately, whilst both a third order and fourth order BM-EOS capture it well within the plotted strain range.

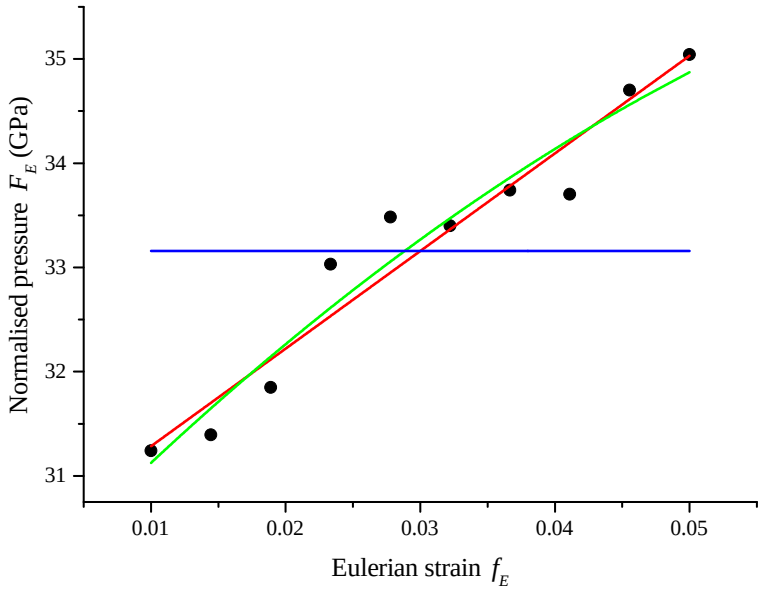

Figure 2-3: Example compression data (•; as constructed from a third order BM-EOS with parameters $B_0 = 30$ GPa and $B_0' = 6$) fitted using a second order BM-EOS (blue line; $B_0 = 33.157$ GPa, $B_0' = 4$); a third order BM-EOS (red line; $B_0 = 30.348$ GPa, $B_0' = 6.057$); and a fourth order BM-EOS (green line; $B_0 = 29.853$ GPa, $B_0' = 6.992$, $B_0'' = -15.543$ GPa^{-1}).

3. Experimental procedure and data analysis

The primary experimental method used in the work to be described in this thesis is neutron diffraction. This chapter describes the experimental procedures for collecting high-quality neutron diffraction data, typically under extreme conditions. The neutron sources and instruments used are described, as well as the use of a Paris-Edinburgh high-pressure press for measuring the structure of samples *in situ* under compression. Finally, a summary is given of the steps required in the data analysis procedure.

3.1 Spallation neutron sources

A spallation neutron source is accelerator-based, where pulses of neutrons are produced by bombarding a heavy element with high-energy particles. The ISIS pulsed neutron source is a spallation source situated at the Rutherford-Appleton Laboratory in Didcot, UK.

At ISIS, high-energy protium pulses with a frequency of 50 Hz are accelerated using a synchrotron to $0.84c$, where c is the speed of light *in vacuo*. These pulses are removed from the synchrotron by a "kicker" magnet and the single electron on each atom is removed to form a proton pulse. This pulse is then accelerated into a tungsten target. Proton-nucleus collisions drive neutrons from the nucleus of the target, producing a large flux of neutrons for use in experiments [68].

The neutrons produced by the target have kinetic energies on the order of MeV, too large for experimental purposes. Hydrogen-based moderators are used to lower the kinetic energy of the neutrons to the meV range through thermal equilibration, whereby scattering events cause many of the neutrons to emerge with a Maxwell-Boltzmann distribution. Some of the neutrons are unable to be slowed down by the moderator material and are known as epithermal neutrons. Differences in moderator type and temperature result in different energy/wavelength distributions. Figure 3-1 shows the neutron flux Φ with respect to wavelength λ for three different moderators used at ISIS.

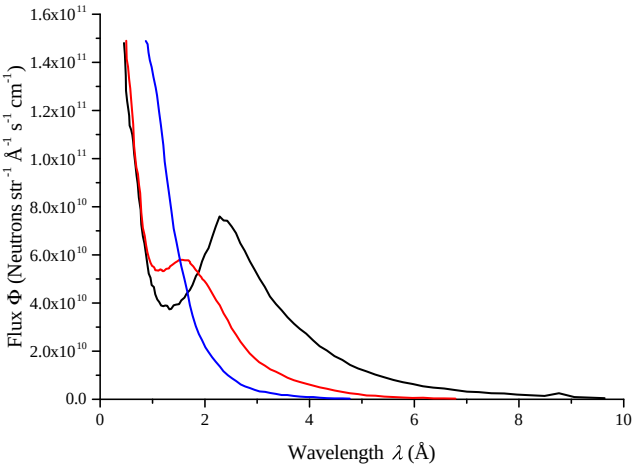

Figure 3-1: The effect of moderator choice on neutron flux for three different liquid moderators from the ISIS pulsed neutron source: hydrogen (black line), methane (blue line), and water (red line).

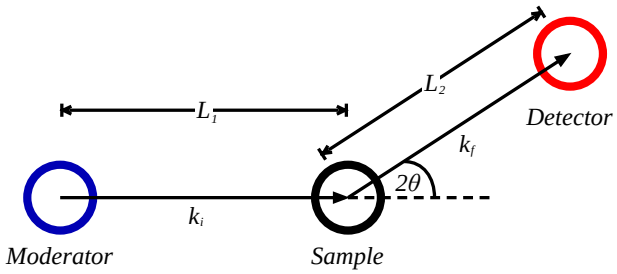

Figure 3-2: Schematic drawing of a time-of-flight diffraction experiment.

3.2 Neutron diffraction using time-of-flight methods

In a time-of-flight neutron diffraction experiment the intensity of neutrons is measured as a function of time-of-flight between the moderator, the sample position, and a detector placed at a scattering angle of 2θ. Consider the example described in figure 3-2 where the incident flight path between the neutron moderator and the sample position has a length L_1, and the scattered flight path between the sample position and the detector has a length L_2. If the energy exchange between the neutron and the sample is small, such that the static approximation holds, then the wavelength λ of the neutron is given by

$$\lambda = \frac{ht}{m_n \left(L_1 + L_2\right)}, \tag{3.1}$$

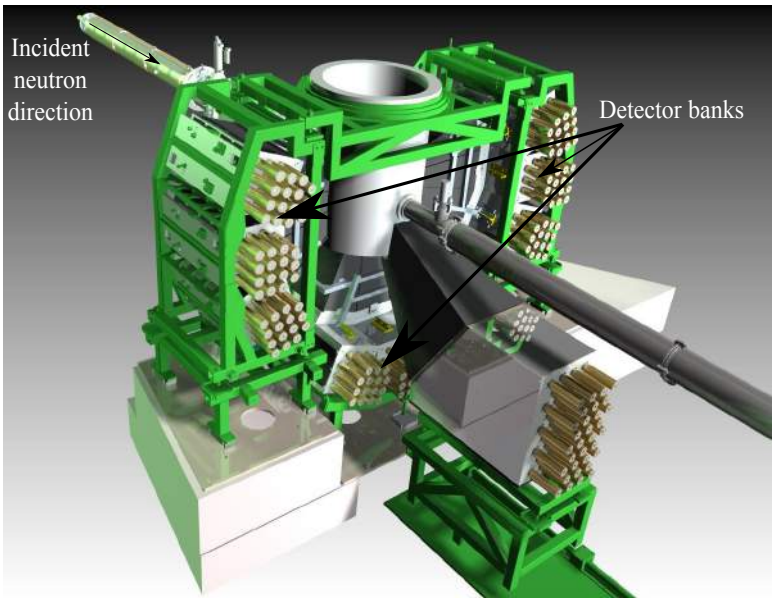

Figure 3-3: Schematic drawing of the PEARL diffractometer showing the incident neutron direction and the radial detector banks. Adapted from Ref. [69].

where t is the total time-of-flight and m_n is the mass of a neutron. Equation (3.1) can be combined with equation (2.9) to calculate the scattering vector amplitude, *i.e.*

$$Q = \frac{4\pi m_\mathrm{n}\,(L_1 + L_2)}{ht}\sin(\theta). \tag{3.2}$$

3.3 PEARL HiPr diffractometer

The PEARL High Pressure (HiPr) time-of-flight diffractometer is an instrument designed specifically for neutron diffraction studies under extreme conditions, specialising in high-pressure studies using the Paris-Edinburgh press (chapter 3.6). PEARL views the methane moderator at ISIS and has nine detector banks covering a small range of scattering angles $83^\circ < 2\theta < 97^\circ$ more-or-less perpendicular to the incident wavevector. PEARL features a primary flight path $L_1 = 12.8\,\mathrm{m}$ and a secondary flight path $L_2 = 0.6\,\mathrm{m}$. Due to the scattering angle restriction, PEARL has an effective scattering vector range of $1.55\,\text{Å}^{-1} \leq Q \leq 19.55\,\text{Å}^{-1}$, where the Q range is derived solely from the incident wavelength range. There is an additional detector bank at small angles which provides access to a lower Q range. This detector bank is not, however, usable when making a high-pressure experiment using a transverse scattering geometry due to the Paris-Edinburgh press blocking the diffracted neutron path (chapter 3.6.4).

3.4 Steady-state neutron sources

A steady-state reactor source is one where neutrons are produced via the nuclear fission process. The Institut Laue-Langevin (ILL) is a steady-state neutron source in Grenoble, France. At the ILL, neutrons n and energy E are produced as a by-product of the nuclear fission of ^{235}U, where a typical reaction is given by

$$n + {}^{235}\mathrm{U} \rightarrow {}^{141}\mathrm{Ba} + {}^{92}\mathrm{K} + 3n + E. \tag{3.3}$$

Although the majority of neutrons are used for neutron scattering measurements, a small percentage is used in self-sustaining the chain reaction. Moderators are used to reduce the kinetic energy of the energetic neutrons to usable levels, and the choice of moderator depends on the science to be performed.

Consider a neutron diffraction experiment, as shown in figure 3-4. The moderator (blue circle) produces a constant flux of neutrons which features a Maxwell-Boltzmann distribution of kinetic energies, controlled by the temperature of the moderator. These neutrons propagate towards a monochromator (green circle) via neutron guides. The monochromator selects a specific wavelength of neutrons through Bragg reflection. The neutrons that are scattered by the sample are then measured by a detector (red circle) as a function of the scattering angle 2θ. The 2θ to Q conversion is given by equation (2.9). Collimation is provided by neutron absorbing material to reduce background scattering. Elements that can be used to absorb neutrons include boron ($^{\mathrm{N}}$B: $\sigma_{\mathrm{a}} = 767(8)$ barn, ^{10}B: $\sigma_{\mathrm{a}} = 3835(9)$ barn), cadmium ($^{\mathrm{N}}$Cd: $\sigma_{\mathrm{a}} = 2520(50)$ barn), and gadolinium ($^{\mathrm{N}}$Gd: $\sigma_{\mathrm{a}} = 49\,700(125)$ barn), where σ_{a} is the absorption cross-section for neutrons with a wavelength $\lambda = 1.798\,\text{Å}$ and N denotes the natural isotope abundance.

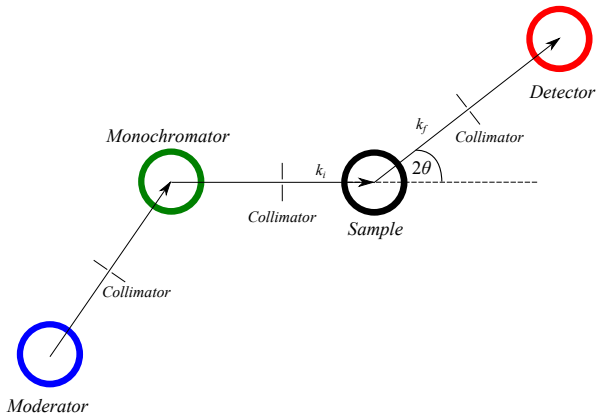

Figure 3-4: Schematic diagram for a neutron diffraction experiment at a steady-state reactor source, such as the ILL.

3.5 D4c diffractometer

D4c is a diffractometer devoted to studying disordered materials at the ILL, as shown in figure 3-5 [70]. D4c views the graphite moderator, which is known as the 'hot source' due to it being kept at a constant temperature of 2400 K.

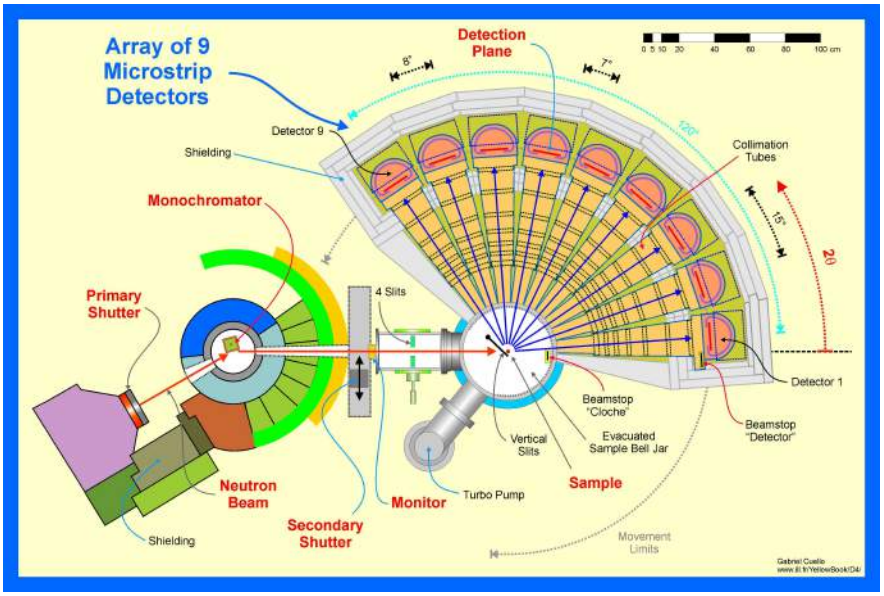

Figure 3-5: Schematic diagram of the D4c diffractometer at the ILL [70].

A Cu monochromator is used to select neutrons with a single wavelength λ of 0.35 Å, 0.5 Å, or 0.7 Å using the (331), (220), or (200) reflections, respectively. Harmonic $\lambda/2$ contamination is removed for $\lambda = 0.5$ Å and 0.7 Å using either Ir or Rh filters, respectively. The incident neutron flux Φ is measured using a monitor positioned between the monochromator and the slits that define the beam profile at the sample position. The sample is contained within a large aluminium bell jar (diameter = 0.46 m, height = 0.55 m) that can be evacuated as necessary.

Scattered neutrons are measured by nine ^{3}He 1D microstrip multi-detectors that cover a large scattering angle range $1.5° \leq 2\theta \leq 137°$. These detectors have excellent count-rate stability [71] that is necessary for making experiments using neutron diffraction with isotope substitution (chapter 2.4). Each detector covers a 2θ range of 8° and there is a gap of $2\theta = 7°$ between each detector bank. The entire detector is able to rotate about the sample position such that a scattering angle range $1.5° \leq 2\theta \leq 137°$ can be covered by the detectors during a measurement. The Q range for the three neutron wavelengths can be calculated from equation (2.9) as

$$\begin{aligned} 0.5\,\text{Å}^{-1} \leq Q \leq 33\,\text{Å}^{-1} \qquad & \text{for } \lambda = 0.35\,\text{Å}, \\ 0.3\,\text{Å}^{-1} \leq Q \leq 24\,\text{Å}^{-1} \qquad & \text{for } \lambda = 0.5\,\text{Å}, \\ \text{and } 0.2\,\text{Å}^{-1} \leq Q \leq 17\,\text{Å}^{-1} \qquad & \text{for } \lambda = 0.7\,\text{Å}. \end{aligned} \tag{3.4}$$

Finally D4c is able to accommodate various sample environments for making *in situ* structural measurements. The sample environments include low-temperature cryostats, high-temperature vanadium furnaces, and a Paris-Edinburgh press (chapter 3.6.5).

3.6 The Paris-Edinburgh press

The Paris-Edinburgh (PE) press is a large-volume, opposed-anvil pressure cell that is often used in conjunction with neutron scattering to provide *in situ* compression of samples [72–75]. The press typically employs anvils having a toroid profile with the sample being supported by an annular gasket arrangement [76]. Neutron diffraction experiments require a large sample volume due to the weak-interaction of neutrons with the sample and the low flux of a typical neutron source. The PE press allows for a much larger sample volume when compared to, for example, a traditional diamond-anvil cell (DAC), meaning that neutron diffraction measurements are viable.

The PE press provides sample compression through two identical opposed anvils. One anvil is situated on the so-called 'breach' and is screwed into place such that it is immobile and withstands movement from its twin. The second anvil is placed opposite the breach on a piston and is pushed into the breach anvil by oil pressure, with the sample and encircling gaskets compressed in between them.

In the work to be described in this thesis two types of anvil were used, the so-called single toroid (ST) and double toroid (DT) anvils (shown in figure 3-6). Anvils with a single toroid profile have a single annular gasket and provide an ambient sample volume of $\sim 92\,\text{mm}^3$. Double toroid anvils have two annular gaskets which, when combined with the reduced ambient sample volume of $\sim 33\,\text{mm}^3$, allows a greater sample pressure to be obtained. Each gasket is formed from a pair of rings, one of which is thicker and sits in the anvil grooves. A relatively small sample volume is necessary in both cases because pressure is defined in terms of applied force per unit area. Whilst single toroid and double toroid anvils can be used to apply pressures up to 15 GPa and 30 GPa, respectively, the pressures are usually not taken this high as it is extremely difficult, if not impossible, to recover the anvils to ambient pressure without them breaking.

The central part of an anvil, known as the die, is constructed from a hardened material, such as sintered diamond or cubic boron nitride. This die holds the sample

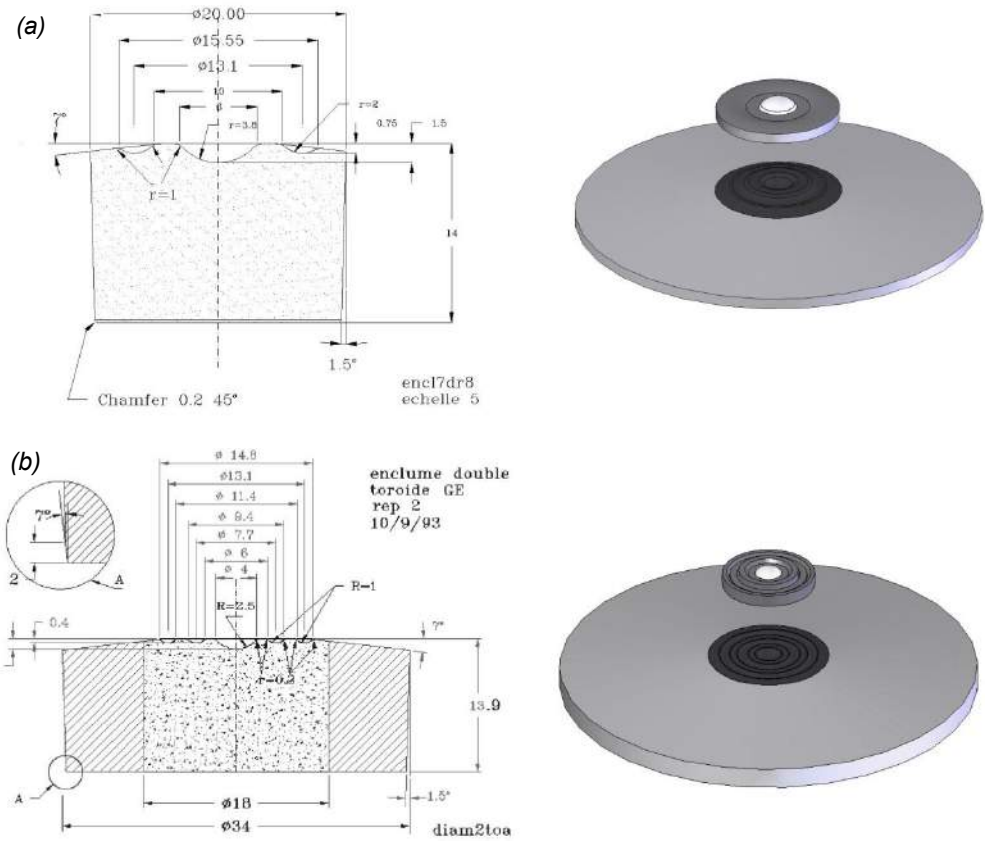

Figure 3-6: Schematic diagram of *(a)* single toroid anvils, and *(b)* double toroid anvils. Reproduced from Ref. [77], original information from Ref. [78].

and gaskets and is shaped through spark erosion. The die is held within a tungsten carbide seat which is further supported by a steel binding ring, causing an inward radial pressure of ~ 1 GPa [66]. The anvils have a 7° bevel angle, allowing an aperture of 14° for neutron transmission.

3.6.1 Pressure samples

Using a Paris-Edinburgh press, it is possible to measure samples of the main three states of matter: solids, liquids, and gases [79–81]. The main topic considered in this thesis is that of amorphous materials under extreme conditions. A typical glassy pellet (figure 3-7) takes the form of a cylinder of height h and radius r_s which is enclosed at either end by two spherical caps of height h_{cap}. Due to shielding by the anvils, scattering from the spherical caps is not measured by the detectors.

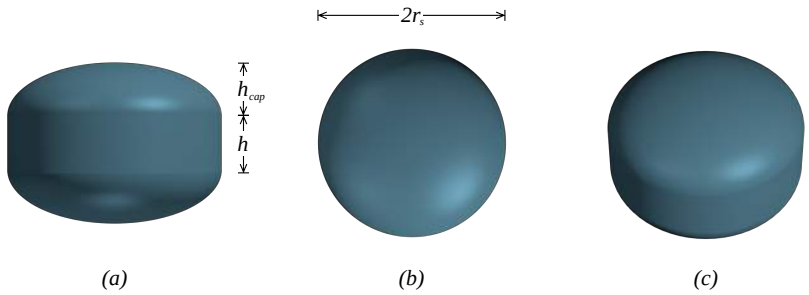

Figure 3-7: A typical sample pellet for use in PE press experiments. The pellet takes the form of a cylinder of height h and radius r_{s} which has two spherical caps of height h_{cap} at either end.

The pellet shape is the same for both single toroid and double toroid experiments although the dimensions differ. For a single toroid experiment: $h = 1.6\,\text{mm}$, $r_{\text{s}} = 3\,\text{mm}$, and $h_{\text{cap}} = 1.6$ mm. For a double toroid experiment: $h = 1.6$ mm, $r_{\text{s}} = 2$ mm, and $h_{\text{cap}} = 1.6$ mm. The volume of a pellet is given by

$$V_{\text{pellet}} = V_{\text{cylinder}} + 2V_{\text{cap}} = \pi h r_{\text{s}}^2 + \frac{\pi h_{\text{cap}}}{3}\left(3r_{\text{s}}^2 + h_{\text{cap}}^2\right), \tag{3.5}$$

giving volumes of 33.719 mm^3 and 91.892 mm^3 for double toroid and single toroid pellets, respectively.

Depending on the nature of the experiment, the sample can either be a singular piece of shaped glass, or formed from a powdered glass that has been compressed to the required shape using a die and press. Single pieces of glass are preferred to a pellet produced from powder because the number of scattering centres within the beam is higher, leading to larger measured intensities. Powdered samples are typically used

when a sample is particularly brittle such that the production of a single pellet is difficult, or when isotope substitution is used since the expense of isotopes prohibits the loss of material that results from machining.

To produce a solid pellet, an over-sized piece of glass is first formed. The mass of this piece is measured and the theoretical mass of a "perfect" pellet then calculated. To gently grind the piece of glass into the required shape, a Dremel® Multitool is used in conjunction with an aluminium oxide grinding stone. The shaping process takes place inside an Ar filled glovebag to limit contamination from the atmosphere. The pellet is ground to as close to the correct shape as possible while the mass is measured at periodic intervals to ensure it is as close as possible to the required mass.

To produce a powdered pellet the sample is first ground using a mortar and pestle in a glovebox. The correct mass (*i.e.* the mass of a "perfect" pellet) is then loaded into a specially designed hardened steel die which replicates the shape of the pellet. The die is then transported to a press. The powder is slowly compressed, allowing periodic relaxation periods where the applied pressure is kept constant. The height of the die is measured before filling with powder and then during compression in a bid to measure the height of the powder inside. Once fully compressed the die is then transported to the PE press and placed in the anvils, taking care to ensure that no powder is left between the anvils and the gaskets.

3.6.2 $\mathbf{Ti_{0.676}Zr_{0.324}}$ gaskets

Toroidal gaskets encircle the sample and provide lateral support to prevent the sample from ejecting radially, perpendicular to the axis of compression. Grooves within the anvils provide a seat for the gaskets to sit in and, upon compression, cause the gaskets to push inwards to withstand the pressure exerted outwards by the sample. The gaskets deform during compression to ensure that there is a uniform pressure distribution across the anvils, which helps to prevent the anvils from breaking [82]. Figures 3-8 and 3-9 show 3-dimensional (3D) models and the dimensions of the double toroid and single toroid gaskets, respectively.

In neutron diffraction experiments, the gaskets are typically produced from the alloy $Ti_{0.676}Zr_{0.324}$. The bound coherent scattering lengths of natural Ti and Zr are $b_{\mathrm{Ti}} = -3.438(2)\,\mathrm{fm}$ and $b_{\mathrm{Zr}} = 7.16(3)\,\mathrm{fm}$. For this particular composition the average coherent scattering length is

$$\langle b \rangle = 0.676 \times 3.438 + 0.324 \times 7.16 \approx 0. \tag{3.6}$$

This composition is known as "null-scattering" Ti-Zr. In a neutron diffraction experiment the total structure factor $F(Q)$ can be defined in terms of the Bhatia-Thornton

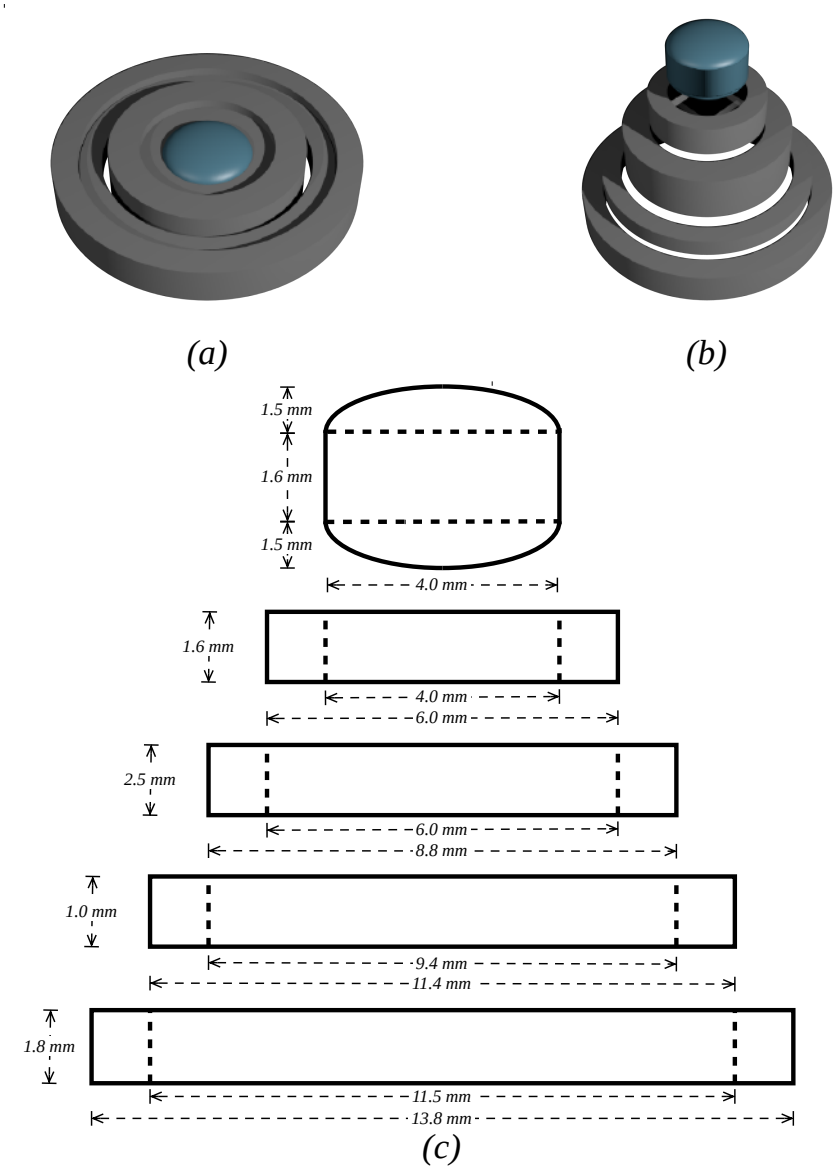

Figure 3-8: Double toroid gasket diagram showing: *(a)* 3D model of a sample contained within uncompressed gaskets; *(b)* 3D model expanded upwards to show the separate pieces; *(c)* schematic diagram (not to scale) detailing the dimensions of the gaskets and sample.

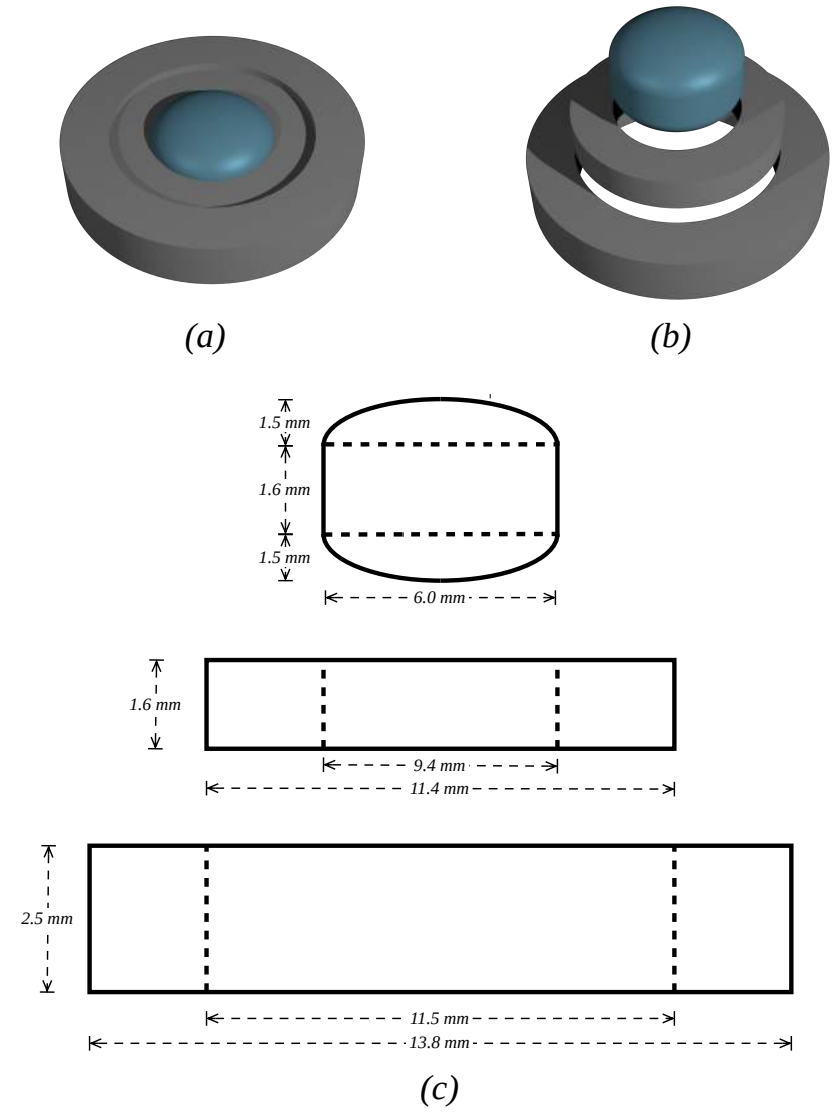

Figure 3-9: Single toroid gasket diagram showing: *(a)* 3D model of a sample contained within uncompressed gaskets; *(b)* 3D model expanded upwards to show the separate pieces; *(c)* schematic diagram (not to scale) detailing the dimensions of the gaskets and sample.

partial structure factors as shown by equation (2.22). In the case when $\langle b \rangle = 0$, the weighting factors for $S^{\mathrm{BT}}_{\mathrm{NN}}(Q)$ and $S^{\mathrm{BT}}_{\mathrm{NC}}(Q)$ are equal to zero, and so the Q dependence of $F(Q)$ is determined solely by the concentration-concentration partial structure factor $S^{\mathrm{BT}}_{\mathrm{CC}}(Q)$, *i.e.*

$$F(Q) = c_\alpha c_\beta \left(b_\alpha - b_\beta\right)^2 \left\{ \left[\frac{S^{\mathrm{BT}}_{\mathrm{CC}}(Q)}{c_\alpha c_\beta} \right] - 1 \right\}. \tag{3.7}$$

If the sample is a random substitutional alloy then $S^{\mathrm{BT}}_{\mathrm{CC}}(Q) = 0$ and the measured total structure factor is independent of Q [51].

$\mathrm{Ti}_{0.676}\mathrm{Zr}_{0.324}$ is produced in a process which involves hot isostatic pressing to aid in the reduction of voids [66]. Unfortunately due to some preference for like-atom bonding the material does not form a perfect random substitutional alloy. As such, concentrations fluctuations can manifest themselves as Q-dependent structure in the measured diffraction pattern. If the crystallites formed from like-atoms are sufficiently large then Bragg peaks can be observed. Due to the presence of crystallites, $\mathrm{Ti}_{0.676}\mathrm{Zr}_{0.324}$ gaskets show measurably different diffraction patterns depending on their orientation. Fortunately the Q-dependent structure decreases in intensity during the process of an experiment; as the compression increases, plastic deformation causes the crystallites to flow and break apart, leading to a more homogeneous distribution which reduces the concentration fluctuations visible in diffraction measurements. Figure 3-10 shows the measured intensity for an uncompressed gasket, two gaskets recovered from pressures of 4.7 GPa and 8.1 GPa and also the empty anvils. As the pressure is increased the curves progress in the order green (ambient) $\rightarrow$ blue (4.7 GPa) $\rightarrow$ black (8.1 GPa), the features at low-angles become less complex but the slope at high-angles increases in intensity as the anvils come closer together and there is a greater contribution from anvil scattering.

The equation of state for $\mathrm{Ti}_{0.676}\mathrm{Zr}_{0.324}$ at room temperature was measured by x-ray diffraction [83], and the relation between the number density ρ and applied pressure P is shown in figure 3-11.

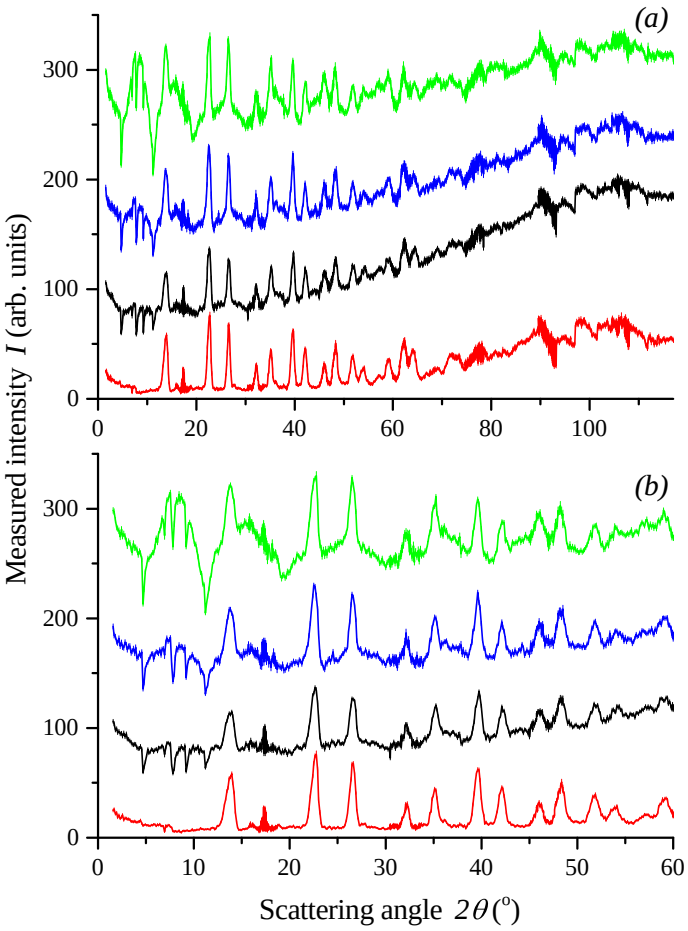

Figure 3-10: Measured diffraction patterns for $Ti_{0.676}Zr_{0.324}$ gaskets. *(a)* shows the full scattering angle range whilst *(b)* shows the low-angle range in greater detail. The measurements shown in the plot are for an uncompressed empty gasket measured under ambient conditions (green curve, shifted down by 500 arb. units), an empty gasket recovered from 4.7 GPa (blue curve, shifted down by 350 arb. units), an empty gasket recovered from 8.1 GPa (black curve, shifted down by 250 arb. units), and empty anvils with no sample or gasket present (red curve).

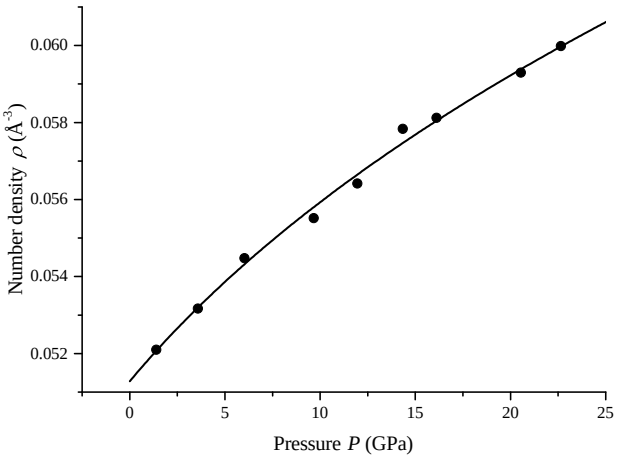

Figure 3-11: The number density ρ of null scattering $Ti_{0.676}Zr_{0.324}$ (•) as a function of pressure P at room temperature [83]. A third-order Birch Murnaghan equation of state is also given (black line; $B_0 = 86.315(3.862)$ GPa, $B_0' = 6.714(0.836)$) [84].

3.6.3 Producing pressure

In an experiment using a PE press, pressure is applied to the system by two opposing anvils that are pushed together. The breach anvil is kept immobile whilst the piston anvil is pushed towards its twin through oil pressure. The oil pressure for the press is provided by a hydraulic pump, either automatically or by hand. The force F on an anvil is given by

$$F = P_{\text{oil}} A = Lg \tag{3.8}$$

where P_{oil} is the oil pressure of the hydraulic system, A is the area of the piston, L is the applied load and $g = 9.81\,\text{m}\,\text{s}^{-2}$. The piston area A differs for different PE press designs. The sample pressure can be determined from the load applied through the use of a calibration curve [85, 86], as discussed in sections 3.6.4 and 3.6.5 for the PEARL and D4c experiments, respectively. It is possible to use a pressure marker along side the sample as an alternative to a calibration curve. For instance, when making a measurement at an x-ray synchrotron the beam is typically collimated to such an extent that measurements can be made for the pressure calibrant or for only the sample material to avoid contamination by scattering from the calibrant. This is not possible in a flux-limited neutron diffraction experiment such that calibration curves must be used to calculate the sample pressure in experiments on glassy materials.

Ref. [85] discusses an alternative method for calculating the pressure, whereby a

parabolic pressure distribution $P(r)$ is assumed for the sample and gasket, and is given by

$$P(r) = -ar^2 + P_0, \tag{3.9}$$

where r is the radial distance from the centre of the sample, a is a derived constant, and P_0 is the maximum pressure at the sample centre.

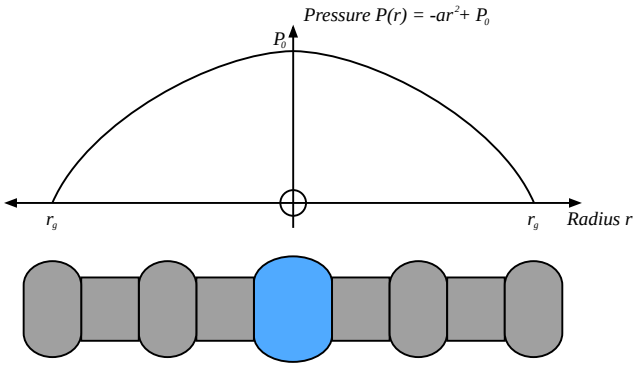

Figure 3-12: Schematic (not to scale) detailing the parabolic pressure profile that is assumed for a sample within a $Ti_{0.676}Zr_{0.324}$ gasket in the PE press.

Consider a sample-gasket assembly, as shown in Figure 3-12, where the outer radius of the gasket is given by r_g. Then the boundary conditions are $P(r = 0) = P_0$, and $P(r = r_g) = 0$. From the boundary conditions it follows that the constant $a = P_0/r_g^2$. The total force applied to the sample and gasket assembly is given by

$$F(r_g) = Lg = 2\pi \int_0^{r_g} rP(r)\,\mathrm{d}r = \frac{\pi P_0 r_g^2}{2}, \tag{3.10}$$

such that the maximum pressure at the sample position is given by

$$P_0 = \frac{2gL}{\pi r_g^2}. \tag{3.11}$$

The effective pressure applied to the gasket assembly can also be expressed in terms of P_0, so that the effective density of the gasket can be found for use in the data reduction. Consider a sample of radius r_s contained within a gasket of outer radius r_g. The force applied to the gasket is given by

$$F_g = F(r_g) - F(r_s). \tag{3.12}$$

Using the pressure distribution from equation (3.9), the force applied to the sample is

given by

$$F(r_s) = 2\pi \int_0^{r_s} rP(r)\,\mathrm{d}r = \pi P_0 r_g^2 \left[\left(\frac{r_s}{r_g} \right)^2 - \frac{1}{2} \left(\frac{r_s}{r_g} \right)^4 \right]. \tag{3.13}$$

Then, by combining equations (3.13) and (3.10), and using the fact that the surface area of the gasket is given by

$$A_g = \pi \left(r_g^2 - r_s^2 \right), \tag{3.14}$$

the average pressure exerted on the gasket is given by

$$P_g = \frac{F_g}{A_g} = \frac{P_0 r_g^2}{r_g^2 - r_s^2} \left[\frac{1}{2} - \left(\frac{r_s}{r_g} \right)^2 + \frac{1}{2} \left(\frac{r_s}{r_g} \right)^4 \right]. \tag{3.15}$$

3.6.4 Using the Paris-Edinburgh press on the PEARL HiPr diffractometer

The PEARL HiPr diffractometer is designed to specialise in extreme conditions experiments using the PE press. When making a measurement on PEARL the press is mounted in a so-called transverse geometry, where scattered neutrons are in a plane that is perpendicular to the incident beam. The incident neutrons impinge upon the breach anvil and are scattered by the sample to detectors at $2\theta \sim 90°$, as shown in figure 3-13.

For the work conducted in this thesis on the PEARL diffractometer a V3 PE press was used in conjunction with double toroid sintered diamond anvils. This assembly allows diffraction measurements at pressures up to $P \sim 17.5\,\mathrm{GPa}$ to be reliably measured.

The incident beam is collimated with a boron nitride block with a drilled hole lined with gadolinium to reduce scattering from the press assembly. The anvils are covered in layers of cadmium shielding to prevent neutrons scattered from the anvil die from leaving the anvils. Finally the scattered neutrons are collimated by further boron nitride shielding to prevent neutrons scattered from the press assembly from reaching the detectors. Pictures of the incident and scattered beam collimation are shown in figure 3-14.

A calibration curve, as shown in figure 3-15, can be used to determine the pressure at the sample position from the load applied through oil pressure [86]. The curve was produced using the results from many separate neutron diffraction experiments. When first applying load to the system there is no pressure increase, which is due to the sample

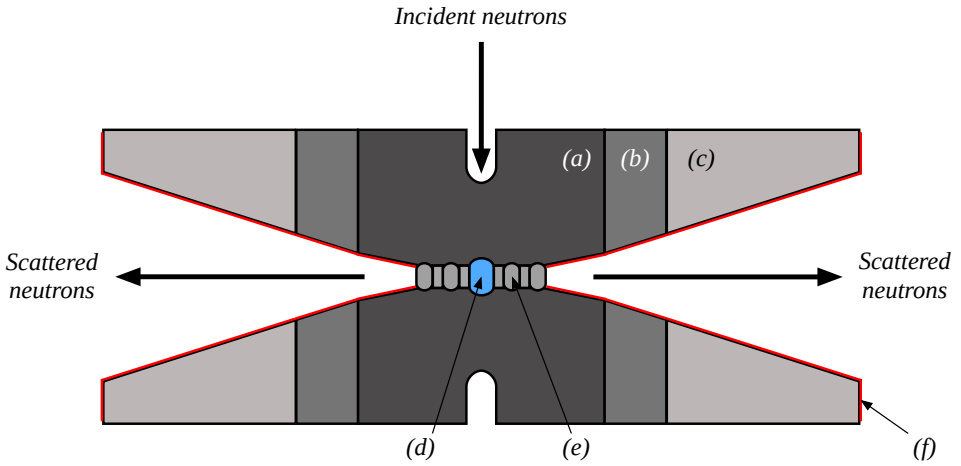

Figure 3-13: Representation (not to scale) of the transverse scattering geometry used on the PEARL HiPr diffractometer. Incident neutrons are scattered by the sample and detected at $2\theta \sim 90°$. Shown in the diagram are the: *(a)* anvil die, *(b)* tungsten carbide ring, *(c)* steel binding ring, *(d)* sample position, *(e)* double toroid gasket, and *(f)* cadmium shielding. Further boron nitride collimation is used for both the incident and scattered neutrons, but it forms part of the press rather than part of the anvils themselves and is not therefore shown.

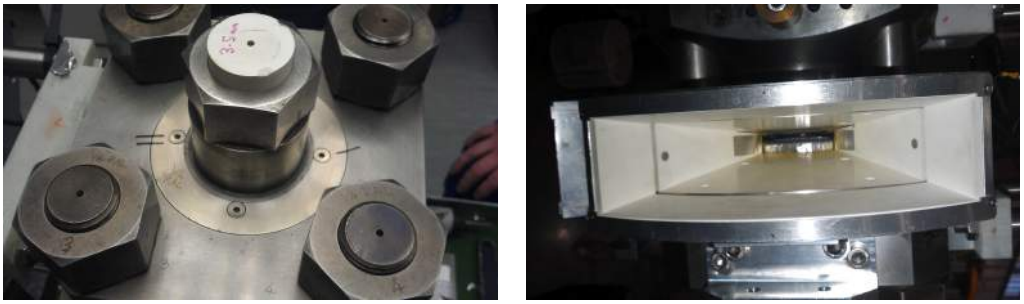

(a) *(b)*

Figure 3-14: Collimation used for a V3 PE press mounted on the PEARL HiPr diffractometer in a transverse scattering geometry. *(a)* The white cylinder with a drilled hole is cubic boron nitride that has been lined internally with gadolinium foil and is mounted on the breach of the press. Incident neutrons pass through the hole and impinge on the sample. *(b)* Boron nitride shields that collimate the scattered beam. There are three shields, one for each detector bank.

and gaskets deforming to fill the grooves in the anvils. The pressure then increases linearly with applied load up to $L \sim 60$ tonnes, corresponding to $P \sim 7.6$ GPa. At this point there is a change in gradient up to $L \sim 90$ tonnes, corresponding to $P \sim 10$ GPa. This change in gradient is thought to correspond to the point where the outer toroid gasket begins to support the inner gasket as it flows outwards under increasing load. Once the outer gasket begins to support the inner gasket and sample, the relationship between pressure and load applied becomes linear again.

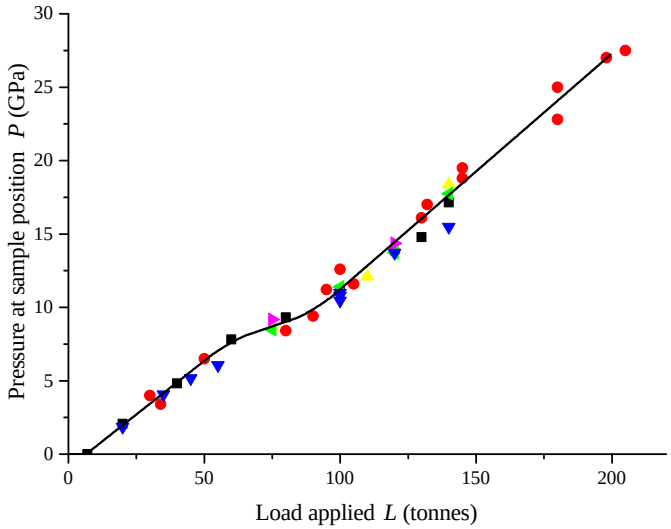

Figure 3-15: Calibration curve giving the load applied to the piston L with respect to the pressure at the sample position P for a V3 PE press using double toroid sintered diamond anvils [86]. The calibration curve was deduced from (i) diffraction patterns measured for a perovskite held in encapsulated $Ti_{0.676}Zr_{0.324}$ gaskets with a methanol-ethanol-water pressure transmitting medium and an MgO pressure marker (■); (ii) diffraction measurements of crystalline ice held in encapsulated $Ti_{0.676}Zr_{0.324}$ gaskets (●); (iii) a Le Bail analysis of the Bragg peaks from sintered diamond anvils, measured when various samples are under compression (B_2O_3 glass (▲), SiO_2 glass (▶), GeO_2 glass (◀), and crystalline V (▼)). For (iii) the unit cell to pressure conversion was made on the basis of the perovskite experiment. The measurements from the Le Bail analysis have been shifted downwards by 2 GPa, but they show the same P vs. L behaviour as (i) and (ii); this was deemed acceptable as there is uncertainty in the absolute values of the diamond Bragg peak data points.

3.6.5 Using the Paris-Edinburgh press on the D4c diffractometer

Unlike PEARL, the D4c diffractometer is not specifically designed to use a PE press. Measurements under high pressure can, however, be made using a VX5 PE press. The

VX5 variant has only two supporting columns, leading to a large aperture such that nearly the entire scattering angle range of the D4c detectors can be used. On D4c the PE press is mounted in a so-called in-plane scattering geometry such that the scattered neutrons are measured in the same plane as the incident beam, as shown in figure 3-16. Due to the available aperture of the PE press the maximum angle is restricted such that, at $\lambda = 0.5\,\text{Å}$, the maximum Q value is $Q_{\text{max}} = 21.5\,\text{Å}^{-1}$.

For the work conducted in this thesis on the D4c diffractometer, a VX5 PE press was used in conjunction with single toroid cubic boron nitride anvils. This assembly allows diffraction measurements up to $P \sim 8.5\,\text{GPa}$ to be made with an accuracy and repeatability that is high enough to allow first-order difference functions to be measured.

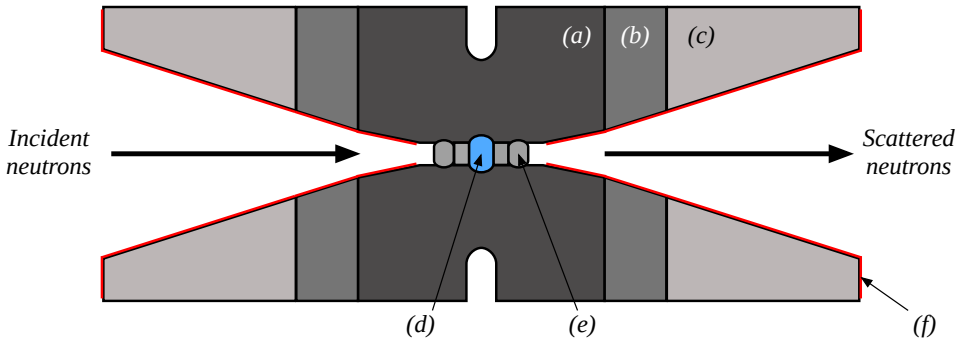

Figure 3-16: Representation (not to scale) of the in-plane geometry used on the D4c diffractometer. Incident neutrons are scattered by the sample and detected within the sample plane. Shown in the diagram are the: *(a)* anvil die, *(b)* tungsten carbide ring, *(c)* steel binding ring, *(d)* sample position, *(e)* single toroid gasket, and *(f)* cadmium shielding.

An incident beam profile of height 4 mm and width 11 mm is chosen which allows for full illumination of the sample and partial illumination of the gaskets. Background scattering is reduced by (i) neutron absorbing $^{10}B_4C$ flags placed just upstream of the PE press, (ii) a neutron absorbing cadmium jacket which is fitted to cover the anvils (shown in figure 3-16 as *(f)*), and (iii) the boron nitride anvils since ^{10}B has a large absorption cross-section.

A calibration curve, as shown in figure 3-17, can be used to determine the pressure at the sample position from the load applied through oil pressure [86]. The curve was produced from the results obtained from different neutron diffraction experiments, as well as using equation (3.11) in conjunction with gaskets recovered different from high pressures.

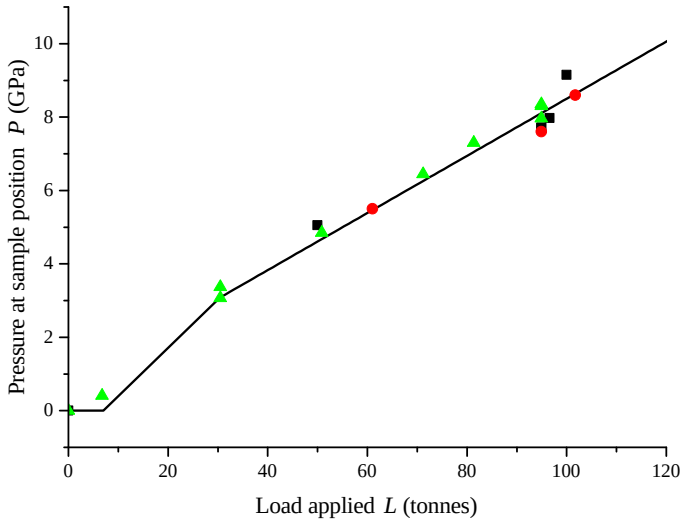

Figure 3-17: Calibration curve giving the load applied to the piston L with respect to the pressure at the sample position P for a VX5 PE press using single toroid cubic boron nitride anvils [86]. The calibration curve was deduced from (i) a calibration measurement using a mixture of crystalline NaCl and amorphous $GeSe_2$ (▲); (ii) use of equation (3.11) with the dimensions of various gaskets that had been recovered from high pressure (●); and (iii) a Rietveld refinement of the diamond Bragg peaks measured when several amorphous GeO_2 pellets were compressed in sintered diamond anvils, with a unit cell volume to pressure conversion made on the basis of previous experiments on crystalline ice VII [87] (■).

3.7 Neutron diffraction data analysis

Consider an experiment made on samples within the small sample limit, such that the neutrons are not attenuated by the sample and there are no multiple scattering events [52]. The single scattered intensity $I_{\mathrm{S}}(\theta)$ measured for N_{S} illuminated sample scattering centres is given by

$$I_{\mathrm{S}}(\theta) = a(\theta) N_{\mathrm{S}} \left.\frac{\mathrm{d}\sigma}{\mathrm{d}\Omega}\right|_{\mathrm{S}}, \tag{3.16}$$

where $\left.\frac{\mathrm{d}\sigma}{\mathrm{d}\Omega}\right|_{\mathrm{S}}$ is the differential scattering cross-section for the sample and $a(\theta)$ is a calibration coefficient that is used to convert cross-sections to measured intensities.

The small sample limit is not, unfortunately, met in most diffraction experiments. The above correction also makes no allowance for a container to hold the sample, such as $Ti_{0.676}Zr_{0.324}$ gaskets. It is therefore necessary to correct for attenuation, multiple scattering, and container scattering. The procedures necessary to correct high-pressure neutron diffraction data for both in-plane and transverse scattering geometries will be given in sections 3.7.1 and 3.7.2, respectively.

3.7.1 In-plane scattering geometry

This section discusses the data reduction procedure used for analysing neutron diffraction data measured on the D4c diffractometer utilising a PE press in an in-plane scattering geometry. The theory for this data analysis method was first discussed in Ref. [85].

The background corrected scattered intensity for a sample S in a container C in a neutron diffraction experiment is denoted by $I_{\mathrm{SC}}^{\mathrm{E}}(\theta)$. Due to the $Ti_{0.676}Zr_{0.324}$ gaskets used to contain the sample and the press assembly there is a non-negligible contribution from gasket and press scattering. The scattered intensities are also affected by attenuation and multiple scattering events. Furthermore these parameters can change with increasing pressure since the geometry changes, *i.e.* on compression the sample and gasket become thinner in the z direction while also growing radially as the anvils get closer together.

Neutron absorption and scattering events lead to attenuation of both the incident and scattered neutrons. The attenuation coefficient $A_{i,j}(\theta)$ corresponds to an event where a neutron scattered in medium i is attenuated in medium j [88]. Corrections must also be made for multiple scattering events and deviations from the static approximation. The multiple scattering cross-section for medium i is given by $M_i(\theta)$ and can be calculated using the quasi-isotropic approximation [89]. For example, the multiple scattering cross section $M_{\mathrm{S}}(\theta)$ for a bare sample S is given by

$$M_{\mathrm{S}}(\theta) = N_{\mathrm{S}} A_{\mathrm{S,S}}(\theta) \frac{\sigma_{\mathrm{S}}}{4\pi} \Delta_{\mathrm{S}}(\theta) \left[1 + P_{\mathrm{S}}(\theta)\right], \tag{3.17}$$

where $\sigma_{\mathrm{S}} = 4\pi \left(b_{\mathrm{S}}^2 + b_{\mathrm{S,inc}}^2\right)$ is the total scattering cross-section of the sample, Δ_{S} is the ratio of multiple scattering to single scattering, and $P_{\mathrm{S}}(\theta)$ is an inelasticity correction.

Consider a diffraction measurement performed at constant wavelength λ and variable scattering angle 2θ as given, for example, by the D4c diffractometer. Let $I_{\mathrm{S}}(\theta)$ and $I_{\mathrm{C}}(\theta)$ be the single scattered intensities for the sample and for an empty container, respectively. The background-corrected measured intensity for a sample in its container is then written as

$$I_{\mathrm{SC}}^{\mathrm{E}}(\theta) = A_{\mathrm{S,SC}}(\theta) I_{\mathrm{S}}(\theta) + A_{\mathrm{C,SC}}(\theta) I_{\mathrm{C}}(\theta) + a(\theta) M_{\mathrm{SC}}(\theta). \tag{3.18}$$

Similarly, the background-corrected measured intensity for an empty container is given by

$$I_{\mathrm{C}}^{\mathrm{E}}(\theta) = A_{\mathrm{C,C}}(\theta) I_{\mathrm{C}}(\theta) + a(\theta) M_{\mathrm{C}}(\theta). \tag{3.19}$$

Thus, it is possible to solve equations (3.16), (3.18), and (3.19) to derive the differential scattering cross-section for the sample

$$\left.\frac{\mathrm{d}\sigma}{\mathrm{d}\Omega}\right|_{\mathrm{S}} = \frac{1}{N_{\mathrm{S}} A_{\mathrm{S,SC}}(\theta)} \left\{ \left[\frac{I_{\mathrm{SC}}^{\mathrm{E}}(\theta)}{a(\theta)} - M_{\mathrm{SC}}(\theta) \right] - \frac{A_{\mathrm{C,SC}}(\theta)}{A_{\mathrm{C,C}}(\theta)} \left[\frac{I_{\mathrm{C}}^{\mathrm{E}}(\theta)}{a(\theta)} - M_{\mathrm{C}}(\theta) \right] \right\}. \tag{3.20}$$

The calibration coefficient $a(\theta)$ can be calculated by making a diffraction measurement using a piece of vanadium in place of the sample. The differential scattering cross section for this piece of vanadium is given by

$$\left.\frac{\mathrm{d}\sigma}{\mathrm{d}\Omega}\right|_{\mathrm{V}} = \frac{1}{N_{\mathrm{V}} A_{\mathrm{V,VC}}(\theta)} \left\{ \left[\frac{I_{\mathrm{VC}}^{\mathrm{E}}(\theta)}{a(\theta)} - M_{\mathrm{VC}}(\theta) \right] - \frac{A_{\mathrm{C,VC}}(\theta)}{A_{\mathrm{C,C}}(\theta)} \left[\frac{I_{\mathrm{C}}^{\mathrm{E}}(\theta)}{a(\theta)} - M_{\mathrm{C}}(\theta) \right] \right\}, \tag{3.21}$$

where N_{V} is the number of vanadium nuclei illuminated by the incident beam. Vanadium has a small coherent scattering length ($b_{\mathrm{V}} = -0.3824(12)\,\mathrm{fm}$) and a large incoherent scattering length ($b_{\mathrm{V,inc}} = 6.35(4)\,\mathrm{fm}$) [53] making it an ideal calibration material: the distinct term in its differential scattering cross section is negligible such that

$$\left.\frac{\mathrm{d}\sigma}{\mathrm{d}\Omega}\right|_{\mathrm{V}} = b_{\mathrm{V,inc}}^2 \left[1 + P_{\mathrm{V}}(Q)\right]. \tag{3.22}$$

Thus, by substituting equation (3.22) into (3.21) the calibration coefficient is given by [90, 91]

$$a(\theta) = \frac{I^{\mathrm{E}}_{\mathrm{VC}}(\theta)}{N_{\mathrm{V}} A_{\mathrm{V,VC}}(\theta) b^2_{\mathrm{V,inc}} \left[1 + P_{\mathrm{V}}(Q)\right] + M_{\mathrm{VC}}(\theta) - \frac{A_{\mathrm{C,VC}}(\theta)}{A_{\mathrm{C,C}}(\theta)} M_{\mathrm{C}}(\theta)}. \tag{3.23}$$

For a typical neutron diffraction experiment on D4c utilising a PE press the following measurements are made:-

- A sample contained within a $Ti_{0.676}Zr_{0.324}$ gasket at several different pressure points with measurements being made sequentially with pressure, *i.e.* measurements are not made upon decompression due to hysteresis within the system and a lack of knowledge of the pressure at the sample position;
- An empty, uncompressed $Ti_{0.676}Zr_{0.324}$ gasket;
- Two or three $Ti_{0.676}Zr_{0.324}$ gaskets that have been recovered from different pressures and the samples have been removed, leaving gaskets that more closely resemble those under compression;
- Two or three empty anvil measurements where no sample or gasket is present, the different measurements featuring different anvil separations corresponding to different stages of compression;
- A full-sized vanadium pellet inside an uncompressed gasket;
- A "medium" sized vanadium pellet in a recovered gasket;
- A "small" sized vanadium pellet in a recovered gasket.

Gaskets cannot be compressed with no sample present because the sample affects the material deformation *i.e.* it withstands the gasket being pushed radially inwards by the anvils. Instead an uncompressed gasket is measured along with two or three gaskets that have been recovered from previous compression measurements. A linear combination of these gaskets has been found to be adequate for correcting the data sets [85]. Equation (3.20) then becomes

$$\left.\frac{\mathrm{d}\sigma}{\mathrm{d}\Omega}\right|_{\mathrm{S}} = \frac{1}{N_{\mathrm{S}} A_{\mathrm{S,SC}}(\theta)} \left\{ \frac{I^{\mathrm{E}*}_{\mathrm{SC}}(\theta)}{a(\theta)} - \left[M_{\mathrm{SC}}(\theta) - \frac{A_{\mathrm{C,SC}}(\theta)}{A_{\mathrm{C,C}}(\theta)} M_{\mathrm{C}}(\theta) \right] \right\}, \tag{3.24}$$

where $I_{\mathrm{SC}}^{\mathrm{E}*}(\theta)$ is the background and container corrected sample intensity. Let the measured intensity for the sample in a container (gasket) be denoted by $I_{\mathrm{SC}}^{\mathrm{E}'}(\theta)$. Then $I_{\mathrm{SC}}^{\mathrm{E}*}(\theta)$ is given by

$$I_{\mathrm{SC}}^{\mathrm{E}*}(\theta) = I_{\mathrm{SC}}^{\mathrm{E}'}(\theta) - I_{\mathrm{C}}^{\mathrm{E}'}(\theta), \tag{3.25}$$

where $I_{\mathrm{C}}^{\mathrm{E}'}(\theta)$ is a linear combination of empty gasket and empty anvil measurements, *i.e.*

$$I_{\mathrm{C}}^{\mathrm{E}'}(\theta) = x_{\mathrm{B}} I_{\mathrm{B}}^{\mathrm{E}'}(\theta) + \sum_{\alpha=1}^{N} x_{\mathrm{C}\alpha} I_{\mathrm{C}\alpha}^{\mathrm{E}'}(\theta) \tag{3.26}$$

where x_{B} is a weighting coefficient for the empty anvils, $I_{\mathrm{B}}^{\mathrm{E}'}(\theta)$ is the measured intensity for the empty anvils, x_α is a weighting coefficient for empty gasket α, and $I_{\mathrm{C}\alpha}^{\mathrm{E}'}(\theta)$ is the measured intensity for empty gasket α. Any scattering angle dependence for the weighting coefficients is neglected as the ratio $A_{\mathrm{C,SC}}(\theta)/A_{\mathrm{C,C}}(\theta)$ is found to have little 2θ-dependence.

Several vanadium calibration measurements are typically made during the course of each experiment. Vanadium pieces of different sizes are used to normalise the sample measurements at different stages of compression. The background and container corrections for the vanadium measurements are made in the same manner as for the samples.

In correcting the neutron diffraction data it is necessary to calculate the attenuation coefficients $A_{i,j}(\theta)$. This calculation was made using the GUDRUN [92] program. Similarly it is necessary to calculate the multiple scattering cross-section $M_i(\theta)$, and the program CYLMULTOF [89] was used for this calculation.

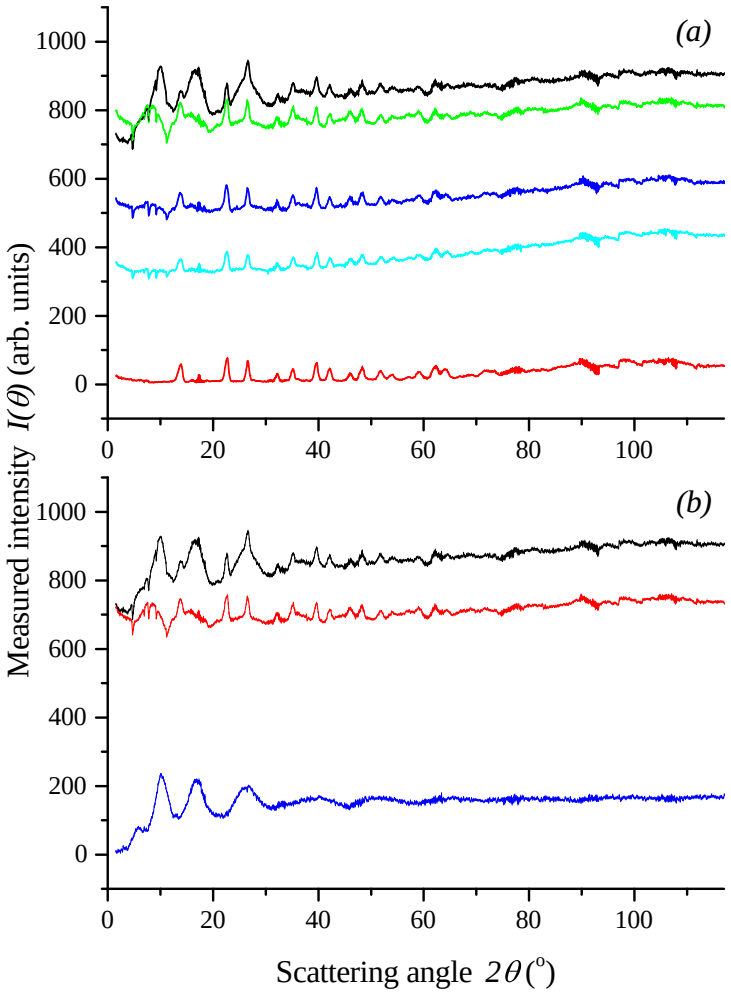

Figure 3-18: Steps in the container and background correction procedure for a sample of As_2Se_3 at ambient pressure using a PE press in an in-plane scattering geometry utilising single toroid cubic boron nitride anvils mounted on the D4c diffractometer. *(a)* The measured intensities for the sample in its container $I^{E'}_{SC}(\theta)$ (black curve); the empty anvils with no sample or gasket present $I^{E'}_{B}(\theta)$ (red curve); an empty un-compressed gasket $I^{E'}_{C1}(\theta)$ (green curve); an empty gasket that has been recovered from 4.7 GPa $I^{E'}_{C2}(\theta)$ (blue curve); and an empty gasket that has been recovered from 8.1 GPa $I^{E'}_{C3}(\theta)$ (cyan curve). *(b)* The measured intensity for the sample in its container $I^{E'}_{SC}(\theta)$ (black curve); the intensity constituted from the linear combination $I^{E'}_{C}(\theta) = x_B I^{E'}_{B}(\theta) + x_{C1} I^{E'}_{C1}(\theta)$ (red curve) with weighting coefficients $x_B = 0.1$ and $x_{C1} = 0.9$; and the background and container corrected sample intensity $I^{E*}_{SC}(\theta) = I^{E'}_{SC}(\theta) - I^{E'}_{C}(\theta)$ (blue curve).

3.7.2 Transverse scattering geometry

This section discusses the data reduction procedure used for the PEARL diffractometer utilising a PE press in transverse scattering geometry. The theory for this data analysis method was first discussed in Ref. [86]. The analysis procedure is summarised at the end of the section in figure 3-21 in the form of a flowchart.

Consider the diffraction experiment shown in figure 3-13, where the scattering angle is limited to $2\theta \simeq 90^\circ$ and the Q-range is controlled by the incident wavelength λ distribution. Due to the small angular range, it is convenient to consider the data analysis procedure in terms of Q as opposed to 2θ. The background-corrected intensity measured for a sample S in a container C can therefore be re-written as [86]

$$I^{\mathrm{E}}_{\mathrm{SC}}(Q) = a(Q) N_{\mathrm{S}} A_{\mathrm{S,SC}}(Q) \left.\frac{\mathrm{d}\sigma}{\mathrm{d}\Omega}\right|_{\mathrm{S}} + a(Q) M_{\mathrm{SC}}(Q), \tag{3.27}$$

whilst the background-corrected intensity for a vanadium pellet V in a container C can be written as

$$I^{\mathrm{E}}_{\mathrm{VC}}(Q) = a(Q) N_{\mathrm{V}} A_{\mathrm{V,VC}}(Q) \left.\frac{\mathrm{d}\sigma}{\mathrm{d}\Omega}\right|_{\mathrm{V}} + a(Q) M_{\mathrm{VC}}(Q). \tag{3.28}$$

If a vanadium calibration measurement is made then combining equation (3.22) with equations (3.27) and (3.28) yields

$$\left.\frac{\mathrm{d}\sigma}{\mathrm{d}\Omega}\right|_{\mathrm{S}} = F(Q) + \frac{\sigma_{\mathrm{self}}}{4\pi} = W(Q)\frac{I^{\mathrm{E}}_{\mathrm{SC}}(Q)}{I^{\mathrm{E}}_{\mathrm{VC}}(Q)} + X(Q), \tag{3.29}$$

where

$$W(Q) = \frac{N_{\mathrm{V}} A_{\mathrm{V,VC}}(Q) b^2_{\mathrm{V,inc}} \left[1 + P_{\mathrm{V}}(Q)\right] + M_{\mathrm{VC}}(Q)}{N_{\mathrm{S}} A_{\mathrm{S,SC}}(Q)}, \tag{3.30}$$

$$X(Q) = \frac{M_{\mathrm{SC}}(Q)}{N_{\mathrm{S}} A_{\mathrm{S,SC}}(Q)}, \tag{3.31}$$

and σ_{self} is the self-scattering cross-section for the sample

$$\frac{\sigma_{\mathrm{self}}}{4\pi} = \sum_{\alpha=1}^{n} c_\alpha \left(b^2_\alpha + b^2_{\alpha,\mathrm{inc}}\right)\left[1 + P_\alpha(Q)\right]. \tag{3.32}$$

The inelasticity correction $P_\alpha(Q)$ is calculated using the PLATOM program [93]. Usually it is found that $X(Q) << \frac{\sigma_{\mathrm{self}}}{4\pi}$ and so the total structure factor $F(Q)$ is given by

$$F(Q) \simeq W(Q)\frac{I^{\mathrm{E}}_{\mathrm{SC}}(Q)}{I^{\mathrm{E}}_{\mathrm{VC}}(Q)} - \frac{\sigma_{\mathrm{self}}}{4\pi}. \tag{3.33}$$

For a typical neutron diffraction experiment on PEARL utilising a PE press in transverse scattering geometry the following measurements are made:

- An empty uncompressed $\mathrm{Ti}_{0.676}\mathrm{Zr}_{0.324}$ gasket;
- A sample contained within a $\mathrm{Ti}_{0.676}\mathrm{Zr}_{0.324}$ gasket at several different pressure points with measurements being made sequentially with pressure, *i.e.* measurements are not made upon decompression due to hysteresis within the system and a lack of knowledge of the pressure at the sample position;
- A vanadium pellet contained within a $\mathrm{Ti}_{0.676}\mathrm{Zr}_{0.324}$ gasket measured at pressures similar to those used for the sample. The vanadium pellet is not necessarily compressed to the same pressure as the sample, but rather it is compressed such that the scattering geometry matches that of the sample as closely as possible.

In practice, it is not possible to measure the empty container intensity for each pressure point as gaskets cannot be compressed on their own, *i.e.* without a sample inside to withstand the inwards forces provided by the anvils. The anvils, made from sintered diamonds, show large Bragg peaks that change position and intensity with applied pressure. An approximation is made in which the corrected sample and vanadium intensities are given by

$$I^{\mathrm{E}*}_{\mathrm{SC}}(Q) = I^{\mathrm{E}'}_{\mathrm{SC}}(Q) - aI^{\mathrm{E}'}_{\mathrm{C}}(Q), \tag{3.34}$$

and

$$I^{\mathrm{E}*}_{\mathrm{VC}}(Q) = I^{\mathrm{E}'}_{\mathrm{SC}}(Q) - bI^{\mathrm{E}'}_{\mathrm{C}}(Q), \tag{3.35}$$

respectively, where $I^{\mathrm{E}'}_{\mathrm{SC}}(Q)$ is the intensity measured for a sample contained within a gasket, $I^{\mathrm{E}'}_{\mathrm{VC}}(Q)$ is the intensity measured for a vanadium pellet contained within a gasket, $I^{\mathrm{E}'}_{\mathrm{C}}(Q)$ is the intensity measured for an empty un-compressed gasket under a small applied load ($\sim 2\,\mathrm{tonnes}$), and a and b are constants. Equation (3.33) can then be re-written as

$$F(Q) \simeq W(Q)\frac{I^{\mathrm{E}'}_{\mathrm{SC}}(Q) - aI^{\mathrm{E}'}_{\mathrm{C}}(Q)}{I^{\mathrm{E}'}_{\mathrm{VC}}(Q) - bI^{\mathrm{E}'}_{\mathrm{C}}(Q)} - \frac{\sigma_{\mathrm{self}}}{4\pi}. \tag{3.36}$$

The constants a and b are chosen by the experimentalist to minimise the slope on the ratio $\left[I^{\mathrm{E}'}_{\mathrm{SC}}(Q) - aI^{\mathrm{E}'}_{\mathrm{C}}(Q)\right] / \left[I^{\mathrm{E}'}_{\mathrm{VC}}(Q) - bI^{\mathrm{E}'}_{\mathrm{C}}(Q)\right]$.

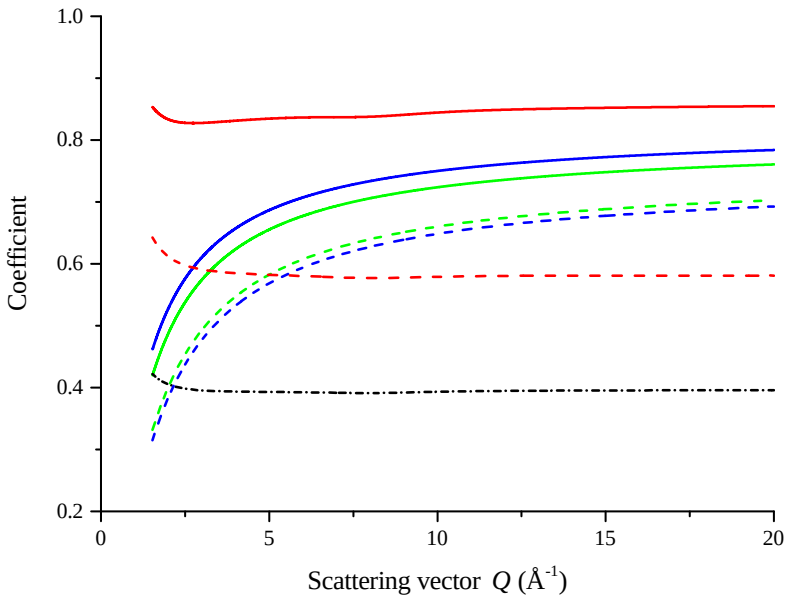

Figure 3-19: The coefficients $A_{\mathrm{S,SC}}(Q)$ (blue curve), $A_{\mathrm{V,VC}}(Q)$ (green curve), and $W(Q)$ (barn) (red curve) for amorphous $GeSe_2$ calculated for the double toroid anvil geometry at ambient pressure (solid curves) and at 16.1 GPa (dashed curves). Also shown is $b^2_{\mathrm{V,inc}}\left[1+P_{\mathrm{V}}(Q)\right]$ (barn) (black chained curve). The coefficients $A_{\mathrm{S,SC}}(Q)$, $A_{\mathrm{V,VC}}(Q)$, $W(Q)$, and $b^2_{\mathrm{V,inc}}\left[1+P_{\mathrm{V}}(Q)\right]$ were calculated using the dimensions of an uncompressed and a recovered gasket for the ambient and high pressure data sets, respectively. The parameters used in the calculations are given in table 3.1. The scattering and absorption cross-sections used in the calculations were taken from Ref. [53].

	Ambient	16.1 GPa
Sample radius r_{S} (cm)	0.2	0.2
Incident beam radius r_{B} (cm)	0.169	0.169
Gasket outer radius r_{g} (cm)	0.69	0.895
Sample height h (cm)	0.16	0.055
$GeSe_2$ number density ρ_{S} (Å^{-3})	0.0324	0.0549
$Ti_{0.676}Zr_{0.324}$ number density ρ_{C} (Å^{-3})	0.0511	0.0579
V number density ρ_{V} (Å^{-3})	0.0721	0.0794

Table 3.1: Dimensions and number densities used for calculating $A_{\mathrm{S,SC}}(Q)$, $A_{\mathrm{V,VC}}(Q)$, $W(Q)$, and $b^2_{\mathrm{V,inc}}\left[1+P_{\mathrm{V}}(Q)\right]$ for amorphous $GeSe_2$ in a double toroid gasket at ambient pressure and at 16.1 GPa. The Q dependence of these coefficients is shown in figure 3-19. The number density of $Ti_{0.676}Zr_{0.324}$ at 16.1 GPa is an over-estimate as it corresponds to the pressure of the sample and not to the pressure applied across the gasket.

Consider an experiment where the volumes illuminated by the incident beam for the sample and the vanadium are comparable. As the contribution of $M_{\mathrm{VC}}(Q)$ to $W(Q)$ is small [86] the scaling factor $W(Q)$ can be re-written as

$$W(Q) = \frac{\rho_{\mathrm{V}} A_{\mathrm{V,VC}}(Q) b^2_{\mathrm{V,inc}} \left[1 + P_{\mathrm{V}}(Q)\right]}{\rho_{\mathrm{S}} A_{\mathrm{S,SC}}(Q)}. \tag{3.37}$$

where ρ_{S} and ρ_{V} are the number densities of the sample and vanadium, respectively.

Figure 3-19 shows the Q dependence of the coefficients $A_{\mathrm{S,SC}}(Q)$, $A_{\mathrm{V,VC}}(Q)$, $W(Q)$, and $b^2_{\mathrm{V,inc}} \left[1 + P_{\mathrm{V}}(Q)\right]$ for amorphous $GeSe_2$ in a double toroid anvil at ambient pressure and at 16.1 GPa. $W(Q)$ shows little variation with Q and so it is assumed in the data analysis procedure that it is constant, Then equation (3.33) can be re-written as

$$F(Q) \simeq W \frac{I^{\mathrm{E}'}_{\mathrm{SC}}(Q) - a I^{\mathrm{E}}_{\mathrm{C}}(Q)}{I^{\mathrm{E}'}_{\mathrm{VC}}(Q) - b I^{\mathrm{E}}_{\mathrm{C}}(Q)} - \frac{\sigma_{\mathrm{self}}}{4\pi}, \tag{3.38}$$

where W is a scaling factor chosen to ensure that the ratio $\left[I^{\mathrm{E}'}_{\mathrm{SC}}(Q) - a I^{\mathrm{E}'}_{\mathrm{C}}(Q)\right]$ / $\left[I^{\mathrm{E}'}_{\mathrm{VC}}(Q) - b I^{\mathrm{E}'}_{\mathrm{C}}(Q)\right]$ oscillates about $\frac{\sigma_{\mathrm{self}}}{4\pi}$. Figure 3-20 shows an example of the data correction procedure for amorphous $GeSe_2$ at 16.1 GPa.

Equation (3.38) yields an initial total structure factor, henceforth labelled as $F_0(Q)$. An iterative procedure is then used to refine this function. $F_0(Q)$ is first scaled by a constant factor Z.

As discussed in section 3.3, $F_0(Q)$ lacks low Q data for $Q < 1.55\,\text{Å}^{-1}$. This region is initially set to the $F(Q \to 0)$ limit and the data are then Fourier transformed to real space. Any large peaks at low-r values are set to the low-r $G(r \to 0)$ limit and the data are back Fourier transformed back to Q-space. This procedure is used to remove any residual slope on the reciprocal space data set. The resulting total structure factor is labelled $F_1(Q)$.

The low-Q region of $F_1(Q)$ is then fitted with a Lorentzian function as this usually provides a good representation of the so-called first-sharp diffraction peak (FSDP) [94, 95]. The Lorentzian function is fit in such a way that it gives the expected $F(Q \to 0)$ limit at $Q = 0$. This limit can be estimated either from ambient measurements (where there is sufficient Q range to approach $Q \to 0$) or from theoretical calculations [57]. This modified total structure factor is labelled $F_2(Q)$.

$F_2(Q)$ is then Fourier transformed and all of the low-r un-physical oscillations are set to the calculated $G(r \to 0)$ limit, before a back Fourier transform is made into reciprocal space. This total structure factor $F_{\mathrm{BT}}(Q)$ should match $F_2(Q)$ within the experimental error. An iterative process is then started where parameters, such as the scaling factor Z, the number of oscillations removed in the slope correction, or the parameters of the Lorentzian, can be modified to ensure that these two functions match.

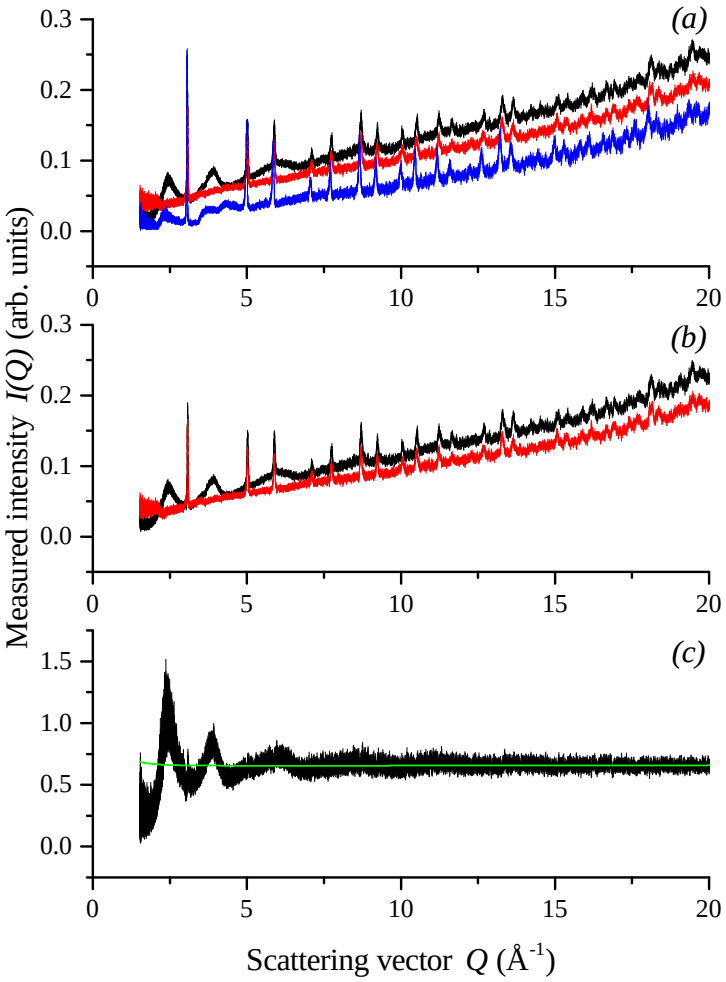

Figure 3-20: Steps in the data correction procedure for $GeSe_2$ at 16.1 GPa where the data sets are measured using a PE press in transverse geometry utilising double toroid sintered diamond anvils mounted on the PEARL diffractometer. The load applied to the sample and vanadium was 130 tonnes whilst the load applied to the empty $Ti_{0.676}Zr_{0.324}$ gasket was 2 tonnes. *(a)* The measured intensities for the sample in its container $I^{\mathrm{E}'}_{\mathrm{SC}}(Q)$ (black curve); vanadium in its container $I^{\mathrm{E}'}_{\mathrm{VC}}(Q)$ (red curve); and empty gasket $I^{\mathrm{E}}_{\mathrm{C}}(Q)$ (blue curve). *(b)* The container-corrected intensities for the sample $I^{\mathrm{E}*}_{\mathrm{SC}}(Q) = I^{\mathrm{E}'}_{\mathrm{SC}}(Q) - aI^{\mathrm{E}}_{\mathrm{C}}(Q)$ (black curve) and for the vanadium $I^{\mathrm{E}*}_{\mathrm{VC}}(Q) = I^{\mathrm{E}'}_{\mathrm{VC}}(Q) - bI^{\mathrm{E}}_{\mathrm{C}}(Q)$ (red curve), where the constants are $a = 0.11$ and $b = 0.13$, respectively. *(c)* The ratio $WI^{\mathrm{E}*}_{\mathrm{SC}}(Q)/I^{\mathrm{E}*}_{\mathrm{VC}}(Q)$ (black curve) and the calculated self-scattering cross-section $\sigma_{\mathrm{self}}/4\pi$ (green curve), with a scaling factor $W = 0.54$.

Once the two total structure factors $F_2(Q)$ and $F_{\mathrm{BT}}(Q)$ match within the experimental error $F_2(Q)$ is taken to be the final total structure factor $F(Q)$ from which results are obtained.

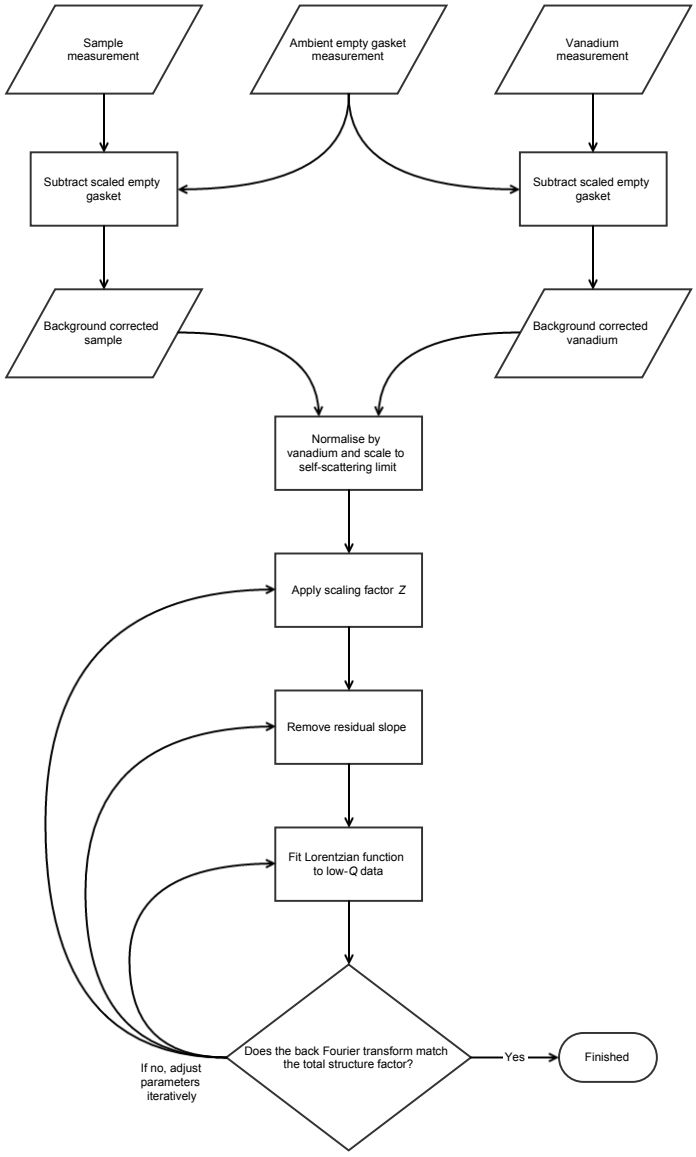

Figure 3-21: The data analysis procedure for neutron diffraction experiments performed using a PE press on the PEARL diffractometer.

4. Density-driven defect-mediated network collapse of $GeSe_2$ glass

The work presented in this chapter was originally published in Wezka, Bouzid, Pizzey *et al.* [79]

4.1 Introduction

The density-driven structural transformations in network-forming glasses lead to changes in their physiochemical properties, which can be abrupt in so-called polyamorphic transitions [19, 21]. The mechanisms of densification will depend on the network topology and, since this is governed by the chemical-bonding scheme, chalcogenide glasses are anticipated to exhibit different behaviour to their oxide counterparts. For example, the ability of chalcogenide glasses to form non-stoichiometric compositions [96] points to flexibility in character of the network-forming structural motifs, *i.e.*, to enhanced structural variability [97, 98]. A prototype is provided by amorphous $GeSe_2$ where the ambient-pressure network, built from a mixture of corner-sharing (CS) and edge-sharing (ES) tetrahedra, incorporates a significant number of Ge-Ge and Se-Se homopolar bonds [6, 99–106]. The nature of the density-driven collapse is, however, uncertain. Different studies at pressures P up to $\sim 9\,\mathrm{GPa}$ find either (i) a continuous structural change [107, 108] or (ii) a discontinuous semiconductor-glass to metal-crystalline transition [31, 32].

In this chapter, *in situ* high-pressure neutron diffraction is used to investigate the structure of $GeSe_2$ glass under compression from ambient pressure to $P \sim 16.2(5)\,\mathrm{GPa}$ at room temperature ($T \sim 300\,\mathrm{K}$). The investigation complements previous work [41] in which the isotope substitution method was applied to disentangle the complexity of correlations associated with a single diffraction pattern [109]. The experimental work is complemented by a set [42] of Car-Parrinello [110] first-principles molecular dynamics

(FPMD) simulations [106, 111–113]. This approach is necessitated by the presence of homopolar bonds, which preclude any reliable modeling based on interatomic potentials [114]. The combined techniques yield a self-consistent picture for the structure at a pressure below $\sim 8.5(5)$ GPa in which there is no change to the mean nearest-neighbour coordination number $\overline{n}$ but an interplay between the fractions of CS versus ES tetrahedra. At pressures beyond this threshold, however, the diffraction and FPMD results follow different pathways of metastability. This outcome is likely to originate from different thermal histories, with the simulations showing an increase of $\overline{n}$ with pressure that is more rapid than found in experiment. In the simulations, further densification proceeds by the formation of higher-coordinated Ge and Se atoms where, on initial formation, large proportions of these higher-coordinated atoms form homopolar bonds. These defects in the chemical ordering therefore play a mediating role in the structural transformation of the modeled glass structure.

4.2 Theory

As discussed in chapter 2, in a neutron diffraction experiment the total structure factor

$$F(Q) = \sum_{\alpha=1}^{n} \sum_{\beta=1}^{n} c_\alpha c_\beta b_\alpha b_\beta \left[S^{\mathrm{FZ}}_{\alpha\beta}(Q) - 1 \right] \tag{4.1}$$

is measured, where α and β denote the chemical species, c_α is the atomic fraction of chemical species α, b_α is the bound coherent scattering length of chemical species α, $S^{\mathrm{FZ}}_{\alpha\beta}(Q)$ is the Faber-Ziman partial structure factor for chemical species α and β [55], and Q is the magnitude of the scattering vector [52].

Consider an experiment where diffraction patterns are measured for three $GeSe_2$ glasses that are identical in every aspect, save for their Ge and/or Se isotopic enrichments. Assuming that the glasses are $^{\mathrm{N}}\mathrm{Ge}^{\mathrm{N}}\mathrm{Se}_2$, $^{70}\mathrm{Ge}^{\mathrm{N}}\mathrm{Se}_2$, and $^{73}\mathrm{Ge}^{76}\mathrm{Se}_2$, where N denotes the natural abundance of an isotope, then the measured total structure factors are ${}^{\mathrm{N}}_{\mathrm{N}}F(Q)$, ${}^{70}_{\mathrm{N}}F(Q)$, and ${}^{73}_{76}F(Q)$, respectively, where the superscript denotes the Ge isotope enrichment and the subscript denotes the Se isotope enrichment.

First-order difference functions can be constructed from these diffraction patterns in which a single correlation is removed at a time. Assuming that the two total structure factors chosen for creating these difference functions are ${}^{70}_{\mathrm{N}}F(Q)$ and ${}^{73}_{76}F(Q)$ then it is

possible to construct the first-order difference functions

$$\begin{aligned}\Delta F(Q)_{\text{no Ge-Ge}} &= {}^{73}_{76}F(Q) - \frac{b^2_{^{73}\text{Ge}}}{b^2_{^{70}\text{Ge}}}{}^{70}_{\text{N}}F(Q) \\ &= c^2_{\text{Se}}\left(b^2_{^{76}\text{Se}} - \frac{b^2_{^{73}\text{Ge}}}{b^2_{^{70}\text{Ge}}}b^2_{^{\text{N}}\text{Se}}\right)\left[S^{\text{FZ}}_{\text{SeSe}}(Q) - 1\right] \\ &+ 2c_{\text{Ge}}c_{\text{Se}}\left(b_{^{73}\text{Ge}}b_{^{76}\text{Se}} - \frac{b^2_{^{73}\text{Ge}}}{b^2_{^{70}\text{Ge}}}b_{^{70}\text{Ge}}b_{^{\text{N}}\text{Se}}\right)\left[S^{\text{FZ}}_{\text{GeSe}}(Q) - 1\right] \qquad (4.2)\end{aligned}$$

and

$$\begin{aligned}\Delta F(Q)_{\text{no Se-Se}} &= {}^{70}_{\text{N}}F(Q) - \frac{b^2_{^{\text{N}}\text{Se}}}{b^2_{^{76}\text{Se}}}{}^{73}_{76}F(Q) \\ &= c^2_{\text{Ge}}\left(b^2_{^{70}\text{Ge}} - \frac{b^2_{^{\text{N}}\text{Se}}}{b^2_{^{76}\text{Se}}}b^2_{^{73}\text{Ge}}\right)\left[S^{\text{FZ}}_{\text{GeGe}}(Q) - 1\right] \\ &+ 2c_{\text{Ge}}c_{\text{Se}}\left(b_{^{70}\text{Ge}}b_{^{\text{N}}\text{Se}} - \frac{b^2_{^{\text{N}}\text{Se}}}{b^2_{^{76}\text{Se}}}b_{^{73}\text{Ge}}b_{^{76}\text{Se}}\right)\left[S^{\text{FZ}}_{\text{GeSe}}(Q) - 1\right]. \qquad (4.3)\end{aligned}$$

The weighting factors for the partial structure factors in the first-order difference functions and total structure factors are given in table 4.1.

	$S^{\text{FZ}}_{\text{GeGe}}(Q)$(barn)	$S^{\text{FZ}}_{\text{SeSe}}(Q)$(barn)	$S^{\text{FZ}}_{\text{GeSe}}(Q)$(barn)
${}^{\text{N}}_{\text{N}}F(Q)$	0.0744(4)	0.2823(6)	0.2899(8)
${}^{70}_{\text{N}}F(Q)$	0.1111(22)	0.2823(6)	0.354(4)
${}^{73}_{76}F(Q)$	0.0288(5)	0.662(11)	0.276(3)
$\Delta F(Q)_{\text{no Ge-Ge}}$	0.000(6)	0.588(11)	0.184(3)
$\Delta F(Q)_{\text{no Se-Se}}$	0.099(2)	0.000(7)	0.236(4)

Table 4.1: The weighting factors for the Ge-Ge, Se-Se, and Ge-Se partial structure factors. All numerical values take into account the isotopic enrichment of the samples used in the experiments. The scattering lengths used were obtained from Ref. [53] and are: $b_{^{\text{N}}\text{Ge}} = 8.185(20)\,\text{fm}$, $b_{^{70}\text{Ge}} = 10.0(1)\,\text{fm}$, $b_{^{73}\text{Ge}} = 5.09(4)\,\text{fm}$, $b_{^{\text{N}}\text{Se}} = 7.970(9)\,\text{fm}$, and $b_{^{76}\text{Se}} = 12.2(1)\,\text{fm}$. The atomic fractions are $c_{\text{Ge}} = 1/3$ and $c_{\text{Se}} = 2/3$ exactly.

Real-space information can be obtained via Fourier transformation of the reciprocal space data. Hence, the total pair-distribution function ${}^{\gamma}_{\delta}G(r)$ and the first-order pair-distribution function $\Delta G(r)_{\text{X}}$ can be obtained where

$${}^{\gamma}_{\delta}G(r) = \frac{1}{2\pi^2 r\rho}\int_0^{\infty} QM(Q){}^{\gamma}_{\delta}F(Q)\sin(Qr)\,\mathrm{d}Q \qquad (4.4)$$

and

$$\Delta G(r)_{\mathrm{X}} = \frac{1}{2\pi^2 r\rho}\int_0^\infty QM(Q)\Delta F(Q)_{\mathrm{X}}\sin(Qr)\,\mathrm{d}Q. \tag{4.5}$$

In these equations, r is a distance in real space, ρ is the number density of the glass, γ and δ are the isotope enrichments of Ge and Se, respectively, X = "no Ge-Ge" or "no Se-Se" denotes the pair correlations that have been removed, and $M(Q)$ is a modification function

$$M(Q) = \begin{cases} 1 & \text{if } Q \leq Q_{\max} \\ 0 & \text{if } Q > Q_{\max}, \end{cases} \tag{4.6}$$

which is introduced because a diffractometer can measure only a finite Q range up to a maximum value $Q_{\max}$. Fourier transformation artefacts can arise from the finite Q range and can be reduced through the use of a Lorch modification function [56]

$$M(Q) = \begin{cases} \frac{\sin(aQ)}{aQ} & \text{if } Q \leq Q_{\max} \\ 0 & \text{if } Q > Q_{\max}, \end{cases} \tag{4.7}$$

at the expense of broadened r-space features. The low-r limits for the total and first-order pair-distribution functions, $G(r \to 0)$ and $\Delta G(r \to 0)_{\mathrm{X}}$, respectively, are given in table 4.2

	Low-r limit (barn)
${}^{\mathrm{N}}_{\mathrm{N}}G(r)$	-0.647(1)
${}^{70}_{\mathrm{N}}G(r)$	-0.747(5)
${}^{73}_{76}G(r)$	-0.966(11)
$\Delta G(r)_{\text{no Ge-Ge}}$	-0.335(7)
$\Delta G(r)_{\text{no Se-Se}}$	-0.773(14)

Table 4.2: Theoretical low-r limits $G(r \to 0)$ and $\Delta G(r \to 0)_{\mathrm{X}}$, where X = "no Ge-Ge" or "no Se-Se".

The total structure factor $F(Q)$ can also be written in terms of the Bhatia-Thornton partial structure factors [58] such that

$$\begin{aligned} F(Q) = \langle b\rangle^2 \left[S^{\mathrm{BT}}_{\mathrm{NN}}(Q) - 1\right] + \\ c_\alpha c_\beta \left(b_\alpha - b_\beta\right)^2 \left\{\left[\frac{S^{\mathrm{BT}}_{\mathrm{CC}}(Q)}{c_\alpha c_\beta}\right] - 1\right\} + \\ 2\langle b\rangle \left(b_\alpha - b_\beta\right) S^{\mathrm{BT}}_{\mathrm{NC}}(Q), \end{aligned} \tag{4.8}$$

where $\langle b \rangle$ is the mean bound coherent scattering length

$$\langle b \rangle = \sum_{\alpha} c_{\alpha} b_{\alpha} = c_{\mathrm{Ge}} b_{\mathrm{Ge}} + c_{\mathrm{Se}} b_{\mathrm{Se}}, \tag{4.9}$$

and $S^{\mathrm{BT}}_{\mathrm{NN}}(Q)$, $S^{\mathrm{BT}}_{\mathrm{CC}}(Q)$, and $S^{\mathrm{BT}}_{\mathrm{NC}}(Q)$ are the so-called Bhatia-Thornton number-number, concentration-concentration, and number-concentration partial structure factors, respectively. Consider the glass ${}^{\mathrm{N}}\mathrm{Ge}{}^{\mathrm{N}}\mathrm{Se}_2$ where the bound coherent scattering lengths of natural Ge and Se are $b_{\mathrm{NGe}} = 8.185(2)\,\mathrm{fm}$ and $b_{\mathrm{NSe}} = 7.970(9)\,\mathrm{fm}$, respectively. As $b_{\mathrm{NGe}} \simeq b_{\mathrm{NSe}}$ an approximation can be made where the weighting factors for the concentration-concentration and number-concentration Bhatia-Thornton partial structure factors, $S^{\mathrm{BT}}_{\mathrm{CC}}(Q)$ and $S^{\mathrm{BT}}_{\mathrm{NC}}(Q)$, are zero, *i.e.*

$${}^{\mathrm{N}}_{\mathrm{N}}F(Q) = \langle b \rangle^2 \left[S^{\mathrm{BT}}_{\mathrm{NN}}(Q) - 1 \right]. \tag{4.10}$$

The Bhatia-Thornton number-number partial pair-distribution function $g^{\mathrm{BT}}_{\mathrm{NN}}(r)$ can be found by substituting ${}^{\mathrm{N}}_{\mathrm{N}}G(r)$ for ${}^{\mathrm{N}}_{\mathrm{N}}F(Q)$ and $g^{\mathrm{BT}}_{\mathrm{NN}}(r)$ for $S^{\mathrm{BT}}_{\mathrm{NN}}(Q)$ in equation (4.10). Using $g^{\mathrm{BT}}_{\mathrm{NN}}(r)$ it is possible to calculate the mean coordination number $\overline{n}$ which is averaged over all types of chemical species

$$\begin{aligned} \overline{n} &= 4\pi\rho \int_{r_1}^{r_2} r^2 g^{\mathrm{BT}}_{\mathrm{NN}}(r)\,\mathrm{d}r \\ &= c_{\mathrm{Ge}} \left(\overline{n}^{\mathrm{Ge}}_{\mathrm{Ge}} + \overline{n}^{\mathrm{Se}}_{\mathrm{Ge}} \right) + c_{\mathrm{Se}} \left(\overline{n}^{\mathrm{Se}}_{\mathrm{Se}} + \overline{n}^{\mathrm{Ge}}_{\mathrm{Se}} \right), \end{aligned} \tag{4.11}$$

where $\overline{n}^{\beta}_{\alpha}$ is the average number of β atoms in a radial shell ($r_1 \leq r \leq r_2$) around a central α atom.

Consider an x-ray diffraction experiment. The diffraction theory is broadly the same as for neutron diffraction, except that the bound coherent scattering length, b_{α}, must be replaced with a Q-dependent atomic form factor $f_{\alpha}(Q)$, which depends strongly on the number of electrons in the atom, *i.e.* the atomic number. The total structure factor for an x-ray experiment is then given by

$$F_{\mathrm{X}}(Q) = \sum_{\alpha=1}^{n} \sum_{\beta=1}^{n} c_{\alpha} c_{\beta} f_{\alpha}(Q) f^{*}_{\beta}(Q) \left[S^{\mathrm{FZ}}_{\alpha\beta}(Q) - 1 \right]. \tag{4.12}$$

In order to remove the associated Q dependent slope and improve the resolution of peaks in the corresponding real-space function, the total structure factor can be re-written as

$$S_{\mathrm{X}}(Q) = 1 + \frac{F_{\mathrm{X}}(Q)}{\left| \langle f(Q) \rangle \right|^2} \tag{4.13}$$

where $\langle f(Q)\rangle = \sum_\alpha c_\alpha f_\alpha(Q)$ is the mean atomic form factor. The equivalent expression for a neutron diffraction experiment is

$$S_{\mathrm{N}}(Q) = 1 + \frac{F(Q)}{\left|\langle b\rangle\right|^2}. \tag{4.14}$$

Due to the similarity of the coherent neutron scattering lengths ($b_{^{\mathrm{N}}\mathrm{Ge}} \simeq b_{^{\mathrm{N}}\mathrm{Se}}$) and the similarity of the atomic numbers for Ge and Se (32 and 34, respectively), the approximation can be made [51] that

$$S_{\mathrm{N}}(Q) \simeq S_{\mathrm{X}}(Q) \simeq S^{\mathrm{BT}}_{\mathrm{NN}}(Q) \tag{4.15}$$

for $^{\mathrm{N}}\mathrm{Ge}^{\mathrm{N}}\mathrm{Se}_2$. Similarly, the real-space functions can be expressed as

$$G_{\mathrm{N}}(r) \simeq G_{\mathrm{X}}(r) \simeq g^{\mathrm{BT}}_{\mathrm{NN}}(r). \tag{4.16}$$

4.3 Experimental procedure

Two neutron diffraction experiments were undertaken to study the structure of GeSe_2 under pressure. One experiment used the isotope substitution method and was performed on the D4c diffractometer utilising a VX5 PE press in an in-plane scattering geometry with single toroid cubic boron nitride anvils to make measurements up to $P = 8.2(5)\,\mathrm{GPa}$. The other experiment was performed on the PEARL HiPr diffractometer utilising a V3 PE press in a transverse scattering geometry with double toroid sintered diamond anvils to make measurements up to $P = 16.1(5)\,\mathrm{GPa}$. First-principles molecular dynamics (FPMD) simulations were also performed within the NVT ensemble to provide further detail on the structural evolution with pressure. The experimental procedure for the D4c experiment is discussed in Ref. [41], while the FSDP simulations are discussed in Ref. [42].

4.3.1 PEARL neutron diffraction experiment

A neutron diffraction experiment was performed to study amorphous $^{\mathrm{N}}\mathrm{Ge}^{\mathrm{N}}\mathrm{Se}_2$ at ambient temperature ($T \sim 300\,\mathrm{K}$) and at pressures up to $P = 16.1(5)\,\mathrm{GPa}$. A V3 Paris-Edinburgh press was mounted in a transverse scattering geometry on the PEARL HiPr diffractometer with double toroid sintered diamond anvils providing compression.

Amorphous $^{\mathrm{N}}\mathrm{Ge}^{\mathrm{N}}\mathrm{Se}_2$ was produced by loading elemental $^{\mathrm{N}}\mathrm{Ge}$ (99.9998%, Sigma-Aldrich) and $^{\mathrm{N}}\mathrm{Se}$ (99.999%, Sigma-Aldrich) into a silica ampoule. To avoid contamination this loading took place inside an inert Ar filled glovebox. The ampoule was evacuated and sealed, and was then heated in a rocking furnace from ambient tem-

perature to 975 °C at 2 °C min^{-1}. Equilibrium periods at $T = 221$ °C (melting point of Se) and 685 °C (melting point of Ge) were maintained during heating where the temperature was kept constant for 4 h. The temperature was kept at 975 °C for 48 h, before being cooled at 1 °C min^{-1} to the quench temperature $T = 842$ °C. After 5 h of equilibration the ampoule was dropped into an ice/salt-water mixture.

Sample	Pellet mass (g)	$Ti_{0.676}Zr_{0.324}$ gasket mass (g)
$^{N}Ge^{N}Se_2$	0.1403(1)	1.0859(1)
Vanadium	0.2056(1)	1.0762(1)

Table 4.3: Pellet and $Ti_{0.676}Zr_{0.324}$ gasket masses for the PEARL $GeSe_2$ experiment.

Before attempting to remove pieces of glass from the ampoule it was annealed at 370 °C to reduce any tension and aid in the production of a solid pellet piece. A $^{N}Ge^{N}Se_2$ pellet was produced from a single piece of glass recovered from the ampoule by gently grinding it to the correct shape using the method discussed in section 3.6.1. A vanadium pellet was produced by taking vanadium foil and placing the correct mass in a specially prepared die which re-creates the shape of a double toroid pellet. This was then compressed as outlined in section 3.6.1. The masses of the $^{N}Ge^{N}Se_2$ and vanadium pellets are given in table 4.3.

Applied load L (tonnes)	Pressure P (GPa)	$^{N}Ge^{N}Se_2$	Vanadium
2	Ambient	✓	✓
75	8.7	✓	✓
98	10.9	✓	✓
110	12.8	✓	✓
120	14.4	✓	✓
130	16.1	✓	

Table 4.4: Pressure points measured during the experiment. The pressure at the sample position P was deduced from the calibration curve given in figure 3-15.

The PEARL diffraction experiment was performed as outlined in section 3.6.4. Measurements were made for two empty $Ti_{0.676}Zr_{0.324}$ gaskets where their masses are given in table 4.3. Neutron diffraction measurements were made for the vanadium and the sample in turn, and the investigated pressure points are given in table 4.4. During the course of a pressure point measurement, the ratio was taken of the measured intensities for different periods of time. If this ratio deviates from unity then the scattered intensity is changing with respect to time. No such deviation was observed during the course of the measurements.

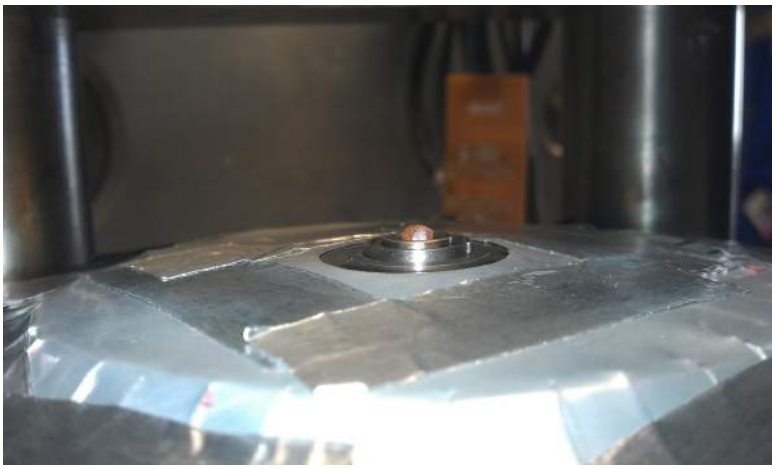

Figure 4-1: $^{\mathrm{N}}\mathrm{Ge}^{\mathrm{N}}\mathrm{Se}_2$ pellet in double toroid $\mathrm{Ti}_{0.676}\mathrm{Zr}_{0.324}$ gaskets sat on a sintered diamond piston anvil. Cadmium shielding and Al tape is placed radially around the anvil to reduce background scattering.

The compression was controlled by an automated machine up to an oil pressure $P_{\mathrm{oil}} = 950\,\mathrm{bar}$, after which a hand pump was used to manually increase the pressure. The automated system kept the pressure constant, *i.e.* if some relaxation occurred that caused the pressure to drop below its set point then the automated system would increase it back to the set point. When using the hand pump this was not possible, and any relaxation (typically $\sim$ 10–20 bar) was allowed to occur. Whilst increasing and decreasing pressure, periodic pauses were taken to allow the system to equilibrate.

The mass density ρ_{m} of GeSe_2 was measured using a helium pycnometer. This yielded an ambient-pressure number density $\rho_0 = 0.0324(1)\,\mathrm{\AA}^{-3}$. The pressure-volume equation of state for GeSe_2 is shown in figure 4-2. A 2nd-order Birch Murnaghan equation of state, given by

$$P(V; V_0, B_0) = \frac{3B_0}{2}\left[\left(\frac{V}{V_0}\right)^{-\frac{7}{3}} - \left(\frac{V}{V_0}\right)^{-\frac{5}{3}}\right], \tag{4.17}$$

was fitted to the data to allow for an extrapolation to higher pressures for use in the PEARL data analysis. The fitted bulk modulus was $B_0 = 10.55(30)\,\mathrm{GPa}$ which is comparable to the bulk modulus for $\mathrm{Ge}_3\mathrm{Se}_7$ found from sound velocity measurements, *i.e.* $B_0 = 14.5\,\mathrm{GPa}$ [115] and $B_0 = 12.64\,\mathrm{GPa}$ [116]. Using the ambient number density ρ_0 and the compression V/V_0 the number density and reduced density for the measured pressure points can be calculated, and the values are given in table 4.5.

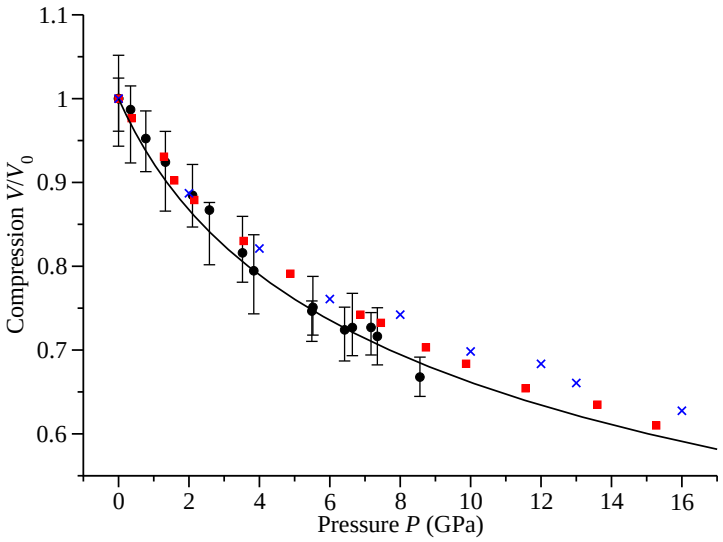

Figure 4-2: The pressure-volume equation of state for $GeSe_2$ under compression as measured experimentally in Ref. [108] (●). Included also are FPMD simulations from Ref. [42] (■) and from Ref. [107] (×). A 2nd-order Birch-Murnaghan equation of state was fitted to the experimental data giving a bulk modulus $B_0 = 10.55(30)$ GPa (solid black curve).

Pressure P (GPa)	Compression V/V_0	Number density ρ (Å^{-3})	Reduced density ρ/ρ_0
Ambient	1.0	0.0324(1)	1.0
8.7(5)	0.6821(8)	0.0475(5)	1.4661(15)
10.9(5)	0.6493(6)	0.0499(4)	1.5401(13)
12.8(5)	0.6243(6)	0.0519(4)	1.6018(13)
14.4(5)	0.6067(6)	0.0534(4)	1.6483(12)
16.1(5)	0.5902(4)	0.0549(3)	1.6943(11)

Table 4.5: Compression V/V_0, number density ρ, and reduced density ρ/ρ_0 for each pressure point measured in the PEARL $GeSe_2$ experiment.

4.3.2 First-principles molecular dynamics simulations

The FPMD simulations used the Car-Parrinello [110] method within the NVT ensemble with $N = 120$ atoms. At most state points, the Becke-Lee-Yang-Parr (BLYP) functional [117, 118] was used to describe the electron exchange and correlation. This functional was chosen because it leads to accurate results for the structure-related properties of liquid and glassy Ge-Se materials [106, 111–113, 119]. Valence electrons were treated explicitly and were represented by a plane-wave basis set expanded at the Γ point of the simulation cell using an energy cutoff of 20 Ry. The valence-core interactions were described by a Troullier-Martins norm-conserving pseudo-potential [120]. The largest cutoff used in the pseudo-potential construction was equal to 1.06 Å. A fictitious electron mass of 1000 a u (*i.e.* in units of $m_e a_0^2$ where m_e is the mass of an electron and a_0 is the Bohr radius) and a time step $\Delta t = 0.24$ fs were used to integrate the equations of motion. The temperature was controlled by a Nosè-Hoover thermostat [121, 122].

The simulations were initiated from ambient P and T configurations with vanishing stress-tensor values [106] that gave best agreement with the measured partial structure factors [101, 103]. The simulation for each new pressure started from a configuration taken from the previous (lower) pressure, after the density had been increased by decreasing the volume V. The system was then taken on a five-step thermal cycle:

- starting at $T = 300$ K for 40 ps,
- increasing to $T = 600$ K for 50 ps,
- increasing to $T = 900$ K for 150 ps,
- decreasing to $T = 600$ K for 70 ps,
- finishing at $T = 300$ K for 150 ps [106].

The dwell time at each temperature could vary by ± 20 ps from one simulation to another, but the dwell times for the cooling part of a cycle were kept longer than for the heating part of a cycle to allow for relaxation. Substantial diffusion at $T = 900$ K, on the scale of several interatomic distances, ensured that no memory was kept of an initial configuration, and that the glasses produced under pressure were statistically uncorrelated. For each pressure, 2-3 different configurations were averaged.

For a single state point at $P = 9$ GPa ($V/V_0 = 0.654$, $\rho/\rho_0 = 1.529$) a hybrid functional was used. The motivation for this switch was to improve the exchange-correlation term to see if this leads to a better reproduction of the experimental results at high pressure. The hybrid functional chosen (Heyd-Scuseria-Ernzerhof HSE06) is a

generalisation of the PBE0 functional [123] proposed in Ref. [124] in which the Perdew-Burke-Ernzerhof (PBE) exchange functional [125] is complemented by the Hartree exact exchange with a properly calibrated mixing coefficient.

The simulation details using the HSE06 functional are the same as for the BLYP functional, the only differences being (a) an energy cutoff of 30 Ry, and (b) a modified thermal cycle that started at $T = 300\,\mathrm{K}$ for 1.2 ps, increased to $T = 1100\,\mathrm{K}$ for 3.4 ps, decreased to $T = 900\,\mathrm{K}$ for 5.8 ps, and finished at $T = 300\,\mathrm{K}$ for 6.6 ps.

In the following, the FPMD results correspond to those made using the BLYP functional unless otherwise stated. The compression V/V_0 calculated for the simulations is compared to to the experimental results of Ref. [108] in figure 4-2. Using an ambient number density $\rho_0 = 0.0326\,\mathrm{Å}^{-3}$, the compression V/V_0, number density, and reduced density for the simulated pressure points can be calculated and are presented in table 4.6.

Pressure P (GPa)	Compression V/V_0	Number density ρ ($\mathrm{Å}^{-3}$)	Reduced density ρ/ρ_0
Ambient	1.0	0.0326	1.0
0.37	0.9766	0.0334	1.0239
1.29	0.9307	0.0351	1.0744
1.58	0.9024	0.0362	1.1081
2.15	0.8790	0.0371	1.1376
3.55	0.8302	0.0393	1.2046
4.88	0.7911	0.0412	1.2641
6.87	0.7423	0.0440	1.3473
7.45	0.7325	0.0445	1.3652
8.73	0.7032	0.0464	1.4221
9.87	0.6837	0.0477	1.4627
9*	0.6544	0.0499	1.5282
11.56	0.6544	0.0499	1.5282
13.6	0.6348	0.0514	1.5753
15.27	0.6101	0.0535	1.6392

Table 4.6: Compression V/V_0, number density ρ, and reduced density ρ/ρ_0 for each pressure point in the $GeSe_2$ FPMD simulations. * denotes a pressure point that made use of the HSE06 functional, where the pressure has been estimated by computing the stress for a relaxed configuration using the BLYP functional.

4.4 Results

Figure 4-3 shows the pressure dependence of the total structure factor $S_{\mathrm{N}}(Q)$ or $S_{\mathrm{X}}(Q)$ for $^{\mathrm{N}}\mathrm{Ge}^{\mathrm{N}}\mathrm{Se}_2$ glass. The figure compares the neutron diffraction $S_{\mathrm{N}}(Q)$ results from the present work and Refs. [41, 79, 101], the FPMD results at similar reduced densities to the neutron diffraction measurements [42], and the x-ray diffraction $S_{\mathrm{X}}(Q)$ results from Ref. [108]. In the case of $S_{\mathrm{N}}(Q)$, the D4c diffractometer was employed for the pressure range up to 4.7(5) GPa and the PEARL diffractometer was employed at higher pressures. The x-ray results have had an unphysical slope removed through the use of a back Fourier transform procedure [79], and as such differ from those originally published in Ref. [108].

At ambient pressure there is good overall agreement between the neutron diffraction, x-ray diffraction, and FPMD results. The smaller size of the first-sharp diffraction peak (FSDP) in the FPMD results may arise from the small size of the simulation cell. There are also occasional sharp peaks in the FPMD results at low-Q that are statistical in nature.

As the pressure is increased the agreement between neutron diffraction, x-ray diffraction, and FPMD results is maintained. The FSDP shifts from $Q_{\mathrm{FSDP}} = 1.00(2)\,\mathrm{\AA}^{-1}$ at ambient to higher-Q values until it disappears entirely at $\sim 8.7(5)$ GPa. Similarly, the principal peak shifts to higher-Q whilst growing in intensity. The x-ray diffraction results show a sharper principal peak when compared to the neutron diffraction results, which is possibly due to differences between the resolution functions of the different diffractometers used.

Figure 4-4 shows the pressure dependence of the total pair-distribution function $G(r)$ for $^{\mathrm{N}}\mathrm{Ge}^{\mathrm{N}}\mathrm{Se}_2$ glass, as obtained by Fourier transforming the data sets shown in figure 4-3. The neutron diffraction results for the pressure range up to 4.7(5) GPa had a cutoff $Q_{\mathrm{max}} = 15.9\,\mathrm{\AA}^{-1}$ for the ambient pressure data set and a cutoff $Q_{\mathrm{max}} = 18.5\,\mathrm{\AA}^{-1}$ for the data sets measured under pressure. The neutron diffraction results for the range 8.7 – 16.1(5) GPa had a cutoff $Q_{\mathrm{max}} = 19.55\,\mathrm{\AA}^{-1}$. The x-ray diffraction results had a cutoff $Q_{\mathrm{max}} = 16.8\,\mathrm{\AA}^{-1}$. In the case of the PEARL neutron diffraction results, the reciprocal space data sets were Fourier transformed using (i) a step modification function (equation (4.6)) and (ii) a Lorch modification function (equation (4.7)) [56]. The data obtained from the first procedure were joined smoothly to the data obtained from the second procedure at a point just beyond the first peak in real space.

The FPMD results were obtained by Fourier transforming the reciprocal space data sets, as opposed to being generated directly in real space. The analysis was undertaken in this way to ensure that the experimental and simulation results can be compared on a like-for-like basis, *i.e.* they have been treated by using the same Fourier transformation

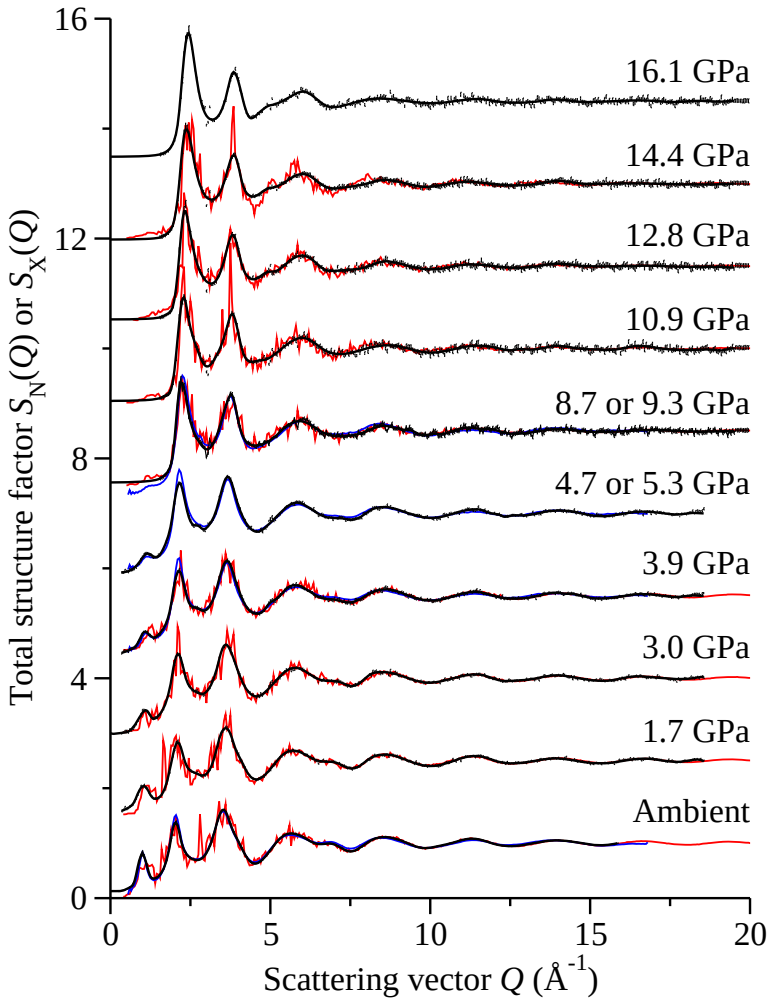

Figure 4-3: The pressure dependence of the neutron total structure factor $S_{\mathrm{N}}(Q)$ and x-ray total structure factor $S_{\mathrm{X}}(Q)$ for $^{\mathrm{N}}\mathrm{Ge}^{\mathrm{N}}\mathrm{Se}_2$, where $S_{\mathrm{N}}(Q) \simeq S_{\mathrm{X}}(Q) \simeq S_{\mathrm{NN}}^{\mathrm{BT}}(Q)$. The solid black curves show spline fits to the experimental data (shown by vertical error bars) for the $S_{\mathrm{N}}(Q)$ data sets measured in Refs. [101, 103] (ambient pressure) and the present work (1.7, 3.0, 3.9. 4.7, 8.7, 10.9, 12.8, 14.4, 16.1 GPa). The red curves show the FPMD results for the same or similar reduced densities and correspond to ambient pressure and to pressures of 2.15, 3.4, 4.88, 9.87, 11.56, 13.82, and 15.27 GPa [79]. The blue curves show the $S_{\mathrm{X}}(Q)$ data sets measured in Ref. [108] at ambient pressure and at 3.9, 5.3, and 9.3 GPa. The $S_{\mathrm{X}}(Q)$ data sets have been corrected for an unphysical slope by using a back Fourier transform method. For the neutron diffraction results in the pressure range $8.7(5)\,\mathrm{GPa} \leq P \leq 16.1(5)\,\mathrm{GPa}$ the region $Q \leq 1.55\,\mathrm{Å}^{-1}$ is experimentally inaccessible due to the limitations of the PEARL diffractometer (section 3.3), and the curves shown in this region correspond to fitted Lorentzian functions (section 3.7.2). The high-pressure curves have been offset vertically for clarity of presentation.

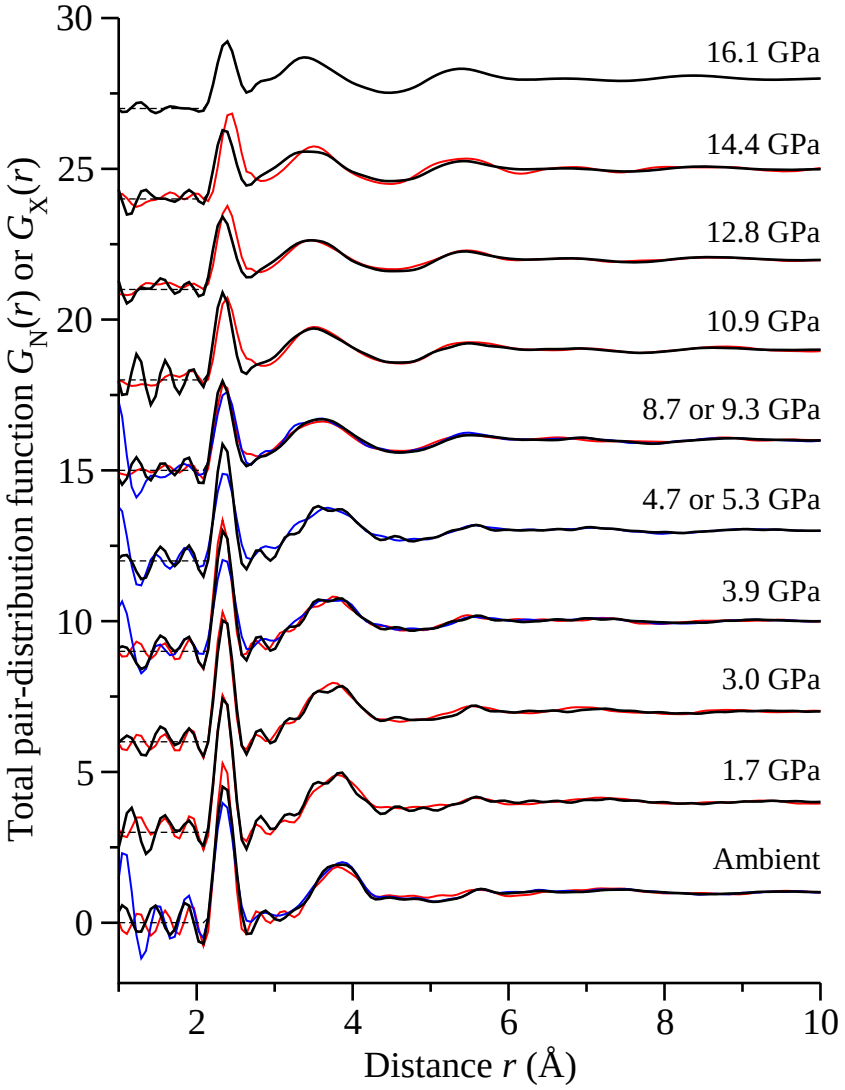

Figure 4-4: The pressure dependence of the neutron total pair-distribution function $G_N(r)$ and x-ray total pair-distribution function $G_X(r)$ for $^{N}Ge^{N}Se_2$, where $G_N(r) \simeq G_X(r) \simeq g_{NN}^{BT}(r)$. The curves shown here correspond to those given in figure 4-3. The solid black curves show the Fourier transforms of the $S_N(Q)$ data sets measured in Refs. [101, 103] (ambient pressure) and the present work (1.7, 3.0, 3.9. 4.7, 8.7, 10.9, 12.8, 14.4, 16.1 GPa). The dashed black curves show the calculated $G_N(r \to 0)$ limits at distances below the closest approach between two atoms. The red curves show the Fourier transforms of the FPMD data sets corresponding to ambient pressure and to pressures of 2.15, 3.4, 4.88, 9.87, 11.56, 13.82, and 15.27 GPa [79]. In the Fourier transformation of the FPMD data sets, the same Q_{max} was used as for the neutron diffraction experimental data. The blue curves show the Fourier transforms of the $S_X(Q)$ data sets measured in Ref. [108] at ambient pressure and at 3.9, 5.3, and 9.3 GPa. The high-pressure curves have been offset vertically for clarity of presentation.

procedure. For all data sets, the unphysical features at low-r oscillate about the correct theoretical limit, which shows that the data sets are correctly normalised.

At ambient pressure there is good agreement between the position of the first and second peaks in the total pair-distribution functions for the neutron diffraction, x-ray diffraction, and FPMD results. The height and width of the second peaks are also in good agreement, although there is a difference in the first peak height. The discrepancy between the neutron diffraction and FPMD results can be removed by Fourier transforming with the same cutoff $Q_{\max}$. The disagreement between the neutron and x-ray diffraction, however, could not be removed in this way. This may arise from large-Q oscillations that have a diminished amplitude relative to the neutron diffraction results.

As the pressure is increased up to $\sim 9.0(5)$ GPa the peak positions for the neutron diffraction, x-ray diffraction, and FPMD results remain consistent with each other. The first peak in $G_{\mathrm{X}}(r)$ continues to show a reduced height and broader width, primarily due to the smaller amplitude of the oscillations in $S_{\mathrm{X}}(Q)$ at high-Q.

Above $\sim 9.0(5)$ GPa the FPMD simulations show a shift in the first peak position to larger-r as well as an increase in height relative to experiment, indicative of more atoms being forced into the first coordination shell. The position and height of the second peak seems, however, to match up to at least 14.4(5) GPa.

A neutron diffraction with isotope substitution experiment was performed using the D4 diffractometer to measure the first-order difference functions for $GeSe_2$ glass under pressure [41]. Diffraction measurements were made using samples of $^{70}Ge^{N}Se_2$ and $^{73}Ge^{76}Se_2$, resulting in two total structure factors ${}^{70}_{\mathrm{N}}F(Q)$ and ${}^{73}_{76}F(Q)$, respectively. First-order difference functions were then calculated following the procedure described in section 4.2. Figure 4-5 shows the first-order difference functions $\Delta F(Q)_{\text{no Se-Se}}$ and $\Delta F(Q)_{\text{no Ge-Ge}}$ for $GeSe_2$ glass as measured at ambient pressure [101] and at pressures of 3.0(5), 4.7(5), 6.3(5), 7.1(5), and 8.2(5) GPa [41]. FPMD results are compared to the neutron diffraction data at similar densities. The FPMD simulations replicate the measured neutron diffraction difference functions.

Figure 4-6 shows the Fourier transforms of the first-order difference functions shown in figure 4-5, *i.e.* $\Delta G(r)_{\text{no Se-Se}}$ and $\Delta G(r)_{\text{no Ge-Ge}}$. The results corresponding to the FPMD simulations were obtained by Fourier transforming the reciprocal space data using the same cutoff $Q_{\max} = 21.5\,\text{Å}^{-1}$ as used for the measured neight diffraction high-pressure data sets.

The differences between the neutron diffraction data sets and the FPMD simulations

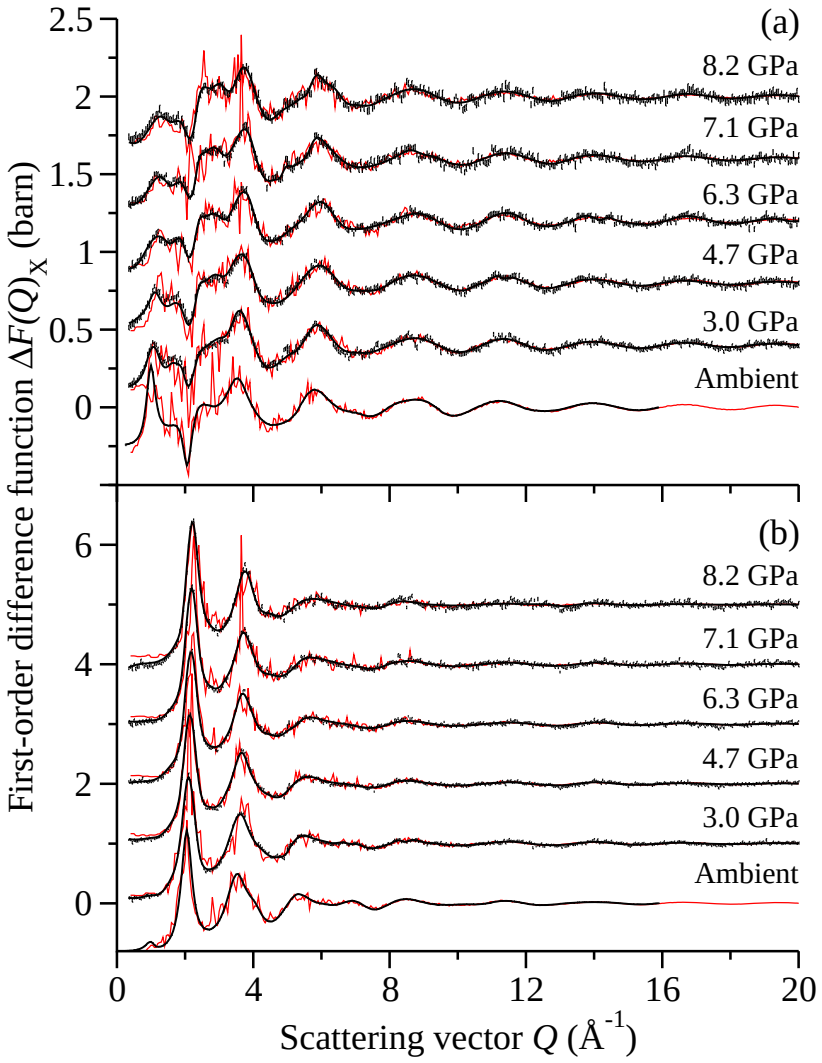

Figure 4-5: The pressure dependence of the first-order difference functions (a) $\Delta F(Q)_{\text{no Se-Se}}$ and (b) $\Delta F(Q)_{\text{no Ge-Ge}}$ for $GeSe_2$ glass, as measured using the D4 diffractometer at ambient pressure [101] and at pressures of 3.0(5), 4.7(5), 6.3(5), 7.1(5), and 8.2(5) GPa [41] (points with vertical error bars). The data sets are compared to FPMD results at ambient pressure and at pressures of 3.4, 4.88, 7.25, 8.73, and 9.87 GPa [42] (light red curves). The solid black curves are the back Fourier transforms of the measured first-order pair-distribution functions shown in figure 4-6. The figure has been adapted from Ref. [79].

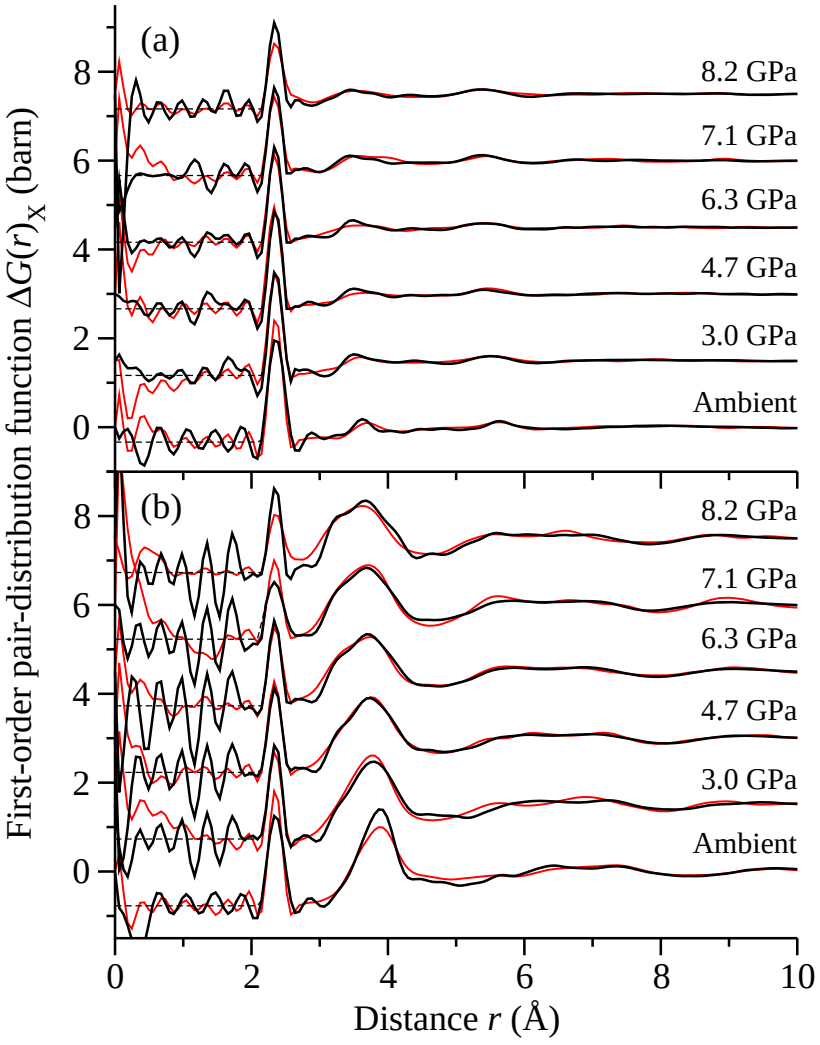

Figure 4-6: The pressure dependence of the first-order pair-distribution functions (a) $\Delta G(r)_{\text{no Se-Se}}$ and (b) $\Delta G(r)_{\text{no Ge-Ge}}$ for $GeSe_2$ glass. The solid black curves were obtained by spline fitting and Fourier transforming the measured Q-space functions shown in figure 4-5 [41, 101]. The red curves give the Fourier transforms of the FPMD results shown in figure 4-5 after applying the same cutoff $Q_{\text{max}} = 20.5\,\text{Å}^{-1}$ as used for the high-P diffraction data [42]. The figure has been adapted from Ref. [79].

can be assessed by using the goodness-of-fit parameter [62, 126]

$$R_\chi = \sqrt{\frac{\sum_i \left[T_{\mathrm{ND}}(r_i) - T_{\mathrm{FPMD}}(r_i)\right]^2}{\sum_i T_{\mathrm{ND}}^2(r_i)}} \tag{4.18}$$

where ND indicates neutron diffraction. The R_χ parameter for the $G_{\mathrm{N}}(r)$ results was calculated using

$$T(r) = 4\pi\rho r \left[G(r) - G(0)\right]. \tag{4.19}$$

For the D4 $G_{\mathrm{N}}(r)$ results, the parameter was 8.7% at ambient pressure and varied from 4.2–4.8% under pressure. For the PEARL $G_{\mathrm{N}}(r)$ results, it varied from 4.5% at 8.7(5) GPa to 8.2% at 14.4(5) GPa. The R_χ parameter for the first-order difference functions was calculated using

$$T(r) = 4\pi\rho r \left[\Delta G_{\mathrm{X}}(r) - \Delta G_{\mathrm{X}}(0)\right], \tag{4.20}$$

where the notation $\Delta G_{\mathrm{X}}(r)$ implies either the $\Delta G(r)_{\text{no Ge-Ge}}$ or $\Delta G(r)_{\text{no Se-Se}}$ function. For $\Delta G(r)_{\text{no Se-Se}}$ the R_χ parameter is 9.4% at ambient and 4.3%–4.8% at higher pressures, whilst for $\Delta G(r)_{\text{no Ge-Ge}}$ it is 12.2% at ambient and 5.4%–11.0% at higher pressures. The range $2\,\text{Å} \leq r \leq 10\,\text{Å}$ was chosen for all of the calculations.

The mean nearest neighbour bond distance $\overline{r}$ and coordination number $\overline{n}$ are shown in figures 4-7(a) and 4-7(b), respectively. There is agreement between the measured data sets and FPMD results up to a pressure $P \sim 8$ GPa within the experimental error. At higher pressures, the measured and simulated results both show an increase in $\overline{n}$ as the first coordination shell expands to incorporate a larger number of neighbours. This process starts at ~ 8.5 GPa ($\rho/\rho_0 \sim 1.42$) for the FPMD results as compared to ~ 12 GPa ($\rho/\rho_0 \sim 1.55$) for the experimental results.

The ρ/ρ_0 dependence for the fractions of n-fold coordinated Ge and Se atoms (n = 2, 3, 4, 5, or, 6) obtained from the FPMD simulations is given in figures 4-7(c) and 4-7(d), and is broken down in figures 4-7(e) and 4-7(f) into the proportions of these n-fold species that contain homopolar bonds. As the density is increased to $\rho/\rho_0 \sim 1.55$, there is no obvious tendency for a suppression of chemical disorder as suggested by previous work [107].

The simulated intra-polyhedral Se-Ge-Se and inter-polyhedral Ge-Se-Ge bond angle distributions

$$P(\theta_{\mathrm{SeGeSe}}) = \frac{B(\theta_{\mathrm{SeGeSe}})}{\sin(\theta_{\mathrm{SeGeSe}})} \tag{4.21}$$

and

$$P(\theta_{\mathrm{GeSeGe}}) = \frac{B(\theta_{\mathrm{GeSeGe}})}{\sin(\theta_{\mathrm{GeSeGe}})} \tag{4.22}$$

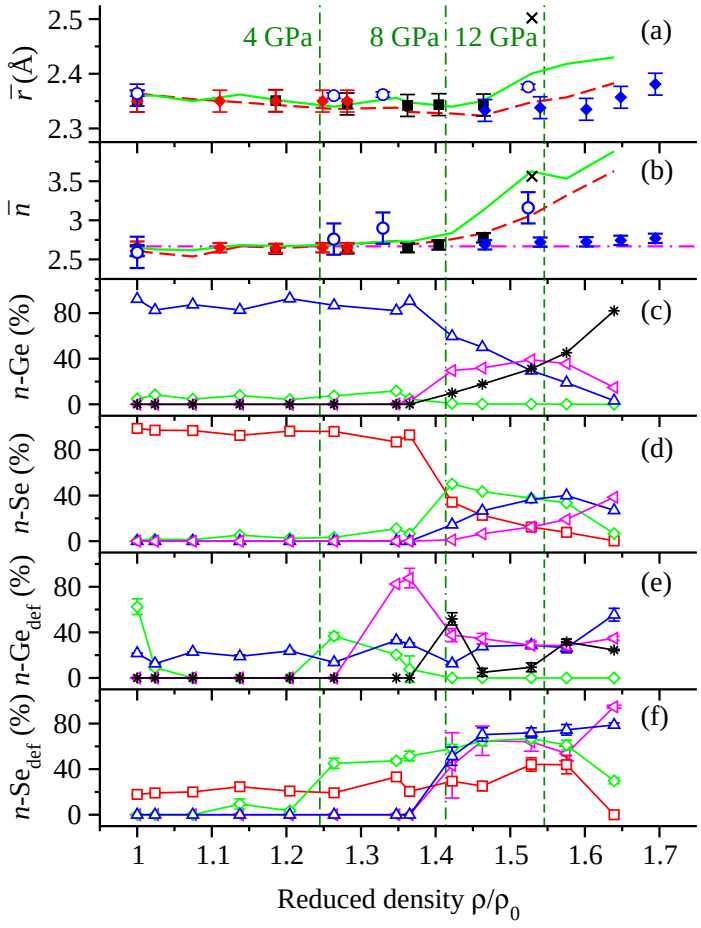

Figure 4-7: The ρ/ρ_0 dependence of the nearest neighbour (a) bond distance $\overline{r}$ and (b) mean coordination number $\overline{n}$ as obtained from (i) neutron diffraction using a $^{\mathrm{N}}\mathrm{Ge}^{\mathrm{N}}\mathrm{Se}_2$ sample on either the D4c [41] (♦) or PEARL (♦) diffractometer, or using $^{70}\mathrm{Ge}^{\mathrm{N}}\mathrm{Se}_2$ and $^{73}\mathrm{Ge}^{76}\mathrm{Se}_2$ samples and averaging the results [41] (♦); (ii) x-ray diffraction [108] (○); FPMD [42] (solid green curves) where the results obtained before the high-temperature anneal at each pressure point are also given (broken red curves); and (iv) FPMD performed using the HSE06 hybrid functional [42] (×). $\overline{n}$ was found from the simulated $\overline{n}_\alpha^\beta$ values by using a cutoff distance specified by the first minimum in $G(r)$. In (b), the horizontal chained magenta line gives the coordination number expected from the "8-N" rule $\overline{n} = 2.67$ [59]. Also given are the FPMD results [42] for the fractions of n-fold coordinated (c) Ge and (d) Se atoms, along with the fractions of these n-fold coordinated (e) Ge and (f) Se atoms that have homopolar bonds. In (c)-(f), the symbols denote twofold (□), threefold (◇), fourfold (△), fivefold (◁), or sixfold (∗) coordinated species, and the error bars (usually smaller than the symbol size) were calculated according to Ref. [105]. The vertical broken green lines correspond to pressures of ∼ 4, 8, and 12 GPa. The figure has been adapted from Ref. [79].

are shown in figures 4-8(a) and 4-8(b), respectively, where the distributions $B(\theta)$ are normalised by $\sin(\theta)$ to remove the effect of a finite sampling volume [127]. The fractions of Ge atoms that are involved either in corner-sharing (CS) or edge-sharing (ES) motifs are given in figure 4-8(c). The CS motifs are denoted by Ge_0 while the ES motifs are broken down into their contributions from Ge_l ($l = 1, 2, 3/4$) centred polyhedra, where l indicates the number of ES connections to other polyhedra and $l = 3/4$ denotes three or four of these connections.

Figure 4-9 shows the ρ/ρ_0 dependence of the mean Se-Ge-Se and Ge-Se-Ge bond angles as estimated from the measured Ge-Se, Ge-Ge, and Se-Se distances using the cosine rule, *i.e.*

$$\cos(\theta_{\mathrm{SeGeSe}}) = 1 - \frac{r^2_{\mathrm{SeSe}}}{2r^2_{\mathrm{GeSe}}} \tag{4.23}$$

and

$$\cos(\theta_{\mathrm{GeSeGe}}) = 1 - \frac{r^2_{\mathrm{GeGe}}}{2r^2_{\mathrm{GeSe}}}. \tag{4.24}$$

The distance r_{GeSe} was taken from the mean of the first peak positions in (i) the total pair-distribution function $G(r)$ for the $^{70}Ge^{N}Se_2$ and $^{73}Ge^{76}Se_2$ samples as measured in Ref. [41] and (ii) the first-order difference functions $\Delta G(r)_{\text{no Se-Se}}$ and $\Delta G(r)_{\text{no Ge-Ge}}$. The distance r_{SeSe} was taken from the second peak in $\Delta G(r)_{\text{no Ge-Ge}}$ which is dominated by the Se-Se partial pair-distribution function: the ratio of weighting factors for the Se-Se:Ge-Se partial pair-distribution functions is 1:0.3129. The distance r_{GeGe} was estimated from the second peak in $\Delta G(r)_{\text{no Se-Se}}$ where the ratio of weighting factors for the Ge-Ge:Ge-Se partial pair-distribution functions is 1:2.3838. The measured results, which correspond to the pressure interval from ambient to 8.2(5) GPa, are compared to the mean bond angles $\langle\theta_{\mathrm{SeGeSe}}\rangle$ and $\langle\theta_{\mathrm{GeSeGe}}\rangle$ obtained from the FPMD bond angle distributions $P(\theta)$. The expression

$$\langle\theta\rangle = \frac{\int \mathrm{d}\theta\theta P(\theta)}{\int \mathrm{d}\theta P(\theta)} \tag{4.25}$$

was used with a high-angle integration cutoff of 140°. The Se-Se distance can be accurately discerned from the measured first-order difference function $\Delta G(r)_{\text{no Ge-Ge}}$ and the ρ/ρ_0 dependence of the simulated $\langle\theta_{\mathrm{SeGeSe}}\rangle$ values tracks that found from experiment. It is, however, more difficult to discern the Ge-Ge distance from the measured first-order difference function $\Delta G(r)_{\text{no Se-Se}}$ and there is an offset between the measured and simulated Ge-Se-Ge bond angles, although both data sets show the same ρ/ρ_0 dependence.

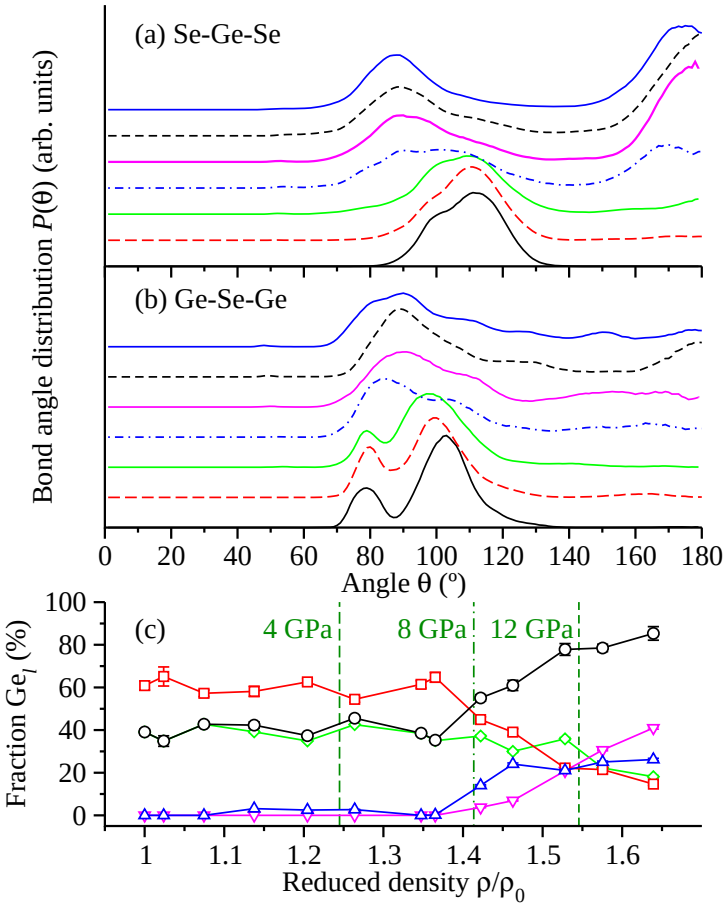

Figure 4-8: FPMD results showing the ρ/ρ_0 dependence of (a) the intrapolyhedral Se-Ge-Se and (b) the interpolyhedral Ge-Se-Ge bond angle distributions where, from bottom to top in each panel, $\rho/\rho_0 = 1$, 1.204, 1.365, 1.463, 1.528, 1.575, or 1.639. In (c), the reduced density dependence of the fractions of corner-sharing (CS) Ge atoms (Ge_0, □) and edge-sharing (ES) Ge atoms (○) is given, together with a breakdown of the latter into its contributions from Ge_1 (◇), Ge_2 (△), and $Ge_{3/4}$ (▽) units. In (c), the error bars (usually smaller than the symbol size) were calculated according to Ref. [105], and the vertical broken green lines correspond to pressures of ∼ 4, 8, and 12 GPa. The figure has been adapted from Ref. [79].

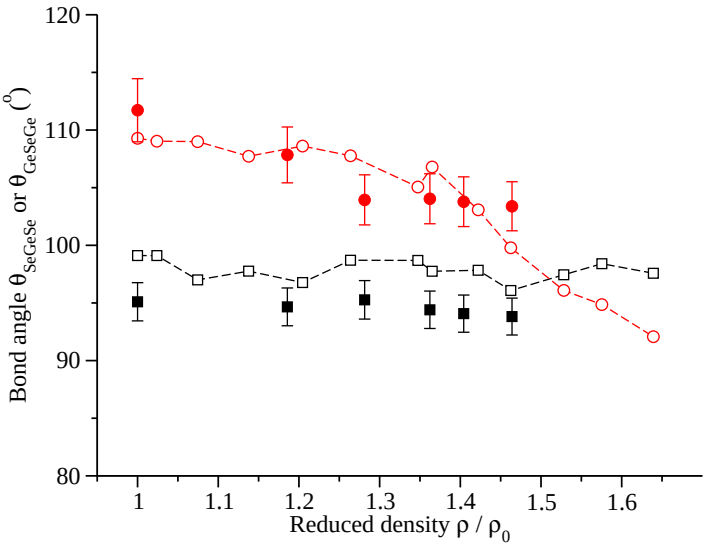

Figure 4-9: The ρ/ρ_0 dependence of the mean intrapolyhedral Se-Ge-Se (●) and interpolyhedral Ge-Se-Ge (■) bond angles as estimated from the measured Ge-Se, Ge-Ge, and Se-Se distances. The experimental results [41] are compared to the mean values $\langle\theta_{\mathrm{SeGeSe}}\rangle$(broken red curve with ○ symbols) and $\langle\theta_{\mathrm{GeSeGe}}\rangle$ (broken black curve with □ symbols) taken from the FPMD simulations. The figure has been adapted from Ref. [79].

4.5 Discussion

The following picture emerges from the measured and FPMD results for a two-stage densification process in amorphous $GeSe_2$. In the first stage where the diffraction and FPMD results are in accord, $\overline{n}$ remains constant as the density increases from ambient to $\rho/\rho_0 \sim 1.42$. The CS to ES ratio increases from 1.3 to 1.7 in the interval $\rho/\rho_0 \sim 1.07$–1.20 ($P \sim 1.29$–$3.55\,\mathrm{GPa}$) (figure 4-8(c)), consistent with the trend found from Raman spectroscopy [128]. The results do not, however, support the model described in Ref. [129] where an increase in $\overline{n}$ was invoked to explain a minimum in the network rigidity at $\simeq 4\,\mathrm{GPa}$ ($\rho/\rho_0 \simeq 1.25$). The prevalence of ES units contrasts to the crystalline phase where transitions are observed from an ambient-pressure two-dimensional (2D) structure comprising equal numbers of ES and CS tetrahedra [130] to three-dimensional (3D) structures of densely packed CS tetrahedra [131, 132]. Higher temperatures are, however, usually required to facilitate these transitions [131–134].

In the second stage, as the density increases beyond $\rho/\rho_0 \sim 1.42$, $\overline{n}$ increases with $\overline{r}$ although these is a discrepancy between the rate of change found from neutron diffraction and FPMD. In the latter, fourfold coordinated Ge atoms make way for fivefold and sixfold coordinated Ge atoms (figure 4-7(c)), twofold coordinated Se atoms make way for higher-coordinated Se atoms (figure 4-7(d)) where homopolar bonds are common (figure 4-7(f)), and there is a monotonic reduction in the CS to ES ratio (figure 4-8(c)). The FPMD results for $\overline{n}$ indicate a bonding scheme that takes an increased metallic character with increasing pressure, whereas the diffraction results are consistent with the retention of semiconducting behaviour.

In an attempt to improve the agreement between simulation and experiment, an additional FPMD simulation was performed at $\rho/\rho_0 = 1.529$ by using a hybrid functional of the HSE06 type [124]. The aim was to determine whether or not inclusion of the Hartree exact exchange is capable of retaining to higher pressures a more ionic and less metallic character for the chemical bonding [135]. The calculations did not, however, lead to improved agreement with experiment (figure 4-7(a) and 4-7(b)). The origin of the discrepancy may therefore lie with the exploration of different pathways of metastability: The glass was cold compressed in the diffraction experiments but was annealed at a high temperature of 900 K at high pressure in the FPMD simulations. The effect of the high-T anneal at a given pressure point can be illustrated by analysing the configurations obtained at the end of the preceding low-T anneal at 300 K. The rate of change of $\overline{r}$ with $\overline{n}$ with density is reduced when $\rho/\rho_0 > 1.42$ (figure 4-7(a) and 4-7(b)). The results therefore indicate the presence of an energy barrier to structural transformation within the high-pressure regime that is partially surmounted by the high-T anneal at 900 K. In other words, a single valley in the energy landscape at pres-

sures up to $\sim 8.5\,\mathrm{GPa}$ ($\rho/\rho_0 \sim 1.42$) bifurcates at higher pressures to give two valleys separated by an energy barrier that can be overcome by heating to a temperature of $\sim 900\,\mathrm{K}$. Figure 4-10 gives an illustration of this bifurcation process for $GeSe_2$.

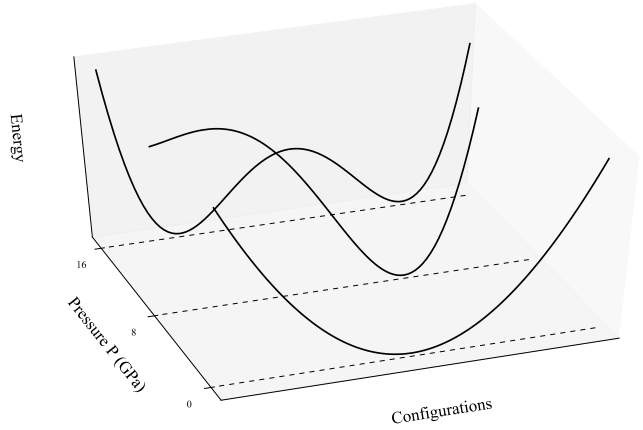

Figure 4-10: A schematic of the bifurcation process in $GeSe_2$. As the pressure is increased, one valley splits into two. To reach the second valley (to the left in the diagram) requires a certain amount of thermal energy which is not available in cold compression experiments.

Figure 4-11 shows typical atomistic configurations from FPMD for different points in the densification process. When ρ/ρ_0 increases beyond 1.42, the Se atoms in Ge_0 motifs make additional bonds with their neighbouring Ge_1 motifs, transforming the latter to fivefold coordinated Ge_2 units having a distorted square pyramidal geometry. As Ge_0 tetrahedra are removed, the Se-Ge-Se bond angle distribution shifts from $\sim 111^\circ$ towards smaller angles, and there is a merger of the twin peaks in the Ge-Se-Ge bond angle distribution (figure 4-8(a) and 4-8(b)). Around $\rho/\rho_0 \simeq 1.53$, the fraction of Ge_0 units continues to decrease, making way for more Ge_2 and a few $Ge_{3/4}$ type configurations, where many of the latter correspond to sixfold coordinated Ge atoms. Accordingly, the main peak in the Se-Ge-Se bond angle distribution shifts to around 90° and a second peak appears at 180°. Eventually, the network develops a pseudocubic arrangement of Ge-centred units for which the main peak in the Ge-Se-Ge bond angle distribution is at $\sim 90^\circ$. In all of this, the fractions of defective fivefold and sixfold coordinated Ge atoms peak at densities around which these species first start to emerge (figure 4-7(e)), *i.e.* homopolar bonds mediate in the initial development of the higher-coordinated Ge-centred polyhedra.

It is also illustrative to follow the transformations of the Ge-centred structural

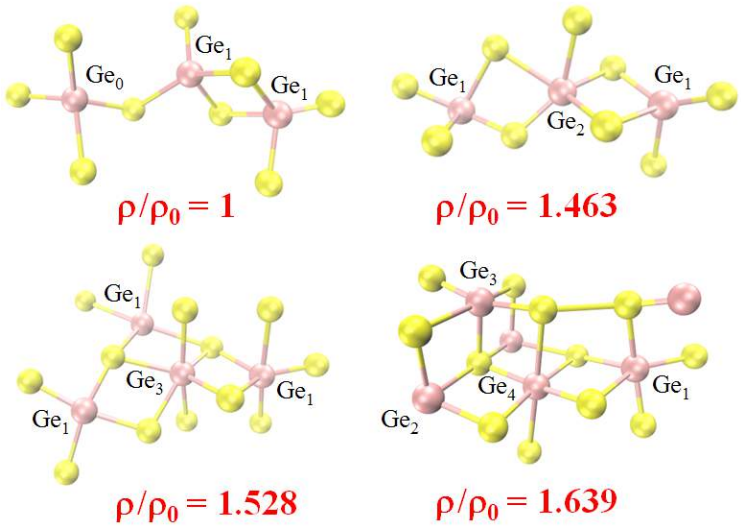

Figure 4-11: Atomistic configurations from FPMD for $GeSe_2$ glass at different reduced densities. Ge atoms are dark (purple) and Se atoms are light (yellow). Bonds are drawn when two atoms are separated by a distance $\leq r_{\min}$ given by the position of the first minimum in $g^{\mathrm{FZ}}_{\mathrm{GeSe}}(r)$. This figure was originally published in Ref. [79].

motifs in terms of the q parameter defined by

$$q = 1 - \frac{3}{8}\sum_{k>i}\left[\frac{1}{3} + \cos\left(\theta_{ijk}\right)\right]^2 \tag{4.26}$$

where θ_{ijk} is the angle formed between a central Ge atom j and its neighbouring atoms i and k [136, 137]. The parameter $q = 1$ if the Ge atom is at the centre of a regular tetrahedron, $q = 0$ if it is at the centre of a regular octahedron, or $q = 53/96 = 0.552$ if it is at the centre of a trigonal bipyramid. In comparison, for a square pyramidal unit in which the central fivefold coordinated Ge atom is located at the base centre then $q = 1/3$. Alternatively, if this Ge atom is displaced toward the apex by a distance $h/5$, where h is the base-to-apex distance, then (i) $q = 0.504$ if all of the edges are equal in length (corresponding, *e.g.*, to equal Se-Se distances in a $GeSe_5$ unit) or (ii) $q = 0.535$ if h is elongated relative to (i) to give the central Ge atom equal nearest-neighbour distances [138]. Figure 4-12 shows the ρ/ρ_0 dependence of the q-parameter distributions obtained from FPMD simulations of $GeSe_2$ glass. At ambient conditions, most of the Ge atoms are fourfold coordinated in distorted tetrahedral units with a maximum in the distribution at $q \simeq 0.966$. In comparison, the mean q value is 0.979 for the high-temperature ambient-pressure crystalline phase of $GeSe_2$ [130]. At higher densities, most of the fivefold coordinated Ge atoms appear in distorted square-pyramidal (as

opposed to trigonal bipyramidal) conformations. The majority of sixfold coordinated Ge atoms are in distorted octahedral environments that give rise to a sharp peak at a small negative q value.

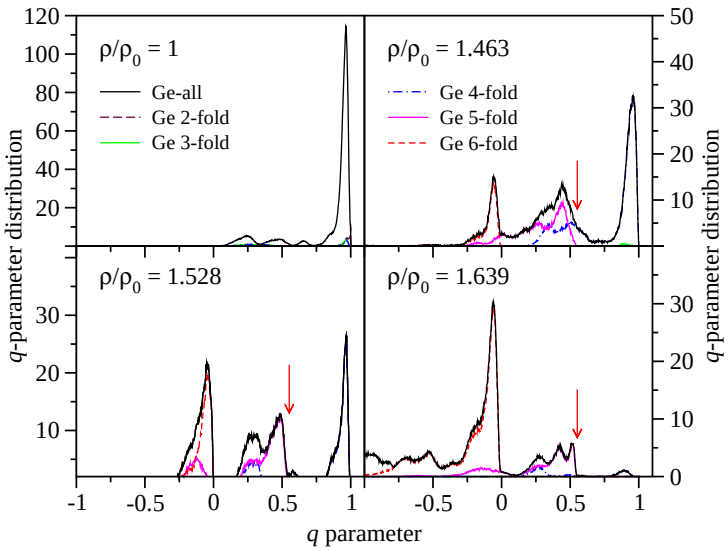

Figure 4-12: The ρ/ρ_0 dependence of the q-parameter distribution as obtained from the FPMD simulations of $GeSe_2$ glass. At each density, the distribution for all Ge atoms is broken down into its contributions from n-fold coordinated Ge atoms (n = 3, 4, 5, or 6). The vertical red arrows mark the q values expected for trigonal bipyramidal units. This figure has been adapted from Ref. [79].

4.6 Conclusions

In the range from ambient pressure to $P \sim 8.5\,\mathrm{GPa}$ ($1 \leq \rho/\rho_0 \leq 1.42$) there is excellent agreement between the neutron diffraction, x-ray diffraction, and FPMD results that can be seen in the total structure factors and pair-distribution functions $S(Q)$ and $G(r)$ (figures 4-3 and 4-4), the first-order difference functions $\Delta F(Q)_{\text{no Se-Se}}$ and $\Delta F(Q)_{\text{no Ge-Ge}}$ (figures 4-5(a) and 4-5(b)), the first-order pair-distribution functions $\Delta G(r)_{\text{no Se-Se}}$ and $\Delta G(r)_{\text{no Ge-Ge}}$ (figures 4-6(a) and 4-6(b)), the mean nearest-neighbour bond distance $\overline{r}$ (figures 4-7(a)), coordination number $\overline{n}$ (figures 4-7(b)), and Se-Ge-Se bond angle distribution (figs. 4-9). For this regime, the ambient-pressure $\overline{n}$ value is retained, and the density-driven structural transformations in $GeSe_2$ differ substantially from those observed in common oxide glasses such as SiO_2, GeO_2, B_2O_3. In particular, ES motifs remain numerous, in contrast to oxide glasses where CS conformations dominate over the density range where the chemical species retain their

ambient-pressure coordination numbers [50, 109, 139–143].

The discrepancy between the neutron diffraction and FPMD results at high pressure is attributed to the presence of an energy barrier to structural rearrangement, which cannot be explored in the cold-compression diffraction experiments but can be accessed via the high-temperature annealing stage in the simulations. In other words, a single valley in the energy landscape at pressures up to $\sim 8.5\,\mathrm{GPa}$ ($\rho/\rho_0 \sim 1.42$) bifurcates at higher pressures to give two valleys separated by an energy barrier that can be overcome by heating to a temperature of $\sim 900\,\mathrm{K}$. It is a moot point as to whether structural relaxation at high temperature in the simulations is enabling access to crystalline-like configurations: A discontinuous semiconductor-glass to metal-crystalline transition has been reported for $GeSe_2$ at $P \simeq 7\,\mathrm{GPa}$ [31, 32].

Notwithstanding, the stability under load of ES tetrahedra, which promote the fragility of glass-forming liquids [144], and the importance of homopolar bonds in mediating the transformations to higher-coordinated polyhedra, are likely to be common features in the mechanisms of network collapse for the class of glass-forming materials where these motifs are prevalent in the ambient-pressure networks.

5. The density-dependent structure of the rigid glass $GeSe_4$

5.1 Introduction

Network-forming glasses in the Ge_xSe_{1-x} ($0 \leq x \leq 1$) system [2] have been extensively studied for their potential use in infra-red optics and photonics [5, 8–10, 12–14, 145, 146]. According to mean-field theory, amorphous networks, such as Ge_xSe_{1-x}, are classified as either *floppy*, where the network is under-constrained, *rigid*, where the network is optimally constrained, or *stressed-rigid*, where the network is over-constrained [147, 148]. This classification is based on whether the number of constraints per atom is less than, equal to, or greater than the number of degrees of freedom per atom. The number of constraints per atom is equal to the number of degrees of freedom per atom at a concentration where the mean coordination $\langle n \rangle = 2.4$ [148].

Further investigations into floppy vs. stressed-rigid networks found that, rather than a sharp transition, there can exist a so-called intermediate phase (IP) [97, 103, 149–157] between the floppy and stressed-rigid compositional windows. Within the intermediate phase, the network is rigid but is not under stress, *i.e.* it is ideally constrained or *isostatic*. The intermediate phase also defines a compositional range for which the non-reversible enthalpy of the glass transition vanishes to zero [158].

It has been proposed that glasses within the intermediate phase are self-organising and exhibit increased structural variability [97]. Self-organisation enables the glass, on formation, to avoid creating over-constrained, stressed regions unless there is no physical alternative. Structural variability refers to the formation of a glass network from a large variety of structural motifs. In the absence of self-organisation and structural variability, there is a single transition from a floppy network to a stressed-rigid one, which occurs when the mean coordination number $\langle n \rangle = 2.4$, *i.e.* there is no intermediate phase.

Consider the Ge_xSe_{1-x} system, where the "8-N" rule gives a mean coordination $\langle n \rangle = 2+2x$. $GeSe_4$ lies at the transition between the floppy and stressed-rigid regimes,

i.e. the mean coordination number for $GeSe_4$ from the "8-N" rule is $\langle n \rangle = 2.4$. $GeSe_4$ also lies within the intermediate phase of the Ge_xSe_{1-x} system, where the intermediate phase is found in the range $0.200(5) \leq x \leq 0.265(5)$ [153].

The effect of compression on amorphous Ge_xSe_{1-x} systems has been studied in the past [22, 31, 32, 43, 44, 79, 107, 108, 129, 159–164]. Previous work has shown a strong decrease in the resistivity of $GeSe_4$ upon the application of pressure which indicates a polyamorphic insulator–to–metal transition [31, 44]. The structural transformation of $GeSe_4$ under compression has also been studied using x-ray diffraction [43] and empirical potential structure refinement (EPSR) with x-ray diffraction [44]. As shall be discussed in section 5.4, there is, however, a lack of agreement between the different sets of structural results. Further work is therefore required to clarify the effect of pressure on the structure of $GeSe_4$.

The work presented in this chapter makes use of neutron diffraction to measure the atomic structure of amorphous $GeSe_4$ *in situ* at pressures up to 14.4(5) GPa, using a Paris-Edinburgh press mounted on the D4c and PEARL diffractometers. The results are compared with two x-ray diffraction investigations and with first-principles molecular dynamics and empirical-potential structure refinement simulations to present a unified picture of the densification of $GeSe_4$ glass.

The chapter is organised as follows. The essential theory for a neutron diffraction experiment is given in section 5.2. The experimental procedure for the work is discussed in section 5.3. The results and the accompanying discussion are presented in sections 5.4 and 5.5, respectively. Finally, conclusions are drawn in section 5.6.

5.2 Theory

As discussed in chapter 2, in a neutron diffraction experiment the total structure factor

$$F(Q) = \sum_{\alpha=1}^{n} \sum_{\beta=1}^{n} c_\alpha c_\beta b_\alpha b_\beta \left[S^{\mathrm{FZ}}_{\alpha\beta}(Q) - 1 \right] \tag{5.1}$$

is measured, where α and β denote the chemical species, c_α is the atomic fraction of chemical species α, b_α is the bound coherent scattering length of chemical species α, $S^{\mathrm{FZ}}_{\alpha\beta}(Q)$ is the Faber-Ziman partial structure factor for chemical species α and β [55], and Q is the magnitude of the scattering vector [52]. The corresponding real-space information can be obtained via Fourier transformation of the reciprocal space data to

give the total pair-distribution function $G(r)$, as given by

$$G(r) = \frac{1}{2\pi^2 r\rho}\int_0^\infty QM(Q)F(Q)\sin(Qr)\,\mathrm{d}Q, \tag{5.2}$$

where r is a distance in real space, ρ is the number density of the glass, and $M(Q)$ is a modification function

$$M(Q) = \begin{cases} 1 & \text{if } Q \leq Q_{\max} \\ 0 & \text{if } Q > Q_{\max}, \end{cases} \tag{5.3}$$

which is introduced because a diffractometer can measure only over a finite Q range up to a maximum value $Q_{\max}$. Fourier transformation artefacts can arise from the finite Q range and can be reduced through the use of a Lorch modification function [56]

$$M(Q) = \begin{cases} \frac{\sin(aQ)}{aQ} & \text{if } Q \leq Q_{\max} \\ 0 & \text{if } Q > Q_{\max}, \end{cases} \tag{5.4}$$

where $a = \pi/Q_{\max}$, at the expense of broadened r-space features. The low-r limit, $G(r \to 0)$, for a total pair-distribution function is given by

$$G(r \to 0) = -\sum_\alpha \sum_\beta c_\alpha c_\beta b_\alpha b_\beta = -\langle b\rangle^2, \tag{5.5}$$

where $\langle b\rangle$ is the mean bound coherent scattering length

$$\langle b\rangle = \sum_\alpha c_\alpha b_\alpha = c_{\mathrm{Ge}} b_{\mathrm{Ge}} + c_{\mathrm{Se}} b_{\mathrm{Se}} \tag{5.6}$$

for glasses in the $\mathrm{Ge}_x\mathrm{Se}_{1-x}$ $(0 \leq x \leq 1)$ system.

The total structure factor $F(Q)$ can also be written in terms of the Bhatia-Thornton partial structure factors [58] such that

$$\begin{aligned} F(Q) = \langle b\rangle^2 \left[S^{\mathrm{BT}}_{\mathrm{NN}}(Q) - 1\right] + \\ c_\alpha c_\beta \left(b_\alpha - b_\beta\right)^2 \left\{\left[\frac{S^{\mathrm{BT}}_{\mathrm{CC}}(Q)}{c_\alpha c_\beta}\right] - 1\right\} + \\ 2\langle b\rangle \left(b_\alpha - b_\beta\right) S^{\mathrm{BT}}_{\mathrm{NC}}(Q), \end{aligned} \tag{5.7}$$

where $S^{\mathrm{BT}}_{\mathrm{NN}}(Q)$, $S^{\mathrm{BT}}_{\mathrm{CC}}(Q)$, and $S^{\mathrm{BT}}_{\mathrm{NC}}(Q)$ are the so-called Bhatia-Thornton number-number, concentration-concentration, and number-concentration partial structure factors,

respectively. Consider the glass $^{\mathrm{N}}\mathrm{Ge}^{\mathrm{N}}\mathrm{Se}_4$ where the bound coherent scattering lengths of natural Ge and Se are $b_{^{\mathrm{N}}\mathrm{Ge}} = 8.185(2)\,\mathrm{fm}$ and $b_{^{\mathrm{N}}\mathrm{Se}} = 7.970(9)\,\mathrm{fm}$, respectively. As $b_{^{\mathrm{N}}\mathrm{Ge}} \simeq b_{^{\mathrm{N}}\mathrm{Se}}$ an approximation can be made where the weighting factors for the concentration-concentration and number-concentration Bhatia-Thornton partial structure factors, $S^{\mathrm{BT}}_{\mathrm{CC}}(Q)$ and $S^{\mathrm{BT}}_{\mathrm{NC}}(Q)$, are zero, *i.e.*

$$F(Q) = \langle b \rangle^2 \left[S^{\mathrm{BT}}_{\mathrm{NN}}(Q) - 1 \right]. \tag{5.8}$$

The Bhatia-Thornton number-number partial pair-distribution function $g^{\mathrm{BT}}_{\mathrm{NN}}(r)$ can be found by substituting $G(r)$ for $F(Q)$ and $g^{\mathrm{BT}}_{\mathrm{NN}}(r)$ for $S^{\mathrm{BT}}_{\mathrm{NN}}(Q)$ in equation (5.8). $g^{\mathrm{BT}}_{\mathrm{NN}}(r)$ can also be defined in terms of the Faber-Ziman partial structure factors [59], *i.e.*

$$g^{\mathrm{BT}}_{\mathrm{NN}}(r) = c_\alpha^2 g^{\mathrm{FZ}}_{\alpha\alpha}(r) + c_\beta^2 g^{\mathrm{FZ}}_{\beta\beta}(r) + 2c_\alpha c_\beta g^{\mathrm{FZ}}_{\alpha\beta}(r). \tag{5.9}$$

Using $g^{\mathrm{BT}}_{\mathrm{NN}}(r)$ it is possible to calculate the mean coordination number $\overline{n}$ which is averaged over all types of chemical species

$$\begin{aligned} \overline{n} &= 4\pi\rho \int_{r_1}^{r_2} r^2 g^{\mathrm{BT}}_{\mathrm{NN}}(r)\,\mathrm{d}r \\ &= c_{\mathrm{Ge}} \left(\overline{n}^{\mathrm{Ge}}_{\mathrm{Ge}} + \overline{n}^{\mathrm{Se}}_{\mathrm{Ge}} \right) + c_{\mathrm{Se}} \left(\overline{n}^{\mathrm{Se}}_{\mathrm{Se}} + \overline{n}^{\mathrm{Ge}}_{\mathrm{Se}} \right), \end{aligned} \tag{5.10}$$

for glasses in the $\mathrm{Ge}_x\mathrm{Se}_{1-x}$ $(0 \leq x \leq 1)$ system, where $\overline{n}^{\beta}_{\alpha}$ is the average number of β atoms in a shell of radius $r_1 \leq r \leq r_2$ around a central α atom.

Consider a neutron diffraction experiment made on $^{\mathrm{N}}\mathrm{Ge}^{\mathrm{N}}\mathrm{Se}_4$ where the coherent scattering lengths of $^{\mathrm{N}}\mathrm{Ge}$ and $^{\mathrm{N}}\mathrm{Se}$ are approximately, but not exactly, equal, *i.e.* $b_{^{\mathrm{N}}\mathrm{Ge}} \simeq b_{^{\mathrm{N}}\mathrm{Se}}$. The mean coordination number corrected for the small difference in scattering lengths $\overline{n}^{\mathrm{expt}}$ is then given by

$$\begin{aligned} \overline{n}^{\mathrm{expt}} &= 4\pi\rho \int_{r_1}^{r_2} r^2 g^{\mathrm{BT}}_{\mathrm{NN}}(r)\,\mathrm{d}r \\ &= 4\pi\rho \int_{r_1}^{r_2} r^2 \frac{G(r) - G(0)}{\langle b \rangle^2}\,\mathrm{d}r \\ &= \frac{4\pi\rho}{\langle b \rangle^2} \int_{r_1}^{r_2} r^2 \left[c^2_{\mathrm{Ge}} b^2_{\mathrm{Ge}} g^{\mathrm{FZ}}_{\mathrm{GeGe}}(r) + c^2_{\mathrm{Se}} b^2_{\mathrm{Se}} g^{\mathrm{FZ}}_{\mathrm{SeSe}}(r) + 2c_{\mathrm{Ge}} c_{\mathrm{Se}} b_{\mathrm{Ge}} b_{\mathrm{Se}} g^{\mathrm{FZ}}_{\mathrm{GeSe}}(r) \right] \mathrm{d}r \\ &= \frac{c_{\mathrm{Ge}} b^2_{\mathrm{Ge}}}{\langle b \rangle^2} \overline{n}^{\mathrm{Ge}}_{\mathrm{Ge}} + \frac{c_{\mathrm{Se}} b^2_{\mathrm{Se}}}{\langle b \rangle^2} \overline{n}^{\mathrm{Se}}_{\mathrm{Se}} + \frac{c_{\mathrm{Ge}} b_{\mathrm{Ge}} b_{\mathrm{Se}}}{\langle b \rangle^2} \overline{n}^{\mathrm{Se}}_{\mathrm{Ge}} + \frac{c_{\mathrm{Se}} b_{\mathrm{Ge}} b_{\mathrm{Se}}}{\langle b \rangle^2} \overline{n}^{\mathrm{Ge}}_{\mathrm{Se}}. \end{aligned} \tag{5.11}$$

Consider an x-ray diffraction experiment. The diffraction theory is broadly the same as for neutron diffraction, except that the bound coherent scattering length, b_α, must be replaced with a Q-dependent atomic form factor $f_\alpha(Q)$, which depends strongly on the number of electrons in the atom, *i.e.* the atomic number. The total structure factor for an x-ray experiment is then given by

$$F_{\mathrm{X}}(Q) = \sum_{\alpha=1}^{n}\sum_{\beta=1}^{n} c_\alpha c_\beta f_\alpha(Q) f_\beta^*(Q)\left[S_{\alpha\beta}^{\mathrm{FZ}}(Q) - 1\right]. \tag{5.12}$$

In order to remove the associated Q dependent slope and improve the resolution of peaks in the corresponding real-space function, the total structure factor can be re-written as

$$S_{\mathrm{X}}(Q) = 1 + \frac{F_{\mathrm{X}}(Q)}{\left|\langle f(Q)\rangle\right|^2} \tag{5.13}$$

where $\langle f(Q)\rangle = \sum_\alpha c_\alpha f_\alpha(Q)$ is the mean atomic form factor. The equivalent expression for a neutron diffraction experiment is

$$S_{\mathrm{N}}(Q) = 1 + \frac{F(Q)}{\left|\langle b\rangle\right|^2}. \tag{5.14}$$

The corresponding real space expressions can be found by substituting $S_{\mathrm{X}}(Q)$, $F_{\mathrm{X}}(Q)$, $S_{\mathrm{N}}(Q)$, and $F(Q)$ for $G_{\mathrm{X}}(r)$, $G_{\mathrm{X}}(r)$, $G_{\mathrm{N}}(r)$, and $G(r)$, respectively, in equations (5.13) and (5.14).

Due to the similarity of the coherent neutron scattering lengths ($b_{^{\mathrm{N}}\mathrm{Ge}} \simeq b_{^{\mathrm{N}}\mathrm{Se}}$) and the similarity of the atomic numbers for Ge and Se (32 and 34, respectively), the approximation can be made [51] that

$$S_{\mathrm{N}}(Q) \simeq S_{\mathrm{X}}(Q) \simeq S_{\mathrm{NN}}^{\mathrm{BT}}(Q) \tag{5.15}$$

for $^{\mathrm{N}}\mathrm{Ge}^{\mathrm{N}}\mathrm{Se}_4$. Similarly, the real-space functions can be expressed as

$$G_{\mathrm{N}}(r) \simeq G_{\mathrm{X}}(r) \simeq g_{\mathrm{NN}}^{\mathrm{BT}}(r). \tag{5.16}$$

There are two major models used to describe the chemical ordering in $\mathrm{Ge}_x\mathrm{Se}_{1-x}$ glasses, the random covalent network (RCN) model and the chemically ordered network (CON) model. Both models assume that the so-called "8-N" rule holds [59]. The RCN model assumes that the distribution of bonds is purely statistical [2], such that the coordination numbers are given by

$$\overline{n}^{\mathrm{Ge}}_{\mathrm{Ge}} = \frac{8c_{\mathrm{Ge}}}{1+c_{\mathrm{Ge}}},$$
$$\overline{n}^{\mathrm{Se}}_{\mathrm{Se}} = 2\frac{1-c_{\mathrm{Ge}}}{1+c_{\mathrm{Ge}}},$$

and,

$$\overline{n}^{\mathrm{Se}}_{\mathrm{Ge}} = 4\frac{1-c_{\mathrm{Ge}}}{1+c_{\mathrm{Ge}}}. \tag{5.17}$$

The CON model, meanwhile, prefers heteropolar Ge-Se bonds, only allowing homopolar Ge-Ge and Se-Se bonds to form when the composition is Ge or Se rich, respectively [2]. $GeSe_4$ is within the Se-rich region, *i.e.* the concentration of Ge-atoms is less than for the stoichiometric composition $GeSe_2$, and so the CON model gives the coordination numbers as [59]

$$\overline{n}^{\mathrm{Ge}}_{\mathrm{Ge}} = 0,$$
$$\overline{n}^{\mathrm{Se}}_{\mathrm{Se}} = 2\frac{1-3c_{\mathrm{Ge}}}{1-c_{\mathrm{Ge}}},$$

and,

$$\overline{n}^{\mathrm{Se}}_{\mathrm{Ge}} = 4. \tag{5.18}$$

5.3 Experimental procedure

Two neutron diffraction experiments were undertaken to study the structure of $GeSe_4$ under pressure. One experiment was performed on the D4c diffractometer utilising a VX5 PE press in an in-plane scattering geometry with single toroid cubic boron nitride anvils to make measurements up to $P = 8.2(5)$ GPa. The other experiment was performed on the PEARL HiPr diffractometer utilising a V3 PE press in a transverse scattering geometry with double toroid sintered diamond anvils to make measurements up to $P = 14.4(5)$ GPa. Within the following work, it is assumed that the natural isotopic composition is used for all elements unless otherwise stated, *i.e.* $GeSe_4$ is equivalent to $^{\mathrm{N}}\mathrm{Ge}^{\mathrm{N}}\mathrm{Se}_4$. The preparation of $GeSe_4$ pellets is discussed in section 5.3.1, the experimental procedures for the D4c and PEARL experiments are discussed in sections 5.3.2 and 5.3.3, respectively, and the pressure-volume equation of state for $GeSe_4$ is discussed in section 5.3.4.

5.3.1 Sample preparation

Amorphous $GeSe_4$ was produced by loading elemental ^{N}Ge (99.9998%, Sigma-Aldrich) and ^{N}Se (99.999%, Sigma-Aldrich) into a silica ampoule. To avoid contamination this loading took place inside an inert Ar-filled glovebox. The ampoule was evacuated and sealed and was then heated in a rocking furnace from ambient temperature to 975 °C at 2 °C min^{-1}. Equilibrium periods at $T = 221$ °C (melting point of Se) and 685 °C (melting point of Ge) were maintained during heating where the temperature was kept constant for 4 h. The temperature was kept constant at 975 °C for 48 h, before being cooled at 1 °C min^{-1} to the quench temperature $T = 754$ °C. After a 5 h equilibration period the ampoule was dropped into an ice/salt-water mixture. The measured glass transition temperature for $GeSe_4$ is 182(2) °C.

Before attempting to remove pieces of glass from the ampoule it was annealed at 130 °C to reduce any tension and aid in the production of a solid pellet piece. A diamond-wire saw was used to cut across the ampoule so that cylindrical pieces of $GeSe_4$ glass could be removed. $GeSe_4$ pellets were then produced from the cylindrical pieces by gently grinding them to the correct shape for either a single toroid or double toroid anvil, using the method discussed in section 3.6.1.

5.3.2 D4c neutron diffraction experiment

A neutron diffraction experiment was performed to study amorphous $GeSe_4$ at ambient temperature ($T \sim 300$ K) and at pressures up to $P = 8.2(5)$ GPa. A VX5 Paris-Edinburgh press was mounted in an in-plane scattering geometry on the D4c diffractometer with single toroid cubic boron nitride anvils providing compression.

Sample	Pellet mass (g)	$Ti_{0.676}Zr_{0.324}$ gasket mass (g)
$GeSe_4{}^{\langle 1\rangle}$	0.40128(1)	1.3985(1)
$GeSe_4{}^{\langle 2\rangle}$	0.40039(1)	1.4041(1)

Table 5.1: Pellet and $Ti_{0.676}Zr_{0.324}$ gasket masses for the D4c $GeSe_4$ experiment.

The mass of an ideal single toroid $GeSe_4$ pellet is 0.401 91 g. Two solid $GeSe_4$ pellets were created as outlined in section 5.3.1, and their masses are given in table 5.1. The pellet labelled $GeSe_4{}^{\langle 1\rangle}$ was used for measurements up to $P = 4.7(5)$ GPa after which it was decompressed and the sample removed, whilst the pellet labelled $GeSe_4{}^{\langle 2\rangle}$ was used for the higher pressure points.

Two pieces of vanadium were machined to match the geometry of the caps of a single toroid anvil, and two cylinders were also machined to be placed between these caps to form a pellet. The cylinders were made with different heights, meaning that

the overall height of the vanadium "pellet" could be adjusted to correct the sample data taken at different pressures.

The D4c diffraction experiment was performed as outlined in section 3.6.5. A measurement of Ni powder in an encapsulated $Ti_{0.676}Zr_{0.324}$ gasket was made to quantify the incident neutron wavelength and the zero-angle correction for the detectors. These parameters were found to be $\lambda = 0.4985\,\text{Å}$ and $2\theta_{\text{zero}} = 0.060°$, respectively.

Neutron diffraction measurements were made for the sample at the pressure points given in table 5.2. Three vanadium measurements were made, two of them using cylinders machined to form a "pellet" with spherical caps at either end, and the third using just the machined spherical caps. Three measurements of empty $Ti_{0.676}Zr_{0.324}$ gaskets were made: an uncompressed gasket, a gasket that had been recovered from 4.7(5) GPa, and a gasket that had been recovered from 8.1(5) GPa. The empty anvils were also measured with the gap between the anvils set at 0.4 mm.

Applied load L (tonnes)	Pressure P (GPa)
6.8	Ambient
30.5	3.0(5)
50.9	4.7(5)
71.2	6.3(5)
81.4	7.0(5)
94.9	8.1(5)

Table 5.2: Pressure points measured during the D4c experiment. The pressure at the sample position P was deduced from the calibration curve given in figure 3-17.

The compression was controlled by a hand pump across the full pressure range. All pressure points were made in sequential order as hysteresis in the system means that the pressure profile upon decompression is not well understood. Upon reaching a given pressure point, any relaxation in the system ($\sim$ 10–20 bar) was allowed to continue without the pressure being increased again. Whilst increasing and decreasing the pressure, periodic pauses were taken to allow the system to equilibrate.

5.3.3 PEARL neutron diffraction experiment

A neutron diffraction experiment was performed to study amorphous $GeSe_4$ at ambient temperature ($T \sim 300\,\text{K}$) and at pressures up to $P = 14.4(5)\,\text{GPa}$. A V3 Paris-Edinburgh press was mounted in a transverse scattering geometry on the PEARL HiPr diffractometer with double toroid sintered diamond anvils providing compression.

The mass of an ideal double toroid $GeSe_4$ pellet is 0.145 26 g. A solid $GeSe_4$ pellet was created as outlined in section 5.3.1. A vanadium pellet was produced by taking

Sample	Pellet mass (g)	$Ti_{0.676}Zr_{0.324}$ gasket mass (g)
$GeSe_4$	0.1528(1)	1.0465(1)
Vanadium	0.2047(1)	1.0506(1)

Table 5.3: Pellet and $Ti_{0.676}Zr_{0.324}$ gasket masses for the PEARL $GeSe_4$ experiment.

vanadium foil and placing the correct mass in a specially prepared die which re-creates the shape of a double toroid pellet. This was then compressed as outlined in section 3.6.1. The masses of the $GeSe_4$ and vanadium pellets are given in table 5.3.

Applied load L (tonnes)	Pressure P (GPa)	$GeSe_4$	Vanadium
2	Ambient	✓	✓
75	8.7(5)	✓	✓
98	10.9(5)	✓	✓
110	12.8(5)	✓	
120	14.4(5)	✓	✓

Table 5.4: Pressure points measured during the PEARL experiment. The pressure at the sample position P was deduced from the calibration curve given in figure 3-15.

The PEARL diffraction experiment was performed as outlined in section 3.6.4. Measurements were made for two empty $Ti_{0.676}Zr_{0.324}$ gaskets with their masses given in table 5.3. Neutron diffraction measurements were made for the vanadium and the sample in turn, and the investigated pressure points are given in table 5.4. During the course of a pressure point measurement, the ratio was taken of the measured intensities for different periods of time. If this ratio deviates from unity then the scattered intensity is changing with time. No such deviation was observed during the course of the measurements.

The compression was controlled by an automated machine up to an oil pressure $P_{\text{oil}} = 950\,\text{bar}$, after which a hand pump was used to manually increase the pressure. The automated system kept the pressure constant, *i.e.* if some relaxation occurred that caused the pressure to drop the automated system would increase it back to the set point. When using the hand pump this was not possible, and any relaxation (typically $\sim$ 10–20 bar) was allowed to occur. Whilst increasing and decreasing pressure, periodic pauses were taken to allow the system to equilibrate.

5.3.4 Equation of state and density measurements

The mass density ρ_{m} of $GeSe_4$ was measured under ambient conditions using a helium pycnometer. This yielded an ambient-pressure number density $\rho_0 = 0.0335(1)\,\text{Å}^{-3}$.

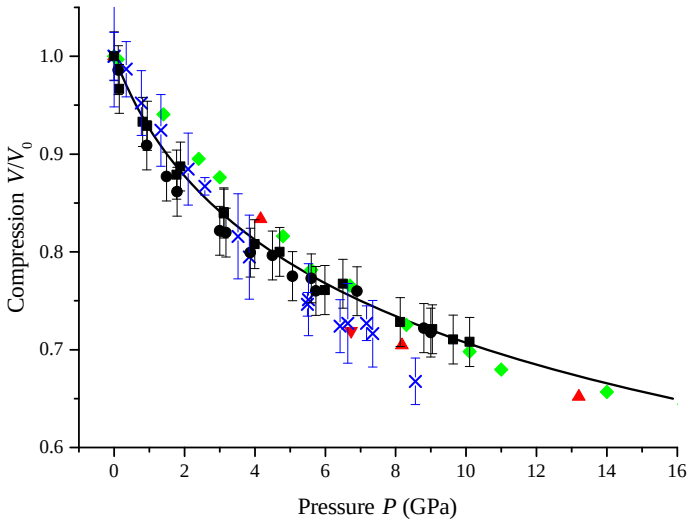

Figure 5-1: The pressure-volume equation of state for $GeSe_4$ as measured in Ref. [43] for both compression (■) and decompression (●). Also included are the results from the FPMD simulations from Ref. [42] (NVT ▼, NPT ▲) and from Ref. [44] (♦). A 3rd-order Birch-Murnaghan equation of state was fitted to the experimental compression data, giving the parameters $B_0 = 10.42(69)$ GPa and $B_0' = 5.96(52)$ [43] (solid black curve). Pressure-volume results for the stressed-rigid chalcogenide glass $GeSe_2$ are also presented for comparison [108] (×).

The pressure-volume equation of state for $GeSe_4$ is shown in figure 5-1. A 3rd-order Birch-Murnaghan equation of state, given by

$$P(V;V_0,B_0,B_0') = \frac{3B_0}{2}\left[\left(\frac{V}{V_0}\right)^{-\frac{7}{3}} - \left(\frac{V}{V_0}\right)^{-\frac{5}{3}}\right] \times \left\{1 + \frac{3}{4}\left(B_0' - 4\right)\left[\left(\frac{V}{V_0}\right)^{-\frac{2}{3}} - 1\right]\right\}, \tag{5.19}$$

was fitted to the data to allow for extrapolation to higher pressures for use in the PEARL data analysis. The fitted parameters were $B_0 = 10.42(69)\,\text{GPa}$ and $B_0' = 5.96(52)$ [43]. This bulk modulus is comparable to the bulk modulus for $GeSe_2$, $B_0 = 10.55(30)\,\text{GPa}$ (chapter 4). Using the ambient-pressure number density ρ_0 and the compression V/V_0, the number density and reduced density for the measured pressure points can be calculated and are shown in table 5.5.

Pressure P (GPa)	Number Density ρ (Å^{-3})	Compression V/V_0	Reduced density ρ/ρ_0
Ambient$^{\dagger *}$	0.0335(1)	1	1
3.0(5)†	0.0398(8)	0.842(17)	1.188(24)
4.7(5)†	0.0422(7)	0.794(13)	1.260(21)
6.3(5)†	0.0440(6)	0.761(11)	1.313(18)
7.0(5)†	0.0447(5)	0.749(9)	1.334(15)
8.1(5)†	0.0457(5)	0.733(8)	1.364(15)
8.7(5)*	0.0463(5)	0.724(8)	1.382(15)
10.9(5)*	0.0481(4)	0.696(6)	1.436(13)
12.8(5)*	0.0495(4)	0.677(6)	1.478(13)
14.4(5)*	0.0506(3)	0.662(4)	1.510(10)

Table 5.5: Compression V/V_0, number density ρ, and reduced density ρ/ρ_0 for each pressure point measured in the neutron diffraction experiments. The symbols † and $*$ denote experiments made using the D4c and PEARL diffractometers, respectively.

5.3.5 First-principles molecular dynamics

FPMD simulations were performed as in Ref. [42] using the Car-Parrinello [110] method within the NPT or NVT ensemble with $N = 120$ atoms. Table 5.6 shows the pressure points that were calculated.

Pressure P (GPa)	Compression V/V_0	Number density ρ (Å^{-3})	Reduced density ρ/ρ_0
Ambient†	0.03123	1	1
4.2†	0.03746	0.83373	1.19943
6.7*	0.04343	0.71907	1.39068
8.2†	0.04433	0.70453	1.41939
13.2†	0.04789	0.65217	1.53334

Table 5.6: Compression V/V_0, number density ρ, and reduced density ρ/ρ_0 for each pressure point calculated in the FPMD simulations. The symbols † and $*$ denote calculations made using the NPT and NVT ensembles, respectively.

5.4 Results

Figure 5-2 shows the pressure dependence of the total structure factor $S_{\mathrm{N}}(Q)$ or $S_{\mathrm{X}}(Q)$ for $GeSe_4$. The figure compares the neutron diffraction $S_{\mathrm{N}}(Q)$ results from the present work with the x-ray diffraction $S_{\mathrm{X}}(Q)$ results measured in Refs. [43, 44]. In the case of $S_{\mathrm{N}}(Q)$, the D4c diffractometer was employed for the pressure range up to 8.1(5) GPa, and the PEARL diffractometer was employed at higher pressures up to a maximum value $P = 14.4(5)$ GPa. The D4c measurements have a cutoff $Q_{\max} = 21.5\,\text{Å}^{-1}$, and the PEARL measurements have a cutoff $Q_{\max} = 19.55\,\text{Å}^{-1}$. The x-ray diffraction results of Refs. [43] and [44] have cutoffs $Q_{\max} = 17.5\,\text{Å}^{-1}$ and $9\,\text{Å}^{-1}$, respectively.

There is good agreement between the neutron diffraction data and the x-ray diffraction data reported in Ref. [43]. The x-ray diffraction results do, however, show sharper features in reciprocal space, possibly due to differences between the resolution functions of the different diffractometers that were employed. The x-ray diffraction results reported in Ref. [44], shown by the green curves in figure 5-2, have a reduced Q-range, $0.8\,\text{Å}^{-1} \leq Q \leq 9\,\text{Å}^{-1}$, which makes a full comparison difficult.

The most significant reciprocal space features that change with pressure are the position and height of the first two peaks at low-Q, namely the first sharp diffraction peak (FSDP) and the principal peak (PP). At ambient pressure, the FSDP and PP are both well-defined in the neutron and x-ray diffraction results. As the pressure is increased, the FSDP shifts to higher Q and reduces in intensity, until it is difficult to discern from the PP. Meanwhile, as the pressure is increased the PP shifts to higher-Q and there is an accompanying increase in both its height and sharpness.

Figure 5-3 shows the pressure dependence of the total pair-distribution function $G_{\mathrm{N}}(r)$ or $G_{\mathrm{X}}(r)$ for $GeSe_4$. In the case of the neutron diffraction results, the reciprocal space data sets were Fourier transformed using (i) a step modification function (equation (5.3)) and (ii) a Lorch modification function (equation (5.4)) [56]. The data

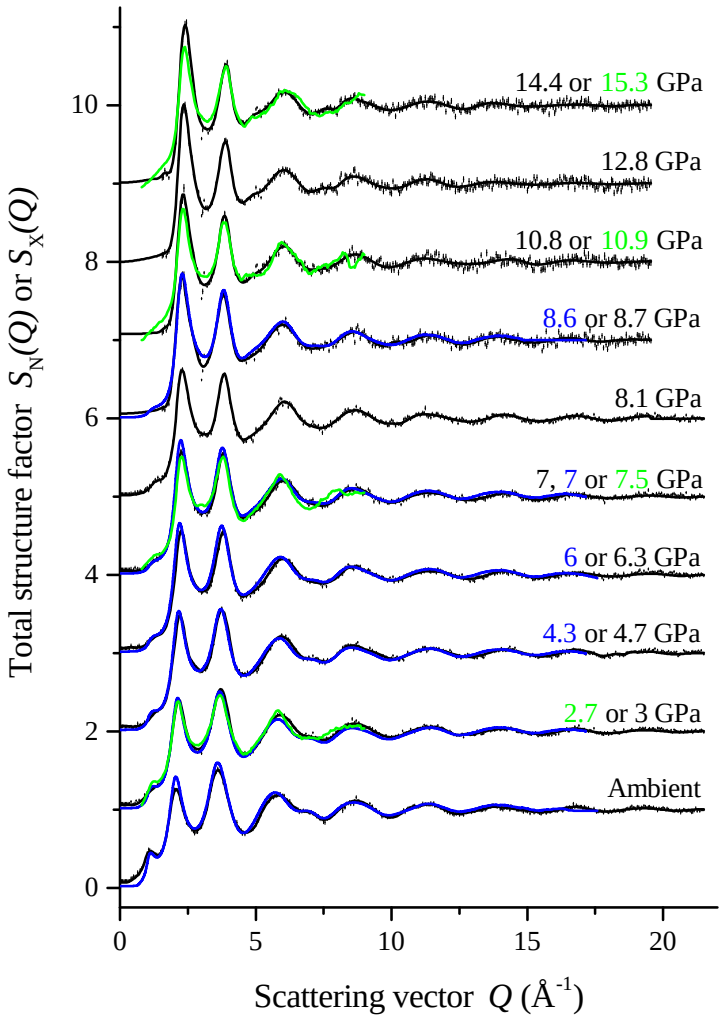

Figure 5-2: The pressure dependence of the neutron total structure factor $S_{\mathrm{N}}(Q)$ and x-ray total structure factor $S_{\mathrm{X}}(Q)$ for $GeSe_4$, where $S_{\mathrm{N}}(Q) \simeq S_{\mathrm{X}}(Q) \simeq S_{\mathrm{NN}}^{\mathrm{BT}}(Q)$. The solid black curves show the back Fourier transforms of spline fits to the experimental data (shown by vertical error bars) for the $S_{\mathrm{N}}(Q)$ data sets measured using the D4c diffractometer at ambient pressure and at pressures of 3.0(5), 4.7(5), 6.3(5), 7.0(5), and 8.1(5) GPa, and using the PEARL diffractometer at pressures of 8.7(5), 10.9(5), 12.8(5), and 14.4(5) GPa. The blue curves show the $S_{\mathrm{X}}(Q)$ data sets reported in Ref. [43] at ambient pressure and at 3, 4.3, 6, 7, and 8.6 GPa. The green curves show the $S_{\mathrm{X}}(Q)$ data sets reported in Ref. [44] at 2.6, 7.5, 10.8, and 15.3 GPa. The high-pressure curves have been offset vertically for clarity of presentation.

obtained from the first procedure were joined smoothly to the data obtained from the second procedure at a point just beyond the first peak in real space. EPSR [165–167] simulations were used to provide the real space information reported in Ref. [44]. The partial pair-distribution functions calculated from the EPSR simulations were used to construct the Bhatia-Thornton number-number partial pair-distribution function $g_{\mathrm{NN}}^{\mathrm{BT}}(r)$.

The results measured in Ref. [43] are in overall accord with those measured by neutron diffraction in the current work. The position of the nearest neighbour peak, shows good agreement, although there is a discrepancy in the height. This discrepancy is primarily due to the difference in $Q_{\max}$ cutoff values and can be eliminated if Fourier transforms are made using the same cutoff value.

The results from EPSR simulations [44] show disagreement with the neutron diffraction results at all pressure points. At lower pressures, the nearest neighbour peak is shifted to higher-r and there is a low-r shoulder, whilst at the higher pressures the peak is split, with a smaller height and larger width.

FPMD simulations were undertaken [42] to study the change in structure of $GeSe_4$ with pressure and provide complementary information to the experimental results. The modelled pressure vs. number density dependence is shown in figure 5-1. Figure 5-4 shows the pressure dependence of the total structure factor $S_{\mathrm{N}}(Q)$ for $GeSe_4$. The figure compares FPMD results [42] with the equivalent-pressure neutron diffraction results. For the FPMD simulations the NPT ensemble was used for all calculations, except for the pressure point at 6.7 GPa where the NVT ensemble was used. The experimental results and FPMD simulations agree well in reciprocal space over the full pressure range.

Figure 5-5 shows the pressure dependence of the total pair-distribution function $G_{\mathrm{N}}(r)$ for $GeSe_4$. This figure shows the Fourier transforms of the curves given in figure 5-4. The FPMD results were obtained by Fourier transforming the reciprocal space data sets, as opposed to being generated directly in real space. The analysis was undertaken in this way to ensure that the experimental and simulation results can be compared on a like-for-like basis, *i.e.* they have been treated with the same Fourier transformation procedure using a cutoff $Q_{\max} = 20.6\,\text{Å}^{-1}$.

At ambient pressure the nearest neighbour peak positions match, although the FPMD simulations show a sharper nearest neighbour peak than the D4c results. As the pressure increases, the nearest neighbour peak broadens and keeps the same position. The second peaks obtained from the FPMD and neutron diffraction results are in agreement at ambient and the highest pressure, but not at intermediate pressures.

The differences between the neutron diffraction and FPMD results can be assessed

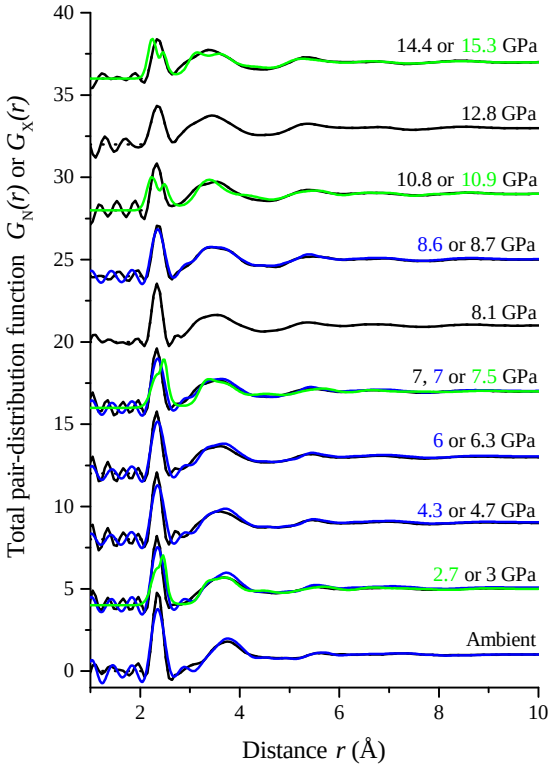

Figure 5-3: The pressure dependence of the neutron total pair-distribution function $G_{\mathrm{N}}(r)$ and x-ray total pair-distribution function $G_{\mathrm{X}}(r)$ for $GeSe_4$, where $G_{\mathrm{N}}(r) \simeq G_{\mathrm{X}}(r) \simeq g_{\mathrm{NN}}^{\mathrm{BT}}(r)$. The curves correspond to those given in figure 5-2. The solid black curves show the Fourier transforms of the spline fits of the $S_{\mathrm{N}}(Q)$ data sets measured at ambient pressure and at pressures of 3.0(5), 4.7(5), 6.3(5), 7.0(5), 8.1(5), 8.7(5), 10.9(5), 12.8(5), and 14.4(5) GPa. The dashed black curves show the calculated $G_{\mathrm{N}}(r \to 0)$ limits at r-values below the distance of closest approach between two atoms. The blue curves show the Fourier transforms of the $S_{\mathrm{X}}(Q)$ data sets reported in Ref. [43] at ambient pressure and at 4, 5.4, 6, 7, and 8.6 GPa. The green curves show the total pair-distribution functions $G(r)$ at 2.7, 7.5, 10.8, and 15.3 GPa, as constructed from the Faber-Ziman partial pair-distribution functions that were calculated using the empirical-potential structure refinement (EPSR) method [165–167] using x-ray diffraction data as a reference [44]. The high-pressure curves have been offset vertically for clarity of presentation.

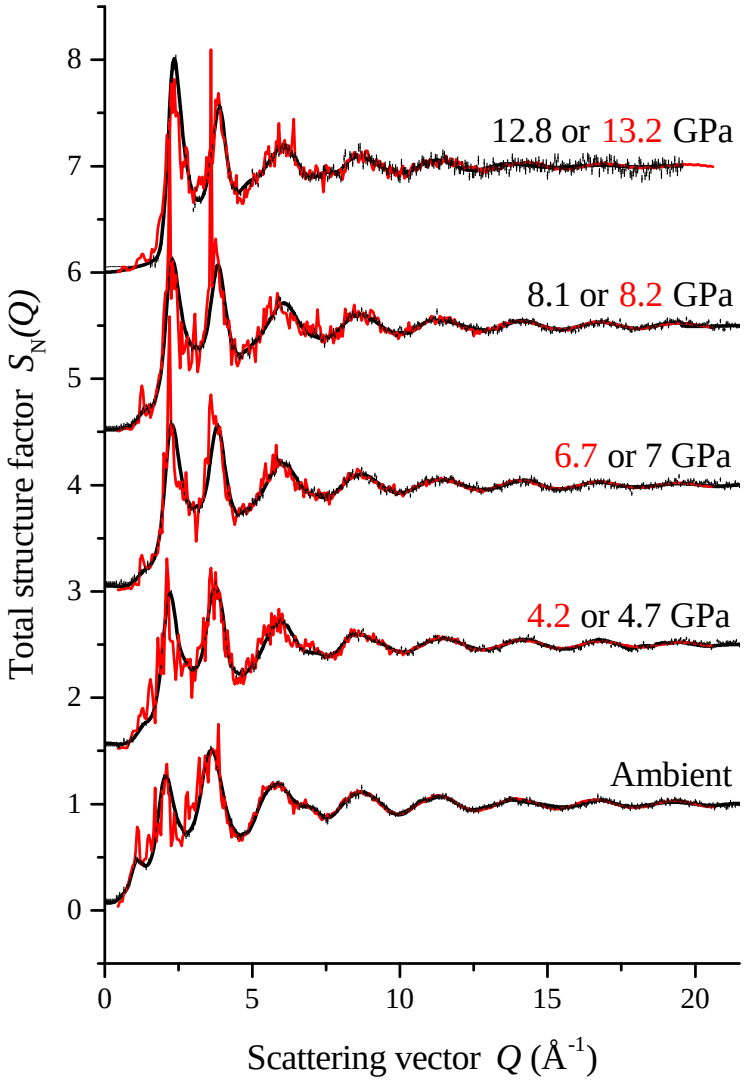

Figure 5-4: The pressure dependence of the total structure factor $S_N(Q)$ for $GeSe_4$. The solid black curves show the back Fourier transforms of spline fits to the experimental data (shown by vertical error bars) for the neutron diffraction data sets measured using the D4c diffractometer at ambient pressure and at pressures of 4.7(5), 7.0(5), and 8.1(5) GPa, and using the PEARL diffractometer at 12.8(5) GPa. The red curves show FPMD data sets [42] calculated at ambient pressure and at 4.2, 8.2, and 13.2 GPa in the NPT ensemble, and at 6.7 GPa in the NVT ensemble. The high-pressure curves have been offset vertically for clarity of presentation.

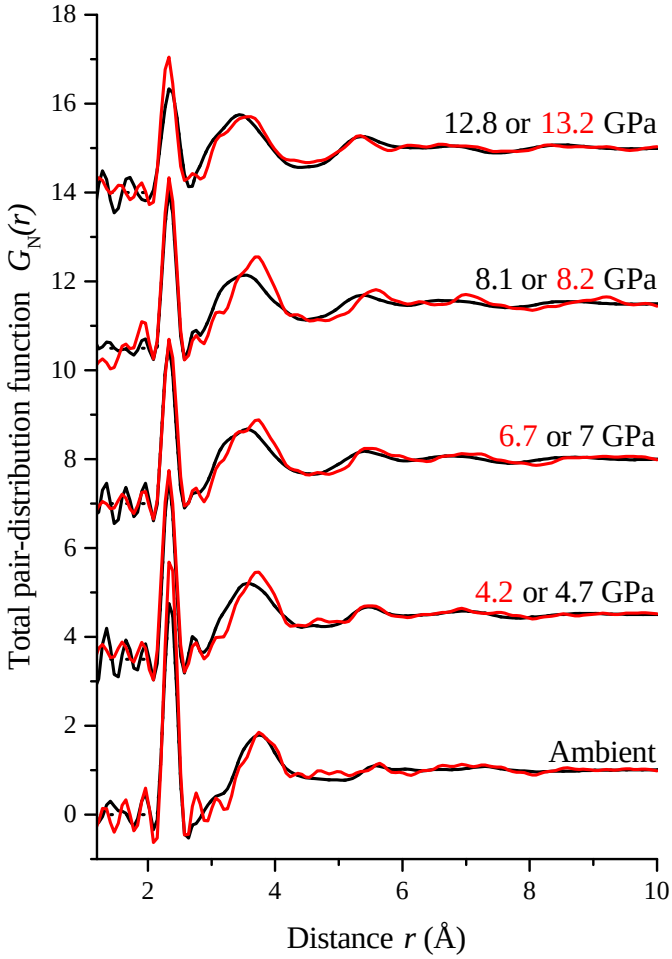

Figure 5-5: The pressure dependence of the neutron total pair-distribution function $G_{\mathrm{N}}(r)$ for $GeSe_4$. The curves correspond to those given in figure 5-4. The solid black curves show the Fourier transforms of the spline fits to the $F(Q)$ data sets measured at ambient pressure and at pressures of 4.7(5), 7.0(5), 8.1(5), and 12.8(5) GPa. The dashed black curves show the calculated $G_{\mathrm{N}}(r \rightarrow 0)$ limits at r-values below the distance of closest approach between two atoms. The red curves show the Fourier transforms of the FPMD data sets [42] calculated at ambient pressure and at 4.2, 8.2, and 13.2 GPa in the NPT ensemble, and at 6.7 GPa in the NVT ensemble. The high-pressure curves have been offset vertically for clarity of presentation.

by using the goodness-of-fit parameter [62, 126]

$$R_\chi = \sqrt{\frac{\sum_i \left[T_{\mathrm{ND}}(r_i) - T_{\mathrm{FPMD}}(r_i)\right]^2}{\sum_i T_{\mathrm{ND}}^2(r_i)}} \tag{5.20}$$

where ND indicates neutron diffraction and $T(r)$ is the total correlation function defined as [168]

$$T(r) = 4\pi\rho r \left[G_{\mathrm{N}}(r) - G_{\mathrm{N}}(0)\right]. \tag{5.21}$$

The calculated values for the R_χ parameter are given in table 5.7 for results obtained at similar pressures.

Neutron diffraction pressure point	FPMD pressure point	R_χ parameter
Ambient	Ambient	9.14%
4.7(5) GPa	4.2 GPa	7.63%
7.0(5) GPa	6.7 GPa	8.51%
8.1(5) GPa	8.2 GPa	11.98%
12.8(5) GPa	13.2 GPa	7.11%

Table 5.7: R_χ goodness-of-fit parameters for the neutron diffraction and FPMD results at similar pressures. The range $2\,\text{Å} \leq r \leq 10\,\text{Å}$ was chosen for all of the calculations.

A density correlation function $D(r)$ can be defined by [52]

$$D(r) = 4\pi\rho r G(r), \tag{5.22}$$

and is an alternative method of presenting real space data which highlights features at larger distances. Following the method shown in Ref. [43], the differential density correlation function $\Delta D(r)$ can be defined as

$$\Delta D(r) = D(r) - D_0(r), \tag{5.23}$$

where $D_0(r)$ denotes the $D(r)$ function at ambient pressure, such that $\Delta D(r)$ shows the change in real-space features relative to the ambient pressure measurement. Figure 5-6 shows a selection of $D(r)$ functions from the neutron diffraction measurements of $GeSe_4$ glass. Also presented are a selection of $\Delta D(r)$ functions which show the changes in structure as a function of pressure. The figure highlights the changes to real-space features as the pressure is increased showing *e.g.* a decrease in height and broadening of the nearest neighbour peak, a shift to lower r and broadening of the second peak, and an increase in height and shift to lower r of the third peak.

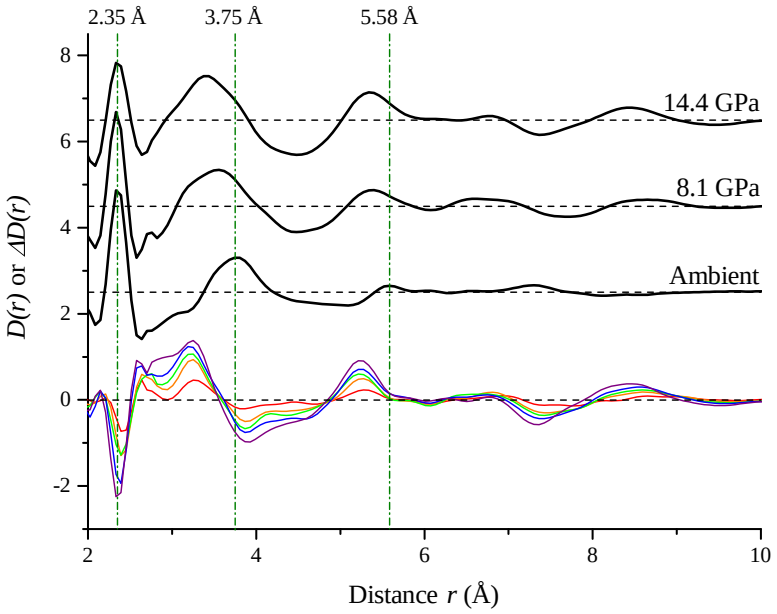

Figure 5-6: The density correlation function $D(r)$ for $GeSe_4$ as measured using neutron diffraction at ambient pressure and at pressures of 8.1(5) GPa and 14.4(5) GPa (black curves). The differential density correlation function $\Delta D(r)$ (see text for definition) is also plotted in colour. The $\Delta D(r)$ functions are plotted for pressures of 3.0(5) (red), 6.3(5) (orange), 8.1(5) (green), 10.9(5) (blue), and 14.4(5) GPa (violet). Three vertical chained green lines mark the positions of the first three peaks at ambient pressure. The horizontal dashed black lines show the high-r limit, $D(r \to \infty)$ or $\Delta D(r \to \infty)$, for each function. The $D(r)$ functions have been offset vertically for clarity of presentation.

Figures 5-7(a) and 5-7(b) show the reduced-density dependence of the mean nearest neighbour bond distance $\overline{r}$ and coordination number $\overline{n}$, respectively. The neutron diffraction, x-ray diffraction [43], and FPMD simulations [42] show that within the reduced-density range investigated, both $\overline{r}$ and $\overline{n}$ remain constant within the experimental error. The EPSR results derived from x-ray diffraction [44] suggest a different story: $\overline{n}$ increases with increasing reduced-density before levelling out and staying relatively stable, whilst $\overline{r}$ shows an erratic reduced-density dependence. The results for the stressed-rigid chalcogenide glass $GeSe_2$ (chapter 4, [79]) are also presented for comparison.

In figure 5-7 the solid black horizontal line shows the coordination number expected from the "8-N" rule [59]. This value is $\overline{n} = 2.4$ for $GeSe_4$ irrespective of whether the coordination numbers are taken from the chemically ordered network (CON, equation (5.17)) model or the random covalent network (RCN, equation (5.18)) model. For the case where the coherent scattering lengths are close but not exactly equal, as is the case for $GeSe_4$, an additional correction can be made to the mean coordination number using equation (5.11). This corrected mean coordination number, $\overline{n}^{\text{expt}} = 2.417$ for both the CON and RCN models, is shown in the figure as the solid horizontal black line.

To investigate the discrepancy between the results of Ref. [44] and the other data sets, the reciprocal space $S_{\text{X}}(Q)$ datasets (figure 5-2) were Fourier transformed and processed in the same manner as that used for the neutron diffraction results. A maximum cutoff $Q_{\text{max}} = 9\,\text{Å}^{-1}$ resulted in strong Fourier transformation artefacts in the resulting real-space functions. To accommodate for this issue, the nearest neighbour peak was fitted with a Gaussian function which had been convoluted with a sinc function [103] (section 2.3) to allow for an accurate calculation of the mean coordination number $\overline{n}$. This fitted mean coordination number, and the associated mean bond distance, are also shown in figure 5-7 and suggest a different story again, where both $\overline{n}$ and $\overline{r}$ first increase to a maximum at $\rho/\rho_0 \sim 1.3$ before decreasing slowly.

In order to check that using a low Q_{max} cutoff was viable for the data from Ref. [44], the neutron diffraction data was also processed in the same manner, using the same cutoff $Q_{\text{max}} = 9\,\text{Å}^{-1}$. The mean coordination numbers (not shown in figure 5-7) were found to match those using the full Q-range, leading to the conclusion that the procedure is reliable. Based on this, the EPSR results from Ref. [44] that were refined using x-ray diffraction data can be excluded from further discussion.

We now present a possible hypothesis as to why the EPSR simulations may have lead to inaccurate results. In an x-ray diffraction measurement on $GeSe_4$, the total structure factor measured is approximately equal to the Bhatia-Thornton number-number partial structure factor, such that $S_{\text{X}}(Q) \simeq S^{\text{BT}}_{\text{NN}}(Q)$. $S^{\text{BT}}_{\text{NN}}(Q)$ treats all atomic sites equally,

and cannot be used to distinguish between the chemical species that occupy those sites. In consequence, any attempt to simulate the difference between homopolar and heteropolar bonds is fraught with difficulty.

Figure 5-8 shows the reduced-density dependence of the mean second-nearest neighbour distance $\overline{r}_2$. The results suggest a two-stage reduction in distance: at low reduced-densities the change in $\overline{r}_2$ with increasing reduced-density is gradual, at some reduced-density the gradient then becomes much steeper and the distance decreases faster. The reduced-density value where the gradient changes is different for the FPMD results when compared to the rest of the results, however, with the FPMD results showing a relatively stable $\overline{r}_2$ value until $\rho/\rho_0 \sim 1.4$.

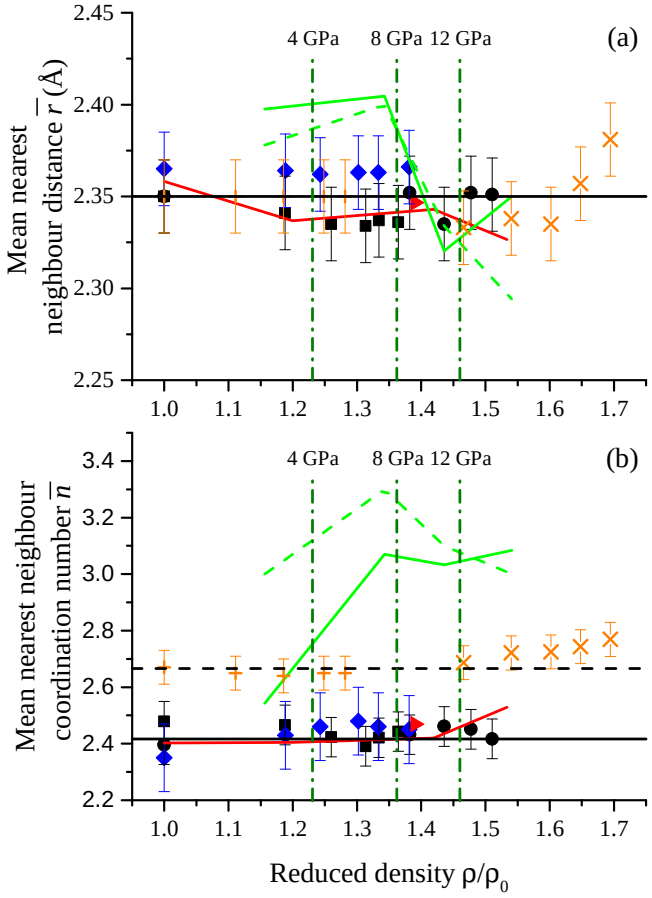

Figure 5-7: The reduced-density dependence of the mean nearest neighbour (a) bond distance $\overline{r}$ and (b) coordination number $\overline{n}$ for amorphous $GeSe_4$ as obtained from (i) neutron diffraction using a $GeSe_4$ sample on either the D4c (■) or PEARL (●) diffractometer; (ii) x-ray diffraction [43] (◆); (iii) x-ray diffraction [44] (broken green curve); (iv) EPSR simulations using x-ray diffraction data [44] (solid green curve); and (v) FPMD [42] simulations using either the NPT (solid red curve) or NVT (▶) ensemble. Neutron diffraction results for amorphous $^{N}Ge^{N}Se_2$ are also shown and were obtained using the (i) D4c [109] (+) and (ii) PEARL (chapter 3) (×) diffractometers. $\overline{n}$ for the FPMD and EPSR simulations was found from the simulated $\overline{n}_{\alpha}^{\beta}$ values by using a cutoff distance specified by the first minimum in $G(r)$. In (a), the horizontal solid black line gives the ambient bond distance $\overline{r} = 2.35$ Å for $GeSe_4$. In (b), the horizontal solid and dashed black lines give the coordination numbers $\overline{n}^{\text{expt}}$ expected from the "8-N" rule (see text) for $GeSe_4$ and $GeSe_2$, respectively [59]. The vertical chained green lines correspond to pressures of $\sim$ 4, 8, and 12 GPa, as calculated using a 3rd-order Birch-Murnaghan equation of state fitted to the $GeSe_4$ compression data from Ref. [43] (section 5.3.4).

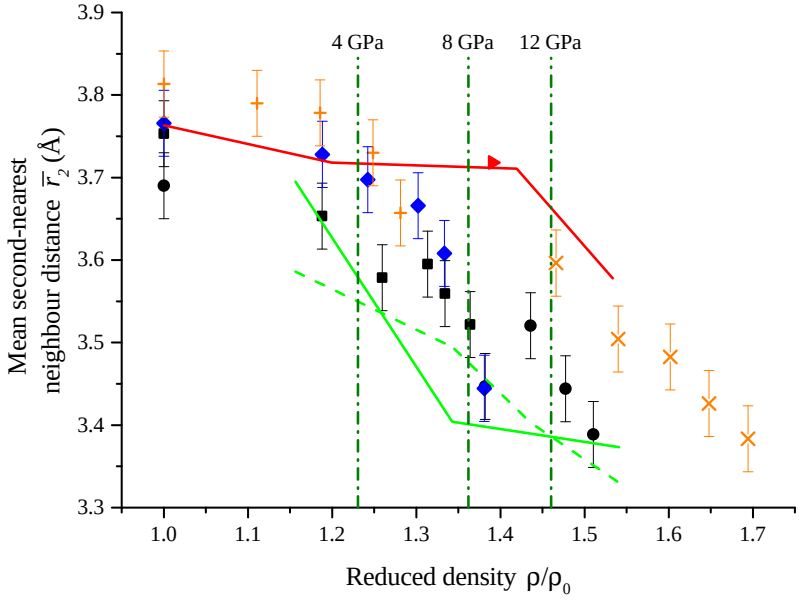

Figure 5-8: The reduced-density dependence of the mean second-nearest neighbour distance $\overline{r}_2$ as obtained from (i) neutron diffraction using a $GeSe_4$ sample on either the D4c (■) or PEARL (●) diffractometer; (ii) x-ray diffraction [43] (♦); (iii) x-ray diffraction [44] (solid green curve); (iv) EPSR simulations using x-ray diffraction data as a reference [44] (dashed green curve); and (v) FPMD [42] simulations using either the NPT (solid red curve) or NVT (▶) ensemble. Neutron diffraction results for amorphous $^{N}Ge^{N}Se_2$ are also shown and were obtained using the (i) D4c [109] (+) and (ii) PEARL (chapter 3) (×) diffractometers. The vertical chained green lines correspond to pressures of ∼ 4, 8, and 12 GPa, as calculated using a 3rd-order Birch-Murnaghan equation of state fitted to the $GeSe_4$ compression data from Ref. [43] (section 5.3.4).

5.5 Discussion

Neutron diffraction measurements, combined with x-ray diffraction results [43] and complementary FPMD simulations [42], show that the mean nearest neighbour bond distance $\overline{r}$ (figure 5-7(a)) and coordination number $\overline{n}$ (figure 5-7(b)) for amorphous $GeSe_4$ remain constant at $\overline{r} \sim 2.35\,\text{Å}$ and $\overline{n} \sim 2.4\,\text{Å}$, respectively, as the pressure is increased from ambient to 14.4(5) GPa ($\rho/\rho_0 \sim 1.51$). This mean coordination number is consistent with the "8-N" rule, which predicts a corrected mean coordination number $\overline{n}^{\text{expt}} = 2.417$ for $GeSe_4$ [59].

The lack of change associated with the nearest neighbour shell in $GeSe_4$ suggests that the structural rearrangement during densification occurs at higher r values, *i.e.* it is associated with the second and higher coordination shells. This structural rearrangement can be seen as a decrease in the second-nearest neighbour distance (figure 5-8) from $\overline{r}_2 \sim 3.75\,\text{Å}$ at ambient to $\overline{r}_2 \sim 3.4\,\text{Å}$ at 14.4(5) GPa.

The mean nearest-neighbour bond distances and coordination numbers for the rigid glass $GeSe_4$ and the stressed-rigid glass $GeSe_2$ are compared in figures 5-7(a) and 5-7(b), respectively. As discussed in chapter 4, $GeSe_2$ is characterised by a two-stage densification process. At first, $\overline{n}$ and $\overline{r}$ remain stable up to 12.8(5) GPa ($\rho/\rho_0 \sim 1.6$). Then, with further compression, both begin to increase as more atoms are pushed into the nearest neighbour shell. For $GeSe_4$, both $\overline{n}$ and $\overline{r}$ are stable up to the maximum measured pressure 14.4(5) GPa. This maximum pressure is, however, equivalent to a smaller reduced density $\rho/\rho_0 \sim 1.51$, which is below the point at which the parameters $\overline{n}$ and $\overline{r}$ begin to increase for $GeSe_2$.

Figure 5-8 compares the reduced-density dependence of the second-nearest neighbour distance $\overline{r}_2$ for both $GeSe_4$ and $GeSe_2$. The figure shows a two-stage densification process, whereby the distance decreases slowly with increasing reduced density up to $\rho/\rho_0 \sim 1.2$ for both glasses. Above $\rho/\rho_0 \sim 1.2$, however, the distance begins to decrease more rapidly, although the rate of change for $GeSe_2$ is not as rapid as that for $GeSe_4$.

The most pronounced pressure dependent changes in the total structure factor features upon pressure are associated with the FSDP and PP positions and heights. The FSDP shifts to higher-Q with increasing pressure and is quickly unable to be distinguished from the PP. Meanwhile, the PP position shifts to higher-Q whilst increasing in height and sharpening. The FSDP and PP are signatures of the intermediate and extended range order within the system, respectively, as characterised by periodicities of $2\pi/Q_{\text{FSDP}}$ and $2\pi/Q_{\text{PP}}$, respectively, where Q_α is the position of peak α. The decrease and increase in the heights of the FSDP and PP, respectively, suggest a change in the network topology: the extended range order increases as the ambient condition open network collapses upon compression [43].

As well as x-ray diffraction and EPSR simulation results, Ref. [44] also includes electrical resistivity results for $GeSe_4$ as a function of pressure which are in good agreement with those previously reported [31]. A relatively sharp and hysteretically reversible decrease in the resistivity was found at approximately 11 GPa. The process of metallisation is expected to be accompanied by an increase in the mean coordination number, which is not seen in the current work. Thus, although the resistivity decreases, it does not result from a marked change in the nearest-neighbour coordination number.

5.6 Conclusions

The *in situ* high-pressure structure of amorphous $GeSe_4$ has been measured using neutron diffraction at pressures ranging from ambient to 14.4(5) GPa using a Paris-Edinburgh press mounted on either the D4c or PEARL diffractometer. The measured total structure factors, and their Fourier transformations, agree with the x-ray diffraction results reported in Ref. [43] and with complementary FPMD [42] results.

Across the measured pressure range, the nearest-neighbour coordination shell remains relatively stable, showing a constant mean bond distance $\overline{r}$ and coordination number $\overline{n}$ up to 14.4(5) GPa ($\rho/\rho_0 \sim 1.51$). The densification processes take place in the second and higher coordination shells. For example, the mean second nearest-neighbour bond distance $\overline{r}_2$ shows a two-stage movement to lower r upon compression, with an initially gradual decrease below $\rho/\rho_0 \sim 1.2$ being followed by a strong, linear decrease at higher ρ/ρ_0 values.

The densification of the rigid glass $GeSe_4$ is compared to that of the stressed-rigid glass $GeSe_2$. When plotted with respect to reduced density, the glasses show similar behaviour for the nearest neighbour $\overline{n}$ and $\overline{r}$ values. Due to differences in equations-of-state, a given pressure point for $GeSe_4$ corresponds to a lower reduced-density as compared to $GeSe_2$. Therefore, it is not possible to say whether $\overline{n}$ and $\overline{r}$ for $GeSe_4$ will increase at the same reduced-density as for amorphous $GeSe_2$.

Further work in analysing the FPMD results would allow the intricacies of densification to be explored. Unfortunately, neutron diffraction measurements at higher pressures may not be viable: the insulator–to–metal transition may cause changes in the bulk properties of a sample, leading to a catastrophic failure of the $Ti_{0.676}Zr_{0.324}$ gaskets as has been observed previously for $GeSe_2$. Further experiments are nonetheless required to probe the high-pressure structure and to search for the structural change that accompanies the insulator-to-metal transition.

6. The use of neutron diffraction with isotope substitution to study the structure of amorphous As_2Se_3 under pressure

6.1 Introduction

As_xSe_{1-x} ($0 \leq x \leq 1$) glasses have extensive technological applications as infra-red transmitting materials, being used in prisms and windows, and as the host matrix for infra-red lasers [5, 9, 12, 13, 145]. Glasses in this system also exhibit photoluminescence and photoconduction, and photo-induced structural changes have also been reported, leading to opto-electronic and opto-mechanical applications [5, 12, 13, 146].

As discussed in chapter 5, mean field theory suggests that amorphous networks can be classified as either *floppy*, where the network is under-constrained, *rigid*, where the network is optimally constrained, or *stressed-rigid*, where the network is over-constrained [147, 148]. Further investigations into glassy networks found that there can exist a so-called intermediate phase (IP) [97, 103, 149–157] between the floppy and stressed-rigid compositional windows, rather than the occurrence of a sharp transition. Within the intermediate phase, the network is rigid but is not under stress, *i.e.* it is ideally constrained or *isostatic*.

It has been proposed that glasses within the intermediate phase are self-organising and exhibit increased structural variability [97]. Self-organisation enables the glass, on formation, to avoid creating over-constrained, stressed regions unless there is no physical alternative. Structural variability refers to the formation of a glass network from a large variety of structural motifs. In the absence of self-organisation and structural variability, there is a single transition from a floppy network to a stressed-rigid one, which occurs when the mean coordination number $\langle n \rangle = 2.4$, *i.e.* there is no intermediate phase.

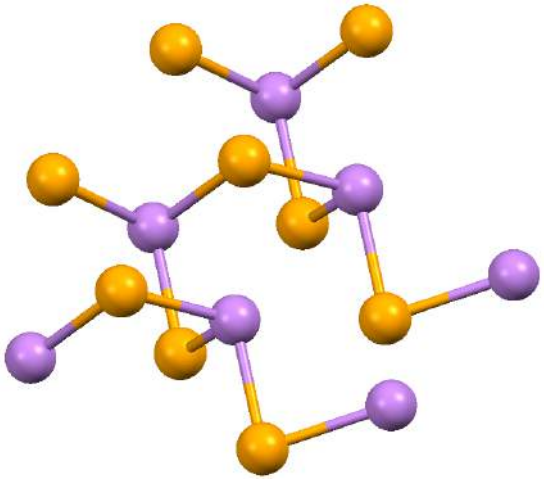

Figure 6-1: Representation of the local connectivity within the ambient conditions crystal structure of As_2Se_3 [169]. Each As atom is surrounded by three Se atoms to form a trigonal pyramid, where the As and Se atoms are shown in purple and yellow, respectively. The image shows an example of corner-sharing $AsSe_3$ trigonal pyramids.

Consider the amorphous As_xSe_{1-x} system, for which the "8-N" rule gives a mean coordination number $\langle n \rangle = 2 + x$. As_2Se_3 lies at the transition between the floppy and stressed-rigid regimes, *i.e.* the mean coordination number for As_2Se_3 from the "8-N" rule is $\langle n \rangle = 2.4$. The intermediate phase for this glass has, however, been found to occur for the composition range $0.29 < x < 0.37$, *i.e.* As_2Se_3 does not lie within the intermediate phase [153]. Additionally, according to the chemically-ordered continuous random network model [2], the As_2Se_3 structure should be formed entirely from heteropolar As-Se bonds. However, recent work [45, 46] has found that there may be homopolar As-As and Se-Se bonds within the glass, which is indicative of chemical disorder.

Amorphous As_xSe_{1-x} materials have been previously studied under extreme conditions [170–179], though the majority of work has focused on the liquid phase at high-temperatures where pressure was applied to prevent evaporation. The atomic structure of amorphous As_xSe_{1-x} materials under high-pressures has yet to be investigated. An investigation of As_2Se_3 under high pressure is of particular interest because the main structural motif is believed to be a pyramidal $AsSe_3$ unit [180–182]. This unit is fundamentally different to the tetrahedra found in other prototypical network-forming glasses, such as $GeSe_2$ and $GeSe_4$, and it is therefore expected that the network collapse of amorphous As_2Se_3 upon compression will differ substantially.

The work presented in this chapter makes use of neutron diffraction to measure the atomic structure of amorphous As_2Se_3 *in situ* at pressures up to 14.4(5) GPa, using a Paris-Edinburgh press mounted on the D4c or PEARL diffractometers. Neutron

diffraction with isotopic substitution (NDIS) is used at pressures up to 8.1(5) GPa and provides access to first-order difference functions where individual partial pair-correlations functions can be removed one at a time.

The chapter is organised as follows. The essential theory for a neutron diffraction experiment is given in section 6.2. The experimental procedure for the work is discussed in section 6.3. The results and the accompanying discussion are presented in sections 6.4 and 6.5, respectively. Finally, conclusions are drawn in section 6.6.

6.2 Theory

In a neutron diffraction experiment the total structure factor

$$F(Q) = \sum_{\alpha=1}^{n}\sum_{\beta=1}^{n} c_\alpha c_\beta b_\alpha b_\beta \left[S^{\mathrm{FZ}}_{\alpha\beta}(Q) - 1\right] \tag{6.1}$$

is measured, where α and β denote the chemical species, c_α is the atomic fraction of chemical species α, b_α is the bound coherent scattering length of chemical species α, $S^{\mathrm{FZ}}_{\alpha\beta}(Q)$ is the Faber-Ziman partial structure factor for chemical species α and β [55], and Q is the magnitude of the scattering vector [52].

Consider an experiment where diffraction patterns are measured for two As_2Se_3 glasses that are identical in every respect, save for their Se isotopic enrichments. Let the glasses be $^{\mathrm{N}}As_2{}^{\mathrm{N}}Se_3$ and $^{\mathrm{N}}As_2{}^{76}Se_3$, where N denotes the natural abundance of an element, and let the measured total structure factors be denoted by ${}^{\mathrm{N}}_{\mathrm{N}}F(Q)$ and ${}^{\mathrm{N}}_{76}F(Q)$, respectively. Here, the superscript denotes the isotopic enrichment of As and the subscript denotes the isotopic enrichment of Se. The total structure factors are given by

$$\begin{aligned} {}^{\mathrm{N}}_{\mathrm{N}}F(Q) = {} & c^2_{\mathrm{As}} b^2_{{}^{\mathrm{N}}\mathrm{As}} \left[S^{\mathrm{FZ}}_{\mathrm{AsAs}}(Q) - 1\right] + c^2_{\mathrm{Se}} b^2_{{}^{\mathrm{N}}\mathrm{Se}} \left[S^{\mathrm{FZ}}_{\mathrm{SeSe}}(Q) - 1\right] + \\ & 2 c_{\mathrm{As}} b_{{}^{\mathrm{N}}\mathrm{As}} c_{\mathrm{Se}} b_{{}^{\mathrm{N}}\mathrm{Se}} \left[S^{\mathrm{FZ}}_{\mathrm{AsSe}}(Q) - 1\right] \end{aligned} \tag{6.2}$$

and

$$\begin{aligned} {}^{\mathrm{N}}_{76}F(Q) = {} & c^2_{\mathrm{As}} b^2_{{}^{\mathrm{N}}\mathrm{As}} \left[S^{\mathrm{FZ}}_{\mathrm{AsAs}}(Q) - 1\right] + c^2_{\mathrm{Se}} b^2_{{}^{76}\mathrm{Se}} \left[S^{\mathrm{FZ}}_{\mathrm{SeSe}}(Q) - 1\right] + \\ & 2 c_{\mathrm{As}} b_{{}^{\mathrm{N}}\mathrm{As}} c_{\mathrm{Se}} b_{{}^{76}\mathrm{Se}} \left[S^{\mathrm{FZ}}_{\mathrm{AsSe}}(Q) - 1\right]. \end{aligned} \tag{6.3}$$

First-order difference functions can be constructed from these total structure fac-

tors, in which a single partial pair-correlation function is removed at a time. The partial structure factor $S^{\mathrm{FZ}}_{\mathrm{AsAs}}(Q)$ can be removed by a direct subtraction of the total structure factors

$$\begin{aligned}\Delta F(Q)_{\text{no As-As}} &= {}^{\mathrm{N}}_{76}F(Q) - {}^{\mathrm{N}}_{\mathrm{N}}F(Q) \\ &= c^2_{\mathrm{Se}}\left(b^2_{^{76}\mathrm{Se}} - b^2_{^{\mathrm{N}}\mathrm{Se}}\right)\left[S^{\mathrm{FZ}}_{\mathrm{SeSe}}(Q) - 1\right] \\ &+ 2c_{\mathrm{As}}c_{\mathrm{Se}}b_{^{\mathrm{N}}\mathrm{As}}\left(b_{^{76}\mathrm{Se}} - b_{^{\mathrm{N}}\mathrm{Se}}\right)\left[S^{\mathrm{FZ}}_{\mathrm{AsSe}}(Q) - 1\right]. \end{aligned} \tag{6.4}$$

The partial structure factor $S^{\mathrm{FZ}}_{\mathrm{SeSe}}(Q)$ can be removed by using the expression

$$\begin{aligned}\Delta F(Q)_{\text{no Se-Se}} &= {}^{\mathrm{N}}_{\mathrm{N}}F(Q) - \frac{b^2_{^{\mathrm{N}}\mathrm{Se}}}{b^2_{^{76}\mathrm{Se}}}{}^{\mathrm{N}}_{76}F(Q) \\ &= c^2_{\mathrm{As}}b^2_{^{\mathrm{N}}\mathrm{As}}\left(1 - \frac{b^2_{^{\mathrm{N}}\mathrm{Se}}}{b^2_{^{76}\mathrm{Se}}}\right)\left[S^{\mathrm{FZ}}_{\mathrm{AsAs}}(Q) - 1\right] \\ &+ 2c_{\mathrm{As}}c_{\mathrm{Se}}b_{^{\mathrm{N}}\mathrm{As}}\left(b_{^{\mathrm{N}}\mathrm{Se}} - \frac{b^2_{^{\mathrm{N}}\mathrm{Se}}}{b_{^{76}\mathrm{Se}}}\right)\left[S^{\mathrm{FZ}}_{\mathrm{AsSe}}(Q) - 1\right], \end{aligned} \tag{6.5}$$

where $b^2_{^{\mathrm{N}}\mathrm{Se}}/b^2_{^{76}\mathrm{Se}} = 0.42733$. Similarly, the partial structure factor $S^{\mathrm{FZ}}_{\mathrm{AsSe}}(Q)$ can be removed by using the expression

$$\begin{aligned}\Delta F(Q)_{\text{no As-Se}} &= \frac{b_{^{\mathrm{N}}\mathrm{Se}}}{b_{^{76}\mathrm{Se}}}{}^{\mathrm{N}}_{76}F(Q) - {}^{\mathrm{N}}_{\mathrm{N}}F(Q) \\ &= c^2_{\mathrm{As}}b^2_{^{\mathrm{N}}\mathrm{As}}\left(\frac{b_{^{\mathrm{N}}\mathrm{Se}}}{b_{^{76}\mathrm{Se}}} - 1\right)\left[S^{\mathrm{FZ}}_{\mathrm{AsAs}}(Q) - 1\right] \\ &+ c^2_{\mathrm{Se}}\left(b_{^{76}\mathrm{Se}}b_{^{\mathrm{N}}\mathrm{Se}} - b^2_{^{\mathrm{N}}\mathrm{Se}}\right)\left[S^{\mathrm{FZ}}_{\mathrm{SeSe}}(Q) - 1\right], \end{aligned} \tag{6.6}$$

where $b_{^{\mathrm{N}}\mathrm{Se}}/b_{^{76}\mathrm{Se}} = 0.6537$. The weighting factors for the partial structure factors in the equations for the total structure factors and first-order difference functions are given in table 6.1.

Real-space information can be obtained via Fourier transformation of the reciprocal space datasets. Hence, the total pair-distribution function ${}^{\gamma}_{\delta}G(r)$ and the first-order difference pair-distribution function $\Delta G(r)_{\mathrm{X}}$ can be obtained where

$${}^{\gamma}_{\delta}G(r) = \frac{1}{2\pi^2 r\rho}\int_0^{\infty} QM(Q){}^{\gamma}_{\delta}F(Q)\sin(Qr)\,\mathrm{d}Q \tag{6.7}$$

	As-As (barn)	Se-Se (barn)	As-Se (barn)
${}^{\mathrm{N}}_{\mathrm{N}}F(Q)$	0.06927(21)	0.2287(5)	0.2517(5)
${}^{\mathrm{N}}_{76}F(Q)$	0.06927(21)	0.536(9)	0.3853(32)
$\Delta F(Q)_{\text{no As-As}}$	0.000	0.307(9)	0.1336(32)
$\Delta F(Q)_{\text{no Se-Se}}$	0.0397(5)	0.000	0.0873(14)
$\Delta F(Q)_{\text{no As-Se}}$	-0.0240(4)	0.1214(29)	0.000

Table 6.1: The weighting factors for the As-As, Se-Se, and As-Se partial structure factors. All numerical values take into account the isotopic enrichment of the samples used in the experiments. The scattering lengths were obtained from Ref. [53] and are: $b_{^{\mathrm{N}}\mathrm{As}} = 6.58(1)$ fm, $b_{^{\mathrm{N}}\mathrm{Se}} = 7.970(9)$ fm, and $b_{^{76}\mathrm{Se}} = 12.2(1)$ fm. The atomic fractions are $c_{\mathrm{As}} = 2/5$ and $c_{\mathrm{Se}} = 3/5$ exactly.

and

$$\Delta G(r)_{\mathrm{X}} = \frac{1}{2\pi^2 r\rho}\int_0^\infty QM(Q)\Delta F(Q)_{\mathrm{X}}\sin(Qr)\,\mathrm{d}Q. \tag{6.8}$$

In these equations, r is a distance in real space, ρ is the number density of the glass, γ and δ are the isotopic enrichments of As and Se, respectively, X = "no As-As", "no Se-Se", or "no As-Se" indicates the pair-correlation function that has been removed, and $M(Q)$ is a modification function

$$M(Q) = \begin{cases} 1 & \text{if } Q \le Q_{\max} \\ 0 & \text{if } Q > Q_{\max}, \end{cases} \tag{6.9}$$

which is introduced because a diffractometer can measure over only a finite Q range up to a maximum value $Q_{\max}$. Fourier transformation artefacts can arise from the finite $Q_{\max}$ value and can be reduced through the use of a Lorch modification function [56]

$$M(Q) = \begin{cases} \frac{\sin(aQ)}{aQ} & \text{if } Q \le Q_{\max} \\ 0 & \text{if } Q > Q_{\max}, \end{cases} \tag{6.10}$$

where $a = \pi/Q_{\max}$, at the expense of broadened r-space features. The low-r limits for the total and first-order difference pair-distribution functions, denoted by ${}^{\gamma}_{\delta}G(r \to 0)$ and $\Delta G(r \to 0)_{\mathrm{X}}$, respectively, are given in table 6.2

The coordination number of a system, $\overline{n}^{\beta}_{\alpha}$, gives the mean number of atoms of chemical species β contained in a volume defined by two concentric spheres of radii r_1 and r_2 centred on an atom of chemical species α and is defined by equation (2.16). For some samples, such as those belonging to the Ge–Se system, the similarity of the coherent

	Low-r limit (barn)
${}^{\mathrm{N}}_{\mathrm{N}}G(r \to 0)$	-0.5497(10)
${}^{\mathrm{N}}_{76}G(r \to 0)$	-0.990(12)
$\Delta G(r \to 0)_{\mathrm{noAs-As}}$	-0.441(12)
$\Delta G(r \to 0)_{\mathrm{noSe-Se}}$	-0.1270(19)
$\Delta G(r \to 0)_{\mathrm{noAs-Se}}$	-0.0973(25)

Table 6.2: Theoretical low-r limits ${}^{\gamma}_{\delta}G(r \to 0)$ and $\Delta G(r \to 0)_{\mathrm{X}}$, where γ and δ are the isotopic enrichments of As and Se, respectively, and X = "no As-As", "no Se-Se", or "no As-Se".

scattering lengths, b_α, for the constituent elements means that an approximation can be readily made to calculate the mean coordination number $\overline{n}$, as discussed in chapters 4 and 5. In the case of As_2Se_3, the coherent scattering lengths for As and Se are not as similar. Nevertheless, it is valuable to calculate an effective coordination number to look at the relative change in the coordination environments during compression. This effective coordination number is defined by

$$
\begin{aligned}
\overline{n}' &= \frac{4\pi\rho}{\left|{}^{\gamma}_{\delta}G(0)\right|}\int_{r_1}^{r_2} r^2\left[{}^{\gamma}_{\delta}G(r) - {}^{\gamma}_{\delta}G(0)\right]\mathrm{d}r \\
&= \frac{4\pi\rho}{\left|{}^{\gamma}_{\delta}G(0)\right|}\int_{r_1}^{r_2} r^2\left[c^2_{\mathrm{As}}b^2_{{}^{\mathrm{N}}\mathrm{As}}g^{\mathrm{FZ}}_{\mathrm{AsAs}}(r) + c^2_{\mathrm{Se}}b^2_{\mathrm{Se}}g^{\mathrm{FZ}}_{\mathrm{SeSe}}(r) + 2c_{\mathrm{As}}c_{\mathrm{Se}}b_{{}^{\mathrm{N}}\mathrm{As}}b_{\mathrm{Se}}g^{\mathrm{FZ}}_{\mathrm{AsSe}}(r)\right]\mathrm{d}r \\
&= \frac{c_{\mathrm{As}}b^2_{{}^{\mathrm{N}}\mathrm{As}}}{\left|{}^{\gamma}_{\delta}G(0)\right|}4\pi\rho c_{\mathrm{As}}\int_{r_1}^{r_2} r^2 g^{\mathrm{FZ}}_{\mathrm{AsAs}}(r)\,\mathrm{d}r + \frac{c_{\mathrm{Se}}b^2_{\mathrm{Se}}}{\left|{}^{\gamma}_{\delta}G(0)\right|}4\pi\rho c_{\mathrm{Se}}\int_{r_1}^{r_2} r^2 g^{\mathrm{FZ}}_{\mathrm{SeSe}}(r)\,\mathrm{d}r \\
&\quad + \frac{2c_{\mathrm{As}}b_{{}^{\mathrm{N}}\mathrm{As}}b_{\mathrm{Se}}}{\left|{}^{\gamma}_{\delta}G(0)\right|}4\pi\rho c_{\mathrm{Se}}\int_{r_1}^{r_2} r^2 g^{\mathrm{FZ}}_{\mathrm{AsSe}}(r)\,\mathrm{d}r \\
&= \frac{c_{\mathrm{As}}b^2_{{}^{\mathrm{N}}\mathrm{As}}}{\left|{}^{\gamma}_{\delta}G(0)\right|}\overline{n}^{\mathrm{As}}_{\mathrm{As}} + \frac{c_{\mathrm{Se}}b^2_{\mathrm{Se}}}{\left|{}^{\gamma}_{\delta}G(0)\right|}\overline{n}^{\mathrm{Se}}_{\mathrm{Se}} + \frac{2c_{\mathrm{As}}b_{{}^{\mathrm{N}}\mathrm{As}}b_{\mathrm{Se}}}{\left|{}^{\gamma}_{\delta}G(0)\right|}\overline{n}^{\mathrm{Se}}_{\mathrm{As}}.
\end{aligned}
\tag{6.11}
$$

Similarly, an effective mean coordination number can be calculated for each first-order difference function using

$$
\overline{n}'_{\mathrm{X}} = \frac{4\pi\rho}{\left|\Delta G(0)_{\mathrm{X}}\right|}\int_{r_1}^{r_2} r^2\left[\Delta G(r)_{\mathrm{X}} - \Delta G(0)_{\mathrm{X}}\right]\mathrm{d}r. \tag{6.12}
$$

This mean coordination number can also be broken down into contributions from the

individual partial coordination numbers. For example, if X = "no As-As", then

$$\begin{aligned}
\overline{n}'_{\text{no As-As}} &= \frac{4\pi\rho}{\left|\Delta G(0)_{\text{no As-As}}\right|}\int_{r_1}^{r_2} r^2\left[\Delta G(r)_{\text{no As-As}} - \Delta G(0)_{\text{no As-As}}\right]\mathrm{d}r \\
&= \frac{4\pi\rho}{\left|\Delta G(0)_{\text{no As-As}}\right|}\int_{r_1}^{r_2} r^2\left[c_{\text{Se}}^2\left(b_{^{76}\text{Se}}^2 - b_{^{\text{N}}\text{Se}}^2\right) g_{\text{SeSe}}^{\text{FZ}}(r)\right. \\
&\quad \left. + 2c_{\text{As}}c_{\text{Se}}b_{^{\text{N}}\text{As}}\left(b_{^{76}\text{Se}} - b_{^{\text{N}}\text{Se}}\right) g_{\text{AsSe}}^{\text{FZ}}(r)\right]\mathrm{d}r \\
&= \frac{c_{\text{Se}}\left(b_{^{76}\text{Se}}^2 - b_{^{\text{N}}\text{Se}}^2\right)}{\left|\Delta G(0)_{\text{no As-As}}\right|} 4\pi c_{\text{Se}}\rho\int_{r_1}^{r_2} r^2 g_{\text{SeSe}}^{\text{FZ}}(r)\,\mathrm{d}r \\
&\quad + \frac{2c_{\text{As}}b_{^{\text{N}}\text{As}}\left(b_{^{76}\text{Se}} - b_{^{\text{N}}\text{Se}}\right)}{\left|\Delta G(0)_{\text{no As-As}}\right|} 4\pi c_{\text{Se}}\rho\int_{r_1}^{r_2} r^2 g_{\text{AsSe}}^{\text{FZ}}(r)\,\mathrm{d}r \\
&= \frac{c_{\text{Se}}\left(b_{^{76}\text{Se}}^2 - b_{^{\text{N}}\text{Se}}^2\right)}{\left|\Delta G(0)_{\text{no As-As}}\right|}\overline{n}_{\text{Se}}^{\text{Se}} + \frac{2c_{\text{As}}b_{^{\text{N}}\text{As}}\left(b_{^{76}\text{Se}} - b_{^{\text{N}}\text{Se}}\right)}{\left|\Delta G(0)_{\text{no As-As}}\right|}\overline{n}_{\text{As}}^{\text{Se}}.
\end{aligned} \tag{6.13}$$

There are two extreme models for describing the chemical ordering in $\text{As}_x\text{Se}_{1-x}$ glasses, the random covalent network (RCN) model and the chemically ordered continuous random network (COCRN) model. Both models assume that the so-called "8-N" rule holds [59]. The RCN model assumes that the distribution of bonds is purely statistical [2], such that the coordination numbers for As_2Se_3 are given by

$$\begin{aligned}
\overline{n}_{\text{As}}^{\text{As}} &= \frac{9c_{\text{As}}}{2 + c_{\text{As}}} = 1.5, \\
\overline{n}_{\text{Se}}^{\text{Se}} &= 4\frac{1 - c_{\text{As}}}{2 + c_{\text{As}}} = 1,
\end{aligned}$$

and,

$$\overline{n}_{\text{As}}^{\text{Se}} = 6\frac{1 - c_{\text{As}}}{2 + c_{\text{As}}} = 1.5. \tag{6.14}$$

The COCRN model assumes that heteropolar As-Se bonds are preferred, allowing homopolar As-As and Se-Se bonds to form only when the composition is As or Se rich, respectively [2]. As_2Se_3 is the stoichiometic composition on the boundary between the As and Se rich compositions, and so the COCRN model gives the coordination numbers [59]

$$\overline{n}^{\mathrm{As}}_{\mathrm{As}} = 0,$$
$$\overline{n}^{\mathrm{Se}}_{\mathrm{Se}} = 0,$$

and,

$$\overline{n}^{\mathrm{Se}}_{\mathrm{As}} = 3 \tag{6.15}$$

6.3 Experimental method

Two neutron diffraction experiments were undertaken to study the structure of As_2Se_3 under pressure. One experiment was performed on the D4c diffractometer utilising a VX5 PE press in an in-plane scattering geometry with single toroid cubic boron nitride anvils to make measurements up to $P = 8.1(5)$ GPa. The other experiment was performed on the PEARL HiPr diffractometer utilising a V3 PE press in a transverse scattering geometry with double toroid sintered diamond anvils to make measurements up to $P = 14.4(5)$ GPa. The D4c experiment used the method of neutron diffraction with isotopic substitution to allow additional structural information to be obtained through the formation of first-order difference functions. The preparation of the As_2Se_3 samples is discussed in section 6.3.1, the experimental procedures for the D4c and PEARL experiments are discussed in sections 6.3.2 and 6.3.3, respectively, and the pressure-volume equation of state for As_2Se_3 is discussed in section 6.3.4.

6.3.1 Sample preparation

Amorphous $^{\mathrm{N}}As_2{}^{\mathrm{N}}Se_3$ and $^{\mathrm{N}}As_2{}^{76}Se_3$ samples were prepared by loading elemental $^{\mathrm{N}}$As (99.9998%, Sigma-Aldrich) and $^{\mathrm{N}}$Se (99.999%, Sigma-Aldrich) or ^{76}Se (99.8% ^{76}Se, 0.2% ^{77}Se, Isoflex USA) into a silica ampoule. To avoid contamination this loading took place inside an inert Ar-filled glovebox. The ampoule was evacuated and sealed and was then heated in a rocking furnace from ambient temperature to 685 °C at 2 °C min^{-1}. Equilibrium periods at $T = 221$ °C (melting point of Se) and 614 °C (melting point of As) were maintained during heating where the temperature was kept constant for 4 h. The temperature was kept constant at 685 °C for 48 h, before being cooled at 1 °C min^{-1} to the quench temperature $T = 400$ °C. After a 5 h equilibration period the ampoule was dropped into an ice/salt-water mixture.

For the D4c experiment, the sample was removed from the ampoule in an inert Ar-filled glovebox and kept in powder form. It was then ground and sufficient mass to make a "perfect" pellet was loaded into a specially designed hardened steel die

which replicates the shape of a single toroid sample. The powder was then slowly compressed while allowing for periodic relaxation periods when the applied pressure was kept constant. The height of the die was measured before filling with powder and then during compression in a bid to measure the height of the powder inside. Once fully compressed the die was then transported to the PE press and the powdered pellet placed in the gasket assembly, taking care to ensure that no powder was deposited between the anvils and the gaskets.

For the PEARL experiment, a pellet was produced from a single piece of $^{\mathrm{N}}As_2{}^{\mathrm{N}}Se_3$ glass. Before attempting to remove pieces of glass from the ampoule it was annealed at 130 °C to reduce any tension and aid in the production of a solid pellet piece. This annealing temperature is below the glass transition temperature $T_g = 191.62(90)$ °C. T_g was measured using modulated differential scanning calorimetry (MDSC) with a ramp rate of $3\,^{\circ}\mathrm{C\,min^{-1}}$ and a modulation rate $1\,^{\circ}\mathrm{C\,min^{-1}}$. The average of the up-ramp and down-ramp for three distinct samples was measured to give a final T_g value. A diamond-wire saw was used to cut across the ampoule so that cylindrical pieces of As_2Se_3 glass could be removed. As_2Se_3 pellets were then produced from the cylindrical pieces by gently grinding them to the correct shape for a double toroid anvil.

6.3.2 D4c neutron diffraction experiment

A neutron diffraction experiment was performed to study amorphous $^{\mathrm{N}}As_2{}^{\mathrm{N}}Se_3$ and $^{\mathrm{N}}As_2{}^{76}Se_3$ at ambient temperature ($T \sim 300$ K) and at pressures up to $P = 8.1(5)$ GPa. A VX5 Paris-Edinburgh press was mounted in an in-plane scattering geometry on the D4c diffractometer with single toroid cubic boron nitride anvils providing compression.

Sample	Pellet mass (g)	$Ti_{0.676}Zr_{0.324}$ gasket mass (g)
$^{\mathrm{N}}As_2{}^{\mathrm{N}}Se_3$	0.42116(1)	1.4138(1)
$^{\mathrm{N}}As_2{}^{76}Se_3$	0.41340(1)	1.4132(1)

Table 6.3: Sample and $Ti_{0.676}Zr_{0.324}$ gasket masses for the D4c As_2Se_3 experiment.

The mass of ideal single toroid $^{\mathrm{N}}As_2{}^{\mathrm{N}}Se_3$ and $^{\mathrm{N}}As_2{}^{76}Se_3$ pellets is 0.422 51 g and 0.412 55 g, respectively. Pellets were created as outlined in section 6.3.1, and their masses are given in table 6.3.

Two pieces of vanadium were machined to match the geometry of the caps of a pair of single toroid anvils, and two cylinders were also machined to be placed between these caps to form a pellet. The cylinders were made with different heights, meaning that the overall height of the vanadium "pellet" could be adjusted to correspond to different anvil spacings at different pressures.

The D4c diffraction experiment was performed as outlined in section 3.6.5. A measurement of Ni powder in an encapsulated $Ti_{0.676}Zr_{0.324}$ gasket was made to quantify the incident neutron wavelength and the zero-angle correction for the detectors. These parameters were found to be $\lambda = 0.4985\,\text{Å}$ and $2\theta_{\text{zero}} = 0.060°$, respectively.

Neutron diffraction measurements were made for the sample at the pressure points given in table 6.4. Three vanadium measurements were made, two of them using cylinders machined to form a "pellet" with spherical caps at either end, and the third using just the machined spherical caps. Three measurements of empty $Ti_{0.676}Zr_{0.324}$ gaskets were made: an uncompressed gasket, a gasket that had been recovered from 4.7(5) GPa, and a gasket that had been recovered from 8.1(5) GPa. The empty anvils were also measured with the gap between the anvils set at 0.4 mm. During the course of a pressure point measurement, the ratio was taken of the measured intensities for different periods of time. If this ratio deviates from unity then the scattered intensity is changing with time. No such deviation was observed during the course of the measurements.

An ambient-pressure diffraction experiment was also performed on D4c using a vanadium can to contain the sample [183]. Three samples with different Se isotopic enrichments were measured, $^{\text{N}}As_2{}^{\text{N}}Se_3$, $^{\text{N}}As_2{}^{76}Se_3$, and $^{\text{N}}As_2{}^{\text{Mix}}Se_3$, where $^{\text{Mix}}$Se denotes a Se composition that is 50% $^{\text{N}}$Se and 50% ^{76}Se. The full set of partial structure factors $S^{\text{FZ}}_{\alpha\beta}(Q)$ were then calculated using matrix inversion, as discussed in section 2.4 [183].

Applied load L (tonnes)	Pressure P (GPa)
6.8	Ambient
30.5	3.0(5)
40.7	3.9(5)
50.9	4.7(5)
61.0	5.5(5)
71.2	6.3(5)
81.4	7.0(5)
94.9	8.1(5)

Table 6.4: Pressure points measured during the D4c experiment. The pressure at the sample position P was deduced from the calibration curve given in figure 3-17.

6.3.3 PEARL neutron diffraction experiment

A neutron diffraction experiment was performed to study amorphous $^{\text{N}}As_2{}^{\text{N}}Se_3$ at ambient temperature ($T \sim 300\,\text{K}$) and at pressures up to $P = 14.4(5)\,\text{GPa}$. A V3 Paris-Edinburgh press was mounted in a transverse scattering geometry on the PEARL

HiPr diffractometer with double toroid sintered diamond anvils providing compression.

Sample	Pellet mass (g)	$Ti_{0.676}Zr_{0.324}$ gasket mass (g)
$^{N}As_2{}^{N}Se_3$	0.14955(1)	1.0560(1)
Vanadium	0.2047(1)	1.0506(1)

Table 6.5: Pellet and $Ti_{0.676}Zr_{0.324}$ gasket masses for the PEARL $^{N}Ge^{N}Se_4$ experiment.

The mass of an ideal double toroid $^{N}As_2{}^{N}Se_3$ pellet is 0.153 26 g. A solid $^{N}As_2{}^{N}Se_3$ pellet was created as outlined in section 6.3.1. A vanadium pellet was produced by taking vanadium foil and placing the correct mass in a specially prepared die which re-creates the shape of a double toroid pellet. This was then compressed as outlined in section 3.6.1. The masses of the $^{N}As_2{}^{N}Se_3$ and vanadium pellets are given in table 6.5.

Applied load L (tonnes)	Pressure P (GPa)	$^{N}Ge^{N}Se_4$	Vanadium
2	Ambient	✓	✓
75	8.7(5)	✓	✓
98	10.9(5)	✓	✓
120	14.4(5)	✓	✓

Table 6.6: Pressure points measured during the PEARL experiment. The pressure at the sample position P was deduced from the calibration curve given in figure 3-15.

The PEARL diffraction experiment was performed as outlined in section 3.6.4. Measurements were made for two empty $Ti_{0.676}Zr_{0.324}$ gaskets with their masses given in table 6.5. Neutron diffraction measurements were made for the vanadium and the sample in turn, and the investigated pressure points are given in table 6.6. During the course of a pressure point measurement, the ratio was taken of the measured intensities for different periods of time. If this ratio deviates from unity then the scattered intensity is changing with time. No such deviation was observed during the course of the measurements.

The compression was controlled by an automated machine up to an applied load $L = 95$ tonnes, after which a hand pump was used to manually increase the pressure. The automated system kept the pressure constant, *i.e.* if some relaxation occurred that caused the pressure to drop the automated system would increase it back to the set point. When using the hand pump this was not possible, and any relaxation (typically $\sim$ 10–20 bar) was allowed to occur. Whilst increasing and decreasing pressure, periodic pauses were taken to allow the system to equilibrate.

6.3.4 Equation of state and density measurements

The mass density $\rho_m = 4.548(8)\,\mathrm{g\,cm^{-3}}$ of amorphous $^{N}As_2{}^{N}Se_3$ was measured under ambient conditions using a helium pycnometer. This yielded an ambient-pressure number density $\rho_0 = 0.0354(1)\,\mathrm{Å^{-3}}$.

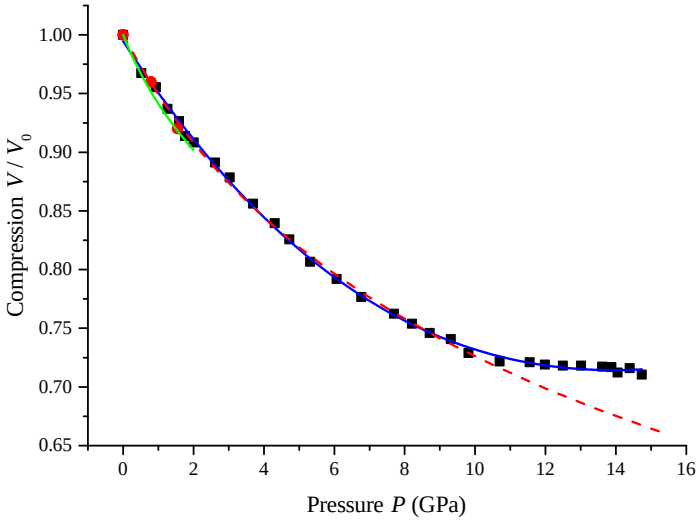

Figure 6-2: The pressure-volume equation of state for As_2Se_3 [184]. Also included are FPMD results from Ref. [47] (●). A cubic polynomial was fitted to the experimental data points (solid blue curve). Experimental values for As_2S_3 [185] (green curve) up to 2 GPa are plotted for comparison. A third-order Birch-Murnaghan equation of state has been fitted to data from Ref. [184] below 10 GPa (dashed red curve) with parameters $B_0 = 17.35(42)$ GPa and $B_0' = 3.71(16)$.

The pressure-volume equation of state for amorphous As_2Se_3 is shown in figure 6-2 [184]. A cubic polynomial was fitted to the experimental results to allow for an interpolation to calculate the number density for use in the data analysis procedure. By using the ambient number density ρ_0 and the compression V/V_0, the number density and reduced density for the measured pressure points can be calculated and are shown in table 6.7. The equation of state is also compared to that measured for As_2S_3 at pressures up to 2 GPa and shows good agreement.

Typically for high pressure experiments, a Birch-Murnaghan equation of state can be used to define the relationship between pressure and volume. At high pressures, the measured equation of state for amorphous As_2Se_3 flattens out significantly and is not reproducible using either a second- or third-order Birch-Murnaghan equation of state. In figure 6-2, a third-order Birch-Murnaghan equation of state has been fitted up to 10 GPa and is extrapolated to higher pressures. The fitted parameters are

$B_0 = 17.35(42)$ GPa and $B_0' = 3.71(16)$. This fitted bulk modulus can be compared to measured values of $B_0 = 14.37$ GPa [23] and 13.2 GPa [186].

Pressure P (GPa)	Number density ρ (Å^{-3})	Compression V/V_0	Reduced density ρ/ρ_0
Ambient$^{\dagger *}$	0.0354(1)	1	1
3.0(5)†	0.0404(8)	0.876(18)	1.141(23)
3.9(5)†	0.0418(7)	0.847(14)	1.181(20)
4.7(5)†	0.0429(7)	0.825(14)	1.212(20)
5.5(5)†	0.0440(6)	0.805(11)	1.243(17)
6.3(5)†	0.0450(6)	0.787(11)	1.271(17)
7.0(5)†	0.0458(5)	0.773(9)	1.294(15)
8.1(5)†	0.0469(4)	0.755(7)	1.325(12)
8.7(5)*	0.0474(4)	0.747(7)	1.339(12)
10.9(5)*	0.0489(4)	0.724(6)	1.381(12)
14.4(5)*	0.0495(3)	0.715(5)	1.398(9)

Table 6.7: Compression V/V_0, number density ρ, and reduced density ρ/ρ_0 for each of the pressure points measured in the neutron diffraction experiments. The symbols $\dagger$ and $*$ denote experiments performed using the D4c and PEARL diffractometers, respectively.

6.4 Results

6.4.1 Total structure factors

Figures 6-3 and 6-4 show the pressure dependence of the measured total structure factors $F(Q)$ for amorphous $^{\mathrm{N}}As_2{}^{\mathrm{N}}Se_3$ and $^{\mathrm{N}}As_2{}^{76}Se_3$, respectively. The figures compare neutron diffraction results for (i) an ambient-pressure vanadium can measurement on D4c [183], (ii) high-pressure measurements up to 8.1(5) GPa on D4c, and (iii) high-pressure measurements from 8.7 to 14.4(5) GPa on PEARL ($^{\mathrm{N}}As_2{}^{\mathrm{N}}Se_3$ only). The D4c ambient-pressure measurement has a cutoff $Q_{\max} = 23.5$ Å^{-1}, the D4c high-pressure measurements have a cutoff $Q_{\max} = 21.5$ Å^{-1}, and the PEARL measurements have a cutoff $Q_{\max} = 19.55$ Å^{-1}.

The ambient-pressure data sets measured using the high-pressure D4c and PEARL set-ups (not shown) are in good agreement with the vanadium can results [183]. As the pressure is increased, the most significant change to the total structure factor is in the position and height of the first two peaks at low-Q, namely the first sharp diffraction peak (FSDP) and the principal peak (PP). The positions of the FSDP and PP are

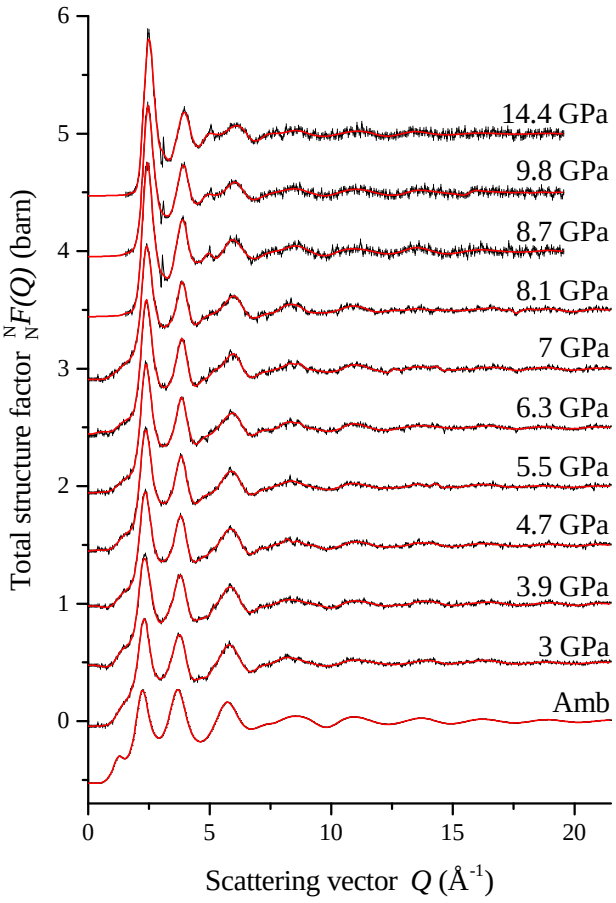

Figure 6-3: The pressure dependence of the total structure factor $^{N}_{N}F(Q)$ for amorphous $^{N}As_2{}^{N}Se_3$. The solid red curves show spline fits to the experimental data (points with vertical error bars) measured using the D4c diffractometer at pressures ranging from ambient pressure to 8.1(5) GPa, and using the PEARL diffractometer at pressures of 8.7, 9.8, and 14.4(5) GPa. The high-pressure curves have been offset vertically for clarity of presentation.

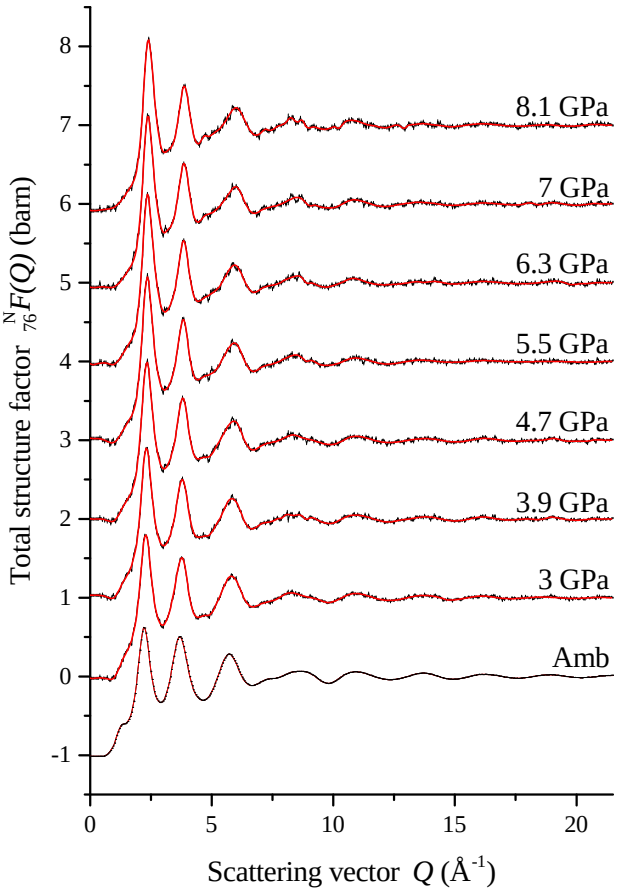

Figure 6-4: The pressure dependence of the total structure factor $^{\mathrm{N}}_{76}F(Q)$ for amorphous $^{\mathrm{N}}\mathrm{As}_2{}^{76}\mathrm{Se}_3$. The solid red curves show spline fits to the experimental data (points with vertical error bars) measured using the D4c diffractometer at pressures ranging from ambient pressure to 8.1(5) GPa. The high-pressure curves have been offset vertically for clarity of presentation.

shown in tables 6.8 and 6.9 for $^{\mathrm{N}}As_2{}^{\mathrm{N}}Se_3$ and $^{\mathrm{N}}As_2{}^{76}Se_3$, respectively. As the pressure is increased, the FSDP at $\sim 1.3\,\text{Å}^{-1}$ shifts to higher Q values and reduces in intensity, until at 6.3(5) GPa it is difficult to discern from the PP. As the pressure is increased, the PP shifts to higher Q values and there is an accompanying increase in both its height and sharpness.

Origin	Pressure (GPa)	FSDP position (Å^{-1})	PP position (Å^{-1})
D4c VC	Ambient	1.30(3)	2.24(3)
D4c	3.0(5) GPa		2.30(3)
	3.9(5) GPa		2.32(3)
	4.7(5) GPa		2.35(3)
	5.5(5) GPa		2.37(3)
	6.3(5) GPa		2.39(3)
	7.0(5) GPa		2.39(3)
	8.1(5) GPa		2.41(3)
PEARL	8.7(5) GPa		2.44(3)
	9.8(5) GPa		2.46(3)
	14.4(5) GPa		2.50(3)

Table 6.8: Peak positions in the ${}^{\mathrm{N}}_{\mathrm{N}}F(Q)$ functions measured for amorphous $^{\mathrm{N}}As_2{}^{\mathrm{N}}Se_3$. "D4c VC" denotes an experiment made at ambient pressure on D4c using a vanadium can [183]. Although the FSDP is distinct from the PP for pressures up to 6.3(5) GPa, it is a broad feature, which makes it difficult to assign a precise value for its position.

Figures 6-5 and 6-6 show the pressure dependence of the measured total pair-distribution function $G(r)$ for $^{\mathrm{N}}As_2{}^{\mathrm{N}}Se_3$ and $^{\mathrm{N}}As_2{}^{76}Se_3$, respectively. The reciprocal space data sets were Fourier transformed using (i) a step modification function (equation (6.9)) and (ii) a Lorch modification function (equation (6.10)) [56]. The data obtained from the first procedure were joined smoothly to the data obtained from the second procedure at a point just beyond the first peak in real space. As the sample is compressed, the nearest-neighbour distance $\overline{r}_1$ decreases in both height and sharpness, whilst the second nearest-neighbour distance $\overline{r}_2$ shifts to lower-r values and begins to develop a shoulder on its low-r side as the region between the first two peaks fills in.

Figures 6-7(a) and 6-7(b) show the effective mean coordination number $\overline{n}'$ for amorphous $^{\mathrm{N}}As_2{}^{\mathrm{N}}Se_3$ and $^{\mathrm{N}}As_2{}^{76}Se_3$, respectively, as calculated by using equation (6.11). At ambient pressure, the results from the the present work are compared with those obtained from (i) a combination of anomalous x-ray scattering and reverse Monte Carlo simulation [45] and (ii) FPMD simulations [45–47].

Figures 6-8(a) and 6-8(b) show the pressure dependence of the nearest-neighbour

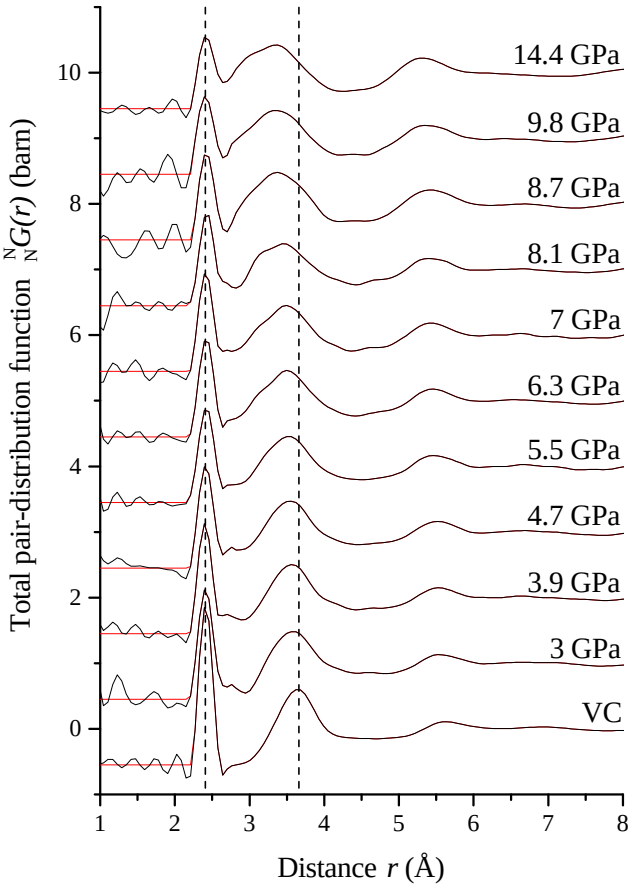

Figure 6-5: The pressure dependence of the total pair-distribution function $^{\mathrm{N}}_{\mathrm{N}}G(r)$ for amorphous $^{\mathrm{N}}\mathrm{As}_2{}^{\mathrm{N}}\mathrm{Se}_3$. The solid black curves show the Fourier transforms of the spline fits given in figure 6-3. The horizontal red curves show the calculated $^{N}_{N}G(r \to 0)$ limits at distances below the closest approach between two atoms. The vertical dashed black curves show the ambient-pressure values for $\overline{r}_1$ and $\overline{r}_2$. The high-pressure curves have been offset vertically for clarity of presentation.

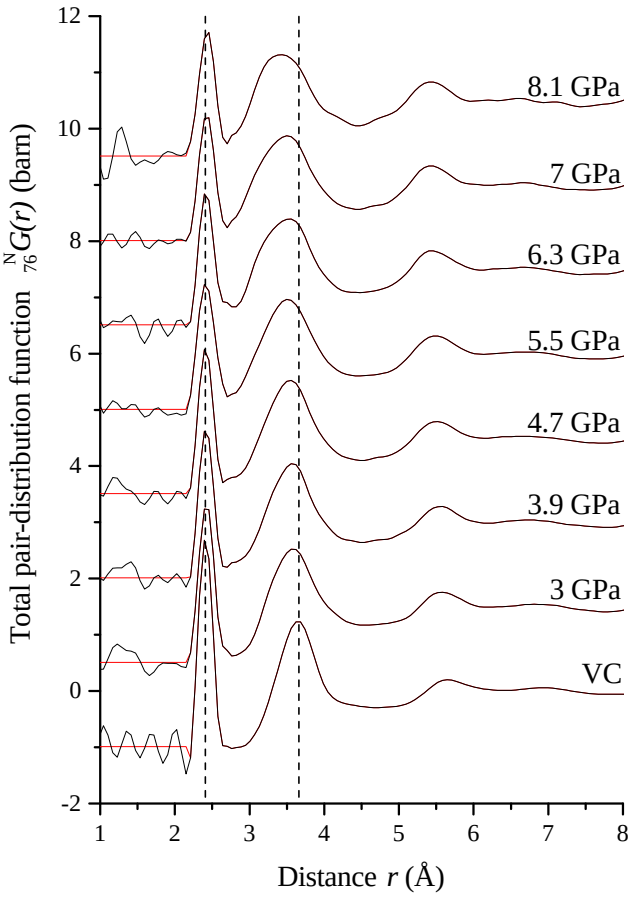

Figure 6-6: The pressure dependence of the total pair-distribution function $^{\mathrm{N}}_{76}G(r)$ for amorphous $^{\mathrm{N}}\mathrm{As}_2{}^{76}\mathrm{Se}_3$. The solid black curves show the Fourier transforms of the spline fits given in figure 6-4. The horizontal red curves show the calculated $^{N}_{76}G(r \to 0)$ limits at distances below the closest approach between two atoms. The high-pressure curves have been offset vertically for clarity of presentation.

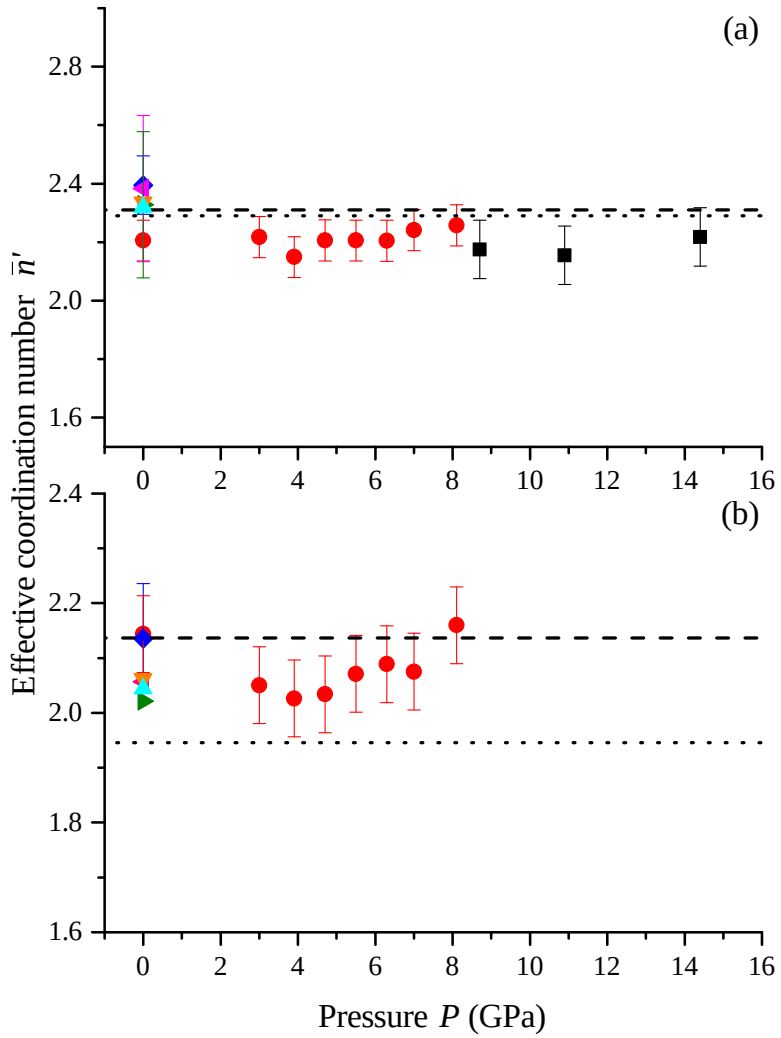

Figure 6-7: The pressure dependence of the effective mean coordination number $\overline{n}'$ for amorphous (a) $^{N}As_2{}^{N}Se_3$ and (b) $^{N}As_2{}^{76}Se_3$. Included are the results from the D4c ambient-pressure vanadium can experiment (◆) [183], the D4c pressure experiment (●), and the PEARL pressure experiment (■). At ambient pressure, results are also shown from an anomalous x-ray scattering with reverse Monte Carlo analysis (◀) and from FPMD (▶) simulations [45]. The FPMD results reported in Ref. [46] (▼) and Ref. [47] (▲) are also included. The effective mean coordination numbers calculated on the basis of the "8-N" rule are also shown for a chemically-ordered continuous random network model (dotted line) and for a random covalent network model (dashed line).

Origin	Pressure (GPa)	FSDP position (Å^{-1})	PP position (Å^{-1})
D4c VC	Ambient	1.39(3)	2.22(3)
D4c	3.0(5) GPa		2.29(3)
	3.9(5) GPa		2.31(3)
	4.7(5) GPa		2.33(3)
	5.5(5) GPa		2.35(3)
	6.3(5) GPa		2.36(3)
	7.0(5) GPa		2.38(3)
	8.1(5) GPa		2.39(3)

Table 6.9: Peak positions in the ${}^{\mathrm{N}}_{76}F(Q)$ functions measured for amorphous ${}^{\mathrm{N}}\mathrm{As}_2{}^{76}\mathrm{Se}_3$. "D4c VC" denotes an experiment made at ambient pressure on D4c using a vanadium can [183]. Although the FSDP is distinct from the PP for pressures up to 6.3(5) GPa, it is a broad feature, which makes it difficult to assign a precise value for its position.

bond distance $\overline{r}_1$ for ${}^{\mathrm{N}}\mathrm{As}_2{}^{\mathrm{N}}\mathrm{Se}_3$ and ${}^{\mathrm{N}}\mathrm{As}_2{}^{76}\mathrm{Se}_3$, respectively. The results of the present work are compared with FPMD results from Refs. [46, 47]. The mean bond distance does not change within the experimental error over the measured pressure range.

Figures 6-7 and 6-8 indicate that the average nearest-neighbour coordination environment is relatively stable up to 14.4(5) GPa. They also show that the $\overline{n}'$ values generally do not agree with those expected from either a chemically-ordered continuous random network (COCRN) or a random covalent network (RCN) model.

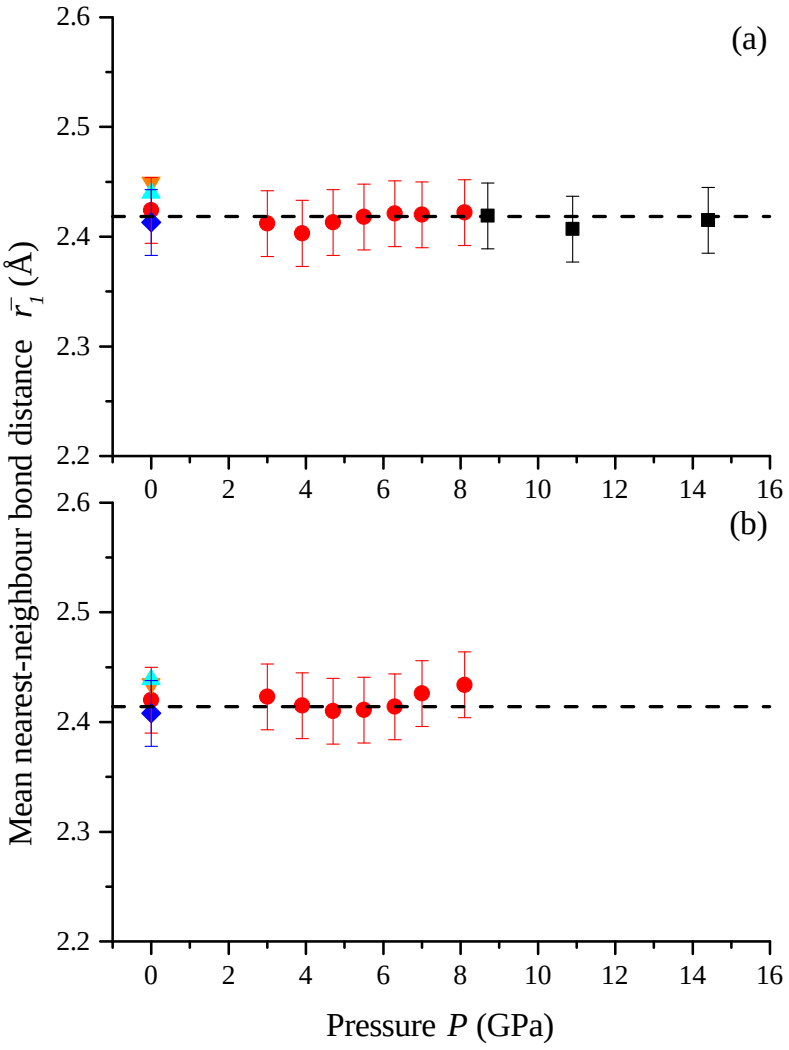

Figure 6-8: The pressure dependence of the mean nearest-neighbour bond distance $\overline{r}_1$ for amorphous (a) $^{\mathrm{N}}As_2{}^{\mathrm{N}}Se_3$ and (b) $^{\mathrm{N}}As_2{}^{76}Se_3$. Included are the results from the D4c ambient-pressure vanadium can experiment (♦) [183], the D4c pressure experiment (●), and the PEARL pressure experiment (■). At ambient conditions, the FPMD results reported in Ref. [46] (▼) and Ref. [47] (▲) are also presented. The black dashed horizontal curves are equal to the average value of $\overline{r}_1$ for the ambient-pressure neutron diffraction measurements, and correspond to (a) 2.418 Å and (b) 2.414 Å.

6.4.2 Difference functions

Total structure factors and their corresponding total pair-distribution functions can be used to glean a moderate amount of information on the pressure dependent structure of amorphous As_2Se_3. However, when there is the possibility of homopolar bonds with comparable distances to those found for heteropolar bonds, as is the case for As_2Se_3, it is difficult to extract chemically-specific information. By using the method of neutron diffraction with isotope substitution, however, further information can be gained from the experimental results by calculating first-order difference functions $\Delta F(Q)_{\mathrm{X}}$, and their corresponding first-order difference pair-distribution functions $\Delta G(r)_{\mathrm{X}}$.

Figures 6-9, 6-10, and 6-11 show the pressure dependence of the first-order difference functions $\Delta F(Q)_{\text{no As-As}}$, $\Delta F(Q)_{\text{no Se-Se}}$, and $\Delta F(Q)_{\text{no As-Se}}$, respectively, for amorphous As_2Se_3. The measurement made at ambient pressure, using a vanadium can on D4c, has a cutoff $Q_{\max} = 23.5\,\text{Å}^{-1}$, while the high-pressure measurements, also made on D4c, have a cutoff $Q_{\max} = 21.5\,\text{Å}^{-1}$.

The FSDP and PP positions for the $\Delta F(Q)_{\mathrm{X}}$ functions are shown in table 6.10. The statistical noise on the $\Delta F(Q)_{\text{no Se-Se}}$ and $\Delta F(Q)_{\text{no As-Se}}$ functions is larger than for the $\Delta F(Q)_{\text{no As-As}}$ function, which is attributed to the relative weighting factors, that are given in table 6.1. As the pressure is increased, the $\Delta F(Q)_{\text{no As-As}}$ and $\Delta F(Q)_{\text{no As-Se}}$ functions show a PP that increases in both height and sharpness as its position moves to higher Q values. The $\Delta F(Q)_{\text{no Se-Se}}$ function has a PP position that changes little across the pressure range, but both the height and sharpness of this feature increase with pressure. $\Delta F(Q)_{\text{no Se-Se}}$ is unique in having a well-defined FSDP. Partial structure factor measurements made at ambient-pressure on D4c suggest that this FSDP is due to both $S^{\mathrm{FZ}}_{\mathrm{AsAs}}(Q)$ and $S^{\mathrm{FZ}}_{\mathrm{AsSe}}(Q)$ [183].

Figures 6-12, 6-13, and 6-14 show the pressure dependence of the first-order difference pair-distribution functions $\Delta G(r)_{\text{no As-As}}$, $\Delta G(r)_{\text{no Se-Se}}$, and $\Delta G(r)_{\text{no As-Se}}$, respectively, for amorphous As_2Se_3. These are the Fourier transforms of the $\Delta F(Q)_{\mathrm{X}}$ functions given in figures 6-9, 6-10, and 6-11, respectively. A Lorch modification function was used in order to reduce the effect of Fourier transform artefacts.

The red curves at low-r values show the theoretical $\Delta G(r \to 0)_{\mathrm{X}}$ cutoff levels, as given in table 6.2. The point at which the unphysical oscillations end, and the nearest-neighbour peak begins, was found from the low-r cutoff distances obtained from the total pair-distribution functions that had been treated in the same manner, *i.e.* a Lorch modification function was used in the Fourier transform procedure. In some of the plots, and in particular for several of the $\Delta G(r)_{\text{no As-Se}}$ functions shown in figure 6-14, it appears that this limit is "cutting off" some of the first peak in real space. This is not the case, however, as these "features" occur at distances below the distance of

Function	Pressure (GPa)	FSDP position (Å^{-1})	PP position (Å^{-1})
$\Delta F(Q)_{\text{no As-As}}$	Ambient		2.22(3)
	3.0(5) GPa		2.29(3)
	3.9(5) GPa		2.31(3)
	4.7(5) GPa		2.33(3)
	5.5(5) GPa		2.35(3)
	6.3(5) GPa		2.36(3)
	7.0(5) GPa		2.38(3)
	8.1(5) GPa		2.39(3)
$\Delta F(Q)_{\text{no Se-Se}}$	Ambient	1.19(3)	2.44(3)
	3.0(5) GPa	1.55(5)	2.47(3)
	3.9(5) GPa	1.35(3)	2.45(3)
	4.7(5) GPa	1.33(3)	2.48(3)
	5.5(5) GPa	1.35(3)	2.49(3)
	6.3(5) GPa	1.24(3)	2.47(3)
	7.0(5) GPa	1.34(3)	2.47(3)
	8.1(5) GPa	1.36(3)	2.48(3)
$\Delta F(Q)_{\text{no As-Se}}$	Ambient		2.18(3)
	3.0(5) GPa		2.24(3)
	3.9(5) GPa		2.27(3)
	4.7(5) GPa		2.31(3)
	5.5(5) GPa		2.31(3)
	6.3(5) GPa		2.30(3)
	7.0(5) GPa		2.32(3)
	8.1(5) GPa		2.34(3)

Table 6.10: Peak positions in the $\Delta F(Q)_{\text{X}}$ functions measured for amorphous As_2Se_3. For the cases of $\Delta F(Q)_{\text{no As-As}}$ and $\Delta F(Q)_{\text{no As-Se}}$ it is not possible to identify clear FSDPs, so values for its position are not given.

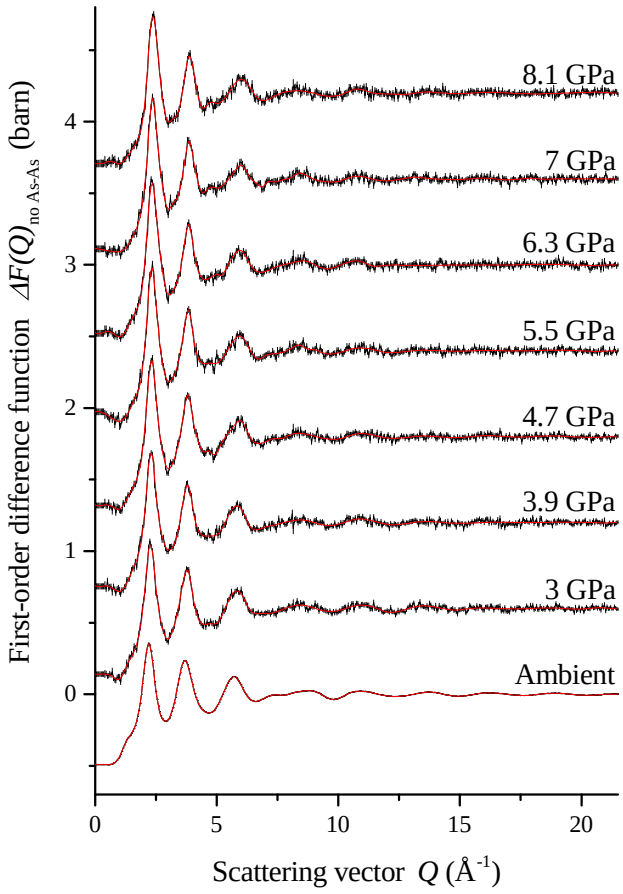

Figure 6-9: The pressure dependence of the first-order difference function $\Delta F(Q)_{\text{no As-As}} = 0.307(9)S^{\text{FZ}}_{\text{SeSe}}(Q) + 0.1336(32)S^{\text{FZ}}_{\text{AsSe}}(Q)$ for amorphous As_2Se_3. The graph shows the measure data sets (points with vertical black error bars) and spline fits to these data sets (red curves). The high-pressure curves have been offset vertically for clarity of presentation.

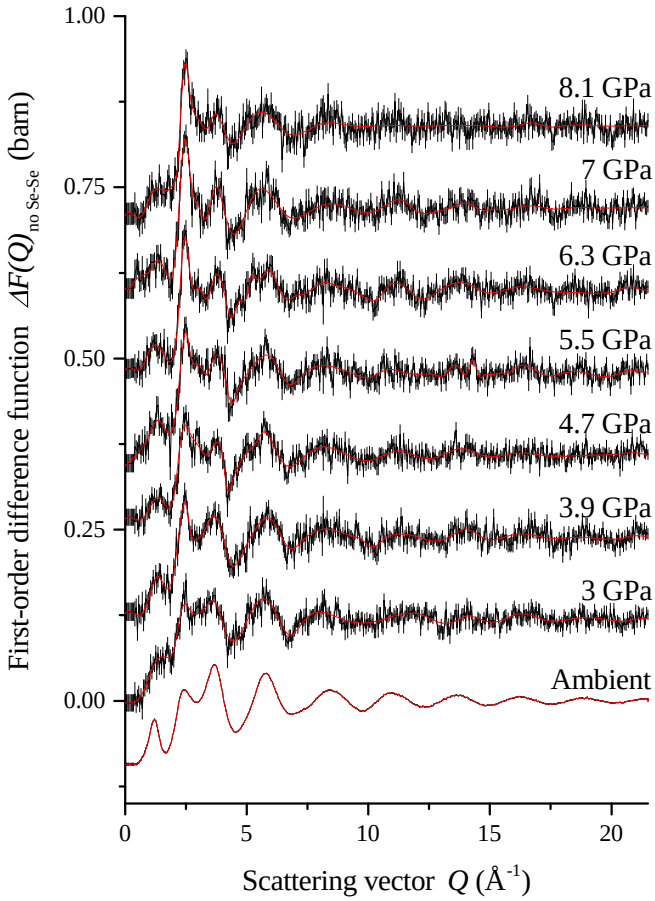

Figure 6-10: The pressure dependence of the first-order difference function $\Delta F(Q)_{\text{no Se-Se}} = 0.0397(5)S^{\text{FZ}}_{\text{AsAs}}(Q) + 0.0873(14)S^{\text{FZ}}_{\text{AsSe}}(Q)$ for amorphous As_2Se_3. The graph shows the measure data sets (points with vertical black error bars) and spline fits to these data sets (red curves). The high-pressure curves have been offset vertically for clarity of presentation.

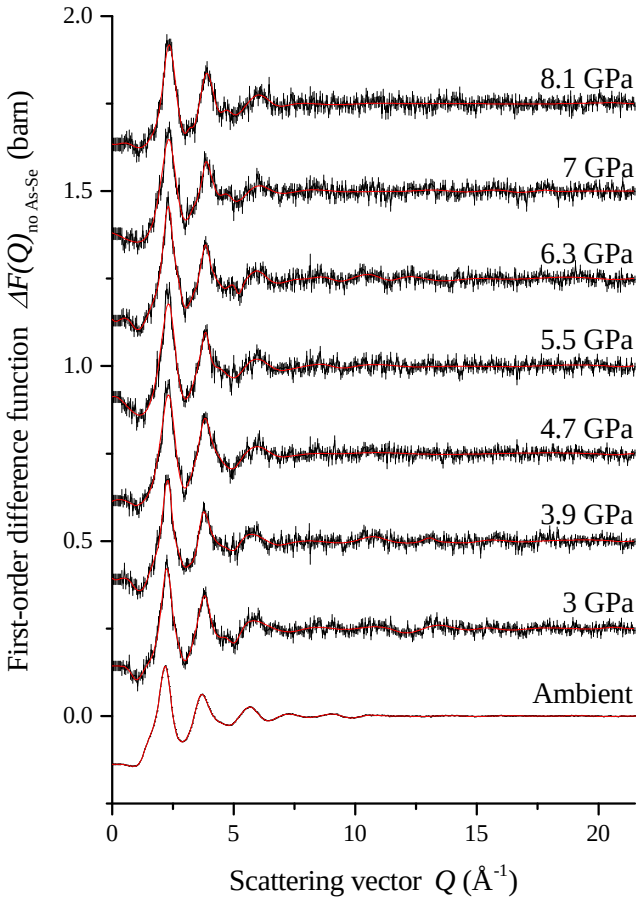

Figure 6-11: The pressure dependence of the first-order difference function $\Delta F(Q)_{\text{no As-Se}} = -0.0240(4)S^{\text{FZ}}_{\text{AsAs}}(Q)+0.1214(29)S^{\text{FZ}}_{\text{SeSe}}(Q)$ for amorphous As_2Se_3. The graph shows the measure data sets (points with vertical black error bars) and spline fits to these data sets (red curves). The high-pressure curves have been offset vertically for clarity of presentation.

closest approach between two atoms as judged from the $G(r)$ functions.

In the case of $\Delta G(r)_{\text{no As-Se}}$, the weighting factors for $g^{\text{FZ}}_{\text{AsAs}}(r)$ and $g^{\text{FZ}}_{\text{SeSe}}(r)$ are $-0.0240(4)$ barn and $0.1214(29)$ barn, respectively. This difference in sign means that a peak in $g^{\text{FZ}}_{\text{AsAs}}(r)$ will appear as a trough in $\Delta G(r)_{\text{no As-Se}}$. It is possible that peaks in $g^{\text{FZ}}_{\text{AsAs}}(r)$ and $g^{\text{FZ}}_{\text{SeSe}}(r)$ overlap, making it difficult to obtain reliable values for parameters such as the bond distances and coordination numbers.

Figure 6-15 shows the pressure dependence of the effective mean coordination number $\overline{n}'_{\text{X}}$ for amorphous As_2Se_3 as calculated from the first-order difference pair-distribution functions with X = "no As-As", "no Se-Se", and "no As-Se", using the method discussed in section 6.2. All three $\overline{n}'_{\text{X}}$ values are constant within the experimental error at pressures lower than 6 GPa. At larger pressures, the coordination numbers $\overline{n}'_{\text{no Se-Se}}$ and $\overline{n}'_{\text{no As-Se}}$ begin to increase. A similar increase in $\overline{n}'$ cannot, however, be seen from figure 6-7 where the values are the same within the experimental error.

Figure 6-16 shows the pressure dependence of the mean nearest-neighbour bond distance $\overline{r}_1$ as found from the first-order difference pair-distribution functions $\Delta G(r)_{\text{X}}$. The difference in sign for the $g^{\text{FZ}}_{\text{AsAs}}(r)$ and $g^{\text{FZ}}_{\text{SeSe}}(r)$ weighting factors in $\Delta G(r)_{\text{no As-Se}}$ leads to a small r-space feature, leading to a large variation of values with increasing pressure.

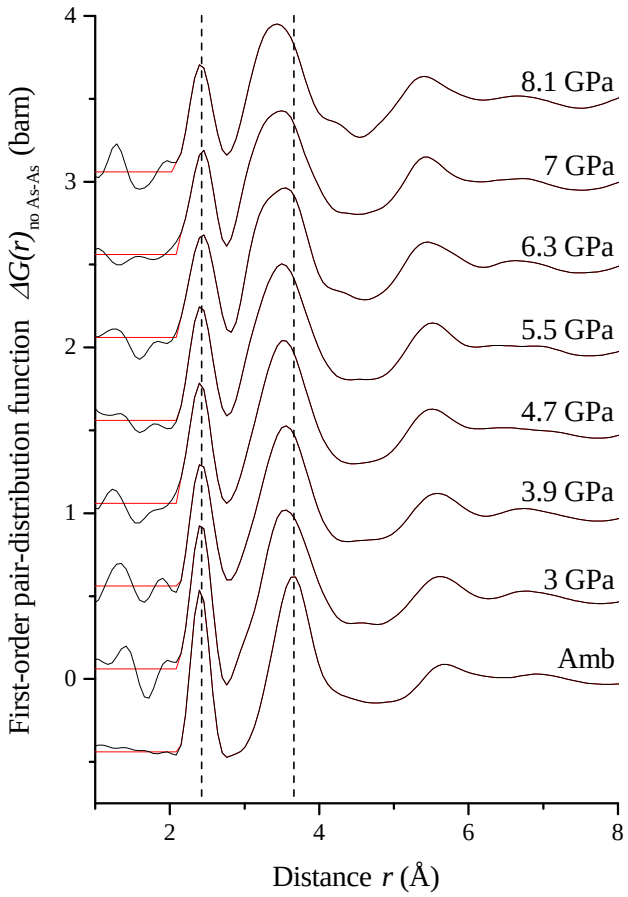

Figure 6-12: The pressure dependence of the first-order difference pair-distribution function $\Delta G(r)_{\text{no As-As}} = 0.307(9)g^{\text{FZ}}_{\text{SeSe}}(r) + 0.1336(32)g^{\text{FZ}}_{\text{AsSe}}(r)$ for amorphous As_2Se_3. The solid black curves show the Fourier transforms of the spline fits given in figure 6-9. The horizontal red curves show the calculated $\Delta G(r \rightarrow 0)_{\text{no As-As}}$ limits at distances below the closest approach between two atoms. The vertical dashed black curves show the ambient-pressure values for $\overline{r}_1$ and $\overline{r}_2$. All Fourier transforms have been made using a Lorch modification function. The high-pressure curves have been offset vertically for clarity of presentation.

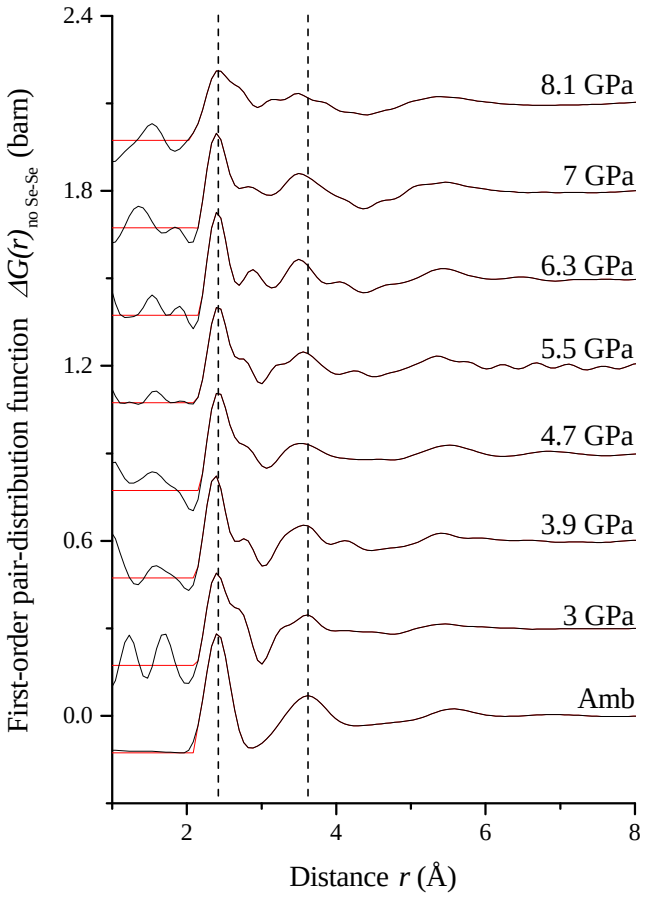

Figure 6-13: The pressure dependence of the first-order difference pair-distribution function $\Delta G(r)_{\text{no Se-Se}} = 0.0397(5)g^{\text{FZ}}_{\text{AsAs}}(r) + 0.0873(14)g^{\text{FZ}}_{\text{AsSe}}(r)$ for amorphous As_2Se_3. The solid black curves show the Fourier transforms of the spline fits given in figure 6-10. The horizontal red curves show the calculated $\Delta G(r \rightarrow 0)_{\text{no Se-Se}}$ limits at distances below the closest approach between two atoms. The vertical dashed black curves show the ambient-pressure values for $\overline{r}_1$ and $\overline{r}_2$. All Fourier transforms have been made using a Lorch modification function. The high-pressure curves have been offset vertically for clarity of presentation.

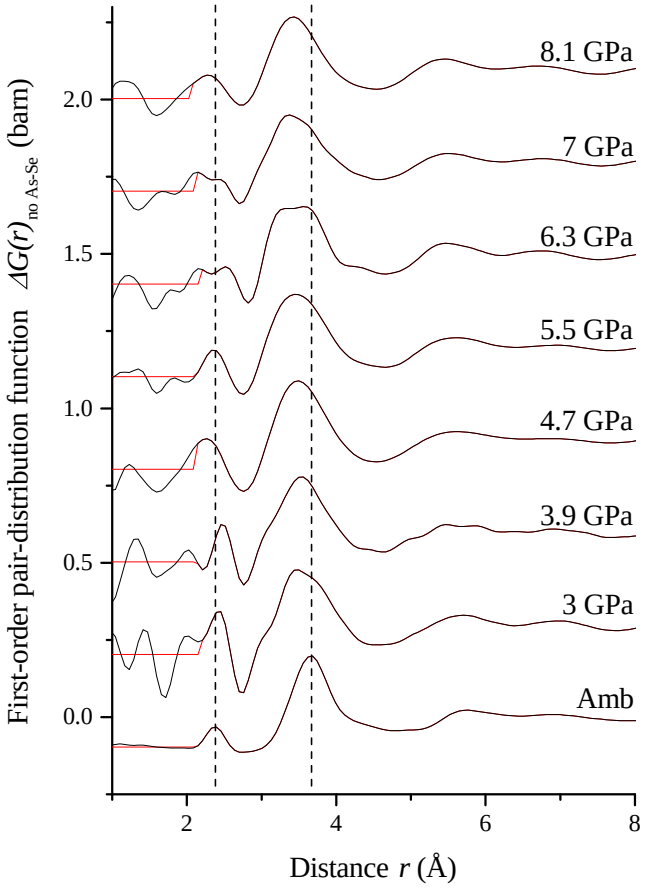

Figure 6-14: The pressure dependence of the first-order difference pair-distribution function $\Delta G(r)_{\text{no As-Se}} = -0.0240(4)g^{\text{FZ}}_{\text{AsAs}}(r) + 0.1214(29)g^{\text{FZ}}_{\text{SeSe}}(r)$ for amorphous As_2Se_3. The solid black curves show the Fourier transforms of the spline fits given in figure 6-11. The horizontal red curves show the calculated $\Delta G(r \to 0)_{\text{no As-Se}}$ limits at distances below the closest approach between two atoms. The vertical dashed black curves show the ambient-pressure values for $\overline{r}_1$ and $\overline{r}_2$. All Fourier transforms have been made using a Lorch modification function. The high-pressure curves have been offset vertically for clarity of presentation.

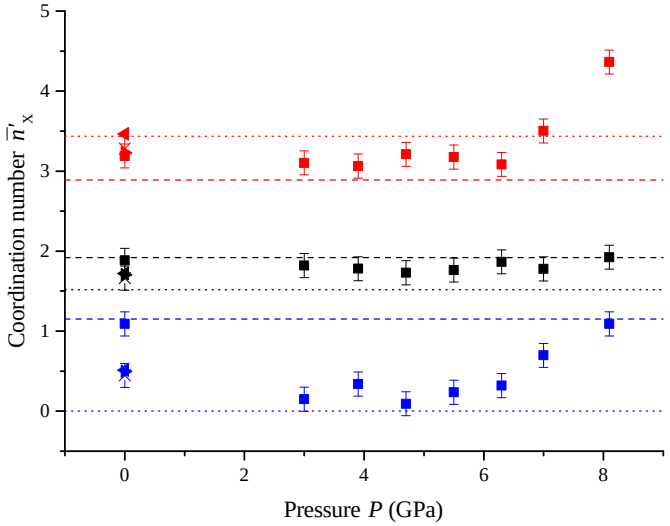

Figure 6-15: The pressure dependence of the effective mean coordination number $\overline{n}'_X$ for amorphous As_2Se_3 as calculated from first-order difference pair-distribution functions, where X = "no As-As" (black), "no Se-Se" (red), or "no As-Se" (blue). Included are the results from the D4c pressure experiment (■), the D4c ambient-pressure vanadium can experiment (●) [183], and the FPMD simulations reported in Ref. [46] (◀) and Ref. [47] (▶). For each difference function, the effective mean coordination number $\overline{n}'_X$ calculated on the basis of the "8-N" rule are also included for the COCRN (dotted curve) and RCN (dashed curve) models.

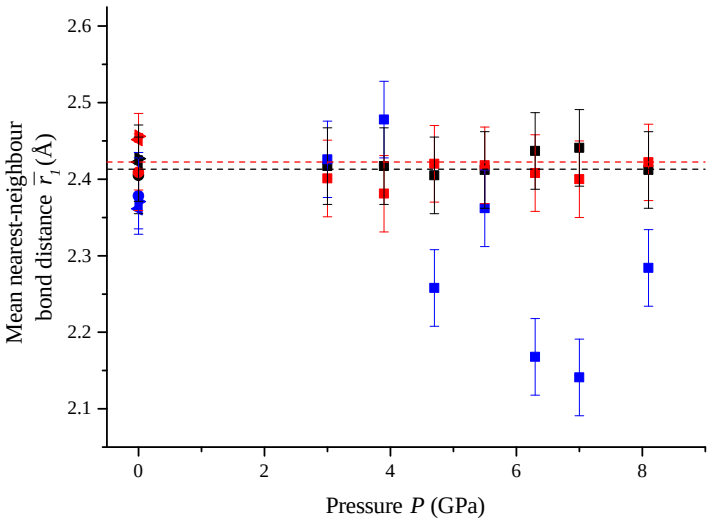

Figure 6-16: The pressure dependence of the mean nearest-neighbour bond distance $\overline{r}_1$ for amorphous As_2Se_3 as obtained from the first-order difference pair-distribution functions. The results for the different first-order difference difference functions are presented separately: "no As-As" (black), "no Se-Se" (red), and "no As-Se" (blue). Included are the results from the D4c pressure experiment (■), the D4c ambient-pressure vanadium can experiment (●) [183], and the FPMD simulations reported in Ref. [46] (◀) and Ref. [47] (▶). The two horizontal dashed curves are equal to the average value of $\overline{r}_1$ for the ambient-pressure neutron diffraction results for $\Delta G(r)_{\text{no As-As}}$ (black) and $\Delta G(r)_{\text{no Se-Se}}$ (red), and correspond to 2.413 Å and 2.4225 Å, respectively.

6.5 Discussion

The neutron diffraction measurements made on amorphous As_2Se_3 show that the effective mean coordination number $\overline{n}'$ (figure 6-7) and the mean nearest-neighbour bond distance $\overline{r}_1$ (figure 6-8) are constant within the experimental error at pressures up to 14.4(5) GPa. Across the measured pressure range, the effective mean coordination number is inconsistent with the values calculated for either a chemically-ordered continuous random network (COCRN) or a random covalent network (RCN) model. This suggests that either the network does not conform to either of these theories, or that the "8-N" rule is breaking down [45].

Figures 6-17(a) and 6-17(b) give a comparison of the ${}^{\mathrm{N}}_{\mathrm{N}}F(Q)$ and ${}^{\mathrm{N}}_{\mathrm{N}}G(r)$ functions measured using D4c at 8.1(5) GPa and using PEARL at 8.7(5) GPa. In reciprocal space, the PEARL data shows sharper features than the D4c data. This difference in sharpness is anticipated because (i) PEARL has a better Q-space resolution function $\Delta Q/Q$ as compared to D4c, and (ii) the PEARL data is at a higher pressure. As discussed in section 6.4, the reciprocal space peaks tend to sharpen with increasing pressure. In real space, the first peak positions are the same, and their intensities are very similar. The second peak does, however, show a difference of intensity and a small difference in position. This can be explained by the higher pressure of the PEARL data that results in shift of the second peak to smaller r-values. Overall, the consistency between the D4c and PEARL results supports the validity of the experimental results.

To further investigate the nearest-neighbour coordination environment, first-order difference pair-distribution functions were used to calculate the effective mean coordination numbers $\overline{n}'_{\mathrm{X}}$ and nearest-neighbour bond distances $\overline{r}_1$, as shown in figures 6-15 and 6-16, respectively. Figure 6-15 shows that the nearest-neighbour coordination environment obtained from $\Delta G(r)_{\text{no As-As}}$ is relatively stable with respect to pressure, suggesting that the first peaks in $g^{\mathrm{FZ}}_{\mathrm{SeSe}}(r)$ and $g^{\mathrm{FZ}}_{\mathrm{AsSe}}(r)$ are not changing, or that they are both changing in such a way as to "cancel" one another out. Figure 6-18 shows the $\Delta G(r)_{\text{no As-As}}$ function compared to FPMD simulations at ambient pressure. It also includes the weighted partial pair-distribution functions $g^{\mathrm{FZ}}_{\mathrm{SeSe}}(r)$ and $g^{\mathrm{FZ}}_{\mathrm{AsSe}}(r)$. It can be seen that the first peak, at $\overline{r}_1 \sim 2.4$ Å, comprises both Se-Se and As-Se bonds, although it is dominated by the latter. The second peak, at $\overline{r}_2 \sim 3.7$ Å, comprises both Se-Se and As-Se correlations and is dominated by the former.

For $\Delta G(r)_{\text{no Se-Se}}$, the mean coordination number is constant up until 6 GPa. At higher pressures, it increases as the region between the first and second peaks is filled in. This change in coordination number coincides with the second peak losing intensity while the first peak broadens out to higher-r. The cutoff used in integrating the coordination number increases from 2.823 Å at ambient pressure to 3.007 Å at 8.1(5) GPa,

whilst the magnitude of the $\Delta G(r)_{\text{no Se-Se}}$ function at these distances also increases. Figure 6-19 shows the $\Delta G(r)_{\text{no Se-Se}}$ function compared to FPMD simulations at ambient pressure. It also includes the weighted partial pair-distribution functions $g^{\text{FZ}}_{\text{AsAs}}(r)$ and $g^{\text{FZ}}_{\text{AsSe}}(r)$. It can be seen that the first peak, at $\overline{r}_1 \sim 2.4\,\text{Å}$, comprises both As-As and As-Se bonds, although it is dominated by the latter. The second peak, at $\overline{r}_2 \sim 3.6\,\text{Å}$, comprises both As-As and As-Se correlations. Unfortunately, it is not obvious how these partial pair-distribution functions change with increasing pressure to give an increase in $\overline{n}'_{\text{no Se-Se}}$.

The difference in sign for the weighting factors of the $g^{\text{FZ}}_{\text{AsAs}}(r)$ and $g^{\text{FZ}}_{\text{SeSe}}(r)$ functions that contribute to $\Delta G(r)_{\text{no As-Se}}$ makes it difficult to ascertain what is happening at the difference function level. The effective mean coordination numbers $\overline{n}'_{\text{no As-Se}}$ show an increase with pressure that begins at $P \sim 6\,\text{GPa}$, but it is not possible to determine if this arises from an increase in the Se-Se coordination number, or from a decrease in the As-As coordination number.

Under ambient conditions, the neutron diffraction results can be compared at the first-order difference pair-distribution level to first-principles molecular dynamics (FPMD) simulations that have been treated in the same manner, *i.e.* the FPMD results have been Fourier transformed using the same Q_{max} cutoff. In figures 6-18, 6-19, and 6-20 two sets of FPMD results are plotted. The first set of simulations correspond to a 2 GPa over-pressure, although the density corresponds to the experimental value ($\rho = 0.0358\,\text{Å}^{-3}$) [46]. The second set of simulations include dispersion forces that result in a lower pressure and are from work that is in progress [47]. Figures 6-18, 6-19, and 6-20 show that there are discrepancies in most of the peak heights and positions when comparing the neutron diffraction and MD simulation results. It is notable that the experimental partial pair-distribution functions confirm the existence of homopolar As-As and Se-Se bonds at a similar distance to the As-Se bonds.

Figures 6-21(a) and 6-21(b) show the crystal structures for two phases of As_2Se_3. Figure 6-21(a) shows the phase at ambient conditions [169], whilst figure 6-21(b) shows a phase that has been recovered to ambient conditions from $P = 1.23\,\text{GPa}$ and $T = 538\,^{\circ}\text{C}$ [187]. Both crystals show a layered structure, but the structure of the recovered phase is markedly different to the ambient-conditions phase. The latter comprises three-fold coordinated As atoms in corner-sharing $AsSe_3$ pyramids. The recovered phase shows a more cubic structure within the layers, with As being both 5-fold and 6-fold coordinated by Se atoms. The distances for these As-Se correlations are in the range 2.5 – 3 Å. The pair-distribution functions ${}^{\text{N}}_{\text{N}}G(r)$, ${}^{\text{N}}_{76}G(r)$, and $\Delta G(r)_{\text{no Se-Se}}$, illustrated in figures 6-5, 6-6, and 6-10, respectively, show an increase of intensity at this distance as the pressure is increased. This increase is manifested in both ${}^{\text{N}}_{\text{N}}G(r)$ and ${}^{\text{N}}_{76}G(r)$ by a shoulder developing on the low-r side of the second peak, and in $\Delta G(r)_{\text{no Se-Se}}$ by an

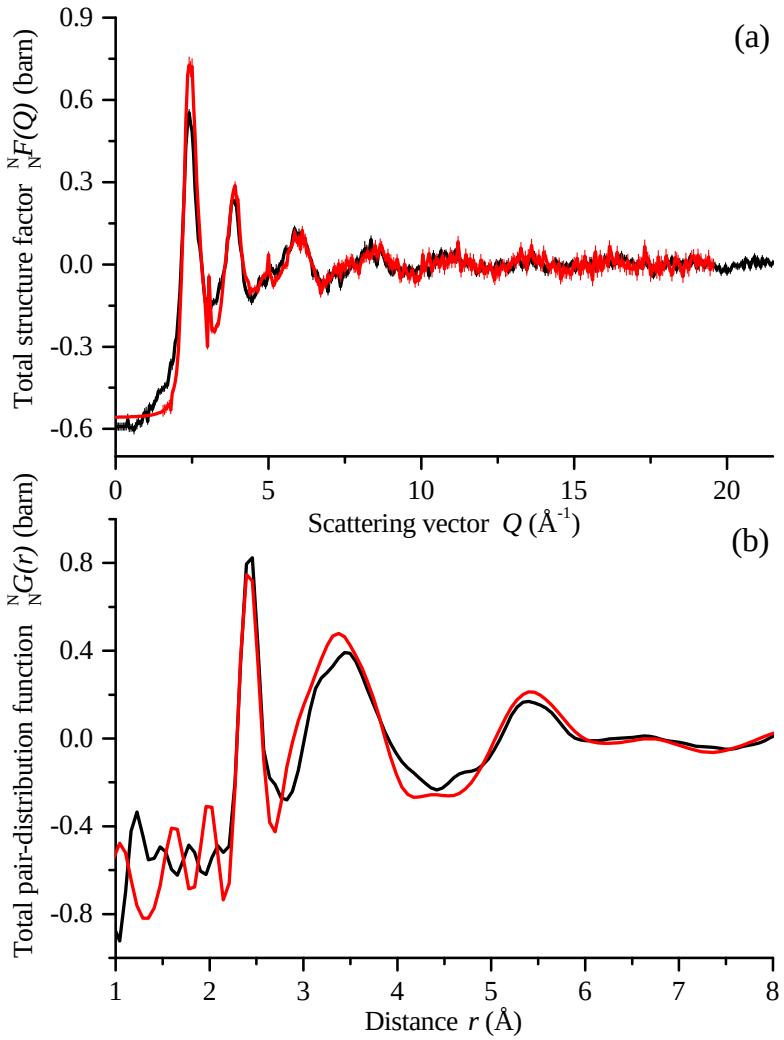

Figure 6-17: Comparison between the high-pressure results for D4c as measured at 8.1(5) GPa (black curves) and for PEARL as measured at 8.7(5) GPa (red curves) in (a) reciprocal space and (b) real space.

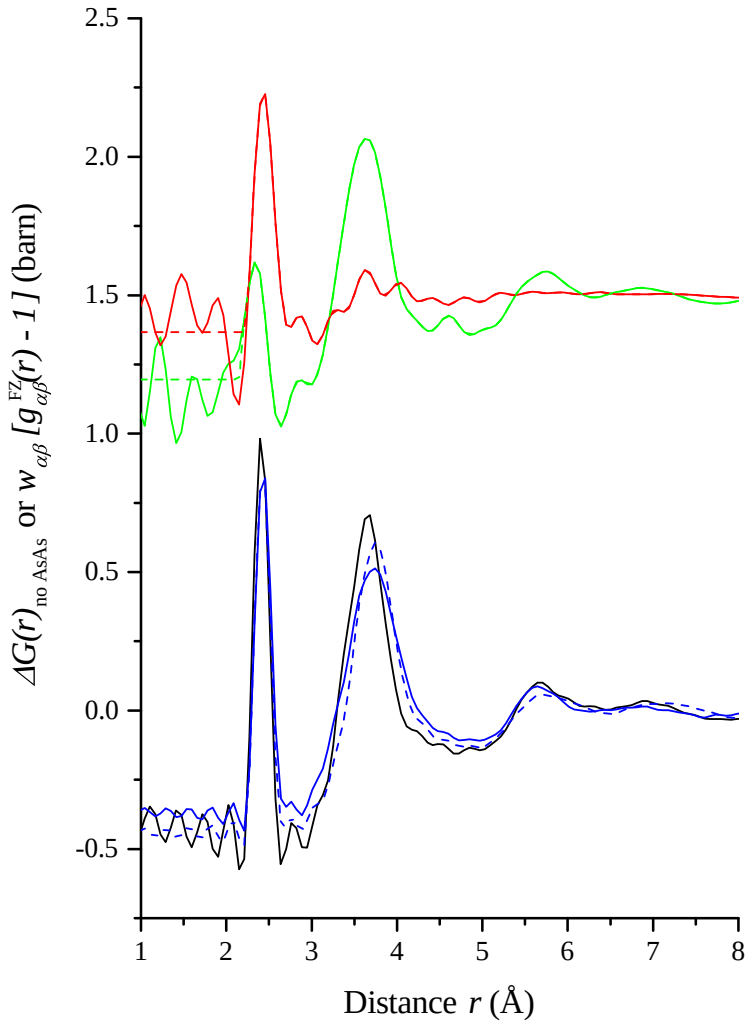

Figure 6-18: The first-order difference pair-distribution difference function $\Delta G(r)_{\text{no As-As}}$ for amorphous As_2Se_3 at ambient pressure. The graph includes experimental data from a vanadium can experiment on D4c (black curve). Two sets of FPMD data are included and are shown by the blue solid [46] and dashed [47] lines. Finally, the partial pair-distribution functions $g^{\text{FZ}}_{\text{SeSe}}(r)$ (green curve) and $g^{\text{FZ}}_{\text{AsSe}}(r)$ (red curve) are included, where the functions have been weighted by the appropriate coefficients $w_{\alpha\beta}$ for $\Delta G(r)_{\text{no As-As}}$, as given in table 6.1. The horizontal dashed curves at low-r correspond to the $w_{\alpha\beta}\left[g^{\text{FZ}}_{\alpha\beta}(r \to 0) - 1\right]$ limits at distances below the closest approach of two atoms. These weighted functions have been offset vertically by 1.5 barn for clarity of presentation.

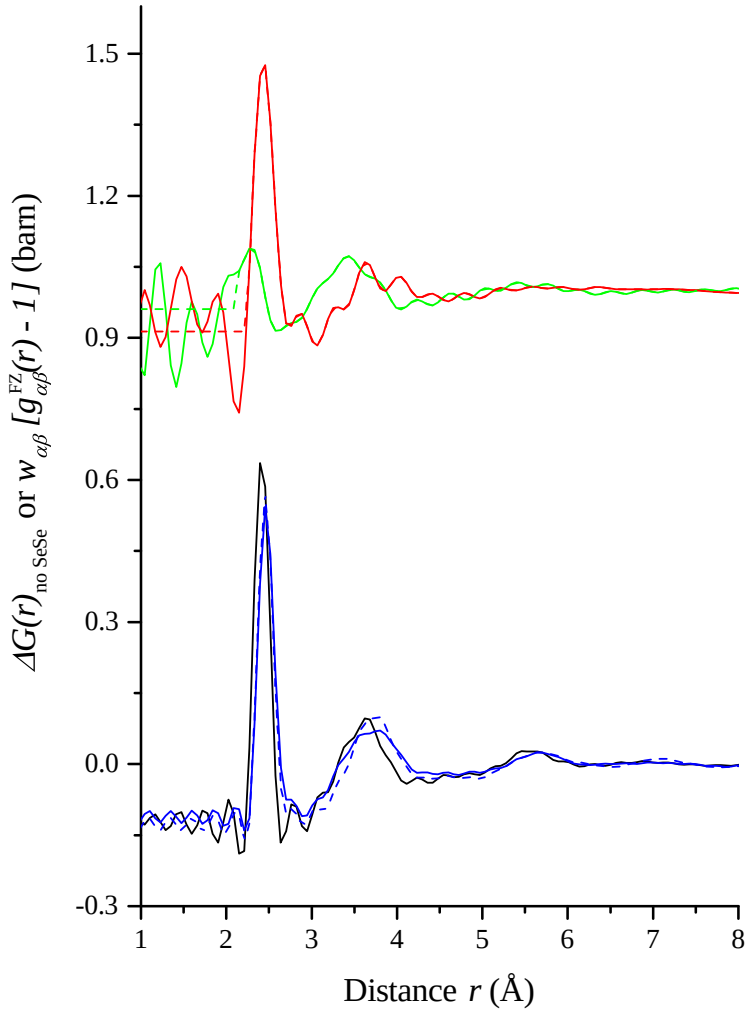

Figure 6-19: The first-order difference pair-distribution difference function $\Delta G(r)_{\text{no Se-Se}}$ for amorphous As_2Se_3 at ambient pressure. The graph includes experimental data from a vanadium can experiment on D4c (black curve). Two sets of FPMD data are included and are shown by the blue solid [46] and dashed [47] lines. Finally, the partial pair-distribution functions $g^{\text{FZ}}_{\text{AsAs}}(r)$ (green curve) and $g^{\text{FZ}}_{\text{AsSe}}(r)$ (red curve) are included, where the functions have been weighted by the appropriate coefficients $w_{\alpha\beta}$ for $\Delta G(r)_{\text{no Se-Se}}$, as given in table 6.1. The horizontal dashed curves at low-r correspond to the weighted $w_{\alpha\beta}\left[g^{\text{FZ}}_{\alpha\beta}(r \to 0) - 1\right]$ limits at distances below the closest approach of two atoms. These weighted functions have been offset vertically by 1 barn for clarity of presentation.

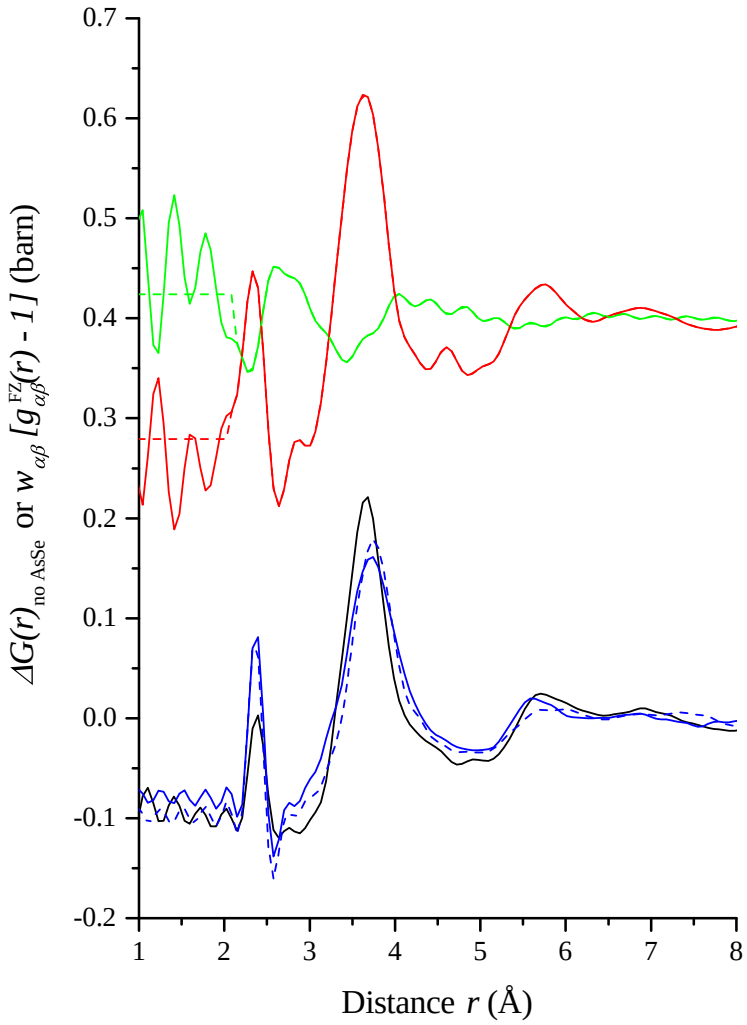

Figure 6-20: The first-order difference pair-distribution difference function $\Delta G(r)_{\text{no As-Se}}$ for amorphous As_2Se_3 at ambient pressure. The graph includes experimental data from a vanadium can experiment on D4c (black curve). Two sets of FPMD data are included and are shown by the blue solid [46] and dashed [47] lines. Finally, the partial pair-distribution functions $g^{\text{FZ}}_{\text{AsAs}}(r)$ (green curve) and $g^{\text{FZ}}_{\text{SeSe}}(r)$ (red curve) are included, where the functions have been weighted by the appropriate coefficients $w_{\alpha\beta}$ for $\Delta G(r)_{\text{no As-Se}}$, as given in table 6.1. The horizontal dashed curves at low-r correspond to the weighted $w_{\alpha\beta}\left[g^{\text{FZ}}_{\alpha\beta}(r \to 0) - 1\right]$ limits at distances below the closest approach of two atoms. These weighted functions have been offset vertically by 0.4 barn for clarity of presentation.

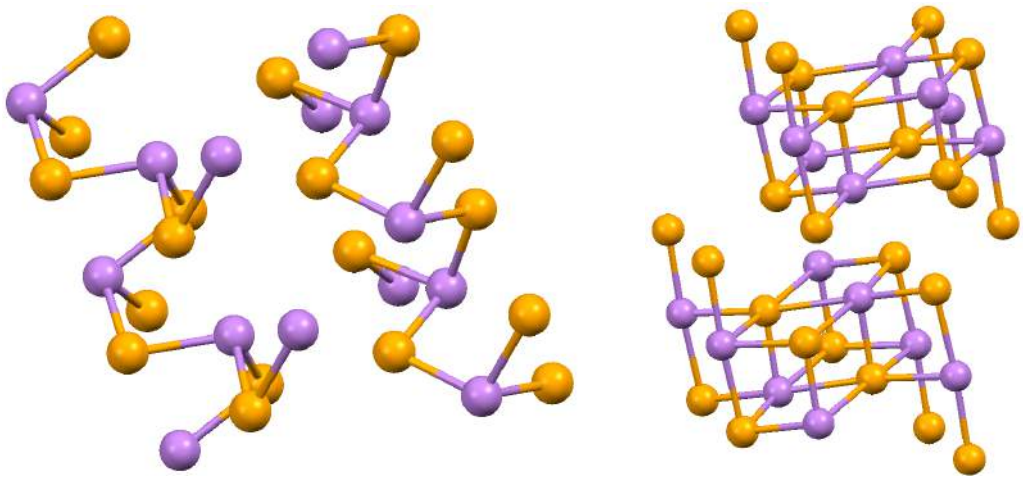

(a) (b)

Figure 6-21: Representations of the crystal structures for two different As_2Se_3 polymorphs. (a) The crystal structure of As_2Se_3 under ambient conditions [169]. (b) The crystal structure of As_2Se_3 recovered to ambient conditions from $P = 1.23\,\text{GPa}$, $T = 538\,^{\circ}\text{C}$ [187].

increase of intensity in a region where $\Delta G(r)_{\text{no Se-Se}} = \Delta G(r \to 0)_{\text{no Se-Se}}$ under ambient conditions. It is possible that this increase of intensity is due to As-Se correlations, as in the crystal structure [187].

6.6 Conclusions

The *in situ* high-pressure structure of amorphous As_2Se_3 has been measured using neutron diffraction at pressures ranging from ambient to 14.4(5) GPa using a Paris-Edinburgh press mounted on either the D4c or PEARL diffractometer. For the D4c experiment, the method of neutron diffraction with isotope substitution (NDIS) was used at pressures up to 8.1(5) GPa to provide information at the first-order difference function level.

The mean nearest-neighbour coordination shell appears to be constant up to 14.4(5) GPa from the total structure factor results, showing a constant mean bond distance $\overline{r}_1$ and effective coordination number $\overline{n}'$. Information at the first-order difference function level suggests, however, that there is some change to the nearest-neighbour coordination environment beginning at 6 GPa, as both $\Delta G(r)_{\text{no Se-Se}}$ and $\Delta G(r)_{\text{no As-Se}}$ show an increase in the effective mean coordination number $\overline{n}'_{\text{X}}$. Unfortunately, it is difficult to ascertain what is causing this change to $\overline{n}'_{\text{X}}$.

Further work is required to pinpoint the mechanisms by which this network-forming glass is modified under compression. For example, it is not obvious how the structural

motifs change with pressure. It is hoped that the neutron diffraction results of the present work, when combined with FPMD simulations [47], will allow these secrets to be unlocked.

7. The structure of amorphous $CaSiO_3$ under compression

7.1 Introduction

Calcium silicates $(CaO)_x(SiO_2)_{1-x}$ $(0 \leq x \leq 1)$ have been extensively studied in the past due to their technological and geological importance [48, 49, 188–209]. For example, they form an integral part of cement and have been used as an alternative to asbestos for high-temperature insulation materials [209, 210]. They are used in so-called bioactive materials, which find applications in bone tissue engineering [196, 201, 202, 204–207]. They have also been used to investigate the properties of so-called "fragile" glass forming liquids at high temperatures [188, 197, 200, 208]. The phase diagram for the CaO–Al_2O_3–SiO_2 system is shown in figure 7-1. The blue curve shows the glass forming region that was found by L. Skinner, where the glasses in this region were formed by quenching aerodynamically levitated liquid droplets [211].

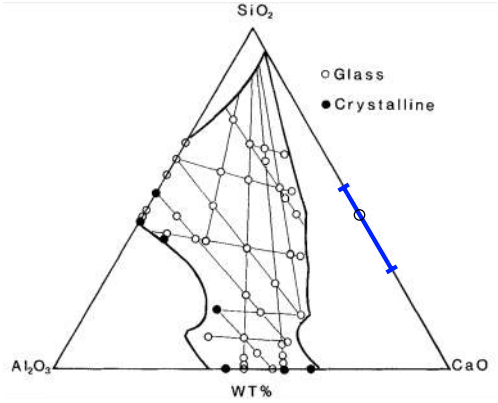

Figure 7-1: CaO–Al_2O_3–SiO_2 glass forming regions. The original diagram was taken from Ref. [190]. The two symbol types, open and filled circles, show materials that are either glassy or crystalline, respectively. The bold black curves indicate a liquidus temperature $T = 1600\,°C$. The light black curves indicate the compositional series that were studied in Ref. [190]. The blue curve indicates an additional glass forming region [211]. The black circle sitting on the blue curve indicates the $CaSiO_3$ composition.

In terms of extreme conditions, calcium silicates are studied because they form a significant component of the Earth's mantle [212] and thus the liquid structure is of interest for understanding geophysical properties, such as the dynamics of magmas [213]. The structural changes that occur to magmas under extreme conditions can govern processes such as volcanic activity and the differentiation of the Earth's interior [15, 16].

Measuring the structure of a geological material such as $(CaO)_x(SiO_2)_{1-x}$ under extreme pressure and temperature conditions is difficult [40]. However, glasses are able to explore localities on an energy landscape that are inaccessible to a crystal. It is hoped that by studying the structure of glasses under extreme conditions, new insights can be found into the structure of the corresponding compressed liquids that are not easily studied by experiment.

The work presented in this chapter makes use of neutron diffraction to measure the atomic structure of amorphous $CaSiO_3$ *in situ* at pressures up to 17.5(5) GPa, using a Paris-Edinburgh press mounted on the PEARL diffractometer. The results are compared with molecular dynamics simulations that have been made between ambient pressure and 15 GPa [48, 49].

The chapter is organised as follows. The essential theory for a neutron diffraction experiment is given in section 7.2. The experimental procedure for the work is discussed in section 7.3. The results and the accompanying discussion are presented in sections 7.4 and 7.5, respectively. Finally, conclusions are drawn in section 7.6.

7.2 Theory

As discussed in chapter 2, in a neutron diffraction experiment the total structure factor

$$F(Q) = \sum_{\alpha}\sum_{\beta} c_\alpha c_\beta b_\alpha b_\beta \left[S^{\mathrm{FZ}}_{\alpha\beta}(Q) - 1\right] \tag{7.1}$$

is measured, where α and β denote the chemical species, c_α is the atomic fraction of chemical species α, b_α is the bound coherent scattering length of chemical species α, $S^{\mathrm{FZ}}_{\alpha\beta}(Q)$ is the Faber-Ziman partial structure factor for chemical species α and β [55], and Q is the magnitude of the scattering vector [52]. The corresponding real-space information can be obtained via Fourier transformation of the reciprocal space data to give the total pair-distribution function $G(r)$, as given by

$$G(r) = \frac{1}{2\pi^2 r\rho}\int_0^\infty QM(Q)F(Q)\sin(Qr)\,\mathrm{d}Q, \tag{7.2}$$

where r is a distance in real space, ρ is the number density of the glass, and $M(Q)$ is a modification function

$$M(Q) = \begin{cases} 1 & \text{if } Q \leq Q_{\max} \\ 0 & \text{if } Q > Q_{\max}, \end{cases} \tag{7.3}$$

which is introduced because a diffractometer can measure over only a finite Q range up to a maximum value $Q_{\max}$. Fourier transformation artefacts can arise from the finite Q range and can be reduced through the use of a Lorch modification function [56]

$$M(Q) = \begin{cases} \frac{\sin(aQ)}{aQ} & \text{if } Q \leq Q_{\max} \\ 0 & \text{if } Q > Q_{\max}, \end{cases} \tag{7.4}$$

where $a = \pi/Q_{\max}$, at the expense of broadened r-space features. The low-r limit, $G(r \to 0)$, for a total pair-distribution function is given by

$$G(r \to 0) = -\sum_{\alpha}\sum_{\beta} c_\alpha c_\beta b_\alpha b_\beta = -\langle b \rangle^2, \tag{7.5}$$

where $\langle b \rangle$ is the mean bound coherent scattering length

$$\langle b \rangle = \sum_{\alpha} c_\alpha b_\alpha. \tag{7.6}$$

For the ternary glass $CaSiO_3$, the total pair-distribution function can be written as

$$\begin{aligned} G(r) = {} & c_{\mathrm{Ca}}^2 b_{\mathrm{Ca}}^2 g_{\mathrm{CaCa}}^{\mathrm{FZ}}(r) + c_{\mathrm{Si}}^2 b_{\mathrm{Si}}^2 g_{\mathrm{SiSi}}^{\mathrm{FZ}}(r) + c_{\mathrm{O}}^2 b_{\mathrm{O}}^2 g_{\mathrm{OO}}^{\mathrm{FZ}}(r) \\ & + 2c_{\mathrm{Ca}} c_{\mathrm{Si}} b_{\mathrm{Ca}} b_{\mathrm{Si}} g_{\mathrm{CaSi}}^{\mathrm{FZ}}(r) + 2c_{\mathrm{Ca}} c_{\mathrm{O}} b_{\mathrm{Ca}} b_{\mathrm{O}} g_{\mathrm{CaO}}^{\mathrm{FZ}}(r) + 2c_{\mathrm{Si}} c_{\mathrm{O}} b_{\mathrm{Si}} b_{\mathrm{O}} g_{\mathrm{SiO}}^{\mathrm{FZ}}(r) \\ & + G(r \to 0). \end{aligned} \tag{7.7}$$

Consider a given r-range $r_1 \leq r \leq r_2$ where all of the Faber-Ziman partial pair-distribution functions $g_{\alpha\beta}^{\mathrm{FZ}}(r)$ are equal to zero apart from the Si-O function $g_{\mathrm{SiO}}^{\mathrm{FZ}}(r)$. In this case, the Si-O partial pair-distribution function can be written as

$$g_{\mathrm{SiO}}^{\mathrm{FZ}}(r) = \frac{G(r) - G(r \to 0)}{2c_{\mathrm{Si}} c_{\mathrm{O}} b_{\mathrm{Si}} b_{\mathrm{O}}}, \tag{7.8}$$

such that the Si-O coordination number $\overline{n}_{\mathrm{Si}}^{\mathrm{O}}$ can be found by using the equation

$$\overline{n}_{\mathrm{Si}}^{\mathrm{O}} = \frac{2\pi\rho}{c_{\mathrm{Si}} b_{\mathrm{Si}} b_{\mathrm{O}}} \int_{r_1}^{r_2} r^2 \left[G(r) - G(r \to 0) \right] \mathrm{d}r. \tag{7.9}$$

7.3 Experimental procedure

A neutron diffraction experiment was performed to study amorphous $CaSiO_3$ at ambient temperature ($T \sim 300\,\mathrm{K}$) and at pressures up to $P = 17.5(5)\,\mathrm{GPa}$. A V3 Paris-Edinburgh press was mounted in a transverse scattering geometry on the PEARL HiPr diffractometer with double toroid sintered diamond anvils providing compression.

To produce amorphous $CaSiO_3$, powdered silica (SiO_2) and calcium carbonate ($CaCO_3$) was first dried at 800 °C and 200 °C, respectively, for approximately 16 hours. The powders were mixed in an equimolar proportion inside a Pt–Rh crucible. This crucible was then used to contain the sample during the heating regime. Starting from ambient temperature, the crucible was first heated to 800 °C and allowed to dwell for 12 hours. This temperature is sufficient to allow the calcium carbonate to decompose to calcium oxide

$$CaSiO_3 \rightarrow CaO + CO_2. \tag{7.10}$$

The crucible was then heated to the quench temperature 1650 °C and allowed to dwell for 3 hours. This temperature is sufficient to allow the silica to melt and mix with the calcium oxide, to form liquid calcium silicate.

To quench the glass, the crucible was quickly removed from the furnace and placed on a copper block which had been previously cooled to 77 K using liquid nitrogen. The crucible was then doused with liquid nitrogen to quickly cool the liquid and form a glass. Once a glass had formed, the crucible was then warmed with a heatgun to bring it to ambient temperature, a step that was undertaken to help reduce moisture forming on the glass.

Sample	Pellet mass (g)	$Ti_{0.676}Zr_{0.324}$ gasket mass (g)
$CaSiO_3$	0.1004(1)	1.0791(1)
Vanadium	0.2060(1)	1.0824(1)

Table 7.1: Pellet and $Ti_{0.676}Zr_{0.324}$ gasket masses for the PEARL $CaSiO_3$ experiment.

Before attempting to remove pieces of $CaSiO_3$ glass from the crucible, it was annealed at 700 °C to reduce any tension and aid in the production of a solid pellet piece. The ideal mass of a double toroid $CaSiO_3$ pellet is 0.098 16 g. A $CaSiO_3$ pellet was produced from a single piece of glass recovered from the crucible by gently grinding it to the correct shape using the method discussed in section 3.6.1. A vanadium pellet was produced by taking vanadium foil and placing the correct mass in a specially prepared die which re-creates the shape of a double toroid pellet. This was then compressed as outlined in section 3.6.1. The masses of the $CaSiO_3$ and vanadium pellets are given in table 7.1.

Applied load L (tonnes)	Pressure P (GPa)	$CaSiO_3$	Vanadium
2	Ambient	✓	✓
75	8.7(5)	✓	✓
98	10.9(5)	✓	✓
120	14.4(5)	✓	✓
140	17.5(5)	✓	✓

Table 7.2: Pressure points measured during the experiment. The pressure at the sample position P was deduced from the calibration curve given in figure 3-15.

The PEARL diffraction experiment was performed as outlined in section 3.6.4. Measurements were made for two empty $Ti_{0.676}Zr_{0.324}$ gaskets where their masses are given in table 7.1. Neutron diffraction measurements were made for the vanadium and the sample in turn, and the investigated pressure points are given in table 7.2. During the course of a pressure point measurement, the ratio was taken of the measured intensities for different periods of time. If this ratio deviates from unity then the scattered intensity is changing with respect to time. No such deviation was observed during the course of the measurements.

The compression was controlled by an automated machine up to an oil pressure $P_{\text{oil}} = 950\,\text{bar}$, after which a hand pump was used to manually increase the pressure. The automated system kept the pressure constant, *i.e.* if some relaxation occurred that caused the pressure to drop below its set point then the automated system would increase it back to the set point. When using the hand pump this was not possible, and any relaxation (typically $\sim$ 10–20 bar) was allowed to occur. Whilst increasing and decreasing pressure, periodic pauses were taken to allow the system to equilibrate.

The mass density $\rho_{\text{m}} = 2.9111(28)\,\text{g}\,\text{cm}^{-3}$ of $CaSiO_3$ was measured using a helium pycnometer. This yielded an ambient-pressure number density $\rho_0 = 0.0755(1)\,\text{Å}^{-3}$. The pressure-volume equation of state for $CaSiO_3$ as calculated in two different sets of molecular dynamics (MD) simulations [48, 49] is shown in figure 7-2. A 3rd-order Birch-Murnaghan equation of state, given by

$$P(V;V_0,B_0,B_0') = \frac{3B_0}{2}\left[\left(\frac{V}{V_0}\right)^{-\frac{7}{3}} - \left(\frac{V}{V_0}\right)^{-\frac{5}{3}}\right]\times \left\{1+\frac{3}{4}\left(B_0'-4\right)\left[\left(\frac{V}{V_0}\right)^{-\frac{2}{3}}-1\right]\right\}, \tag{7.11}$$

was fitted to the data from Ref. [49] to allow for an extrapolation to higher pressures for

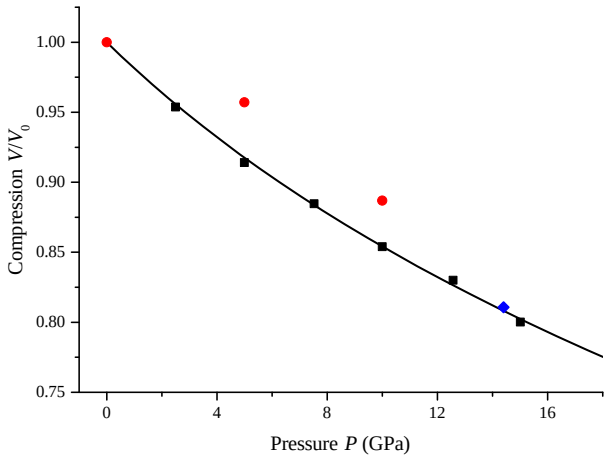

Figure 7-2: The pressure-volume equation of state for $CaSiO_3$ under compression. Included are two sets of molecular dynamics results from Ref. [49] (■) and Ref. [48] (●). Also included is a data point (◆) based on when the Si-O coordination number $\overline{n}^{\mathrm{O}}_{\mathrm{Si}}$ begins to change (see the text). A 3rd-order Birch-Murnaghan equation of state was fitted to the data from Ref. [49], giving the parameters $B_0 = 51.96(2.18)$ GPa and $B_0' = 2.68(36)$ (solid black curve).

use in the PEARL data analysis. The fitted parameters were $B_0 = 51.96(2.18)$ GPa and $B_0' = 2.68(36)$. This bulk modulus differs to that measured using Brillouin scattering, $B_0 = 69.2$ GPa [214]. The same data set was also fitted with a 2nd-order Birch-Murnaghan equation of state, which gave a fitted bulk modulus $B_0 = 45.12(82)$ GPa. It was found, however, that the 3rd-order equation of state more accurately fitted the data.

Figure 7-2 presents a data point based on the pressure at which the Si-O coordination number $\overline{n}^{\mathrm{O}}_{\mathrm{Si}}$ begins to change. For liquid and amorphous oxides a general theory has been proposed for mapping regimes of topological change, *i.e.* a change in the coordination number of a network-forming species such as Si, to the oxygen-packing fraction of the system [215]. Once the data analysis was complete, the pressure at which $\overline{n}^{\mathrm{O}}_{\mathrm{Si}}$ begins to change was estimated. Using the figures presented in Ref. [215], it was then possible to calculate the number density, and hence compression, for this pressure point. This data point was not used in choosing an equation of state, but is added to figure 7-2 as a self-check that the simulated equation of state is plausible.

Using the ambient number density ρ_0 and the compression V/V_0 the number density and reduced density for the measured pressure points can be calculated. The values are given in table 7.3.

Pressure P (GPa)	Compression V/V_0	Number density ρ (Å^{-3})	Reduced density ρ/ρ_0
Ambient	1	0.0755	1
8.7(5)	0.869(8)	0.0868(8)	1.150(10)
10.9(5)	0.845(7)	0.0894(7)	1.184(9)
14.4(5)	0.808(5)	0.0934(6)	1.237(8)
17.5(5)	0.780(5)	0.0968(6)	1.282(8)

Table 7.3: Compression V/V_0, number density ρ, and reduced density ρ/ρ_0 for each pressure point measured in the PEARL $CaSiO_3$ experiment.

7.3.1 Molecular dynamics simulations

The experimental work reported in this chapter is compared to two different sets of separate molecular dynamics (MD) simulations [48, 49]. The first study, undertaken by Shimoda and Okuno [49], investigated $CaSiO_3$ at ambient pressure and at pressures of 7.5 GPa and 15 GPa. The MD simulations were performed using the MXDORTO codes developed in Ref. [216]. The pair potentials that were used consisted of Coulombic, short-range repulsion, van der Waals attraction, and Morse potential terms. 2000 atoms were used with periodic boundary conditions and a time-step of 2 fs. The initial structure was generated randomly and the following thermal/pressure history applied:

- The system was equilibriated at 4000 K for 500,000 steps.
- The temperature was reduced to 3500 K at a rate of −0.01 K/step.
- The temperature was equilibrated for 950,000 steps.
- This process of temperature reduction and equilibration was repeated every 500 K down to 1000 K.
- The temperature was then quenched to 300 K at a rate of −0.01 K/step and allowed to equilibrate for 950,000 steps.
- Homogeneous compressions were then applied up to 15 GPa with 2.5 GPa steps. At each pressure structural relaxation was allowed to proceed with a 1,000,000 step equilibration period.

The second study, undertaken by Mead and Mountjoy [48], investigated $CaSiO_3$ at ambient pressure and at pressures of 5 GPa and 10 GPa. The MD simulations were performed using the DLPOLY program [217] with a 2 fs time step, 1000 atoms, and periodic boundary conditions. The pair potentials that were used consisted of Coulombic,

short-range repulsion, and van der Waals attraction terms. Models were made using the Berensden NVT and NPT algorithms at ambient and high-pressure, respectively. The initial structure was generated randomly under pressure and the following thermal history applied:

- Temperature baths were applied for 80,000 steps at 6000 K, 4000 K, and either 2000 K, 2400 K, or 2600 K depending on whether the pressure point was ambient, 5 GPa, or 10 GPa, respectively.
- The atoms were quenched to 300 K at a rate of $13\,\mathrm{K\,s^{-1}}$.
- A further temperature bath of 80,000 steps was applied at 300 K.

Due to differences in the thermal history, the work of Ref. [48] can be classed as a liquid that has been quenched into a glass under high-pressure conditions. This is different to the work of Ref. [49], where the glass was first formed under ambient conditions and then cold-compressed.

7.4 Results

Figure 7-3 shows the pressure dependence of the total structure factor $F(Q)$ for amorphous $CaSiO_3$. The figure compares the neutron diffraction results from the present work with MD results at ambient pressure, 5 GPa, and 10 GPa [48], and with MD results at ambient pressure, 7.5 GPa, and 15 GPa [49]. For the neutron diffraction work, the D4c diffractometer was employed to make a high-precision measurement at ambient conditions, whilst a V3 Paris-Edinburgh press was utilised on the PEARL diffractometer to make measurements between ambient pressure and 17.5(5) GPa. A high-precision measurement was also made under ambient conditions using the GEM diffractometer, but the corresponding $F(Q)$ is not shown for clarity of presentation. The ambient-pressure D4c measurement has a cutoff $Q_{\mathrm{max}} = 23.5\,\mathrm{\AA^{-1}}$, whilst the high-pressure PEARL measurements have a cutoff $Q_{\mathrm{max}} = 19.55\,\mathrm{\AA^{-1}}$.

In figure 7-3, $F(Q)$ was obtained for the MD simulations of Ref. [48] by taking the individual partial structure factors $S^{\mathrm{FZ}}_{\alpha\beta}(Q)$ and summing them with the appropriate weighting factors (equation (7.1)). In the case of the MD simulations of Ref. [49], however, no reciprocal space data were available. Instead, the partial pair-distribution functions $g^{\mathrm{FZ}}_{\alpha\beta}(r)$ were first summed to give the total pair-distribution function $G(r)$. This function was then Fourier transformed into reciprocal space to give a total structure factor $F(Q)$, a process that leads to unphysical oscillations at low-Q. These artefacts arise from the need to use a relatively small cutoff $r_{\mathrm{max}} = 6\,\mathrm{\AA}$.

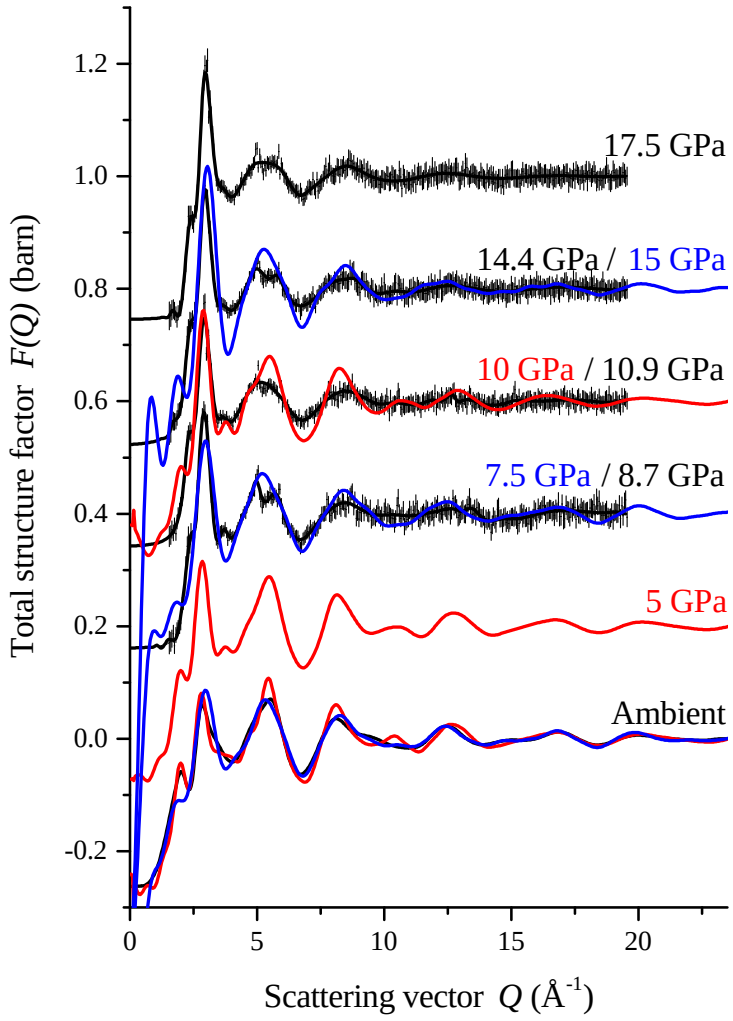

Figure 7-3: The pressure dependence of the total structure factor $F(Q)$ for amorphous $CaSiO_3$. The solid black curves show the back Fourier transforms of spline fits to the experimental data (shown by vertical error bars) for data sets measured using the D4c diffractometer at ambient pressure, and using the PEARL diffractometer at pressures of 8.7(5), 10.9(5), 14.4(5), and 17.5(5) GPa. The blue curves show MD results at ambient pressure and at 7.5 and 15 GPa and were obtained by Fourier transforming the simulated total pair-distribution functions using a cutoff $r_{max} = 6$ Å [49]. The red curves show MD results at ambient pressure and at 5 and 10 GPa and were obtained by adding the simulated partial structure factors together with the appropriate weighting factors [48]. The high-pressure curves have been offset vertically for clarity of presentation.

Origin	Pressure (GPa)	FSDP position (Å^{-1})	PP position (Å^{-1})
D4c	Ambient	2.02(3)	2.85(3)
PEARL	8.7(5)	2.41(7)	2.91(3)
	10.9(5)	2.37(7)	2.92(3)
	14.4(5)	2.45(7)	2.95(3)
	17.5(5)	2.44(7)	2.97(3)
Ref. [48]	Ambient	1.99(3)	2.81(3)
	5	2.00(3)	2.84(3)
	10	2.02(3)	2.87(3)
Ref. [49]	Ambient	N/A	2.97(3)
	7.5	N/A	2.97(3)
	15	N/A	3.05(3)

Table 7.4: Peak positions in the $F(Q)$ functions for amorphous $CaSiO_3$. The FSDP positions for Ref. [49] are not available due to the presence of unphysical low-Q oscillations (see the text).

Under ambient conditions, reciprocal space features in the MD work of Ref. [48], such as the first-sharp diffraction peak (FSDP) and principal peak (PP), have similar heights and positions as the neutron diffraction results. There is, however, a difference at higher-Q values in the height and phase of certain peaks. The data from Ref. [49] show a reduced FSDP height and a shift in position for both the FSDP and PP when compared to the neutron diffraction results.

As the pressure is increased, all data sets show a shift in the PP position to higher-Q, as well as a sharpening of this peak and an increase in its height. The FSDP shows a marked change in position between ambient and 8.7(5) GPa for the neutron diffraction results, although at higher pressures it seems to be relatively stable, as shown in table 7.4. Both sets of MD simulations show high-Q oscillations that have a larger amplitude by comparison with the neutron diffraction results.

Figure 7-4 shows the pressure dependence of the total pair-distribution function $G(r)$ for amorphous $CaSiO_3$. In the case of the neutron diffraction results, the reciprocal space data sets were Fourier transformed using (i) a step modification function (equation (7.3)) and (ii) a Lorch modification function (equation (7.4)) [56]. The data obtained from the first procedure were joined smoothly to the data obtained from the second procedure at a point just beyond the first peak in real space. The Fourier transforms of the MD $F(Q)$ functions used the same $Q_{\max}$ cutoffs as their neutron diffraction counterparts.

At ambient pressure, the Si-O peak position from Ref. [48] is in good agreement

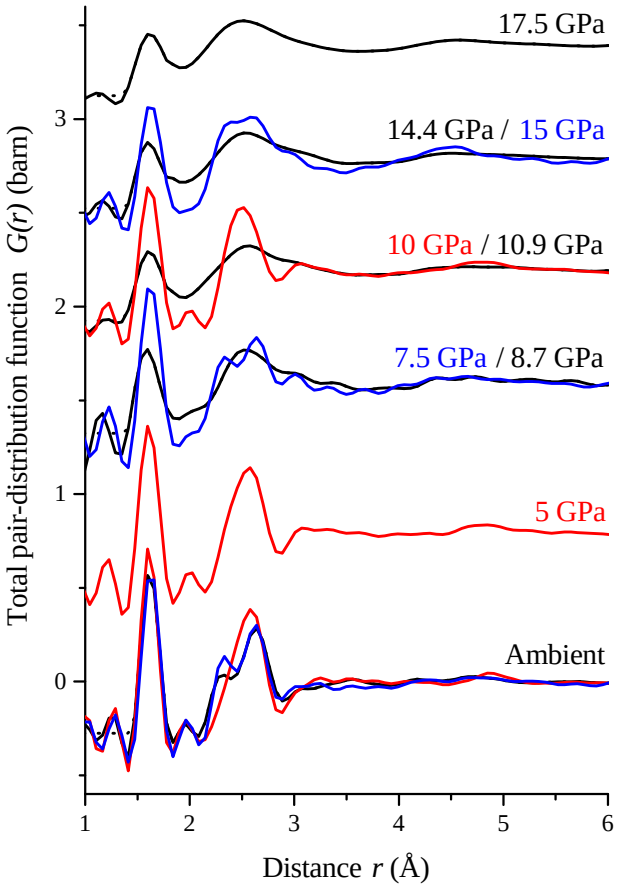

Figure 7-4: The pressure dependence of the total pair-distribution function $G(r)$ for amorphous $CaSiO_3$. The curves shown here correspond to those given in figure 7-3. The solid black curves show the Fourier transforms of spline fits to the $F(Q)$ data sets measured at ambient pressure and at pressures of 8.7(5), 10.9(5), 14.4(5), and 17.5(5) GPa. The dashed black curves show the calculated $G_N(r \rightarrow 0)$ limits at distances below the closest approach between two atoms. The blue curves show the Fourier transforms of the MD data sets at ambient pressure and at 7.5 and 15 GPa [49]. The red curves show the Fourier transforms of the MD data sets at ambient pressure and at 5 and 10 GPa [48]. The MD data were Fourier transformed using the same Q_{max} as the neutron diffraction results, namely 23.5 $Å^{-1}$ and 19.55 $Å^{-1}$ for ambient and high-pressure, respectively. The high-pressure curves have been offset vertically for clarity of presentation.

with the neutron diffraction results, although the height of the simulated peak is larger. There is a discrepancy, however, between the shape and position of the second nearest-neighbour peak. The MD results of Ref. [48] show a single peak, whilst the neutron diffraction results show a peak with a shoulder on its low-r side. At ambient pressure, the Si-O peak position and height from Ref. [49] are in good agreement with the neutron diffraction results. Furthermore, the position and shape of the second nearest-neighbour peak is also in agreement, though the height of the low-r shoulder is slightly higher for the MD results.

As the pressure increases, the agreement between the neutron diffraction and MD $G(r)$ functions begins to decrease. The first peak positions remain broadly the same, as shown in figure 7-5, although the MD simulations show much larger peak heights. As the Fourier transformations of all data sets were made with the same cutoff $Q_{\max}$ value, this increase in peak height must be primarily due to the increased oscillations at high-Q found in the MD results, *i.e.* the MD results show a Si-O nearest-neighbour coordination environment that is better defined than found by neutron diffraction. For the neutron diffraction results, the region between the first and second peaks in $G(r)$ begins to fill in with increasing pressure, a feature that is not seen in either of the MD simulations.

Figures 7-5(a) and 7-5(b) show the pressure dependence of the Si-O bond distance and mean nearest-neighbour coordination number, respectively. The coordination numbers for the MD simulations are those quoted in Refs. [48, 49], and correspond to the values obtained by integrating over the first peak in a Si-O partial pair-distribution function.

The neutron diffraction and MD results from Refs. [48, 49] show that the Si-O bond distance r_{SiO} remains relatively stable up to 17.5(5) GPa. The neutron diffraction and MD results from Ref. [49] show that the mean Si-O coordination number $\overline{n}^{\mathrm{O}}_{\mathrm{Si}}$ stays constant up to ~ 11 GPa before starting to increase. In comparison, the results reported in Ref. [48] suggested that the mean coordination number begins to increase at a much lower pressure $P \sim 5$ GPa. This increase in the mean Si-O coordination number can be seen in figure 7-4 as a growing asymmetry on the high-r side of the Si-O peak for both the neutron diffraction results and MD results from Ref. [49].

The Si-O bond distances and mean coordination numbers for amorphous SiO_2 under pressure are also presented in figures 7-5(a) and 7-5(b), respectively. The Si-O bond distance for SiO_2 is smaller than that for $CaSiO_3$ and decreases with increasing pressure. The mean coordination number is constant at pressures up to 15 GPa, and then starts to increase. This behaviour is similar to $CaSiO_3$, although it begins to increase at a lower pressure of $P \sim 13$ GPa.

In figure 7-5(a), the horizontal solid black line shows the average bond distance

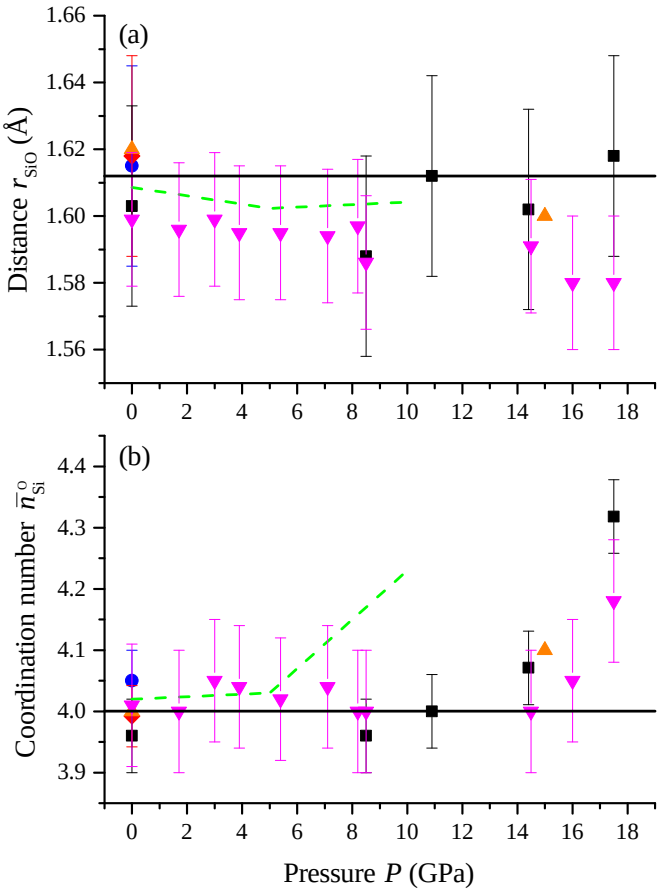

Figure 7-5: The pressure dependence of the Si-O (a) bond distance r_{SiO} and (b) coordination number $\overline{n}^{O}_{Si}$ for amorphous $CaSiO_3$ as obtained from (i) neutron diffraction using a $CaSiO_3$ sample on either the D4c (●), GEM (♦), or PEARL (■) diffractometer; (ii) MD simulations [48] (dashed green line); and (iii) MD simulations [49] (▲). Results for amorphous SiO_2 are also given and were obtained by using neutron diffraction [50] (▼). In (a), the horizontal solid black line gives the mean of the measured ambient-pressure bond distances $\overline{r} = 1.612$ Å. In (b), the horizontal solid black line gives the coordination number expected for an SiO_4 tetrahedron $\overline{n}^{O}_{Si} = 4$.

$\overline{r}_{\mathrm{SiO}} = 1.612\,\text{Å}$ for amorphous $CaSiO_3$ as calculated from the measured bond distances at ambient for measurements made using either a Paris-Edinburgh press on PEARL or a vanadium can on D4c and GEM. In figure 7-5(b), the horizontal solid black line shows the mean Si-O coordination number for a SiO_4 tetrahedron $\overline{n}^{\mathrm{O}}_{\mathrm{Si}} = 4$.

7.5 Discussion

The neutron diffraction results show that the Si-O bond distance r_{SiO} stays constant, within the experimental error, across the measured pressure range up to 17.5(5) GPa. In comparison, the mean Si-O coordination number $\overline{n}^{\mathrm{O}}_{\mathrm{Si}} = 4$ up to a threshold pressure of 13 GPa, before starting to increase. At pressures below this threshold, the $\overline{n}^{\mathrm{O}}_{\mathrm{Si}}$ value is consistent with the persistence of SiO_4 tetrahedra. The neutron diffraction results for r_{SiO} and $\overline{n}^{\mathrm{O}}_{\mathrm{Si}}$ are in accord with the MD results reported in Ref. [49]. In contrast, the MD results reported in Ref. [48] suggest that $\overline{n}^{\mathrm{O}}_{\mathrm{Si}}$ begins to increase at a much lower pressure $P \sim 5$ GPa.

The mean Si-O bond distance r_{SiO} and coordination number $\overline{n}^{\mathrm{O}}_{\mathrm{Si}}$ for amorphous SiO_2 [50] are plotted for comparison with the $CaSiO_3$ results in figures 7-5(a) and 7-5(b), respectively. Above 14 GPa, r_{SiO} shows a small decrease in distance, which is in contrast to the results for $CaSiO_3$ where the distance is constant up to at least 17.5(5) GPa. Similar to the $CaSiO_3$ results, $\overline{n}^{\mathrm{O}}_{\mathrm{Si}}$ is constant up to a threshold pressure before beginning to increase. This threshold pressure is, however, different for the two glasses, with the change in coordination number beginning at $P \sim 13(1)$ GPa and $\sim 15.0(5)$ GPa for $CaSiO_3$ and SiO_2, respectively. This shows that the inclusion of network-modifying Ca^{2+} ions has an effect on the densification mechanism.

The MD results reported in Refs. [48, 49] are compared to the neutron diffraction results of the present work in reciprocal and in real space in figures 7-3 and 7-4, respectively. At ambient pressure, the MD results presented in Ref. [49] perform much better than those from Ref. [48] in both real and reciprocal space. In particular, the second peak in $G(r)$ from Ref. [48] does not show a low-r shoulder. The second peak in $G(r)$ is formed mainly from the $g^{\mathrm{FZ}}_{\mathrm{CaO}}(r)$ and $g^{\mathrm{FZ}}_{\mathrm{OO}}(r)$ functions, as seen in figure 7-6. The different MD simulations show different nearest-neighbour Ca-O peak positions.

As the pressure is increased, here is disagreement in reciprocal and real space between the neutron diffraction results and both sets of MD results. The latter show larger amplitude high-Q oscillations in reciprocal space, and better defined first and second nearest-neighbour peaks in real space. This suggests that the pair potentials used in the MD simulations are not able to adequately replicate the high-pressure structure of $CaSiO_3$.

The MD simulations reported in Ref. [48] show an increase in the mean coordination

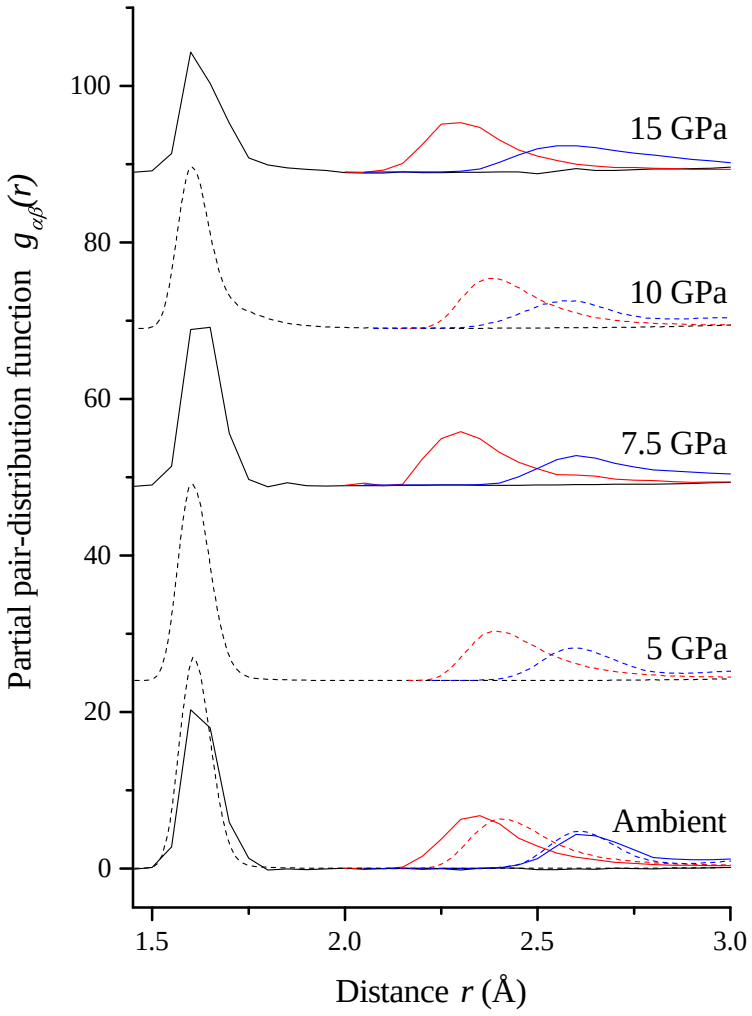

Figure 7-6: The pressure dependence of the partial pair-distribution functions $g^{\mathrm{FZ}}_{\alpha\beta}(r)$ for amorphous $CaSiO_3$. Included are the $g^{\mathrm{FZ}}_{\mathrm{SiO}}(r)$ (black), $g^{\mathrm{FZ}}_{\mathrm{CaO}}(r)$ (red), and $g^{\mathrm{FZ}}_{\mathrm{OO}}(r)$ (blue) functions. The solid and dashed curves show the MD results from Ref. [49] and Ref. [48], respectively. The high-pressure curves have been offset vertically for clarity of presentation.

number at a pressure that is much lower than found in the current work or in the MD simulations reported in Ref. [49]. This discrepancy may originate from the choice of pair-potentials used, as has already been discussed. It may also originate from the MD simulations in Ref. [48] using a different thermal history under pressure, as compared to the MD simulations in Ref. [49].

In the neutron diffraction work, the sample was cold-compressed, *i.e.* it was not heated under compression. As discussed in section 7.3.1, the results from Ref. [49] were obtained by using a cold compression protocol, whereas the results from Ref. [48] were obtained by using a quench-from-the-melt protocol. Quenching a liquid from high-temperature while under pressure may have allowed the MD simulations to explore different structural configurations, possibly explaining the increase of $\overline{n}^{\mathrm{O}}_{\mathrm{Si}}$ at a much lower pressure and the larger heights of the peaks in real space. Figure 7-6 shows three of the partial pair-distribution functions for $CaSiO_3$ as simulated in Refs. [48, 49].

7.6 Conclusions

The *in situ* high-pressure structure of amorphous $CaSiO_3$ has been measured using neutron diffraction at pressures ranging from ambient to 17.5(5) GPa using a Paris-Edinburgh press mounted on the PEARL diffractometer. The measured total structure factors $F(Q)$, their Fourier transforms $G(r)$, and derived parameters such as the Si-O coordination number and bond distance, are compared with the MD simulations reported in Refs. [48] and [49].

Under ambient conditions, the MD results of Ref. [49] are in better agreement with the neutron diffraction results in both reciprocal and real space. For example, the results of Ref. [48] do not adequately reproduce the shape of the first and second peaks in $G(r)$. It is theorised that this is due to the MD simulations from Ref. [48] using pair-potentials that are either unsuitable or badly parameterised.

The first coordination shell of Si is found to be relatively stable up to $P \sim 13$ GPa, with an Si-O bond distance $r_{\mathrm{SiO}} = 1.61(2)$ Å and coordination number $\overline{n}^{\mathrm{O}}_{\mathrm{Si}} = 4.0(1)$. As the pressure is increased beyond $P \sim 13$ GPa, however, $\overline{n}^{\mathrm{O}}_{\mathrm{Si}}$ begins to increase as the region between the first and second peaks in $G(r)$ gains intensity.

The change in the Si-O coordination number with pressure reported in Ref. [49] agrees with the neutron diffraction results of the current work. The results reported in Ref. [48] show, however, an increase in $\overline{n}^{\mathrm{O}}_{\mathrm{Si}}$ at much lower pressures. This may be due, in part, to the MD simulations having having a different thermal history to the neutron diffraction experiments, thus allowing the MD simulations to access different structural configurations.

The pressure-dependence of the nearest neighbour Si-O shell is compared for both

amorphous $CaSiO_3$ and SiO_2 [50]. The pressure-dependence of $\overline{n}_{Si}^{O}$ is found to be similar, although the coordination number begins to change at a higher pressure, $P \sim 15\,\mathrm{GPa}$, for SiO_2. Based on the difference between the $CaSiO_3$ and SiO_2 results, further work is required to study how network-modifying atoms, such as Ca, Mg, and Na, can be used to alter the densification properties of silicate glasses.

Finally, it would be of interest to investigate the pressure dependence of glasses in which Si is substituted with Ge. For example, GeO_2 is a structural analogue of SiO_2 and provides similar pressure-induced structural changes but at lower pressures [85, 86], making for easier experiments. A study of *e.g.* $CaGeO_3$ would therefore provide complementary information on the structural transformations of network-forming glasses at high pressures.

8. Overall Conclusions

In this work, the atomic structure of four network-forming glasses $GeSe_2$, $GeSe_4$, As_2Se_3, and $CaSiO_3$ was studied using *in situ* high-pressure neutron diffraction with a Paris-Edinburgh press at pressures up to 17.5(5) GPa. The neutron diffraction results were compared to both simulated and experimental results, helping to build a unified picture of how the structure of important prototypical network-forming glasses change under extreme conditions.

In chapter 4, the structure of amorphous $GeSe_2$ was investigated at pressures up to 16.2(5) GPa. NDIS was used with the D4c diffractometer at pressures up to 8.2(5) GPa [79], and higher-pressures were accessed by using the PEARL instrument. The experimental results were also compared to those obtained from complementary first-principles molecular dynamics (FPMD) simulations [42]. It was found that the density-driven network collapse of $GeSe_2$ comprises two distinct regimes with a threshold pressure $P = 8.5$ GPa. Below this threshold, the mean coordination number $\overline{n}$ remains constant and structural change manifests itself on an intermediate length scale by the re-organisation of $GeSe_4$ tetrahedra. Above this threshold, both $\overline{n}$ and the mean nearest-neighbour distance $\overline{r}$ begin to increase as 5- and 6- fold coordinated Ge atoms begin to form. Unfortunately, there is a discrepancy between the neutron diffraction and MD results at pressures greater than 8.5 GPa. This discrepancy is attributed to the presence of an energy barrier to structural rearrangement, which cannot be explored in the cold-compression diffraction experiments but can be accessed via a high-temperature annealing stage in the simulations.

In chapter 5, the *in situ* high-pressure structure of amorphous $GeSe_4$ was investigated at pressures ranging from ambient to 14.4(5) GPa (reduced density $\rho/\rho_0 \sim 1.51$) using a Paris-Edinburgh press mounted on either the D4c or PEARL diffractometer. The neutron diffraction results were compared with complementary FPMD simulations [42]. The neutron diffraction results were also used to test the validity of two sets of competing x-ray diffraction results [43, 44]. The neutron diffraction results agree well with the results from Ref. [43], whilst questions were raised with regards to the validity of the results from Ref. [44]. The nearest-neighbour coordination shell remains

relatively stable, showing a constant mean bond distance $\overline{r}_1$ and coordination number $\overline{n}$ up to a pressure of 14.4(5) GPa. Densification takes place on an intermediate range *e.g.*, the mean second nearest-neighbour distance $\overline{r}_2$ shows a two-stage movement to lower r upon compression, where an initially gradual decrease below a reduced density $\rho/\rho_0 \sim 1.2$ is followed by a steeper decrease at higher ρ/ρ_0 values. The results were also compared to the results presented in chapter 4 for the chalcogenide glass $GeSe_2$. It was found that due to differences in the equations of state, $GeSe_4$ was measured in the reduced-density range where the local structure of $GeSe_2$ is similarly constant.

In chapter 6, neutron diffraction experiments were made to investigate the structural transformations in amorphous As_2Se_3 at pressures up to 14.4(5) GPa using a Paris-Edinburgh press mounted on either the D4c or PEARL diffractometer. For the D4c results, NDIS was used at pressures up to 8.1(5) GPa to provide further information at the first-order difference function level. The neutron diffraction results at ambient conditions were compared with reverse Monte Carlo results derived from anomalous x-ray scattering [45] and FPMD simulations [45–47]. The mean nearest-neighbour coordination shell appears to be constant up to 14.4(5) GPa from the total structure factor results, showing a constant mean bond distance $\overline{r}_1$ and effective mean coordination number $\overline{n}'$. Information at the first-order difference pair-distribution function level suggests, however, that there is some change to the nearest-neighbour coordination environment beginning at 6 GPa, as both $\Delta G(r)_{\text{no Se-Se}}$ and $\Delta G(r)_{\text{no As-Se}}$ show an increase in the effective mean coordination number. Unfortunately, it is difficult to ascertain what is causing these changes to $\overline{n}'_{\text{X}}$. It is hoped that the neutron diffraction results of the present work in combination with further molecular dynamics simulations currently being undertaken [47] will provide further detail on the compression mechanisms.

In chapter 7, the high-pressure structure of amorphous $CaSiO_3$ was measured using neutron diffraction at pressures up to 17.5(5) GPa using a Paris-Edinburgh press mounted on the PEARL diffractometer. The neutron diffraction results were compared with two sets of different molecular dynamics (MD) results [48, 49]. The first coordination shell of Si was found to be relatively stable up to $P \sim 13$ GPa, with an Si-O bond distance $r_{\text{SiO}} = 1.61(2)$ Å and coordination number $\overline{n}^{\text{O}}_{\text{Si}} = 4.0(1)$. As the pressure is increased beyond $P \sim 13$ GPa, $\overline{n}^{\text{O}}_{\text{Si}}$ begins to increase as the region between the first and second peaks in $G(r)$ gains in intensity. The change in the Si-O coordination number with pressure reported in the MD work of Ref. [49] agrees with the neutron diffraction results of the current work. The MD results reported in Ref. [48] show, however, an increase in $\overline{n}^{\text{O}}_{\text{Si}}$ at much lower pressures. It is theorised that this is due to (i) the MD simulations using pair-potentials that are unsuitable for high-pressure simulations, or (ii) the use of a different thermal history to the neutron diffraction measurements, that

allows the MD simulations to access different structural configurations as compared to experiment. The pressure-dependence of the nearest neighbour Si-O shell was compared to results obtained for amorphous SiO_2 [50]. It was found that the threshold pressure at which $\overline{n}_{\mathrm{Si}}^{\mathrm{O}}$ begins to change is different for the two materials.

Looking further ahead, the next logical step is to extend the Paris-Edinburgh press such that both high-pressures and high-temperatures can be used in the experimental work. This would be useful for the field of geophysics, where pressures and temperatures of 16 GPa and 2000 K, respectively, would provide access by experiment to upper mantle conditions. Another potential outcome of using high-pressures and high-temperatures would be the ability to recover glasses to ambient conditions that have chosen *e.g.* optoelectronic properties. This would allow the glasses to be "tuned" for specific uses through changes to their structure.

Bibliography

[1] N. E. Cusack. *The Physics of Structurally Disordered Matter: An Introduction.* IOP Publishing, Bristol, 1987.

[2] S. R. Elliott. *Physics of Amorphous Materials.* Longman Group UK, Essex, 2nd. edition, 1990.

[3] A. Feltz. *Amorphous Inorganic Materials and Glasses.* Weinheim, VCH, 1993.

[4] P. N. Kumta and S. H. Risbud. Rare-earth chalcogenides: an emerging class of optical materials. *J. Mater. Sci.*, 29:1135–1158, 1994. 10.1007/BF00975057.

[5] M. Yamane and Y. Asahara. *Glasses for Photonics.* Cambridge University Press, Cambridge, 2000.

[6] P. Boolchand. *Insulating and Semiconducting Glasses.* World Scientific, Singapore, 2000.

[7] J. S. Sanghara, I. D. Aggarwal, L. B. Shaw, L. E. Busse, P. Thielen, V. Nguyen, P. Pureza, S. Bayya, and F. Kung. Applications of chalcogenide glass optical fibers at NRL. *J. Optoelec. Adv. Mat.*, 3:627, 2001.

[8] A. Zakery and S. R. Elliott. Optical Properties and Applications of Chalcogenide Glasses: A Review. *J. Non-Cryst. Solids*, 330:1, 2003.

[9] D. Lezal, J. Pedlikova, and J. Zavadil. Chalcogenide glasses for optical and photonics applications. *Chal. Lett.*, 1:11, 2004.

[10] N. Mehta. Applications of chalcogenide glasses in electronics and optoelectronics: A review. *J. Sci. Indus. Res*, 65:777, 2006.

[11] G. N. Greaves and S. Sen. Inorganic glasses, glass-forming liquids and amorphizing solids. *Adv. Phys.*, 56:1, 2007.

[12] A. Zakery and S. R. Elliott. *Optical Nonlinearities in Chalcogenide Glasses and their Applications.* Springer, Berlin, 2007.

[13] A. R. Hilton. *Chalcogenide Glasses for Infrared Optics*. McGraw-Hill, New York, 2009.

[14] B. J. Eggleton, B. Luther-Davies, and K. Richardson. Chalcogenide photonics. *Nature Phot.*, 5:141, 2011.

[15] J. P. Poirier. *Introduction to the Physics of the Earth's Interior*. Cambridge University Press, Cambridge, 1991.

[16] D. L. Anderson. *New Theory of the Earth*. Cambridge University Press, Cambridge, 2007.

[17] F. Franks. *Water: A Matrix of Life*. Cambridge University Press, Cambridge, 2nd edition, 2000.

[18] F. Paesani and G. A. Voth. The Properties of Water: Insights from Quantum Simulations. *J. Phys. Chem. B*, 113:5702, 2009.

[19] V. V. Brazhkin and A. G. Lyapin. High-pressure phase transformations in liquids and amorphous solids. *J. Phys.: Condens. Matter*, 15(36):6059, 2003.

[20] P. F. McMillan. Polyamorphic transformations in liquids and glasses. *J. Mater. Chem.*, 14:1506, 2004.

[21] M. C. Wilding, M. Wilson, and P. F. McMillan. Structural studies and polymorphism in amorphous solids and liquids at high pressure. *Chem. Soc. Rev.*, 35:964, 2006.

[22] K. Arai, K. Kumata, K. Kadota, K. Yamamoto, H. Namikawa, and S. Saito. Pressure effects on electrical conduction in glasses. *J. Non-Cryst. Solids*, 13:131, 1973.

[23] N. Soga and M. Kunugi. Elastic properties of Se and As2Se3 glasses under pressure and temperature. *J. Phys. Chem. Solids*, 34:2143, 1973.

[24] G. Pfister. Pressure dependent electronic transport in amorphous As_2Se_3. *Phys. Rev. Lett.*, 33:1474, 1974.

[25] R. Ota and O. L. Anderson. Variations in the mechanical properties of glass by induced high-pressure phase change. *J. Non-Cryst. Solids*, 24:235, 1977.

[26] J. C. Thompson and K. E. Bailey. A survey of the elastic properties of some semiconducting glasses under pressure. *J. Non-Cryst. Solids*, 27:161, 1978.

[27] G. Parthasarathy and E. S. R. Gopah. Effect of high pressure on chalcogenide glasses. *Bull. Mater. Sci.*, 7:271, 1985.

[28] M. Xu, Q. Cheng, L. Wang, H. W. Sheng, Y. Meng, W. G. Yang, X. D. Han, and E. Ma. Pressure tunes electrical resistivity by four orders of magnitude in amorphous $Ge_2Sb_2Te_5$ phase-change memory alloy. *Proc. Natl. Acad. Sci. USA*, 102:E1055, 2012.

[29] M. Wuttig and N. Yamada. Phase-change materials for rewriteable data storage. *Nat. Mater.*, 6:824, 2007.

[30] S. Raoux, G. W. Burr, M. J. Breitwish, C. T. Rettner, Y.-C. Chen, R. M. Shelby, M. Salinga, D. Krebs, S.-H. Chen, H.-L. Lung, and C. H. Lam. Phase-change random access memory: A scalable technology. *IBM J. Res. & Dev.*, 52:465, 2008.

[31] S. Asokan, M. V. N. Prasad, G. Parthasarathy, and E. S. R. Gopal. Mechanical and chemical thresholds in IV-VI chalcogenide glasses. *Phys. Rev. Lett.*, 62:808, 1989.

[32] M. V. N. Prasad, S. Asokan, and G. Parthasarathy. Electrical-resistivity studies on Ge-Se glasses at high-pressures and low-temperatures. *Phys. Chem. Glasses*, 34:199, 1993.

[33] V. V. Brazhkin, E. Bychkov, and M. V. Kondrin. Metallization in the molten and solid state and phase diagrams of the $GeSe_2$ and GeS_2 under high pressure. *JETP Letters*, 100:451, 2014.

[34] Z. He, X. Liu, D. Zhang, L. Zhang, and S. Hong. Pressure effect on thermal-induced crystallization of amorphous selenium up to 5.5 GPa. *Solid State Commun.*, 197:30, 2014.

[35] J. F. Stebbins and P. F. McMillan. Five- and six-coordination Si in $K_2Si_4O_9$ liquid at 1.9 GPa and 1200 °C. *Am. Mineral.*, 74:965, 1989.

[36] X. Xue, J. F. Stebbins, M. Kanzaki, and R. G. Trönnes. Silicon coordination and speciation changes in a silicate liquid at high pressure. *Science*, 245:962, 1989.

[37] J. F. Stebbins and D. Sykes. The structure of $NaAlSi_3O_8$ liquids at high pressure: new constraints from NMR spectroscopy. *Am. Mineral.*, 75:943, 1990.

[38] S. A. Amin, K. Leinenweber, C. J. Benmore, J. K. R. Weber, and J. L. Yarger. Characterizing Pressure-Induced Coordination Changes in $CaAl_2O_4$ Glass Using ^{27}Al NMR. *J. Phys. Chem. C*, 116:2068, 2012.

[39] S. K. Lee, Y. S. Yi, G. D. Cody, K. Mibe, Y. Fei, and B. O. Mysen. Effect of Network Polymerization on the Pressure-Induced Structural Changes in Sodium Aluminosilicate Glasses and Melts: ^{27}Al and ^{17}O Solid-State NMR Study. *J. Phys. Chem. C*, 116:2183, 2012.

[40] N. Funamori. Exploratory studies of silicate melt structure at high pressures and temperatures by *in situ* x-ray diffraction. *J. Geophys. Res*, 109:B03203, 2004.

[41] K. Wezka. *Pressure induced structural transformations of network forming glasses*. PhD thesis, University of Bath, 2013.

[42] A. Bouzid. *First-principles investigation of binary and ternary amorphous chalcogenide systems*. PhD thesis, University of Strasbourg, 2014.

[43] L. B. Skinner, C. J. Benmore, S. Antao, E. Soignard, S. A. Amin, E. Bychkov, E. Rissi, J. B. Parise, and J. L. Yarger. Structural changes in vitreous $GeSe_4$ under pressure. *J. Phys. Chem. C*, 116:2212, 2012.

[44] B. Kalkan, R. P. Dias, C.-S. Yoo, S. M. Clark, and S. Sen. Polyamorphism and pressure induced metallization at the rigidity percolation threshold in densified $GeSe_4$ glass. *J. Phys. Chem. C*, 118:5110, 2014.

[45] S. Hosokawa, A. Koura, Brar J-F., W-C. Pilgrim, Kohara S., and F. Shimojo. Does the 8-N bonding rule break down in As_2Se_3 glass? *Europhys. Lett.*, 102:66008, 2013.

[46] M. Bauchy, M. Micoulaut, M. Boero, and Massobrio C. Compositional thresholds and anomalies in connection with stiffness transitions in network glasses. *Phys. Rev. Lett.*, 110:165501, 2013.

[47] M. Micoulaut. Private communication, 2014.

[48] R. N. Mead and G. Mountjoy. A molecular dynamics study of densification mechanisms in calcium silicate glasses $CaSi_2O_5$ and $CaSiO_3$ at pressures of 5 and 10 GPa. *J. Chem. Phys.*, 125:154501, 2006.

[49] K. Shimoda and M. Okuno. Molecular dynamics study of $CaSiO_3$-$MgSiO_3$ glasses under high pressure. *J. Phys.: Condens. Matter*, 18:6531, 2006.

[50] A. Zeidler, K. Wezka, R. F. Rowlands, D. A. J. Whittaker, P. S. Salmon, A. Polidori, J. W. E. Drewitt, S. Klotz, H. E. Fischer, M. C. Wilding, C. L. Bull, M. G. Tucker, and M. Wilson. High-pressure transformation of SiO_2 glass from a tetrahedral to an octahedral network: A joint approach using neutron diffraction and molecular dynamics. *Phys. Rev. Lett.*, 113:135501, 2014.

[51] P. S. Salmon and A. Zeidler. Networks under pressure: The development of *in situ* high-pressure neutron diffraction for glassy and liquid materials. *J. Phys.: Condens. Matter*, 27:133201, 2015.

[52] H. E. Fischer, A. C. Barnes, and P. S. Salmon. Neutron and x-ray diffraction studies of liquids and glasses. *Rep. Prog. Phys.*, 69:233, 2006.

[53] V. F. Sears. Neutron scattering lengths and cross sections. *Neutron News*, 3:26–37, 1992.

[54] G. Placzek. The scattering of neutrons by systems of heavy nuclei. *Phys. Rev.*, 86(3):377, 1952.

[55] T. E. Faber and J. M. Ziman. A theory of the electrical properties of liquid metals. *Philos. Mag.*, 11:153, 1965.

[56] E. Lorch. Neutron diffraction by germania, silica and radiation-damaged silica glasses. *J. Phys. C*, 2:229, 1969.

[57] P. S. Salmon. Decay of the pair correlations and small-angle scattering for binary liquids and glasses. *J. Phys.: Condens. Matter*, 18:11443, 2006.

[58] A. B. Bhatia and D. E. Thornton. Structural aspects of the electrical resistivity of binary alloys. *Phys. Rev. B*, 2:3004, 1970.

[59] P. S. Salmon. Structure of liquids and glasses in the Ge-Se binary system. *J. Non-Cryst. Solids*, 353:2959–2974, 2007.

[60] P. S. Salmon. The structure of molten and glassy 2:1 binary systems: an approach using the Bhatia-Thornton formalism. *Proc. R. Soc. Lond. A.*, 437:591, 1992.

[61] R. A. Martin, P. S. Salmon, H. E. Fischer, and G. J. Cuello. Structure of dysprosium and holmium phosphate glasses by the method of isomorphic substitution in neutron diffraction. *J. Phys.: Condens. Matter*, 15:8235, 2003.

[62] D. I. Grimley and A. C. Wright. Neutron scattering from vitreous silica IV. time-of-flight diffraction. *J. Non-Cryst. Solids*, 119:49, 1990.

[63] R. Angel. Equations of state. *Rev. Miner. Geo. Chem.*, 41:35, 2000.

[64] O. L. Anderson. *Equations of State of Solids for Geophysics and Ceramic Science.* Oxford University Press, Oxford, 1995.

[65] F. D. Murnaghan. The compressibility of media under extreme pressures. *Proc. Natl. Acad. Sci. USA*, 30:244, 1944.

[66] S. Klotz. *Techniques in high pressure neutron scattering.* CRC Press, Boca Raton, FL, 2013.

[67] F. Birch. Finite elastic strain of cubic crystals. *Phys. Rev.*, 71(11):809, 1947.

[68] J. M. Carpenter. Pulsed spallation neutron sources for slow neutron scattering. *Nucl. Instrum. Methods*, 145:91, 1977.

[69] http://www.isis.stfc.ac.uk/instruments/pearl/pearl2122.html.

[70] H. E. Fischer, G. J. Cuello, P. Palleau, D. Feltin, A. C. Barnes, Y. S. Badyal, and J. M. Simonson. D4c: A very high precision diffractometer for disordered materials. *Appl. Phys. A: Mater. Sci. & Proc.*, 74:s160, 2002.

[71] A. Zeidler, P. S. Salmon, H. E. Fischer, J. C. Neuefeind, J. M. Simonson, H. Lemmel, H. Rauch, and T. E. Markland. Oxygen as a site specific probe of the strucure of water and oxide materials. *Phys. Rev. Lett.*, 107:145501, 2011.

[72] J. M. Besson, R. J. Nelmes, G. Hamel, J. S. Loveday, G. Weill, and S. Hull. Neutron powder diffraction above 10 GPa. *Physica B: Condensed Matter*, 180 - 181(2):907, 1992.

[73] J. M. Besson, Ph. Pruzan, S. Klotz, G. Hamel, B. Silvi, R. J. Nelmes, J. S. Loveday, R. M. Wilson, and S. Hull. Variation of interatomic distances in ice VIII to 10 GPa. *Phys. Rev. B*, 49:12540, 1994.

[74] S. Klotz, J. M. Besson, G. Hamel, R. J. Nelmes, J. S. Loveday, W. G. Marshall, and R. M. Wilson. Neutron powder diffraction at pressures beyond 25 GPa. *Appl. Phys. Lett.*, 66(14):1735, 1995.

[75] S. Klotz, Th. Strässle, G. Rousse, G. Hamel, and V. Pomjakushin. Angle-dispersive neutron diffraction under high pressure to 10 GPa. *Appl. Phys. Lett.*, 86(3):031917, 2005.

[76] L. G. Khvostantsev, V. N. Slesarev, and V. V. Brazhkin. Toroid type high-pressure device: history and prospects. *High. Press. Res.*, 24(3):371, 2004.

[77] J. W. E. Drewitt. *Structure of copper halide melts, rare earth chalcogenide glasses, and glassy germania at high pressure.* PhD thesis, University of Bath, 2009.

[78] S. Klotz. Private communication, 2010.

[79] K. Wezka, A. Bouzid, K. J. Pizzey, P. S. Salmon, A. Zeidler, S. Klotz, H. E. Fischer, C. L. Bull, M. G. Tucker, M. Boero, S. Le Roux, C. Tugèue, and C. Massobrio. Density-driven defect-mediated network collapse of $GeSe_2$ glass. *Phys. Rev. B*, 90:054206, 2014.

[80] L. E. Bove, S. Klotz, J. Phillipe, and A. M. Saitta. Pressure-induced polyamorphism in salty water. *Phys. Rev. Lett.*, 106:125701, 2011.

[81] S. Klotz, J. Phillippe, C. L. Bull, J. S. Loveday, and R. J. Nelmes. A 3 kbar hydrogen-compatible gas loader for Paris-Edinburgh presses. *High. Press. Res*, 33:214, 2013.

[82] C. L. Bull, M. Guthrie, S. Klotz, J. Philippe, Th. Strässle, R. J. Nelmes, J. S. Loveday, and G. Hamel. Toroidal anvils for single-crystal neutron studies. *High. Press. Res*, 25(4):229, 2005.

[83] M. Guthrie. Private communication, 2014.

[84] A. Zeidler, M. Guthrie, and P. S. Salmon. Pressure dependent structure of the null-scattering alloy $Ti_{0.676}Zr_{0.324}$, submitted to *High Press. Res.*, 2015.

[85] J. W. E. Drewitt, P. S. Salmon, A. C. Barnes, S. Klotz, H. E. Fischer, and W. A. Crichton. Structure of GeO_2 glass at pressures up to 8.6 GPa. *Phys. Rev. B*, 81:014202, 2010.

[86] P. S. Salmon, J. W. E. Drewitt, D. A. J. Whittaker, A. Zeidler, K. Wezka, C. L. Bull, M. G. Tucker, M. C. Wilding, M. Guthrie, and D. Marrocchelli. High pressure neutron diffraction study of GeO_2 glass up to 17.5 GPa. *J. Phys.: Condens. Matter*, 24:415102, 2012.

[87] R. J. Hemley, A. P. Jephcoat, H. K. Mao, C. S. Zha, L. W. Finger, and D. E. Cox. Static compression of H_2O-ice to 128 GPa (1.28 Mbar). *Nature*, 330:737, 1987.

[88] H. H. Paalman and C. J. Pings. Numerical evaluation of x-ray absorption factors for cylindrical samples and annular sample cells. *J. Appl. Phys.*, 33(8):2635–2639, 1962.

[89] A. K. Soper and P. A. Egelstaff. Multiple scattering and attenuation of neutrons in concentric cylinders. *Nuc. Inst. Meth.*, 178(2-3):415, 1980.

[90] J. E. Enderby, D. M. North, and P. A. Egelstaff. The partial structure factors of liquid Cu-Sn. *Phil. Mag.*, 14:961, 1966.

[91] D. M. North, J. E. Enderby, and P. A. Egelstaff. The structure factor for liquid metals I. the application of neutron diffraction techniques. *J. Phys. C*, 1:784, 1968.

[92] S. E. McLain, D. T. Bowron, A. C. Hannon, and A. K. Soper. GUDRUN: A computer program developed for analysis of neutron diffraction data. Technical report, ISIS Facility, Rutherford Appleton Laboratory, 2009.

[93] M. A. Howe, R. L. McGreevy, and W. S. Howells. The analysis of liquid structure data from time-of-flight neutron diffractometry. *J. Phys.: Condens. Matter*, 1(22):3433, 1989.

[94] P. S. Salmon and J. Liu. The relation between the melt topology and glass-forming ability for liquid Ge-Se alloys. *J. Phys.: Condens. Matter*, 6:1449, 1994.

[95] A. P. Sokolov, A. Kishuk, M. Soltwisch, and D. Quitmann. Medium-range order in glasses: Comparison of Raman and diffraction measurements. *Phys. Rev. Lett.*, 69:1540, 1992.

[96] Z. U. Borisova. *Glassy Semiconductors*. Plenum Press, New York, 1981.

[97] A. Sartbaeva, S. A. Wells, A. Huerta, and M. F. Thorpe. Local structural variability and the intermediate phase window in network glasses. *Phys. Rev. B*, 75:224204, 2007.

[98] C. Massobrio, M. Celino, P. S. Salmon, R. A. Martin, M. Micoulaut, and A. Pasquarello. Atomic structure of the two intermediate phase glasses $SiSe_4$ and $GeSe_4$. *Phys. Rev. B*, 79(17):174201, 2009.

[99] P. Boolchand, J. Grothaus, W. J. Bresser, and P. Suranyi. Structural origin of broken chemical order in a $GeSe_2$ glass. *Phys. Rev. B*, 25:2975, 1982.

[100] M. Cobb, D. A. Drabold, and R. L. Cappelletti. *Ab initio* molecular-dynamics study of the structural, vibrational, and electronic properties of glassy $GeSe_2$. *Physical Review B*, 54:12162, 1996.

[101] I. Petri, P. S. Salmon, and H. E. Fischer. Defects in a disordered world: The structure of glassy $GeSe_2$. *Phys. Rev. Lett.*, 84(11):2413, 2000.

[102] X. Zhang and D. A. Drabold. Structural and electronic properties of glassy $GeSe_2$ surfaces. *Phys. Rev. B*, 62:15695, 2000.

[103] P. S. Salmon and I. Petri. Structure of glassy and liquid $GeSe_2$. *J. Phys.: Condens. Matter*, 15:S1509, 2003.

[104] P. S. Salmon, A. C. Barnes, R. A. Martin, and G. J. Cuello. Structure of glassy GeO_2. *J. Phys.: Condens. Matter*, 19(41):415110, 2007.

[105] C. Massobrio and A. Pasquarello. Short and intermediate range order in amorphous $GeSe_2$. *Phys. Rev. B*, 77(14):144207, 2008.

[106] A. Bouzid and C. Massobrio. Note: Accounting for pressure effects on the calculated equilibrium structure of glassy $GeSe_2$. *J. Chem. Phys.*, 137:046101, 2012.

[107] M. Durandurdu and D. A. Drabold. Simulation of pressure-induced polyamorphism in a chalcogenide glass $GeSe_2$. *Phys. Rev. B*, 65:104208, 2002.

[108] Q. Mei, C. J. Benmore, R. T. Hart, E. Bychkov, P. S. Salmon, C. D. Martin, F. M. Michel, S. M. Antao, P. J. Chupas, P. L. Lee, S. D. Shastri, J. B. Parise, K. Leinenweber, S. Amin, and J. L. Yarger. Topological changes in glassy $GeSe_2$ at pressures up to 9.3 GPa determined by high-energy x-ray and neutron diffraction measurements. *Phys. Rev. B*, 74:014203, 2006.

[109] K. Wezka, P. S. Salmon, A. Zeidler, D. A. J. Whittaker, J. W. E. Drewitt, S. Klotz, H. E. Fischer, and D. Marrocchelli. Mechanisms of network collapse in GeO_2 glass: high-pressure neutron diffraction with isotope substitution as arbitrator of competing models. *J. Phys.: Condens. Matter*, 24:502101, 2012.

[110] R. Car and M. Parrinello. Unified approach for molecular dynamics and density-functional theory. *Phys. Rev. Lett.*, 55:2471, 1985.

[111] M. Micoulaut, R. Vuilleumier, and C. Massobrio. Improved modeling of liquid $GeSe_2$: Impact of the exchange-correlation functional. *Phys. Rev. B*, 79:214205, 2009.

[112] S. Le Roux, A. Zeidler, P. S. Salmon, M. Boero, M. Micoulaut, and C. Massobrio. Structural properties of liquid Ge_2Se_3: A first-principles study. *Phys. Rev. B*, 84:134203, 2011.

[113] S. Le Roux, A. Bouzid, M. Boero, and C. Massobrio. Structural properties of glassy Ge_2Se_3 from first-principles molecular dynamics. *Phys. Rev. B*, 86:224201, 2012.

[114] M. Wilson, B. K. Sharma, and C. Massobrio. Ionicity in disordered $GeSe_2$: A comparison of first-principles and atomistic potential models. *J. Chem. Phys.*, 128:244505, 2008.

[115] R. Ota, T. Yamate, N. Soga, and M. Kunugi. Elastic properties of Ge-Se glass under pressure. *J. Non-Cryst. Solids*, 29(1):67, 1978.

[116] J.-P. Guin, T. Rouxel, J. C. Sangleboeuf, I. Melscoët, and J. Lucas. Elastic properties of Ge-Se glass under pressure. *J. Am. Ceram. Soc.*, 85:1545, 2002.

[117] A. D. Becke. Density-functional exchange-energy approximation with correct asymptotic behavior. *Phys. Rev. A.*, 38:3098, 1988.

[118] C. Lee, W. Yang, and R. G. Parr. Development of the Colle-Salvetti correlation-energy formula into a functional of the electron density. *Phys. Rev. B.*, 37:785, 1988.

[119] C. Massobrio, M. Micoulaut, and P. S. Salmon. Impact of the exchange-correlation functional on the structure of glassy $GeSe_2$. *Solid State Sci.*, 12:199, 2012.

[120] N. Troullier and J. L. Martins. Efficient pseudopotentials for plane-wave calculations. *Phys. Rev. B*, 43:1993, 1991.

[121] S. Nosé. A molecular dynamics method for simulations in the canonical ensemble. *Mol. Phys.*, 52:255, 1984.

[122] W. G. Hoover. Canonical dynamics: Equilibrium phase-space distributions. *Phys. Rev. A*, 31:1695, 1985.

[123] C. Adamo and V. Barone. Toward reliable density functional methods without adjustable parameters: The PBE0 model. *J. Chem. Phys.*, 110:6158, 1999.

[124] A. V. Krukau, O. A. Vydrov, A. F. Izmaylov, and G. E. Scuseria. Influence of the exchange screening parameter on the performance of screened hybrid functionals. *J. Chem. Phys.*, 125:224106, 2006.

[125] J. P. Perdew, M. Ernzerhof, and K. Burke. Rationale for mixing exact exchange with density functional approximations. *J. Chem. Phys.*, 105(22):9982, 1996.

[126] A. C. Wright. The comparison of molecular dynamics simulations with diffraction experiments. *J. Non-Cryst. Solids*, 159:264, 1993.

[127] A. Zeidler, P. S. Salmon, R. A. Martin, T. Usuki, P. E. Mason, G. J. Cuello, S. Kohara, and H. E. Fischer. Structure of liquid and glassy $ZnCl_2$. *Phys. Rev. B*, 82:104208, 2010.

[128] F. Wang, S. Mamedov, P. Boolchand, B. Goodman, and M. Chandrasekhar. Pressure Raman effects and internal stress in network glasses. *Phys. Rev. B*, 71:174201, 2005.

[129] S. M. Antao, C. J. Benmore, B. Li, L. Wang, E. Bychkov, and J. B. Parise. Network rigidity in $GeSe_2$ glass at high pressure. *Phys. Rev. Lett.*, 100:115501, 2008.

[130] G. Dittmar and H. Schäfer. Die kristallstruktur von germaniumdiselenid. *Acta Crystallogr. B*, 32:2726, 1976.

[131] A. Grzechnik, S. Stølen, E. Bakken, T. Grande, and M. Mezouar. Structural transformations in three-dimensional crystalline $GeSe_2$ at high pressures and high temperatures. *J. Solid State Chem.*, 150:121, 2000.

[132] T. Grande, M. Ishii, M. Akaishi, S. Aasland, H. Fjellvåg, and S. Stölen. Structural properties of $GeSe_2$ at high pressures. *J. Solid State Chem.*, 145:167, 1999.

[133] M. Shimada and F. Dachille. Crystallisation of amorphous germanium sulfide and germanium selenide under pressure. *Inorg. Chem.*, 16:2094, 1977.

[134] L. F. Kulikova, L. M. Lityagina, I. P. Zibrov, T. I. Dyuzheva, N. A. Nikolaev, and V. V. Brazhkin. High-pressure, high-temperature study of GeS_2 and $GeSe_2$. *Inorg. Mater.*, 50:768, 2014.

[135] K. Y. Kim, D.-Y. Cho, B. Cheong, D. Kim, H. Horii, and S. Han. Competing local orders in liquid and amorphous structures of $Ge_2Sb_2Te_5$: Influence of exchange-correlation functional. *J. Appl. Phys.*, 113:134302, 2013.

[136] P.-L. Chau and A. J. Hardwick. A new order parameter for tetrahedral configurations. *Mol. Phys.*, 93:511, 1998.

[137] J. R. Errington and P. G. Debenedetti. Relationship between structural order and the anomalies of liquid water. *Nature*, 409:318, 2001.

[138] L. B. Skinner, A. C. Barnes, P. S. Salmon, L. Hennet, H. E. Fischer, C. J. Benmore, S. Kohara, J. K. R. Weber, A. Bytchkov, M. C. Wilding, J. B. Parise, T. O. Farmer, I. Pozdnyakova, S. K. Tumber, and K. Ohara. Joint diffraction and modeling approach to the structure of liquid alumina. *Phys. Rev. B*, 87:024201, 2013.

[139] L. P. Dávila, M.-J. Caturla, A. Kubota, B. Sadigh, T. D. de la Rubia, J. F. Shackelford, S. H. Risbud, and S. H. Garofalini. Transformations in the medium-range order of fused silica under high pressure. *Phys. Rev. Lett.*, 91:205501, 2003.

[140] S. K. Lee, K. Mibe, Y. Fei, G. D. Cody, and B. O. Mysen. Structure of B_2O_3 glass at high pressure: A ^{11}B solid-state NMR study. *Phys. Rev. Lett.*, 94:165507, 2005.

[141] Y. Liang, C. R. Miranda, and S. Scandolo. Mechanical strength and coordination defects in compressed silica glass: Molecular dynamics simulations. *Phys. Rev. B*, 75:024205, 2007.

[142] D. Marrocchelli, M. Salanne, and P. A. Madden. High-pressure behaviour of GeO_2: a simulation study. *J. Phys.: Condens. Matter*, 22:152102, 2010.

[143] A. Zeidler, K. Wezka, D. A. J. Whittaker, P. S. Salmon, A. Baroni, S. Klotz, H. E. Fischer, M. C. Wilding, C. L. Bull, M. G. Tucker, M. Salanne, G. Ferlat, and M. Micoulaut. Density-driven structural transformations in B_2O_3. *Phys. Rev. B*, 90:024206, 2014.

[144] M. Wilson and P. S. Salmon. Network topology and the fragility of tetrahedral glass-forming liquids. *Phys. Rev. Lett.*, 103:157801, 2009.

[145] A. R. Hilton. Nonoxide Chalcogenide Glasses as Infrared Optical Materials. *Appl. Opt.*, 5:1877, 1966.

[146] G. Chen, H. Jain, M. Vlcek, and A. Ganjoo. Photoinduced volume change in arsenic chalcogenides by band-gap light. *Phys. Rev. B*, 74:174203, 2006.

[147] J. C. Phillips. Topology of covalent non-crystalline solids I: Short-range order in chalcogenide alloys. *J. Non-Cryst. Solids*, 34(2):153, 1979.

[148] M. Thorpe. Continuous deformations in random networks. *J. Non-Cryst. Solids*, 57:355, 1983.

[149] J. C. Phillips. Vibrational thresholds near critical average coordination in alloy network glasses. *Phys. Rev. B*, 31:8157, 1985.

[150] M. F. Thorpe, D. J. Jacobs, M. V. Chubynsky, and J. C. Phillips. Self-organization in network glasses. *J. Non-Cryst. Solids*, 266:859, 2000.

[151] D. Selvanathan, W. J. Bresser, P. Boolchand, and B. Goodman. Thermally reversing window and stiffness transitions in chalcogenide glasses. *Solid State Commun.*, 111(11):619, 1999.

[152] D. Selvanathan, W. J. Bresser, and P. Boolchand. Stiffness transitions in Si_xSe_{1-x} glasses from Raman scattering and temperature-modulated differential scanning calorimetry. *Phys. Rev. B*, 61:15061, 2000.

[153] P. Boolchand, D. G. Georgiev, and B. Goodman. Discovery of the intermediate phase in chalcogenide glasses. *J. Opto. Adv. Mat,*, 3:703, 2001.

[154] Y. Wang, J. Wells, D. G. Georgiev, and P. Boolchand. Sharp Rigid to Floppy Phase Transition Induced by Dangling Ends in a Network Glass. *Phys. Rev. Lett.*, 87:185503, 2001.

[155] M. V. Chubynsky and M. F. Thorpe. Self-organization and rigidity in network glasses. *Curr. Op. Sol. State Mater.*, 5:525, 2001.

[156] C. Massobrio, M. Celino, and A. Pasquarello. Evidence of concentration fluctuations in disordered network-forming systems: the case of $GeSe_4$ and $SiSe_2$. *J. Phys.: Condens. Matter*, 15:S1537, 2003.

[157] M. T. M. Shatnawi, C. L. Farrow, P. Chen, P. Boolchand, A. Sartbaeva, M. F. Thorpe, and S. J. L. Billinge. Search for a structural response to the intermediate phase in Ge_xSe_{1-x} glasses. *Phys. Rev. B*, 77:094134, 2008.

[158] U. Vempati and P. Boolchand. The thermally reversing window in ternary $Ge_xP_xS_{1-2x}$ glasses. *J. Phys.: Condens. Matter*, 16:S5121, 2004.

[159] S. Kohli, V. K. Sachdev, R. M. Mehra, and P. C. Mathur. High pressure studies on n-Type Se-In-Pb chalcogenide glasses. *Phys Stat. Sol. (b)*, 209:389, 1998.

[160] B. H. Sharmila, J. T. Devaraju, and S. Asokan. High-pressure resistivity behavior of AsTeIn glasses - the effect of network topological thresholds. *J. Non-Cryst. Solids*, 303:372, 2002.

[161] J. C. Mauro and A. K. Varshneya. Multiscale modeling of $GeSe_2$ glass structure. *J. Am. Ceram. Soc.*, 89(7):2323, 2006.

[162] S. Sen, S. J. Gaudio, B. G. Aitken, and C. E. Lesher. Observation of a pressure-induced first-order polyamorphic transition in a chalcogenide glass at ambient temperature. *Phys. Rev. Lett.*, 97:025504, 2006.

[163] M. Durandurdu. High-density amorphous phase of GeS_2 glass under pressure. *Phys. Rev. B*, 79:205202, 2009.

[164] K. Ramesh. Pressure dependence of glass transition in As_2Te_3 glass. *J. Phys. Chem. B*, 118:8848, 2014.

[165] A. K. Soper. Partial structure factors from disordered materials diffraction data: An approach using empirical potential structure refinement. *Phys. Rev. B*, 72:104204, 2005.

[166] A. K. Soper. On the uniqueness of structure extracted from diffraction experiments on liquids and glasses. *J. Phys.: Condens. Matter*, 19:415108, 2007.

[167] A. K. Soper. Joint structure refinement of x-ray and neutron diffraction data on disordered materials: application to liquid water. *J. Phys.: Condens. Matter*, 19:335206, 2007.

[168] D. A. Keen. A comparison of various commonly used correlation functions for describing total scattering. *J. Appl. Cryst.*, 34:172, 2000.

[169] A. C. Stergiou and P. J. Rentzeperis. The crystal structure of arsenic selenide, As_2Se_3. *Zeitschrift fuer Kristallographie*, 173:185, 1985.

[170] K. Tamura, S. Hosokawa, M. Inui, M. Yao, H. Endo, and H. Hoshino. EXAFS measurements for liquid As_2Se_3 at high temperatures and pressures. *J. Non-Cryst. Solids*, 150:351, 1992.

[171] S. Hosokawa, Y. Sakaguchi, and K. Tamura. X-ray diffraction measurements for liquid As_2Se_3 up to the semiconductor-metal transition region. *J. Non-Cryst. Solids*, 150:35, 1992.

[172] M. Inui. EXAFS Studies of Liquid Semiconductors. *Jpn. J. Appl. Phys.*, 32:165, 1993.

[173] H. Hoshino, Miyanagam T., H. Ikemoto, S. Hosokawa, and H. Endo. The semiconductor-metal transition of liquid arsenic-selenium mixtures at high temperatures and high pressures. *J. Non-Cryst. Solids*, 205-207:43, 1996.

[174] F. Shimojo, S. Munejiri, H. Hoshino, and Y. Zempo. The microscopic mechanism of the semiconductormetal transition in liquid arsenic triselenide. *J. Phys.: Condens. Matter*, 11:L153, 1999.

[175] S. Hosokawa and W.-C. Pilgrim. SemiconductorMetal Transition in Liquid As_2Se_3 at High Temperatures under Pressure. *Phys Stat. Sol. (b)*, 223:145, 2001.

[176] S. Hosokawa, Y. Kawakita, W.-C. Pilgrim, and F. Hensel. Local structures in glassy and liquid As_2Se_3 - an anomalous X-ray scattering study. *J. Non-Cryst. Solids*, 392:153, 2001.

[177] K. Ramesh, N. Ramesh Rao, K. S. Sangunni, and E. S. R. Gopal. Electrical resistivity of Cu doped AsSe glasses at high pressure. *Phys Stat. Sol. (b)*, 235:536, 2003.

[178] S. Hosokawa and K. Tamura. Temperature driven semiconductor-metal transition and structural changes in liquid As_2Se_3. *J. Phys.: Condens. Matter*, 16:R1465, 2004.

[179] M. Inui, Y. Kajihara, M. Matsuda, S. Hosokawa, K. Tamura, M. Yao, Y. Tsuchiya, D. Ishikawa, S. Tsutsui, and A. Q. R. Baron. Inelastic x-ray scattering measurements of dynamical cross-over in liquid As_2Se_3 at high temperature and pressure. *Eur. Phys. J. Special Topics*, 196:167, 2011.

[180] A. L. Renninger and B. L. Averbach. Atomic radial distribution functions of As-Se glasses. *Phys. Rev. B*, 8:1507, 1973.

[181] C. J. Benmore and P. S. Salmon. Structure of fast ion conducting and semiconducting glassy chalcogenide alloys. *Phys. Rev. Lett.*, 73:264, 1994.

[182] S. Xin, J. Liu, and P. S. Salmon. Structure of CuAsSe glasses investigated by neutron diffraction with copper isotope substitution. *Phys. Rev. B*, 78:064207, 2008.

[183] K. J. Pizzey and A. Zeidler. Private communication, 2015.

[184] E. Soignard. Private communication, April 2012.

[185] D. Gerlich, E. Litov, and O. L. Anderson. Effect of pressure on the elastic properties of vitreous As_2S_3. *Phys. Rev. B*, 20:2529, 1979.

[186] H. Kaga, S. Kashida, and S. Umehara. Ultrasonic properties of pure and Ag-doped amorphous chalcogenides (As_2S_3, As_2S_3). *J. Phys. Soc. Jpn.*, 44:1208, 1978.

[187] V. A. Kirkinskii and V.G. Yakushev. A new polymorphic modification of arsenic selenide obtained at high presssures. *Doklady Chemistry*, 182:896, 1968.

[188] J. O'M Bockris and D. C. Lowe. Viscosity and the structure of molten silicates. *Proc. R. Soc. Lond. A.*, 226:423, 1954.

[189] J. F. Stebbins, I. S. E. Carmichael, and L. K. Moret. Heat capacities and entropies of silicate liquids and glasses. *Contrib. Mineral. Petrol.*, 86:131, 1984.

[190] J. E. Shelby. Formation and properties of calcium aluminosilicate glasses. *J. Am. Ceram. Soc.*, 68:155, 1985.

[191] C. D. Yin, M. Okuno, H. Morikawa, F. Marumo, and T. Yamanaka. Structural analysis of $CaSiO_3$ glass by x-ray diffraction and Raman spectroscopy. *J. Non-Cryst. Solids*, 80:167, 1986.

[192] M. C. Eckersley, P. H. Gaskell, A. C. Barnes, and P. Chieux. Structural ordering in calcium silicate glass. *Nature*, 355:525, 1988.

[193] P. H. Gaskell, M. C. Eckersley, A. C. Barnes, and P. Chieux. Medium-range order in the cation distribution of a calcium silicate glass. *Nature*, 350:675, 1991.

[194] T. Taniguchi, M. Okuno, and T. Matsumoto. X-ray diffraction and EXAFS studies of silicate glasses containing Mg, Ca and Ba atoms. *J. Non-Cryst. Solids*, 211:56, 1997.

[195] H. Doweidar. Density-structure correlations in silicate glasses. *J. Non-Cryst. Solids*, 249:194, 1999.

[196] T. Kokubo, H.-M. Kim, and M. Kawashita. Novel bioactive materials with different mechanical properties. *Biomaterials*, 24:2161, 2003.

[197] M. Maiki and P. Echegut. Electrical conductivity of the CaO-SiO_2 system in the solid and the molten states. *J. Non-Cryst. Solids*, 323:131, 2003.

[198] P. Saravanapavan and L. L Hench. Mesoporous calcium silicate glasses. I. Synthesis. *J. Non-Cryst. Solids*, 318:1, 2003.

[199] K. Shimoda, H. Miyamoto, M. Kikuchi, K. Kusaba, and M. Okuno. Structural evolutions of $CaSiO_3$ and $CaMgSi_2O_6$ metasilicate glasses by static compression. *Chem. Geol.*, 222:83, 2005.

[200] M. Solvang, Y.-Z. Yue, S. L. Jensen, and D. B. Dingwell. Rheological and thermodynamic behavior of calcium aluminosilicate melts within the anorthite wollastonitegehlenite compatibility triangle. *J. Non-Cryst. Solids*, 351:499, 2005.

[201] W. Zhao, J. Wang, W. Zhai, Z. Wang, and J. Chang. The self-setting properties and in vitro bioactivity of tricalcium silicate. *Biomaterials*, 26:6113, 2005.

[202] J. R. Jones, L. M Ehrenfried, and L. L Hench. Optimising bioactive glass scaffolds for bone tissue engineering. *Biomaterials*, 27:964, 2006.

[203] R. N. Mead and G. Mountjoy. A molecular dynamics study of the atomic structure of $(CaO)_x(SiO_2)_{1-x}$ glasses. *J. Phys. Chem. B*, 110:14273, 2006.

[204] X. Li, J. Shi, Y. Zhu, W. Shen, H. Li, J. Liang, and J. Gao. A template route to the preparation of mesoporous amorphous calcium silicate with high *in vitro* bone-forming bioactivity. *J. Biomed. Mater. Res., Part B*, 83B:431, 2007.

[205] X. Liu, M. Morra, A. Carpi, and B. Li. Bioactive calcium silicate ceramics and coatings. *Biomed. Pharma.*, 62:526, 2008.

[206] S. Xu, K. Lin, Z. Wang, J. Chang, J. Lu, and C. Ning. Reconstruction of calvarial defect of rabbits using porous calcium silicate bioactive ceramics. *Biomaterials*, 29:2588, 2008.

[207] S.-J. Ding, M.-Y. Shie, and C.-Y. Wang. Novel fast-setting calcium silicate bone cements with high bioactivity and enhanced osteogenesis *in vitro*. *J. Mater. Chem.*, 19:1183, 2009.

[208] C. J. Benmore, J. K. R. Weber, M. C. Wilding, J. Du, and J. B. Parise. Temperature-dependent structural heterogeneity in calcium silicate liquids. *Phys. Rev. B*, 82:224202, 2010.

[209] L. B. Skinner, S. R. Chae, C. J. Benmore, H. R. Wenk, and P. J. M. Monteiro. Nanostructure of calcium silicate hydrates in cements. *Phys. Rev. Lett.*, 104:195502, 2010.

[210] P. C. Hewlett. *Lea's Chemistry of Cement and Concrete*. Elsevier, Amsterdam, 1998.

[211] L. B. Skinner. Private communication, 2015.

[212] T. S. Duffy. Synchrotron facilities and the study of the Earth's deep interior. *Rep. Prog. Phys.*, 68:1811, 2005.

[213] S. Y. Park and S. K. Lee. Structure and disorder in basaltic glasses and melts: Insights from high-resolution solid-state NMR study of glasses in diopside-Ca-tschermakite join and diopsideanorthite eutectic composition. *Geochim. Cosmochim. Acta*, 80:125, 2012.

[214] A. Yeganeh-Haeri, C. T. Ho, J. K. R. Weber, J. Diefenbacher, and P. F. McMillan. Elastic properties of aluminate glasses via Brillouin spectroscopy. *J. Non-Cryst. Solids*, 241:200, 1998.

[215] A. Zeidler, P. S. Salmon, and L. B. Skinner. Packing and the structural transformations in liquid and amorphous oxides from ambient to extreme conditions. *Proc. Natl. Acad. Sci. USA*, 111:10045, 2014.

[216] K. Kawamura. MXDORTO. Japan Chemistry Program Exchange, P029, 1996.

[217] W. Smith and T. R. Forester. DLPOLY2.0: A general-purpose parallel molecular dynamics simulation package. *J. Mol. Graphics*, 14:136, 1996.